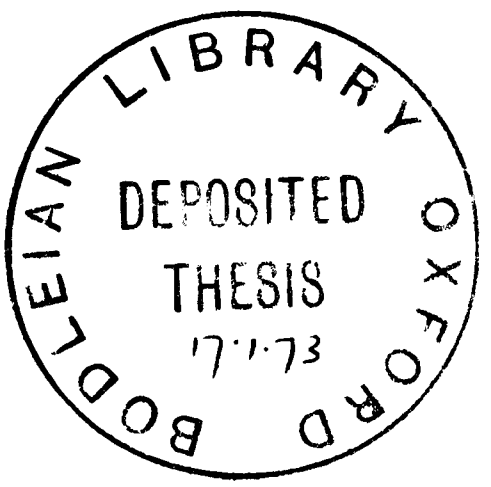
GROWTH AND INVESTIGATION OF EPITAXIAL SEMICONDUCTOR FILMS

A.G. CULLIS, M.A.

Wadham College, Oxford



A dissertation submitted for the degree of Doctor of Philosophy in the University of Oxford. August 1972.

ABSTRACT

The work described in this thesis is concerned with the growth and examination of thin Si and Ge films. These were deposited by sublimation and evaporation techniques in UHV, using apparatus constructed by the author. The source of deposited material was heated by electron bombardment, while the substrates were heated either directly by the passage of an electric current or indirectly upon a Si bar, depending upon their electrical conductivity. The various substrates used were Si and the insulators sapphire, diamond and β - SiC. The grown films were studied by use of the optical microscope, the transmission electron microscope and the scanning electron microscope. The main object of the work was to investigate the structural perfection of these films, to deduce information concerning their growth mechanisms and to compare the observations with suitable theoretical models.

The initial growth of Si films on unpreheated (111) Si substrates, held at temperatures around 900°C, was deduced to have been by nucleation (after an initial induction period), since irregular Si growth centres were produced. These eventually overlapped to give a channelled film containing few crystallographic defects. The dependence of the number density of Si growth centres upon deposition conditions was correlated with different theoretical relationships derived separately by Joyce et al (1967) and Logan (1969). It was deduced that the smallest stable nuclei contained 3 Si atoms, and that the activation energy for surface diffusion of Si was $\sim 0{\cdot}55$ eV (Joyce et al) or $\sim 1{\cdot}1$ eV (Logan). These observations and deductions were compared with analogous results obtained by Joyce et al, who grew Si films by silane pyrolysis. All the results were discussed in relation to initial growth processes, and various suggestions were put forward to account for certain unexpected features. Possible impurity

effects were considered in detail and related to observed film growth characteristics.

When (111) Si substrates were cleaned using heat treatment at 1250°C in UHV surface steps were generated, and these moved across the substrates in a $[\bar{1}\bar{1}2]$ type direction. When Si deposition was initiated the direction of step motion reversed as growth took place. The steps were pinned in many places by impurity particles, which caused the production of deep pits in the grown films. Transmission electron energy loss analysis showed that the particles were SiC. The dependence of the Si film growth upon deposition conditions, the state of the substrate surface and the presence of contaminating gases was also investigated. The nature of both sublimation and growth step motion across substrate surfaces was analysed using theoretical models, and this showed that in the absence of pinning effects, the motion was generally that expected for a clean surface.

Ge films were deposited on to (111) Si substrates at temperatures around 800°C. The thinnest films were composed of growth centres which were mostly triangular in shape, and this showed that initial growth had been by nucleation. A tentative comparison of experimental data with theoretical models indicated that the smallest stable Ge nucleus may have been composed of 4 atoms. TEM examination of the Ge films showed that they grew with the same crystallographic orientation as their Si substrates. However, the films contained many crystallographic defects, and some of the most prominent were continuous networks of misfit dislocations, which occurred over each entire Ge/Si interface. The spacings of the dislocations in such networks were non-ideal, and this was taken to indicate that considerable Ge/Si alloy formation had taken place.

Deposition of Si on to heated (0001) sapphire substrates gave films which grew by initial nucleation with the epitaxial relationships $(111)_{Si}//(0001)_{Al_2O_3}$ and $[1\bar{1}0]_{Si}//[11\bar{2}0]_{Al_2O_3}$. The thinnest films were

composed of equal proportions of two 60° rotational twins, and often contained large numbers of planar defects. However, films a substantial fraction of a micron in thickness contained misorientations of a more general nature, and with increasing thickness ultimately became polycrystalline. High resolution TEM studies provided no evidence of an interfacial misfit dislocation network, but instead indicated that a chemical reaction had taken place between the Si and the sapphire during deposition. Si films were also grown upon both (111) diamond and (111) β-SiC substrates, and once again initial growth was by nucleation. Thicker films on diamond substrates exhibited significant orientation retention despite the very large crystallographic mismatch.

Work was also carried out involving the high resolution TEM studies of closely spaced misfit edge dislocation networks at the Ge/(111)Si interface. It was generally possible to obtain either fringe or structural images depending upon the nature of the diffraction conditions, and this behaviour was examined in detail and discussed with special reference to the work of Thölén (1970). Use of the weak-beam technique (Cockayne et al, 1969) enabled the network structures to be investigated in detail. While it was observed that all the intrinsic dislocation nodes had a relatively uniform extension, the extrinsic nodes had mostly a much smaller extension and approximately half appeared to be completely contracted. Also, using $11\bar{1}$ type Bragg reflections, the intensity of the TEM contrast exhibited by the different kinds of node stacking fault were markedly dissimilar, and depended upon the sense of the deviation from the exact Bragg position.

These studies were extended to observations of dislocation networks produced by deformation in single crystal Si. Measurements of the dimensions of intrinsic nodes, which were all extended, yielded values for the intrinsic stacking fault energy in Si of ~ 58 or ~ 71 ergs cm^{-2}, depending upon the type of measurement employed. Only half the extrinsic

nodes were extended, and this behaviour was interpreted in terms of an energy barrier to node extension. Using $11\bar{1}$ type reflections, the node contrast behaviour was analogous to that observed in the Ge/(111)Si system. This was correlated with the contrast behaviour of inclined stacking faults, and the image intensity appeared to depend upon the sign of (g.R)s. Using $22\bar{4}$ type reflections, dissociated dislocation contrast was interpreted in terms of interactions between the strain fields of the bounding partial dislocations.

In conclusion, suggestions were put forward concerning possible extensions of the present work, and these involved both film growth studies and investigations of TEM contrast behaviour.

CONTENTS

		Page
Preface		i
Introduction		1
Chapter 1	Equipment and Experimental Techniques	5
Chapter 2	The Growth of Silicon on Silicon - Unpreheated Substrates	23
Chapter 3	The Growth of Silicon on Silicon - Preheated Substrates	53
Chapter 4	The Growth of Germanium on Silicon	84
Chapter 5	The Growth of Silicon on Insulators	106
Chapter 6	High Resolution TEM Studies of Crystal Defects	132
Chapter 7	Suggestions for Future Work	166
Appendix A	Review of Heterogeneous Nucleation Theory	172
Appendix B	Review of Selected Nucleation Studies	182
Appendix C	Silicon Surface Structure	184
References		186

PREFACE

This dissertation is an account of work carried out by the author in the Department of Metallurgy, Oxford University, since October 1968 under the supervision of Dr. G.R. Booker. No part of this work has been submitted for a degree at any other University. Also, any studies by other workers mentioned in the text are duly acknowledged, and an alphabetical list of references is given at the end of the thesis.

The author would like to thank Prof. P.B. Hirsch, F.R.S., for the provision of laboratory facilities. Furthermore, he is extremely grateful to Dr. G.R. Booker for his constant encouragement and guidance at all stages of the work. Dr. Booker also supplied the sample of β-SiC grown in the Valdrè TEM hot stage (chapter 3).

To others, who have provided assistance during this work, the author would like to express his sincere thanks. He is particularly grateful to:

Dr. B.A. Joyce (formerly at Plessey Co.Ltd., Caswell, and now at Mullard Co.Ltd., Redhill) for informative and stimulating discussions concerning many aspects of Si film growth.

Dr. B.E. Watts and Mr. R.R. Bradley (Plessey Co.Ltd., Caswell) for helpful advice, and final gas polishing of Si substrate bars.

Dr. M.J. Whelan (Dept. of Metallurgy, Oxford) for discussions concerning the interpretation of TEM images, especially with regard to dislocation network image contrast (chapter 6).

Mr. R.W. Ditchfield (Dept. of Metallurgy, Oxford) for invaluable assistance and advice concerning the electron energy loss analysis studies (chapter 3).

Drs. I.L.F. Ray and D.J.H. Cockayne (Dept. of Metallurgy, Oxford) for discussions concerning the weak-beam technique of electron microscopy (chapter 6).

Dr. E.A.D. White (Imperial College, London) for supplying vapour grown sapphire platelets (chapter 5).

Drs. J. and E. Wilks (Dept. of Physics, Oxford) for supplying diamonds and providing advice on mechanical polishing (chapter 5).

Dr. M.P. Callaghan (General Electric Co.Ltd., London) for supplying the single crystal β-SiC substrate (chapter 5), and also the pure material used in the particle analysis (chapter 3).

Special thanks are due to Drs. W. Bardsley, J. Filby and J.B. Mullin (Royal Radar Establishment, Malvern) for initially stimulating the author's interest in the growth of thin films and for helpful discussions.

The author is also grateful to many members of the Department of Metallurgy (Oxford) for useful discussions and assistance, in particular Dr. C.J. Humphreys, Dr. D.C. Joy, Mr. R.J. Wolff, Mr. H.R. Pettit, Mr. R.H. Donaghay and Mr. G. Dixon-Brown. He also greatly appreciates the careful photographic work of both Mr. C. Bacon and Mr. A. McKnight.

The author wishes to thank the Plessey Co.Ltd. and the Ministry of Defence (C.V.D.) for financial support.

Finally, he would like to express great appreciation to his mother for her untiring efforts in carrying out the typing of this manuscript.

Some sections of the work described in this thesis have been published as follows:

Proc. 7th Intern. Conf. Electron Microscopy, Grenoble, vol.2, pp.125 and 423 (1970).

J. Crystal Growth 2, 132 (1971)

Proc. 25th Anniversary Meeting EMAG, Inst. Phys., Cambridge, p.320 (1971)

Proc. European Conf. Electron Microscopy, Manchester, (1972, in press)

Wadham College,
Oxford
August 1972

A.G. Cullis

INTRODUCTION

Single crystal Si is now used almost exclusively as the starting material for the fabrication of solid state electronic devices such as diodes, transistors, integrated circuits etc. Two different techniques are usually employed to produce the required distributions of impurity atoms (dopants). One of these is diffusion, which is generally a two step process; first an impurity is diffused into the surface of a Si crystal, and next it is driven in to the required depth by thermal treatment alone. The other technique is the direct growth upon a suitably prepared Si substrate of a single crystal Si film with the same orientation as the substrate, and with the required impurity concentration. This process is termed epitaxy. More recently, a third method has been introduced, involving the direct implantation of high energy dopant ions into the Si. While this process shows great promise for the future, it is still in a state of development, and is not widely used at the present time.

In principle, many devices could be fabricated using either diffusion or epitaxy exclusively. However, if more than two diffusions are required in the same crystal area, it can be quite difficult to control the process and to obtain the required impurity distribution. Also, since expitaxial growth, as presently employed for manufacturing purposes, is generally a high temperature process, accompanying impurity diffusion renders it less controllable than might otherwise be expected. Nevertheless, the quality of epitaxial Si films can be significantly better than that of the substrates, and e.g. lateral resistivity variations may be suppressed. In practice, both epitaxial growth and diffusion processes are used sequentially during production procedures, so that the resulting devices have optimum electrical characteristics.

Often, a uniform epitaxial Si film is grown over the whole surface of a suitably doped Si substrate, to produce e.g. an initial p-n junction. Following this, diffusion procedures are used to fabricate the required devices directly in this film.

The methods used for growing such epitaxial Si films have mostly been the H_2 reduction of halogen derivatives of silane (SiH_4), or more recently, the pyrolytic decomposition of SiH_4 itself. Although these chemical methods are capable of producing good quality films, they possess disadvantages such as the occurrence of undesirable impurity diffusion already mentioned, and the possibility of film autodoping by vapour transport of unwanted impurity species in the gas stream. While some work has been done towards the elimination of the first of these by the development of lower temperature chemical processes, both disadvantages may be removed if Si is deposited directly by UHV sublimation or evaporation. Since the use of this technique does not involve a deposition rate limiting chemical reaction, it offers the possibility of Si film growth at much lower temperatures. Therefore, it is important to study the growth processes occurring during UHV deposition, with special emphasis placed on the production of very thin films, which e.g. would be required for the base regions of high frequency transistors.

The epitaxial growth of Si films on Si substrates may be termed homoepitaxy. However in some circumstances it is necessary to produce other film/substrate combinations, and when these are of different materials the growth process is termed heteroepitaxy. For example, this is required for specialized applications such as heterojunction lasers (e.g. GaAs/$Al_xGa_{1-x}As$). Also it would sometimes be desirable to fabricate semiconducting devices in single crystal Si films grown directly on electrically insulating substrates (e.g. Si/sapphire). This could remove some problems concerning high frequency operation.

Quite apart from its technological significance, the growth of semiconductor films is of fundamental scientific importance. The initial film growth is often by nucleation, and experimental measurements may then be used to test current theoretical models. During subsequent growth, crystallographic defects are sometimes formed, and it is of interest to determine their nature and TEM contrast behaviour. Such defects and any associated crystal lattice strain can have a detrimental effect upon electrical properties, especially if they induce impurity precipitation. This provides an additional reason for detailed studies of these defects and their formation mechanisms, since their elimination could be beneficial to film characteristics. Heteroepitaxial systems are of special importance, since a complex defect structure is often produced due to crystallographic mismatch.

For these reasons, and because of the potential technological advantages of the UHV deposition method for the growth of epitaxial Si films, together with the need to produce different film/substrate combinations, a detailed investigation of the growth of such films was undertaken. The main aim of the work was to study the early stages of growth, in order to provide fundamental information concerning the growth mechanisms. A better understanding of these mechanisms should enable the conditions necessary for improved epitaxial film quality to be determined.

To investigate the film growth in sufficient detail, several different methods of examination were employed. These involved the use of the optical microscope, the transmission electron microscope (TEM) and the scanning electron microscope (SEM). The particular systems studied were Si/Si, Ge/Si, Si/sapphire, Si/diamond and Si/β-SiC. Particular attention was given to the nature and origin of defects present in the films.

Chapter 1 gives details of the apparatus and general experimental procedures used during the work. Both film deposition and film examination are described. When Si was grown homoepitaxially on (111) Si substrates in UHV, the form of the growth depended critically upon the state of the substrate surface, just prior to deposition. One cleaning procedure involved heating the substrates to a high temperature for a short period, and chapters 2 and 3 describe the deposition of Si on unpreheated and preheated substrates, respectively. The initial film growth is discussed in detail, and where possible, related to established theory. The heteroepitaxial growth of Ge on (111) Si substrates is described in chapter 4, with special emphasis placed upon the effects of the crystallographic mismatch between the two substances. The deposition of Si on (0001) sapphire, (111) diamond and (111) β-SiC is considered in chapter 5, since these substrate materials have useful insulating properties. In order to make a detailed TEM study of film crystallographic defects, particularly those closely spaced, a high resolution method was required, which involved the use of weakly excited Bragg reflections. This work is described in chapter 7, together with some basic investigations of contrast effects, necessary to fully understand the nature of the film defects, which exhibited some unusual contrast behaviour. Finally, Appendices A and B give an important background to film nucleation phenomena from theoretical and experimental bases, respectively. Appendix C presents information concerning the nature of the (111) Si surface, which has relevance to an understanding of some basic surface processes.

CHAPTER 1 EQUIPMENT AND EXPERIMENTAL TECHNIQUES

	Page
1.1) Introduction	6
1.2) The Vacuum Apparatus	6
1.2.1) Initial Considerations	6
1.2.2) General Description of Apparatus	8
1.2.3) Source Assembly	9
1.2.4) Substrate Assembly and Associated Units	11
1.2.5) Mass Spectrometer	12
1.3) General Deposition Techniques	13
1.3.1) Preparation of Source and Substrate Material	13
1.3.2) The Experimental Run	13
1.4) Optical Microscope Film Examination	16
1.5) TEM Film Examination	17
1.5.1) Specimen Preparation	17
1.5.2) Microscopy	19
1.6) SEM Film Examination	21

1.1) Introduction

This chapter gives a general description of the apparatus and experimental techniques used during the present work. However, certain points of detail, which are of specific importance to individual parts of the work, will be described later in their appropriate sections.

The growth of the thin semiconductor films, which were studied during these investigations, was carried out by sublimation or evaporation onto heated substrates in UHV. While the basic vacuum system had been previously constructed by the author (Cullis, 1968), during the present work it was greatly modified and extended, with e.g. the addition of a high purity gas-feed system and the provision of facilities for mass spectrographic studies. The first part of the chapter is concerned with a description of the various units and their experimental operation.

The remainder of the chapter gives an account of the film examination techniques, which involved the use of both optical and electron microscopy. Emphasis is placed upon important practical considerations, since the microscopes themselves are described in detail elsewhere (e.g. in the instrument manuals provided by the manufacturers).

1.2) The Vacuum Apparatus

1.2.1) Initial Considerations

At the present time, the choice of a clean pump for a conventional UHV system lies between either an ion pump or a suitably trapped vapour diffusion pump. The former has the advantage of inherently clean operation, while it is the more expensive option for a given pumping speed. The pumping unit of the present system used a diffusion pump employing a very low vapour pressure fluid which was trapped by a water cooled Chevron baffle and a bakeable molecular sieve trap (Biondi, 1960).

The design of this trapping unit was based on that evolved by Joyce and Bradley (1966). A molecular sieve trap was preferred to a liquid nitrogen cold trap, since a film of pump fluid could creep through the latter. Also, molecular sieve had a great affinity for polar molecules, such as H_2O and CO, which would have been rapidly adsorbed.

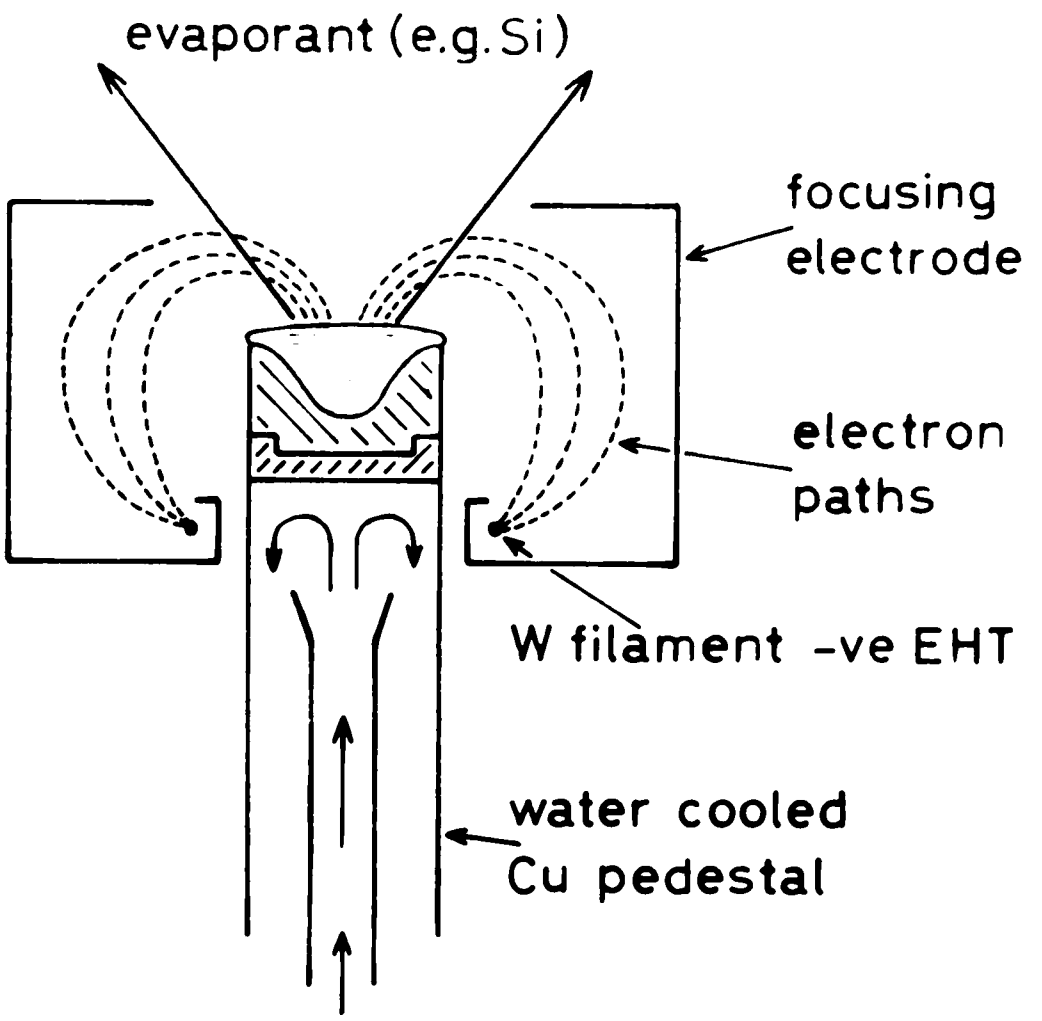
The design of the vacuum system has been completely vindicated by its operational performance. The base pressure of the vacuum chamber was typically in the region of 10^{-10} torr (best ever 5×10^{-11} torr), when the residual gases detected by a mass spectrometer were mainly CO and CH_4, together with a little H_2. The amount of pump fluid vapour present was specifically determined, and found to be negligible. The fluid, Convalex 10, had a cracking pattern which would yield substantial spectrometer peaks at m/e (molecular weight per unit charge) values of 77 and 51 (Craig and Harden, 1966); these were absent down to the limit of detection, around 10^{-12} torr.

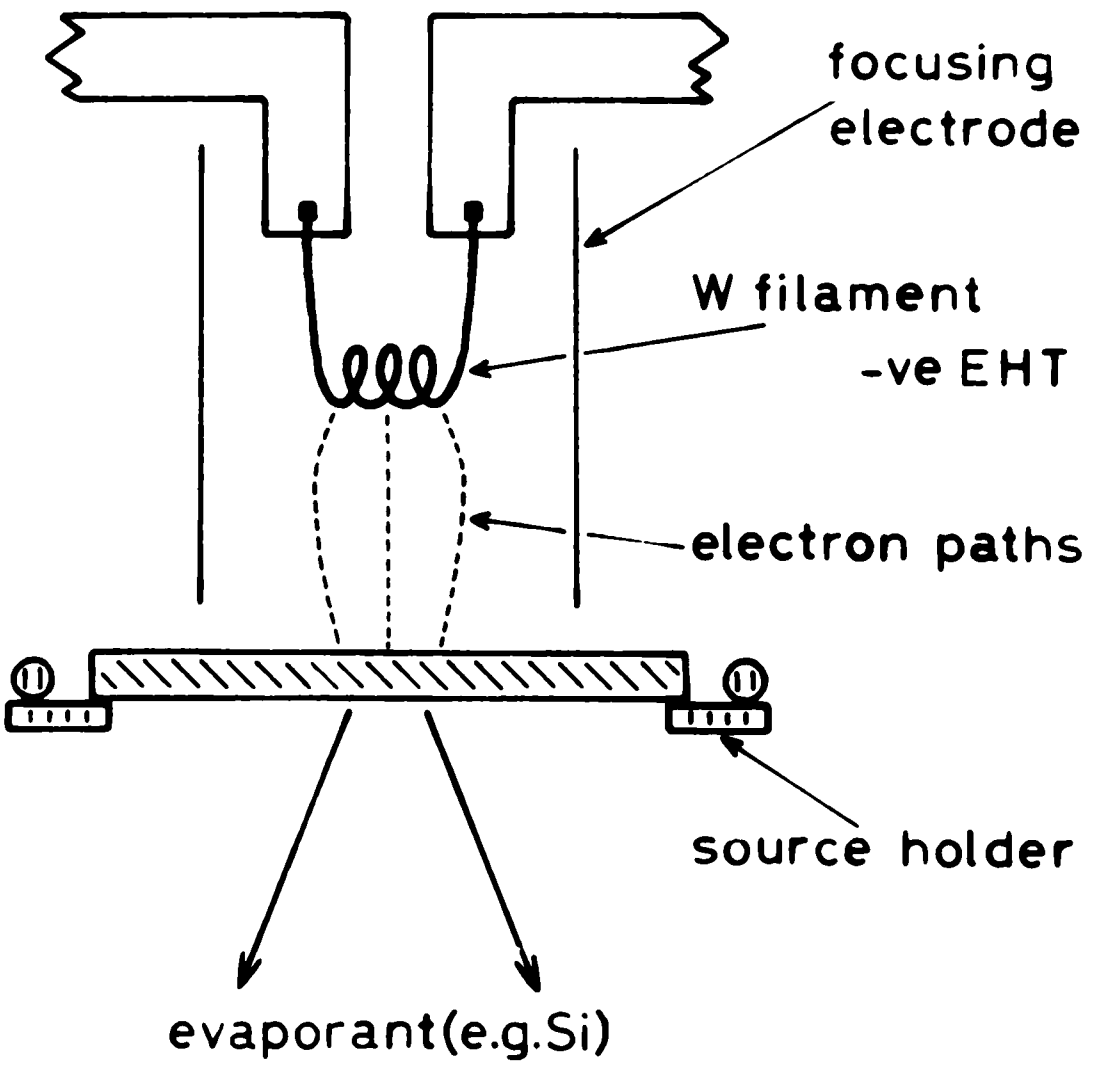
A further point to be noted is the choice of heating techniques for Si substrate and source materials. Joyce and Bradley (1966) used direct resistance heating for their substrates which were bars of Si held in Ta clips. This method was found to work well and the bars were heated uniformly without the introduction of significant contamination. Therefore, this technique was considered to be satisfactory for the present series of experiments.

A contamination-free sublimation/evaporation source for the deposited Si (or Ge) was carefully chosen. For most experiments a directly heated crucible or wire source was considered to be unsuitable because of the great reactivity of e.g. Si at elevated temperatures (see however section 4.3.1). An alternative to these was the conventional type of bent-beam electron bombardment arrangement (fig 1.1a) where the Si is held in a water cooled copper hearth (e.g. Unvala and Booker, 1964).

Fig 1.1a Bent-beam electron bombardment heated source, for sublimation/evaporation (after Unvala and Booker, 1964).

Fig 1.1b Electron bombardment heated source, as used in the present experiments.


evaporant (e.g. Si)
focusing electrode
electron paths
W filament -ve EHT
water cooled Cu pedestal


focusing electrode
W filament -ve EHT
electron paths
source holder
evaporant(e.g.Si)

However, this also has disadvantages which might be serious, since the Si is heated from the side which is exposed to the substrate. It is possible that either stray electrons from the electron gun may strike the substrate, or since evaporated material must pass through the electron beam, the substrate may be subjected to bombardment by ionized atoms. Both possibilities could lead to spurious effects which would serve to complicate existing layer growth problems. Therefore, in the present case in order to avoid these difficulties, a disc of source material was heated by electron bombardment from one side, while sublimation/evaporation took place from the other (fig 1.1b).

1.2.2) General Description of Apparatus

The complete apparatus is shown schematically in fig 1.2. The vacuum chamber, supplied by Vacuum Generators (VG), was of stainless steel construction with flat flanges for gold wire seals, and comprised a 6-way cross (2" diameter tube) linked to a similar 4-way cross. The former contained the substrate and source assemblies (to be described later), together with a 2" viewing port and a Torr-Vac 'wobble-drive' mechanical feed-through which operated a shutter between the source and the substrate. The subsidiary 4-way cross supported the Centronic Q 806 mass spectrometer (also described later) with a VG VIG 10 Bayard-Alpert ionization gauge and a VG M6 UHV leak valve. The relative positions of the units are shown in fig 1.3.

The pumping unit joined the chamber at the 6th remaining arm of the 6-way cross. The unit employed an Edwards E04 diffusion pump with an unbaffled pumping speed of 600 litres sec^{-1}, which contained Convalex 10 fluid produced by Consolidated Vacuum Corporation. This fluid was a polyphenyl ether with a vapour pressure of only 10^{-9} torr at $20^{o}C$ (Holland, 1965). The diffusion pump was connected by gold wire seals

to the vacuum chamber through first a water cooled Chevron baffle, and then the bakeable stainless steel Biondi molecular sieve trap containing Union Carbide sieve type 13X, which had the large pore diameter of 10 Å.

The diffusion pump was backed by an Edwards ES150 mechanical rotary pump, with a pumping speed of 150 litres min^{-1}. The backing line pressure was monitored by a Pirani gauge, and a molecular sieve trap (again using type 13X sieve) was provided to minimize the passage of rotary pump oil vapour into the remainder of the system. Facilities were also provided for admitting dry N_2 into the apparatus, and also if required, for exhausting gas from the apparatus through a flowmeter.

Experimental gases could be admitted to the main chamber through the UHV leak valve, previously mentioned, from a stainless steel gas line. This had a coiled section which could be cooled with e.g. liquid N_2 to form a cold trap, and was isolated from the supply cylinder by a British Oxygen packless control valve model 4353, which permitted pressures lower than 10^{-4} torr to be maintained at its outlet. A gauge in the line indicated pressures in the range from vacuum up to 30 psi.

Bake-out of the Biondi sieve trap required the use of an insulated Electrothermal armoured heater wound around the unit, while bake-out of the main chamber employed an asbestos box containing two 1 kW electric fire bar elements. Part of the gas line was baked by an Electrothermal heating tape, and all heaters were controlled by Variacs.

The complete system is shown in fig 1.4.

1.2.3) Source Assembly

For most experiments the source of deposit was an electron beam heated disc of the appropriate material, and the complete source assembly was mounted on 40 A, 5 kV electrical lead-throughs held in a

Fig 1.2 Schematic diagram of the UHV thin film deposition apparatus.

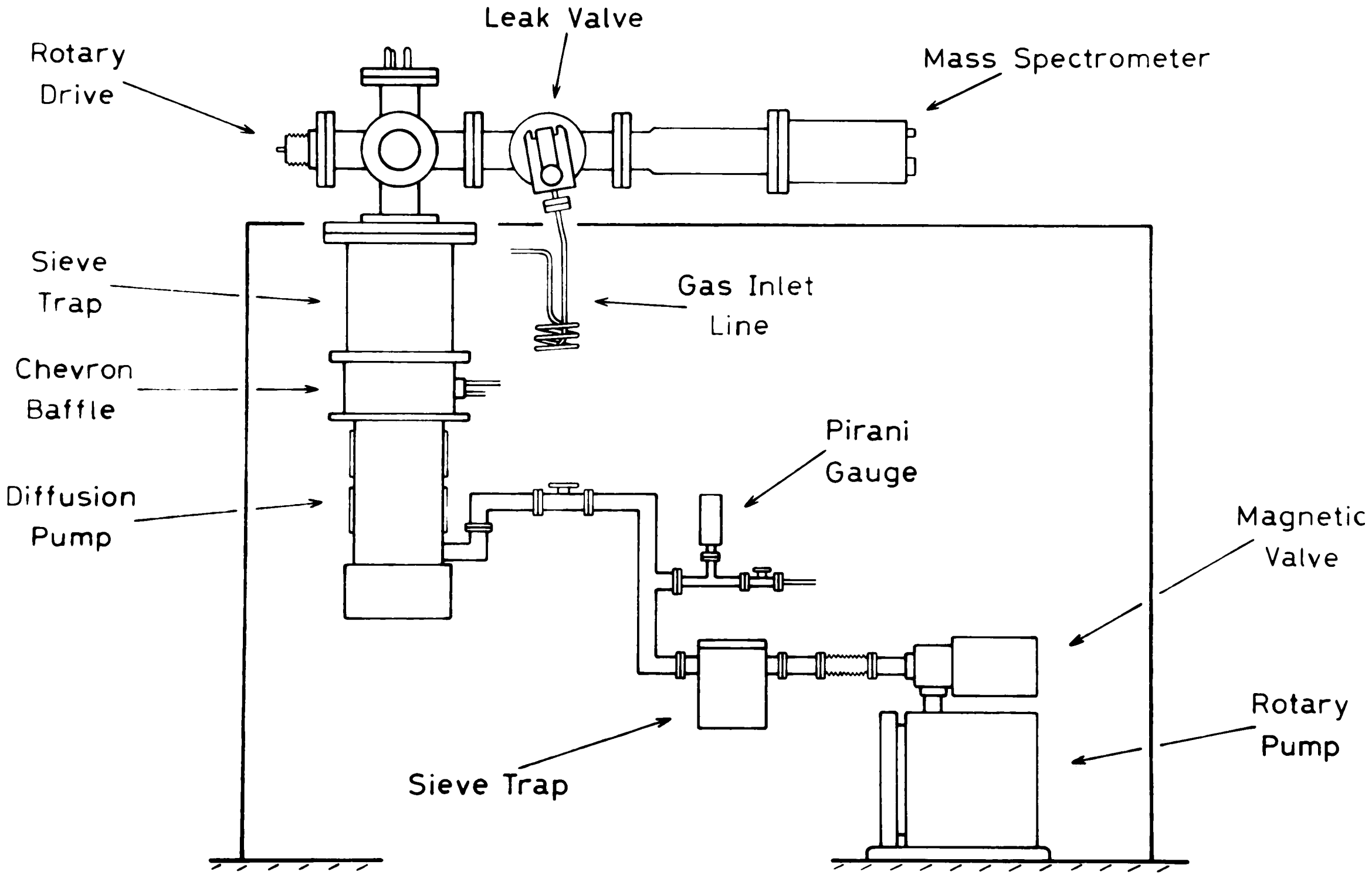
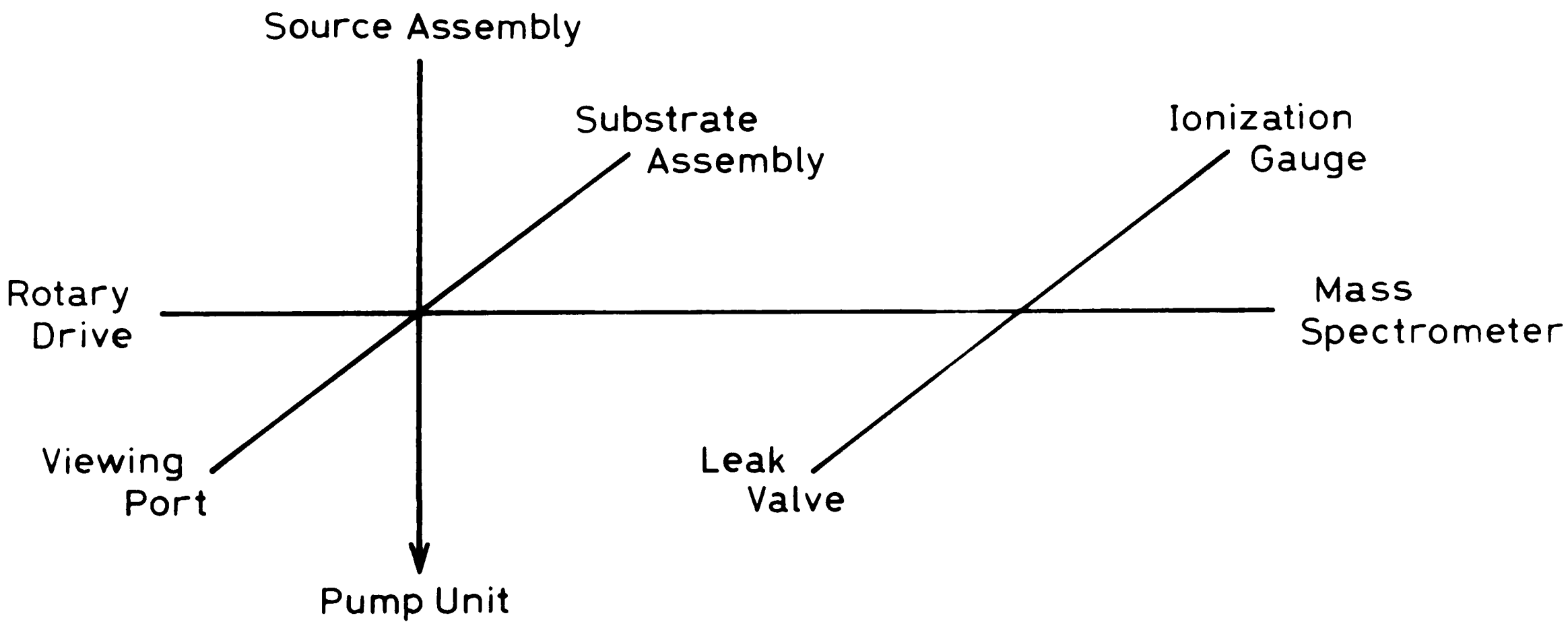

Leak Valve
Rotary
Drive
Mass Spectrometer
Sieve
Trap
Gas Inlet
Line
Chevron
Baffle
Pirani
Gauge
Diffusion
Pump
Magnetic
Valve
Rotary
Pump
Sieve Trap

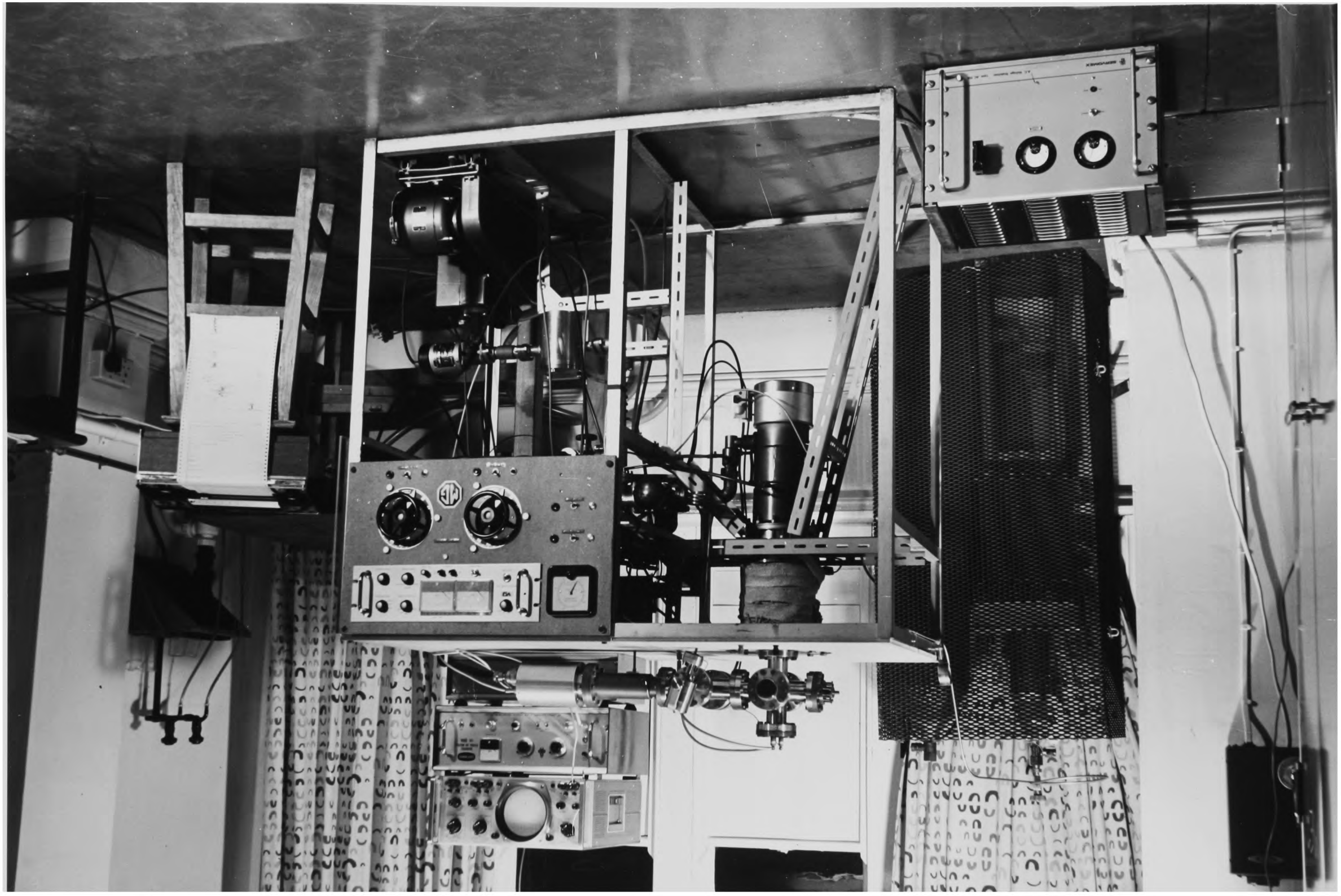
Fig 1.3 Relative positions of vacuum chamber assemblies.



Six-Way Cross

Four-Way Cross

Fig 1.4 The UHV thin film deposition apparatus.



vacuum chamber flange (fig 1.5a). For Si deposition, the disc (20 mm diameter x 1.5 mm thick) was of Wacker, low-oxygen, 300 Ω cm n-type material, while for Ge deposition 25Ωcm n-type Ge was employed. The disc itself was held in an electropolished Mo wire holder, which was in the form of a ring with four spot welded wire protrusions, and these alone touched the disc at four points around its edge. This was the coolest part of the disc since the hot zone was in the central region, and the latter could be melted if necessary, whereupon surface tension forces held the molten droplet in place.

The electron gun used a coiled W filament taken from a Philips 'quartz-iodine' lamp. This filament gave copious electron emission, enabling it to be operated at relatively low temperatures thus minimizing its ability to act as a source of W contamination. Indeed only one filament was required for 4 years of experimental work, after which period there was no noticeable reduction in the W wire thickness. The filament was spot welded to relatively thick stainless steel attachment strips, which were themselves bolted directly to the electrical lead-throughs. A Mo focusing cylinder surrounded the filament, and both were maintained at the same negative EHT potential with respect to the source disc, which was grounded. A screening plate, also at filament potential, was positioned behind the focusing cylinder, and served both to prevent electron bombardment of other structures and to avoid deposition of semiconductor films on the ceramic lead-through insulators.

The electron gun EHT and LT supplies are shown in fig 1.5b, and both were electrically smoothed. High value resistor chains in parallel with the EHT diodes equalized the potential drops across the diodes when they were reverse-biased.

1.2.4) Substrate Assembly and Associated Units

In all of the experiments performed, a Si bar (26 x 6 x 1.5 mm, Lopex grade, low-oxygen, 25Ωcm n-type material) was heated either as the substrate itself, or as the heating element for other substrates. Such bars were held at their ends by chemically polished strips of 0.25 mm Ta, which were themselves bolted to 40 A electrical lead-throughs in a vacuum chamber flange (fig 1.6a). The bars were heated directly by the passage of an electric current derived from the supply shown in fig 1.6b. To be compatible with the negative temperature coefficient of resistance of Si, the supply could be operated in either of two modes: high voltage - low current, or low voltage - high current. In the latter mode, used at temperatures in the deposition range, the variable series resistor provided a higher electrical resistance than the Si bar, which was therefore stabilized against changes in temperature.

The rate of deposition of epitaxial films was determined from the thickness of deposit collected on a glass slide placed adjacent to the substrate bar. A Ta holder shielded the slide almost up to its leading edge so that a step was produced in the deposit at this position. The measurement of the height of this step is described later (section 1.4). Positions laterally along the step were related to corresponding positions on the substrate bar by measurement from a second step produced in both of the deposits by an overlapping Ta reference strip. The complete rate monitor unit (fig 1.7) was supported in a side-arm of the vacuum chamber, and could be moved while inside the chamber by magnetic coupling with an iron 'slug' incorporated in the Ta holder. During an experimental run, the side-arm was cooled indirectly with liquid N_2 so that the rate monitor was maintained at a relatively low temperature.

A shutter operated by the mechanical rotary drive (already mentioned) was positioned between the source and the substrate/rate monitor

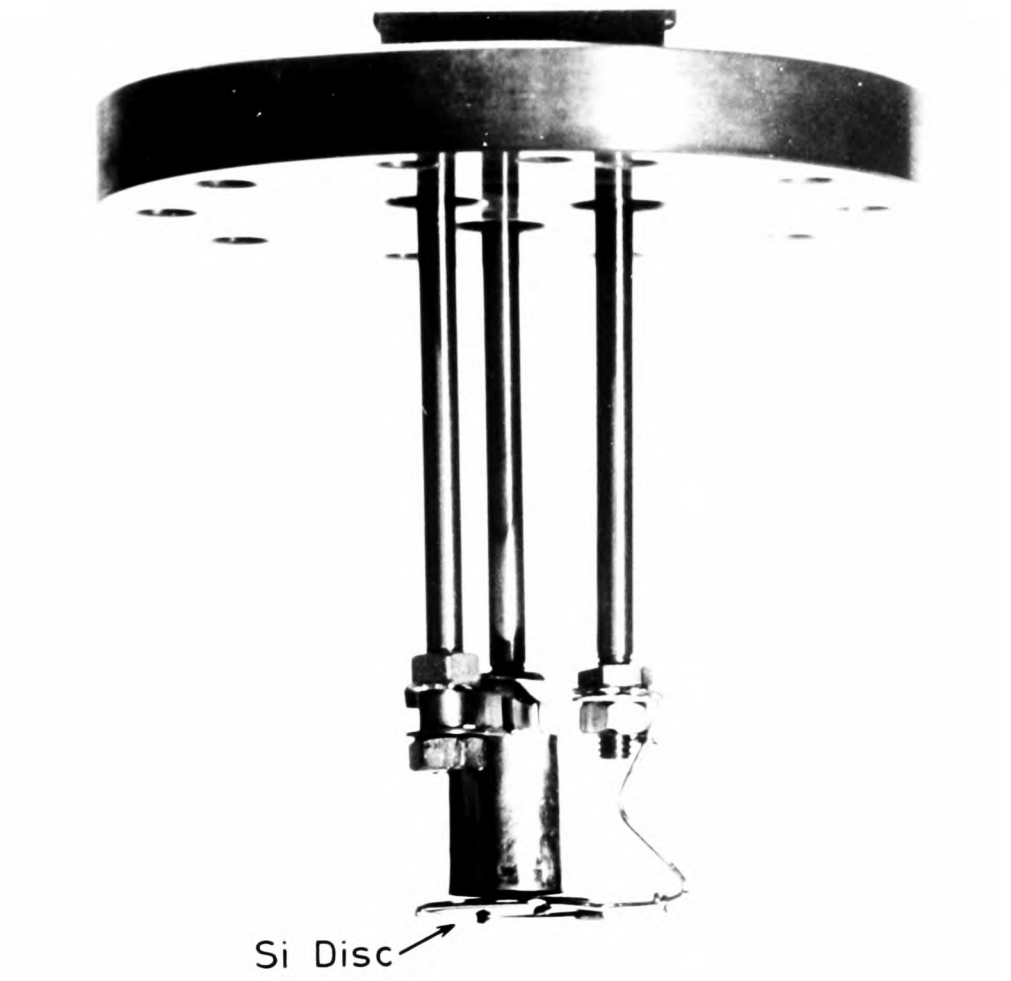
combination. The electropolished Mo shutter was driven by a stainless steel 2 BA nut which moved along a threaded stainless steel shaft attached to the drive. The shutter was maintained in a horizontal plane by a guide bolted to the spare lead-through in the flange shown in fig 1.6a.

1.2.5) Mass Spectrometer

Mass spectrometers at the present time have either quadrupole or magnetic analysers which drive detectors either with or without electron multipliers. The instrument chosen for the present work was the Twentieth Century Electronics Q 806, a quadrupole unit operating with an electron multiplier to give high sensitivity (down to 10^{-12} torr) coupled with a fast scanning capability (1 - 100 amu in 10 msec). A quadrupole analyser was preferred to a magnetic unit since all functions were directly controlled electronically, including the balance of resolution and sensitivity. Also, a fast scan permitted the immediate assimilation of any changes in an observed mass spectrum. A demountable solid state RF generator fitted directly on to the quadrupole head, substantially decreasing the required oscillator power. A compromise in the acceptance of a relatively restricted mass range (1 - 100 amu) was not considered detrimental, since most compounds yield identifiable mass peaks in this region. Further, the range of the instrument could be expanded with the sacrifice of some resolution simply by capacitatively loading the RF oscillator, which would lower its frequency of operation.

Fig 1.5a The standard electron bombardment heated source for sublimation/evaporation, with disc of Si in position.

Fig 1.5b Circuit diagram of the EHT and LT electrical supplies required for the electron gun.


Si Disc

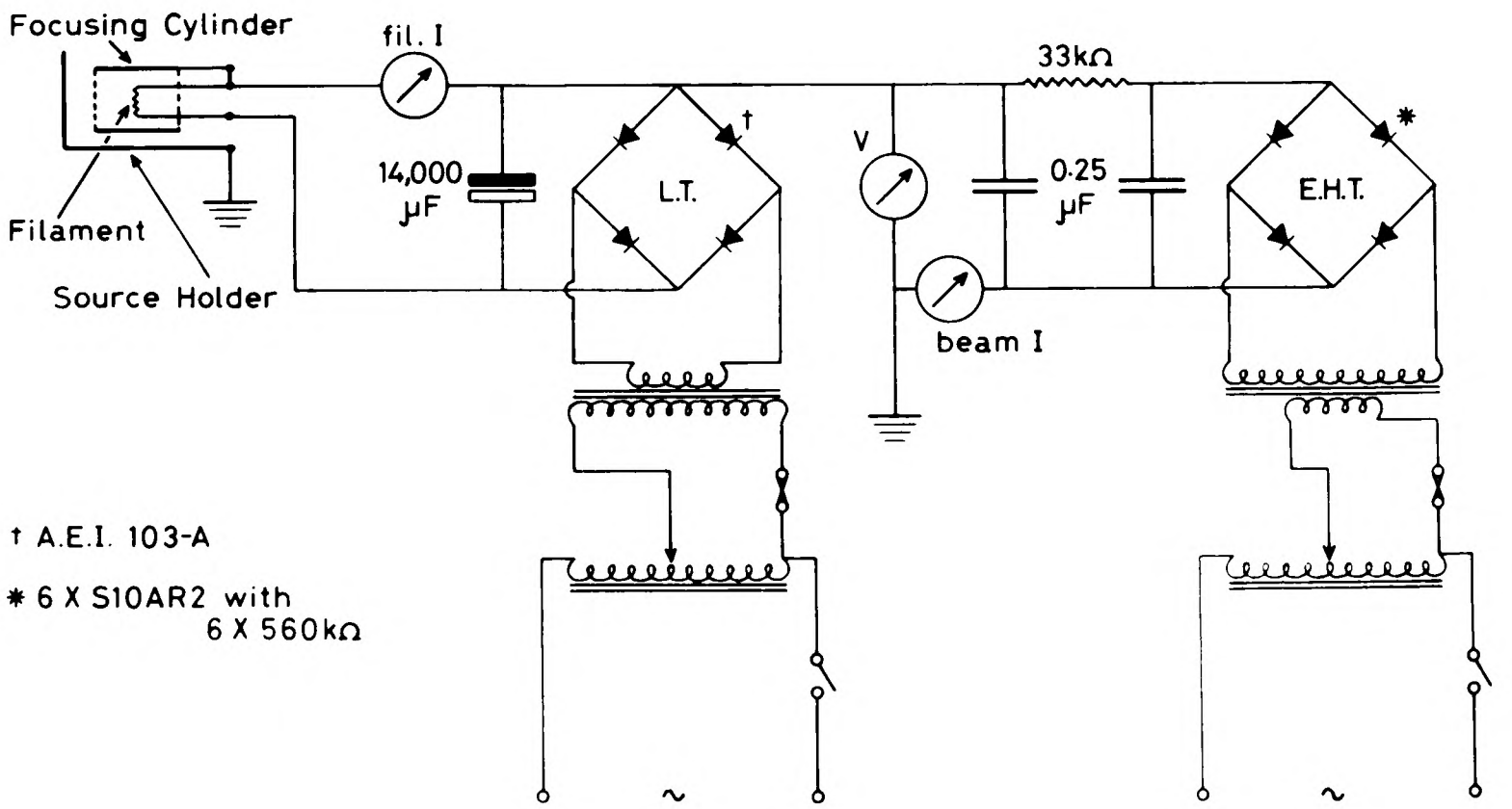
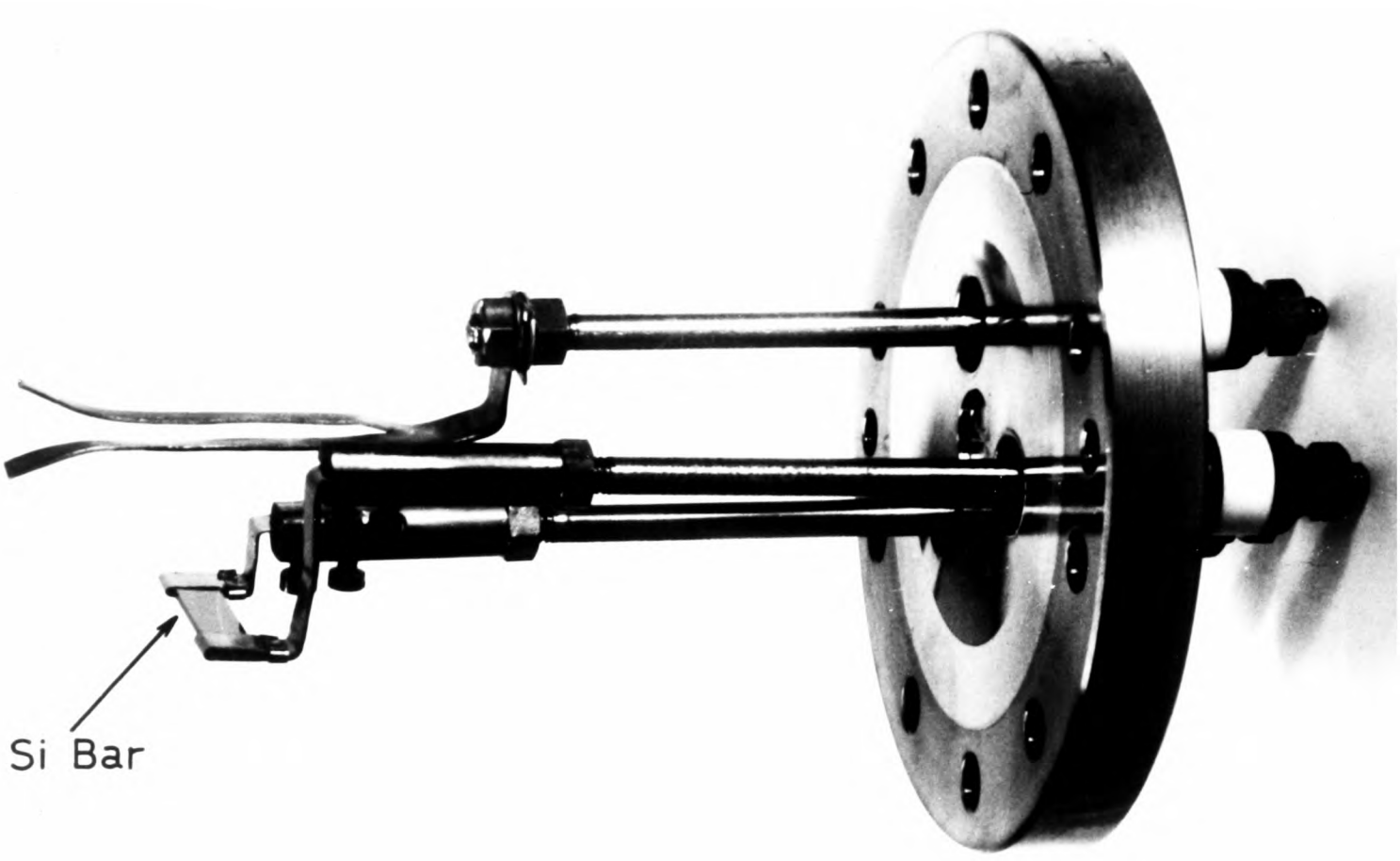
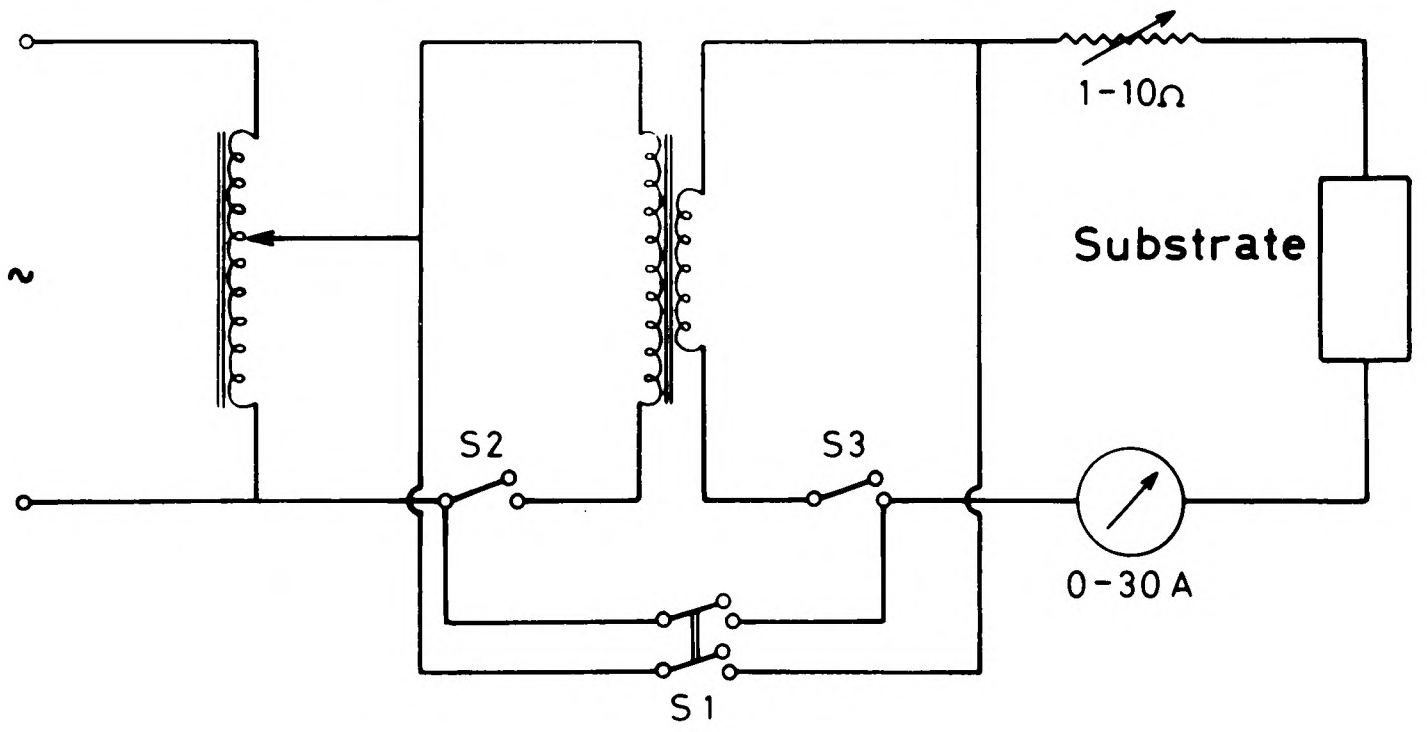

Focusing Cylinder
fil. I
33kΩ
14,000 μF
L.T.
†
V
0·25 μF
E.H.T.
*
Filament
Source Holder
beam I
† A.E.I. 103-A
* 6 X S10AR2 with 6 X 560kΩ

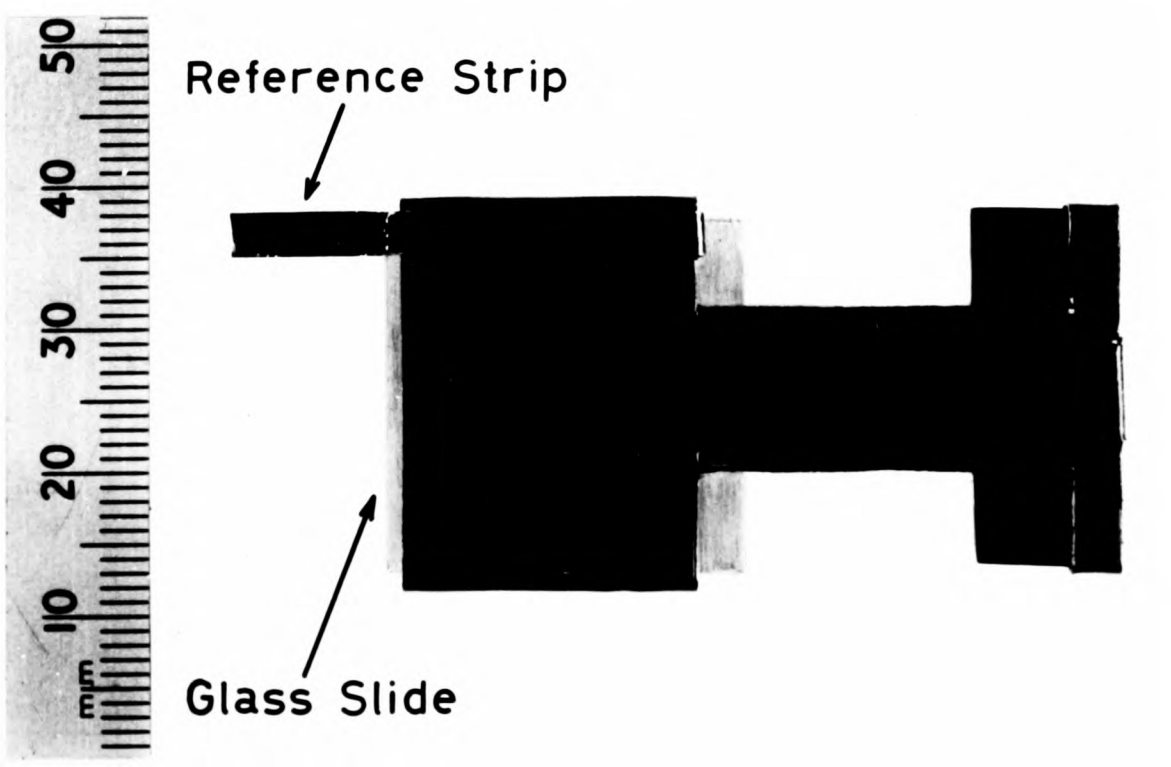
Fig 1.6a The substrate assembly, with Si bar held in Ta clips.

Fig 1.6b Circuit diagram of the electrical supplies required to heat Si substrate bar.

Fig 1.7 The deposition rate monitor assembly with glass slide in position.


Si Bar


1-10Ω
Substrate
S2
S3
S1
0-30A


Reference Strip
Glass Slide
mm
10
20
30
40
50

1.3) General Deposition Techniques

1.3.1) Preparation of Source and Substrate Material

The Si and Ge discs for the electron beam heated source were cut from their respective materials (section 1.2.3) and then mechanically polished, finishing with 0.25μ diamond abrasive. The discs were given a final chemical polish with the appropriate CP4 reagent ($5\,HNO_3$ (conc) + $3\,HF$ (40%) + $3\,CH_3 \cdot CO_2H$ (glacial) for Si, and this mixture + 0.6%Br_2 for Ge), and then carefully washed with distilled water. Their surfaces were slightly undulating on a macroscopic scale, though the brightness of the polish indicated microscopic smoothness.

The preparation of Si substrate bars has been important for much of the work (see chapter 5 for other substrate materials), and these were cut from (111) slices of Lopex grade Si (section 1.2.4). The slices were sawn with a diamond impregnated circular blade from a single crystal rod with [111] axis, and their surface orientation was maintained within $\pm\ 2^\circ$ of (111) by checks made using the Laue X-ray back reflection technique. The slices were polished with carborundum powder, finishing with grade 600, and then the bars were cut out as required. Surface preparation of the bars was continued with Lustrox polish, a ZrO_2 based agent that produced an excellent finish (Dale, private communication) by both mechanical and chemical action, somewhat superior to approximately 0.25μ diamond abrasive. The final polish was provided by treatment with HBr vapour at 1250°C, which yielded a mirror finish of very high quality (section 2.4).

1.3.2) The Experimental Run

After setting up the individual units of the deposition apparatus, the vacuum chamber flanges were sealed with gold wire gaskets. Each of these was prepared from a length of 0.5 mm gold wire which was

annealed and supported with tweezers so that its ends almost touched one another. These were then welded together to give a uniform joint using the flame from a town gas/compressed air torch. On many occasions a gasket was required to seal a vertically located vacuum flange. In such a case, it was initially held in position on its flange by means of strips of flattened gold wire taken from a used gasket which had been re-annealed.

An experimental run was initiated by allowing the pumping unit to obtain a preliminary vacuum in the work chamber, with the leak valve open, of around 5×10^{-6} torr. This usually took 2-3 hours since the molecular sieve in the Biondi trap released H_2O vapour. At this point, bake-out of the chamber and sieve trap was commenced, and by increasing heater power in stages the final temperatures (chamber 300°C, trap 350°C) were attained after a further 3 hours. The gas inlet line between the leak valve and the coiled section was also baked at around 150°C. The complete bake-out was usually allowed to continue for approximately 8 hours, following which the sieve trap was first cooled to below 150°C before the work chamber was also cooled slowly towards room temperature. This procedure ensured that the trap was operating efficiently before UHV was achieved, and the ultimate base pressure was typically around 10^{-10} torr, after closure of the leak valve. If the latter was to be used for the admission of gas during the subsequent run, the gas line was allowed to remain hot until the coiled portion had been cooled to the appropriate temperature to form a cold trap.

In the unusual event of a suspected air leak into the vacuum chamber (indicated by abnormally high pressure coupled with significant mass spectrometer peaks at m/e values of 28 (N_2) and 32 (O_2)), the spectrometer was tuned to scan around m/e = 40 with high sensitivity and low resolution. This would then indicate the possible entrance of

argon, which was next squirted at test points around the chamber until the site of the leak had been determined.

To perform a standard deposition run, the internal shutter was first positioned to completely shield the substrate from the source, and after all electrical connections had been made to the chamber the source was 'run up' towards its operating temperature. The electron beam heated unit was required for most runs, and when the electron gun filament was initially heated, CO was liberated, though later appreciable quantities of CO_2 were evolved as other components became hot. By regulating the EHT voltage, the temperature of the disc of source material was normally held at a dull red heat for some time to permit outgassing to take place. During this and subsequent heating and outgassing procedures, the chamber pressure was not usually allowed to rise above $\sim 5 \times 10^{-8}$ torr. Copper braid was also wrapped around the arms of the vacuum chamber, and the free ends were dipped into dewars filled with liquid N_2. This cooled the chamber walls together with the internal deposition rate monitor, and also limited outgassing problems.

Next, the Si substrate bar was slowly heated, and at first power was supplied directly from the Variac (fig 1.6b) with switch S1 closed (S2 and S3 open). As the temperature of the Si bar increased and its ohmic resistance decreased, it eventually became possible to use the low voltage transformer, and to do this, at an appropriate moment the settings of the three switches were reversed. After carrying out any special substrate heat pretreatment that might have been required, the current consumed by a Si bar was usually 5 - 8 amps to produce a temperature in the usual range 700 - 1000°C. Temperatures were measured by observation through the viewing port with an Evershed disappearing filament pyrometer, and readings were corrected for the emissivity of Si (Allen, 1957). The absolute accuracy of the pyrometer was $\pm$ 5°C (indirect NPL calibration),

while the relative accuracy (between individual readings) was $\pm$ 2°C.

If it was necessary to adjust the position of the deposition rate monitor within the chamber, this was carried out by the use of a magnet. Next, the source was heated to its final required temperature by increasing the EHT voltage, often to around 3 kV giving an electron beam current of 25 - 35 mA. To initiate deposition, when the chamber pressure had fallen to $< 2 \times 10^{-8}$ torr, the shutter was rapidly withdrawn and often used as a selective mask to regulate the process. At the end of a run the ambient pressure had usually fallen to $< 10^{-8}$ torr, and termination was carried out by extending the shutter so that it once again completely screened the substrate and deposition rate monitor from the source. The source and the substrate were then carefully cooled to avoid producing any unnecessary thermal shocks, and both diffusion and rotary pumps were switched off. The backing line valve was also closed to avoid undesirable contamination of the UHV sieve trap with rotary pump oil vapour. When access to the vacuum chamber was later required, the whole apparatus was filled with dry N_2 at atmospheric pressure. Special attention was then given to rapidly transferring the deposition rate monitor to a vacuum desiccator, in which it was held for the short time before measurements were carried out (section 1.4).

1.4) Optical Microscope Film Examination

Initial examination of the overall film structure was carried out with a Leitz Ortholux optical microscope. This was equipped with fluorite apochromatic objectives for normal work, but long focal length achromatic objectives were available for use with a Tolansky multiple beam interferometer. Illumination was provided by either tungsten lamps or monochromatic sources, and either bright-field or phase contrast modes

of operation could be chosen.

The Tolansky interferometer, with a 'sodium' light source, was used principally to determine the thickness of films deposited upon the deposition rate monitor glass slides, and this was accomplished by measuring the height of a step produced in the deposit (section 1.2.4). To enhance the reflectivity of the film surface and to avoid multiple reflections, a uniform layer of Al, ~ 1000 Å thick, was first deposited over the whole slide. This layer accurately reproduced the underlying surface topography (Tolansky, 1960), and the required step height could then be measured with the interferometer, in which a 94% reflecting reference plate was usually installed. This was lowered towards the specimen surface until narrow interference fringes could be seen, and these were then set perpendicular to the step with a suitable overall spacing, by adjusting the mirror tilt controls. Typical fringes are shown in fig 1.8. The wavelength (λ_{Na}) of the incident light was known, so that the required step height was given by the proportional displacement of the fringes at the step edge, which was measured 'in situ' with a graticule eyepiece. 1 fringe displacement corresponded to a $0.5\lambda_{Na}$ step height, i.e. 2947 Å. In general for greatest accuracy, a measurement at a given position was taken as the mean of at least ten separate determinations made using different fringe settings, and these frequently gave results which were reproducible to within $\pm$ 6 - 8 Å.

1.5) TEM Film Examination

1.5.1) Specimen Preparation

Many specimens from Si substrate bars, with Si or Ge films grown upon one of the sides, were thinned to permit film examination using the TEM. The film on the bar was first protected by the application

of a layer of Lacomit (an acid resistant lacquer), and then the treated surface was waxed to a glass slide. The bar was next ground down to a thickness of ~ 0.25 mm, and afterwards 2.3 mm discs were cut from selected regions using an ultrasonic drill. These discs were detached from the glass slide and finally thinned from the substrate side using a jet of chemical polishing reagent (Booker and Stickler, 1962a), usually 13% HF (40%) + 87% HNO_3 (conc). The jet thinning apparatus is illustrated in fig 1.9. The specimen was attached by Lacomit to a Teflon holder, so that the jet of polishing reagent played upon its ground surface. The specimen was gradually 'dished' by the polishing action, and after typically 10 - 20 min the instant of formation of a small hole could be detected by the sudden change in transmitted light intensity. At this time the acid jet was immediately diluted with a stream of tap water to stop the thinning action, and the specimen was removed and examined with a low power optical microscope. If the thinning had been satisfactory, the specimen was detached from the Teflon holder by removing the Lacomit with Analar acetone.

Certain specimens could not easily be thinned by conventional chemical polishing techniques, and accordingly in such cases the ion beam method was chosen. An Edwards ion beam machining unit was used (model IBMA1), and this is shown schematically in fig 1.10. Twin ion guns provided the facility for bombarding specimens from both sides at once, although almost always thinning from one side only was required. Typically, one of the guns would be set to give a 6 kV beam of argon ions yielding a current of 20 - 50 μA over a specimen area of 2 - 3 sq mm.

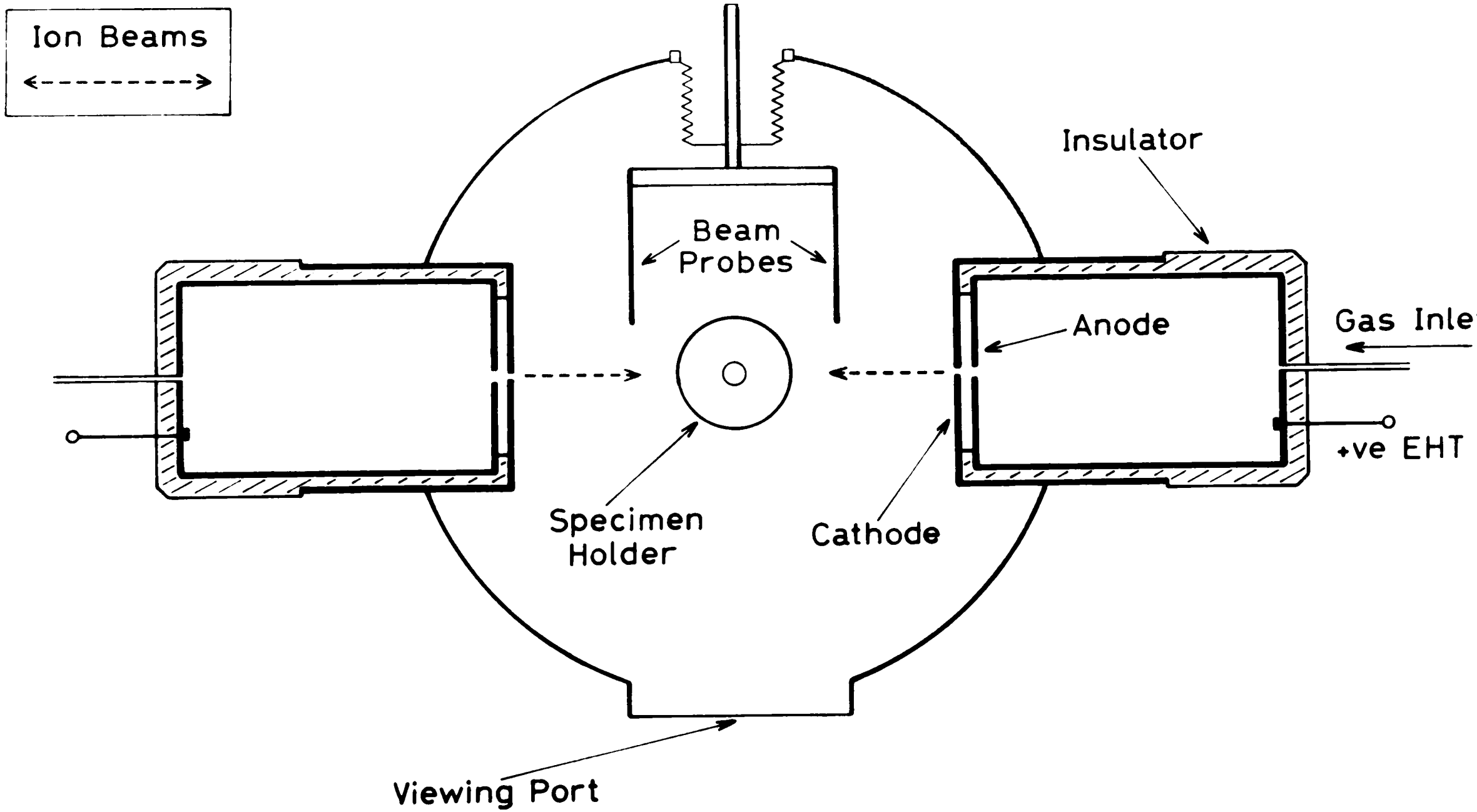
The initial preparation and form of specimens required for this type of thinning was extremely important, since the rate of removal of material was very low. The systems for which this technique was used were Ge/Si, Si/sapphire and Si/diamond, and because each of these has

Fig 1.8 Tolansky multiple beam interference fringes, obtained from an aluminized step in a Si film.

Fig 1.9 Schematic diagram of the chemical jet thinning apparatus.

From Acid
Reservoir
Mirror 45°
Holder
Water
Jet
Perspex
Illumination
To Sink

Fig 1.10 Schematic diagram of the vacuum work chamber in the Edwards ion beam machining unit, model IBMA 1.


Ion Beams
Beam Probes
Insulator
Anode
Gas Inlet
+ve EHT
Specimen Holder
Cathode
Viewing Port

its own special considerations, details of initial preparation will be given later in the relevant sections. However, in general, the specimen to be thinned was mounted in the vacuum work chamber between Ta plates in a holder which could be rotated at a shallow angle, often $\sim 15 - 20^{\circ}$, to an incident ion beam. This arrangement has been shown to be generally satisfactory (Paulus and Reverchon, 1961). Using the stated conditions, the thinning of e.g. sapphire to the point of perforation usually required several hours for completion, when the initial specimen thickness was in the region of 1μ. Thus, this method of TEM specimen preparation, when applied to sapphire, could be 10^3 times slower than the chemical thinning of Si.

1.5.2) Microscopy

For most of the TEM investigations reported in this work a modified Siemens Elmiskop 1A was used. This microscope employed a double condenser lens system, together with three stages of image magnification. An electron accelerating voltage of 100 kV was mostly used, and transmission electron micrographs in the text were taken at this voltage unless otherwise stated. Apertures could be inserted into the condenser system to define the illuminating spot, into the objective lens to produce diffraction contrast and into the intermediate lens for selected-area diffraction work. Also, electromagnetic deflectors were provided above the specimen stage to facilitate experiments which required the use of beam tilting techniques, and an anticontaminator, cooled by liquid N_2, was situated in the same region.

The specimen under observation was usually held in a Valdré holder which permitted tilting in two mutually perpendicular directions at up to $\pm 20^{\circ}$, while being seated in a stage which could be moved laterally. Images could be recorded on photographic plates (Ilford, type EM4) contained

in a camera beneath the final fluorescent screen. The microscope was aligned and operated using standard procedures, and the reader is referred to the instrument manual for details of these together with the principles of operation.

The variation in magnification produced by the instrument under different operating conditions was taken to be the mean of several separate determinations, carried out using diffraction grating replicas of known periodicity. Image rotation, as a function of magnification, was determined by observations of small MoO_3 single crystals, in the usual manner (Hirsch et al, 1965).

In certain investigations (chapter 6) it was necessary to operate the Elmiskop 1A at the highest resolution consistent with preparations which could be made on a reasonably routine basis, as a prelude to each run with the instrument. The electron gun was fitted with a type MP pointed filament (C.W. French Inc.), which had an orientated, single crystal, pointed tip. This enabled an especially small and intense illuminating spot to be obtained, which, for a given image intensity, gave a decreased heat load on the specimen when compared with standard operation. This in turn reduced problems of specimen drift during long (30 sec) photographic plate exposures, and decreased the overall rate of specimen contamination. Also, to maximize the intensity of the final image, the microscope was sometimes operated at 125 kV, which achieved the greatest electron penetration of the specimen.

A key factor in the attainment of optimum performance was the suppression of image aberrations introduced by the objective lens. To minimize spherical aberration, the distance between this lens and the specimen was usually set so that nearly maximum lens excitation was required at focus. Also the electron beam tilting controls were adjusted to ensure that the direct or diffracted beam of interest passed accurately

down the objective lens axis. Furthermore, residual astigmatism was corrected using the objective stigmator, by observations of the overfocus fringe around a hole in a carbon film. This was always carried out with a contrast aperture (of the self-cleaning, thin film type) in position, to ensure that the astigmatism did not change during subsequent use.

Immediately prior to investigations using the microscope, the EHT and lenses were allowed to remain on under operating conditions for ~1 hour, so that general stability would be improved. After these preparations, the highest resolution achieved was regularly better than 10 Å.

Certain investigations were carried out using an energy analysing electron microscope. However, the instrument will be described later in the appropriate section (chapter 3).

1.6) SEM Film Examination

The electron microscope used was a modified Cambridge Instruments Stereoscan Mk 2A, which had preset alignment of its three-lens electron optical column. Operating procedures were standard as detailed in the instrument manual. Usually, no special specimen preparation was required, but it was necessary to ensure that there was good electrical contact between the specimen and its mounting stub, in order to avoid problems of electrostatic charging.

During the present investigations the use of a pointed filament to give a higher electron gun brightness enabled a reduced electron probe size to be used, giving an attendant improvement in resolution. The microscope was used in both the secondary electron and specimen current modes of operation. With the former, it was found to be particularly important to have an evenly aluminised light pipe scintillator, otherwise

the collected signal was degraded. Tilting the specimen to fairly high angles ($\sim 60^{\circ}$ or so) also improved the signal/noise ratio in the secondary electron mode, though the image became progressively foreshortened. However, an electronic signal processing unit which corrected this distortion was available for some of the work.

Electron channelling patterns (Booker, 1970) were obtained from a number of specimen surfaces. In this way, crystallographic information could be rapidly obtained from solid specimens, i.e. there was no need to thin the specimens as for TEM examinations. This technique was in standard use and a control unit was available to provide the necessary functions. These varied depending upon the mode chosen (general or selected-area), but they usually involved modification of the currents in the scan coils and final lens.

CHAPTER 2 THE GROWTH OF SILICON ON SILICON - UNPREHEATED SUBSTRATES

		Page
2.1)	Introduction	24
2.2)	Review of Previous Literature	25
2.3)	Experimental Details	30
2.4)	The Si Substrates	32
2.5)	Silicon Deposition	32
2.5.1)	General Film Structure	32
2.5.2)	Nucleation Behaviour	34
2.6)	Correlation of Present Results with Nucleation Theory	36
2.6.1)	Correlation with the Theory of Joyce et al (1967)	37
2.6.2)	Correlation with the Theory of Logan (1969)	39
2.7)	Discussion	43
2.7.1)	The Number Density Discrepancy	43
2.7.2)	Energy Considerations	46
2.7.3)	Impurity Effects	47
2.7.4)	Silicon Film Structure	50
2.8)	Summary	51

2.1) Introduction

The nature of Si film growth depends upon many factors. In this chapter, results will be presented for experiments which involved the UHV sublimation of Si on to (111) Si substrates, in cases when the deposition took place under conditions which led to the initial formation of optically observable growth centres. These results will be related, as far as possible, to various theories of nucleation, and the complications involved will be discussed in detail. Some of the numerical results, which will be mentioned, were obtained by the author during a Chemistry Honours Degree course at this University (Cullis, 1968). Therefore, they will be clearly marked and attributed to that source when they are encountered. The series of deposition experiments which gave these results were initially conceived as a comparison with a comprehensive series of earlier experiments performed by Joyce et al (1967), who used SiH_4 pyrolysis as the Si growth technique. These workers also interpreted their results in terms of surface nucleation processes, after taking into account the chemical pyrolysis reaction upon which the deposition depended. In the present work, since direct Si sublimation involves no chemical reaction, the theoretical treatment is correspondingly simplified.

Many investigators have found that the form of the growth of epitaxial Si films is a sensitive function of the initial state of the Si substrate surface. Various pretreatments have been devised to improve the uniformity and perfection of the Si films, and an especially favoured procedure has been to preheat the substrate to a high temperature for a short period prior to deposition. The use of this cleaning pretreatment will be described and discussed in the next chapter.

2.2) Review of Previous Literature

A review will now be given of previous literature which deals with Si epitaxial growth related to the work presented in both chapters 2 and 3. The growth of Si films by vacuum sublimation/evaporation has been studied in many laboratories, and the influence of residual ambient gases, deposition temperature, deposition rate and state of the substrate surface have each been investigated. Booker and Unvala (1964, 1965) studied the effect of deposition rate on film perfection for growth with a substrate temperature of 1200°C and vacuum of 10^{-6} torr. They found that the number density of stacking faults was zero for rates $\gtrsim 167$ Å sec^{-1}, while faults occurred in increasingly large numbers as the deposition rate was reduced. They suggested that oxide contamination, originally present on the substrate surface, produced these faults by introducing disregistries into the growing Si film. Since incident Si could act as a getter for this oxide, it was postulated that the efficiency of oxide removal increased with increasing deposition rate.

Many workers have investigated factors which influence the so-called 'epitaxial temperature'; that is, the growth temperature below which deposited Si films are either polycrystalline or amorphous. In general, prevailing vacuum, deposition rate and substrate orientation have a decisive effect. Thus, Unvala and Booker (1964) found it to be 1100°C at 10^{-5} torr on (111) Si, Handelman and Povilonis (1964) 830°C at 10^{-8} torr, Widmer (1964) 550°C at 10^{-10} torr and Jona (1966), using very low deposition rates, found 400°C at 10^{-10} torr on (111) Si and as low as room temperature on (100) Si. Weisberg (1967) used low-oxygen Si source material, and found that even with a vacuum of 10^{-8} torr the epitaxial temperature could be as low as 450°C on (111) Si and 380°C on (100) Si. Methods of film examination were often electron diffraction techniques, and one criterion for the presence of an initially clean (111) Si substrate surface was

taken to be the development of a Si (111)-7 x 7 low energy electron diffraction (LEED) pattern, (see Appendix C).

Thomas and Francombe (1967 a, b) carried out LEED and TEM studies of thick homoepitaxial Si films grown on substrates cleaned by being preheated in vacuum. They found that at 10^{-10} torr the films could be stacking fault free at substrate temperatures as low as 600°C on (111) Si and 400°C on (100) Si. They further correlated the appearance of faults below 600°C on (111) Si with the development of a mixed Si (111)-5 x 5 and Si (111)-7 x 7 LEED pattern obtained from the growing surface. More recently, these investigators (Thomas and Francombe, 1971) showed that there was a strong correlation between the type of surface structure generated and the metallic impurity content of the Si substrates, as estimated from minority carrier lifetimes, and they speculated as to the exact significance of the Si (111)-7 x 7 LEED pattern. TEM indicated that the number density of stacking faults in the grown films increased progressively as the growth temperature was lowered and the deposition rate increased (compare Unvala and Booker, 1965). Also the films deposited on high lifetime Si contained fewer faults than those grown on low lifetime substrates. These results suggested that the faults originated on the substrate surface at microprecipitates consisting of fast diffusing, low solubility, impurity species, e.g. Fe, Cu, Au, etc.

Thomas and Francombe (1969) also extended their experiments with objectives, (a) to determine whether doped homoepitaxial films could be grown reproducibly at temperatures in the range 500 - 650°C with uniform impurity content and good structural quality; and (b) to attempt the growth of good quality p - n junctions at these temperatures. They found that uniform dopant transfer from Si source to growing film did not take place until $\frac{1}{3}$ to $\frac{1}{2}$ of the source material had been consumed. Further, out - diffusion of dopants from Si substrates occurred while the initial

cleaning at high temperature (1200°C) was in progress, and although this was most undesirable, no alternative pretreatment appeared to be satisfactory. Under optimum conditions p - n junctions were fabricated with sharp resistivity profiles and very good reverse breakdown characteristics. p - Films grown on n - substrates were found to be somewhat better than n - films grown on p - substrates. In an effort to eliminate the effect of dopant out - diffusion from the substrates, the sequential deposition of two films was carried out, to form structures such as $n^- p^+$ on n. While the results were generally good, for certain combinations graded junctions were formed with cross doping between the two Si sources.

An important series of experiments was undertaken by Joyce and Bradley (1966) and Joyce et al (1967, 1969a), who grew epitaxial Si films on gas polished Si substrates by the pyrolysis of a molecular beam of SiH_4. The reaction was constrained to be completely heterogeneous at the substrate surface, since the beam was collision - free to eliminate any possible homogeneous component of the decomposition. Deposition took place in a chamber which ultimately had a base pressure in the region of 10^{-10} torr, and for the first experiments the substrates were given no heat pretreatment in the apparatus. When pyrolysis was initiated no growth occurred for a well-defined period, and it was concluded that the inhibition was produced by the presence of a residual oxide film on the substrate surface. The length of this induction period varied in a regular manner with both beam intensity and substrate temperature, consistent with the hypothesis that the surface oxide was gradually removed as volatile SiO due to combination with deposited Si.

$$Si + SiO_2 \rightarrow 2\,SiO\uparrow$$

When growth did commence, geometrical growth centres were formed, and their number density rapidly reached a saturation value, N_s. The centres had a high crystallographic perfection, and were triangular on (111) Si

and square or rectangular on (100) Si. On substrates of both orientation, N_s values exhibited clearly defined dependences upon substrate temperature and SiH_4 beam intensity, and these were compared with nucleation theory assuming complete condensation of deposited Si (see Appendix A and section 2.6). From this analysis, it was shown that for growth on a (111) Si surface, 3 Si atoms formed the smallest stable nucleus, and the activation energy for surface diffusion of Si was $\sim$ 2.5 eV. For (100) Si surfaces, the corresponding values were 4 Si atoms, and 1.75 eV, respectively.

These workers also investigated the effect of contaminants on initial growth behaviour. For the above mentioned system, when contaminating hydrocarbon vapours were admitted, some of the growth centres were irregular and in twin orientation, occasionally with doubly twinned sections (Booker and Joyce, 1966). Further studies (Joyce et al, 1969b) with substrates which had been preheated in UHV to high temperatures prior to deposition, showed that the mode of growth gradually changed from three-dimensional growth centre formation to a 'two-dimensional' mechanism, as the preheating temperature was increased in the range 1100 - 1200^{o}C. This latter work was carried out in collaboration with Charig and Skinner (1969), who studied the substrates with LEED and Auger spectroscopy. They found that although carbon was initially present on Si substrates, after heat pretreatment at even 1100^{o}C it was no longer detectable, and a Si (111)-7 x 7 LEED pattern which increased in sharpness at the highest pretreatment temperatures was obtained. It was postulated that a fraction of a monolayer of a carbon impurity was sufficient to change the form of Si growth. To confirm this idea, previously cleaned substrates were recontaminated with carbon by exposure to ethylene. It was found that Si deposition once more gave three-dimensional growth centres if the exposure was sufficient to give an amount of carbon detectable by Auger

spectroscopy, although the Si (111)- 7 x 7 LEED pattern was comparatively insensitive to the effects of this recontamination. Other contaminating gases such as O_2, CO and CO_2 yielded different and relatively insignificant effects.

Carbide contamination of (111) Si surfaces was also studied by Henderson et al (1970, 1971). Surface preparation involved steam oxidation followed by various procedures including HF etching and H_2 annealing. Reflection high energy electron diffraction (RHEED) studies showed that UHV heat treatment in the range 800 - 1000°C produced a surface covered by well orientated β-SiC crystallites. These were misorientated for treatment at temperatures between 1000 - 1100°C, while initial heating to above 1100°C yielded surfaces showing no trace of β-SiC. The gases CO and CO_2 were evolved when all substrates were heated above 800°C. It was also found that if a carbide - free surface was left in vacuum for a sufficient time (10^5 secs at 5×10^{-10} torr) or re-exposed to air, β-SiC reappeared on heating to 800°C.

TEM studies of surface replicas showed that the β-SiC, produced by treatments at 950°C and 1050°C, was present as particles ~ 400 Å in size within protuberances at the surface. Their number density varied from 2×10^7 up to 6×10^9 cm^{-2}, and they were seen to have pinned steps which had been moving across the Si surface. Surfaces treated at only 850°C exhibited no particles down to the limits of detection (20 Å). In general, the presence of β-SiC was correlated with a chemical reaction between the Si surface and a carbon-containing adsorbate, demonstrated to be of gaseous origin, or possibly present as a residue from the initial chemical cleaning.

Abbink et al (1968) deposited Si by UHV sublimation on to (111) Si substrates which had been preannealed at 900°C in vacuum. A high resolution TEM replica technique showed that after this pretreatment, a substrate

surface was covered by numerous thermal etch steps pinned at contaminant β-SiC particles. Nevertheless, such a surface gave a Si (111)-7 x 7 LEED pattern. Initial Si film growth was by nucleation, giving observable growth centres surrounded by a roughened surface. The surface of a thicker film was found to be covered by pinned growth steps, often only one atom high. By an analysis of the diffusion processes, the activation energy for surface diffusion of Si was found to be 0.2 eV (compare Joyce et al, 1967) and a minimum value of the self diffusion coefficient at 800°C was estimated to be 10^{-3} $cm^2 sec^{-1}$. Straight surface growth steps were found to move in the opposite direction to etch steps ($[\bar{1}\bar{1}2]$ as opposed to $[11\bar{2}]$), although there was some uncertainty about the crystallographic notation used.

2.3) Experimental Details

The series of experiments described here concern Si deposition at rates around 3×10^{-2} Å sec^{-1}, on to (111) Si substrates which had been heated directly, whilst in the vacuum apparatus, to deposition temperatures in the range 800 - 1000°C. The substrate bars received no form of heat treatment prior to deposition (this alternative case is studied in the next chapter). The general experimental details have already been given (section 1.2), but some special considerations concerning the measurement of deposition rate are now mentioned.

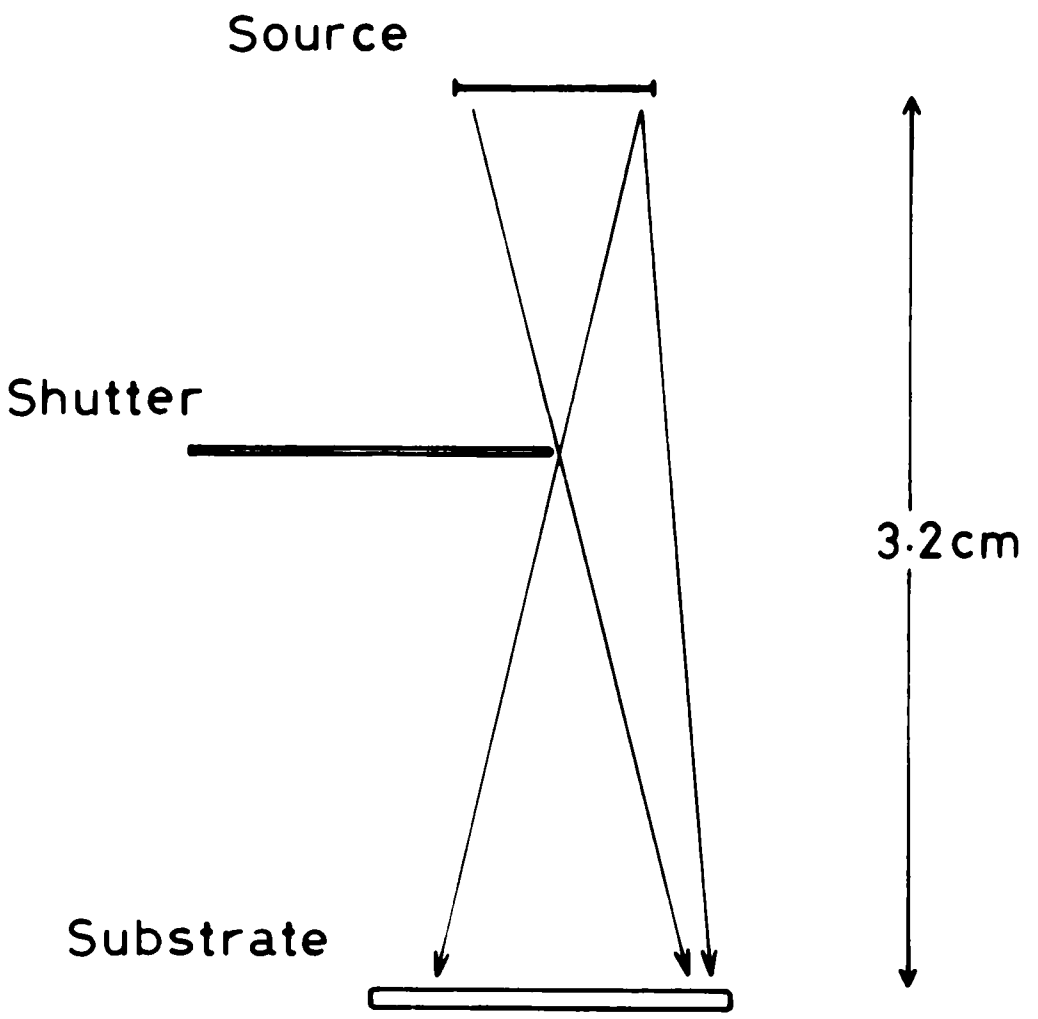
The deposition rate at a given point on the substrate bar was determined by extrapolation from that deduced at the nearest point on the rate monitor glass slide, itself obtained from deposition time and Si thickness measurements (section 1.3.1). Two small corrections were applied to produce this extrapolation. The first was a factor to allow for the difference in position between the substrate bar and the glass

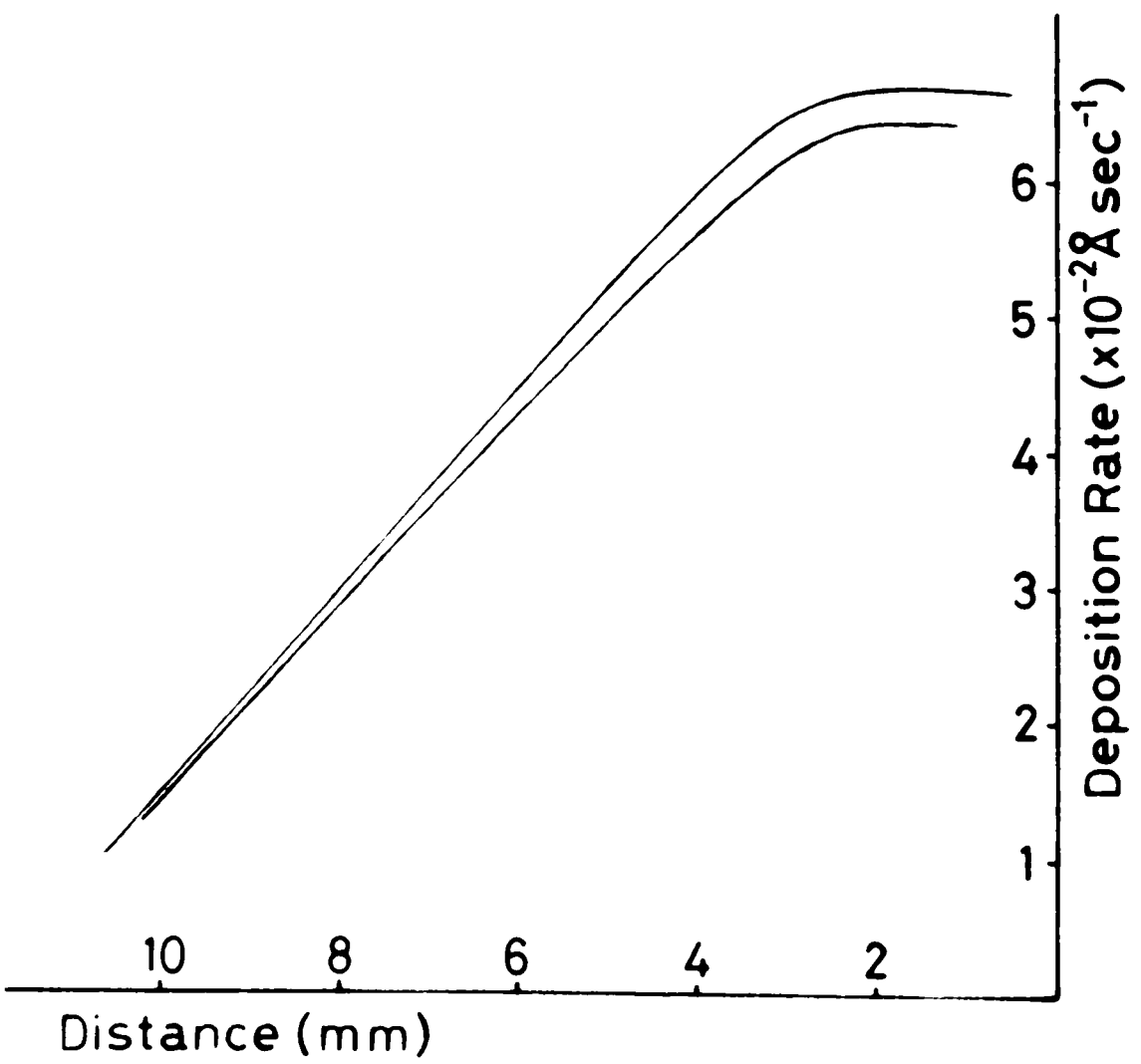
slide. A schematic diagram showing the geometrical relationship between source disc, shutter and substrate bar is given in fig 2.1. The actual source of Si atoms was, in fact, a short line in the centre of the heated disc, orientated parallel to the length of the substrate bar and with approximate dimensions 7 x 2 mm. This configuration was produced by the emission characteristics of the coiled electron gun filament, and the line source was often set at temperatures around 1300°C to produce the desired deposition. The straight-edged shutter below the source cast a diffuse shadow upon the substrate bar, and in the region of lowest deposition rate the effective source size was a hot zone approximately 2 x 2 mm. Since it was arranged that accurate deposition rate measurements were only required for the deposit in this region (for nucleation data, section 2.5.2), the source was treated as a mathematical point and the correction was calculated by simple geometrical reasoning. The magnitude of this correction was typically $< 10\%$.

The second correction was an allowance for the fact that the Si deposited on the cooled glass slide would be amorphous, and not crystalline as was the deposit on the substrate bar. Based on the work of Richter and Breiting (1958), the magnitude of this second correction was always taken to be 10%. Fig 2.2 shows the variation of deposition rate along the edge of a typical deposition rate monitor glass slide; also shown is the corrected curve which applies to the adjacent edge of the substrate bar. Two points should be noted. First, the two corrections tended to cancel each other, so that the corrected curve is only slightly displaced from the measured one. Second, any small errors possibly present in the correction factors would make little difference to the subsequent interpretation of trends in the nucleation data, because any such minor errors would be virtually constant percentages, and therefore discrepancies of a relative nature would not be introduced.

Fig 2.1 Diagram showing relative positions of source disc, shutter and substrate, and also illustrating the way in which the shutter cast a diffuse shadow along a substrate bar.

Fig 2.2 Diagram illustrating the form of the variation in deposition rate along a substrate bar: upper curve obtained directly from thickness measurements; lower curve after application of density and distance corrections (see text).


Source
Shutter
Substrate
3·2cm


Deposition Rate (x10⁻²Å sec⁻¹)
1
2
3
4
5
6
10
8
6
4
2
Distance (mm)

2.4) The Si Substrates

The detailed preparation of (111) Si substrate bars has already been given in section 1.3.1. Optical microscopy of the as-received gas polished substrates revealed a mirror surface with no large scale structure. Use of the TEM showed such surfaces to be featureless to the limits detectable using thickness fringe contrast. These observations are entirely consistent with those of Joyce et al (1967) who found that their similarly prepared substrates also had apparently featureless surfaces.

After such substrates were placed in the vacuum chamber there were undoubtedly many oxygen- and carbon-containing impurity species present on their surfaces (Joyce et al, 1969b). The way in which these behaved on heating to a deposition temperature in the range 800 - 1000°C, however, is uncertain. While substrates in the present series of experiments were not themselves examined, Booker and Joyce (1966) and Joyce et al (1967) showed, by the use of RHEED, that in their experiments such surfaces remained relatively 'clean', and no β-SiC was formed. Since substrates used in the present experiments received a preparation identical to that of substrates used by Joyce et al, it is reasonable to expect that they also behaved similarly when heated in UHV.

2.5) Silicon Deposition

2.5.1) General Film Structure

During previous experiments by the author (Cullis, 1968) it was shown that when UHV deposition of Si on to a (111) Si substrate was initiated, no growth took place for a period which depended upon deposition conditions. This induction period was observed to increase with decreasing deposition rate, but little more than this qualitative dependence can be given, since only a small number of measurements were made. The main

difficulty lay in the precise detection of the onset of growth. After the induction period was completed, when Si growth took place at rates of $\sim 10^{-1}$ to 10^{-2} Å sec^{-1} on substrates held at temperatures in the range 800 - 1000°C, optical microscopy showed that irregular growth centres occurred.

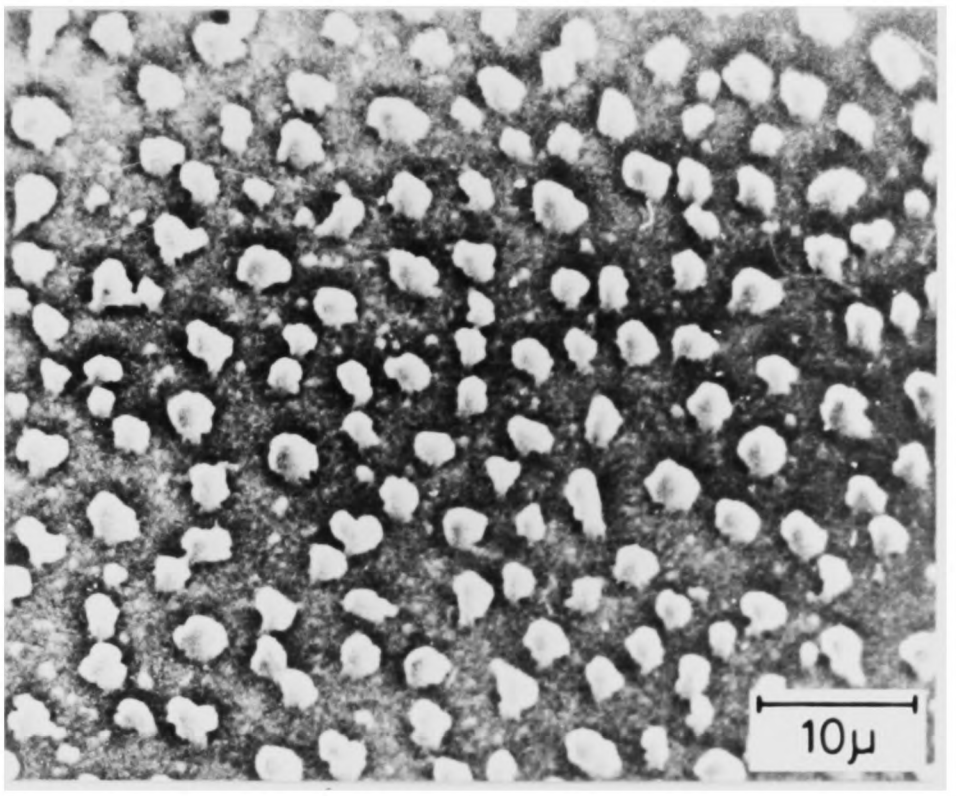
In the present work, further experimental runs were carried out, and considerably more detailed examinations of the growth behaviour were performed. These results confirmed the previous findings, but also provided additional information. Thus, a substrate surface roughening was found to be present between the growth centres (fig 2.3). The TEM showed this roughening to consist of numerous extremely small centres, unresolvable by optical microscopy, and in various stages of overlapping. Fig 2.4 shows such structure at an early stage of growth using TEM thickness fringe contrast. A is one of the larger centres, i.e. one that could just be seen with the optical microscope.

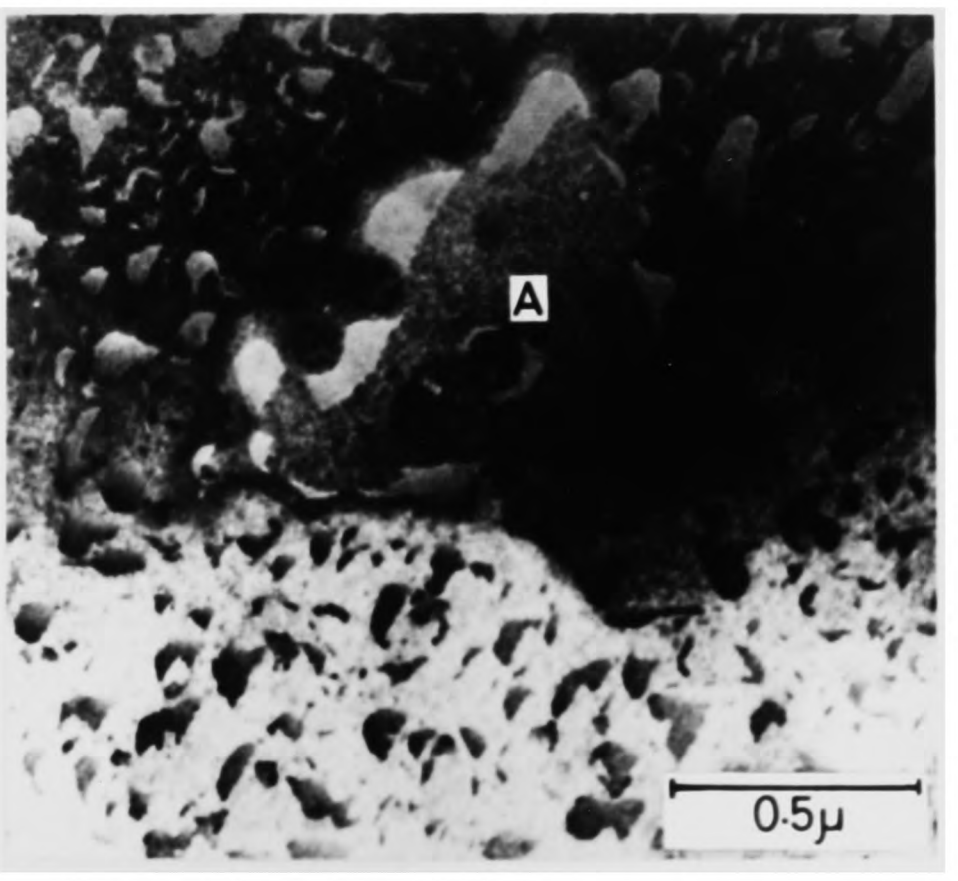
Fig 2.5 shows optically observable Si centres at a later stage of growth. None of the centres contained any stacking fault defects, and dislocations were only occasionally present. However, an array of fine particles was present in the interfacial region between the deposit and the substrate. The substrate surface between the larger centres was covered with an irregular thin growth structure, presumably formed by overlapping of the previously described minute growth centres. For a given rate of deposition, the rate at which the larger centres grew laterally and overlapped was observed to vary from substrate to substrate. Occasionally, the larger centres spread and overlapped early in the growth, giving a semi-continuous irregular structure, for a mean deposit thickness of only 100 - 200 Å. However, usually the centres had become substantially overlapped only after $\simeq 500$ Å of Si had been deposited. The films then gradually assumed a channelled or worm-like appearance, and fig 2.6 shows

Fig 2.3 Si growth centres on (111) Si substrate. (Optical micrograph, phase contrast)

Fig 2.4 Optically observable Si growth centre at A surrounded by background growth. (Transmission electron micrograph, thickness fringe contrast)

Fig 2.5 Si growth centres at a later stage of growth than shown in fig 2.4. (Transmission electron micrograph)


10μ


A
0·5μ

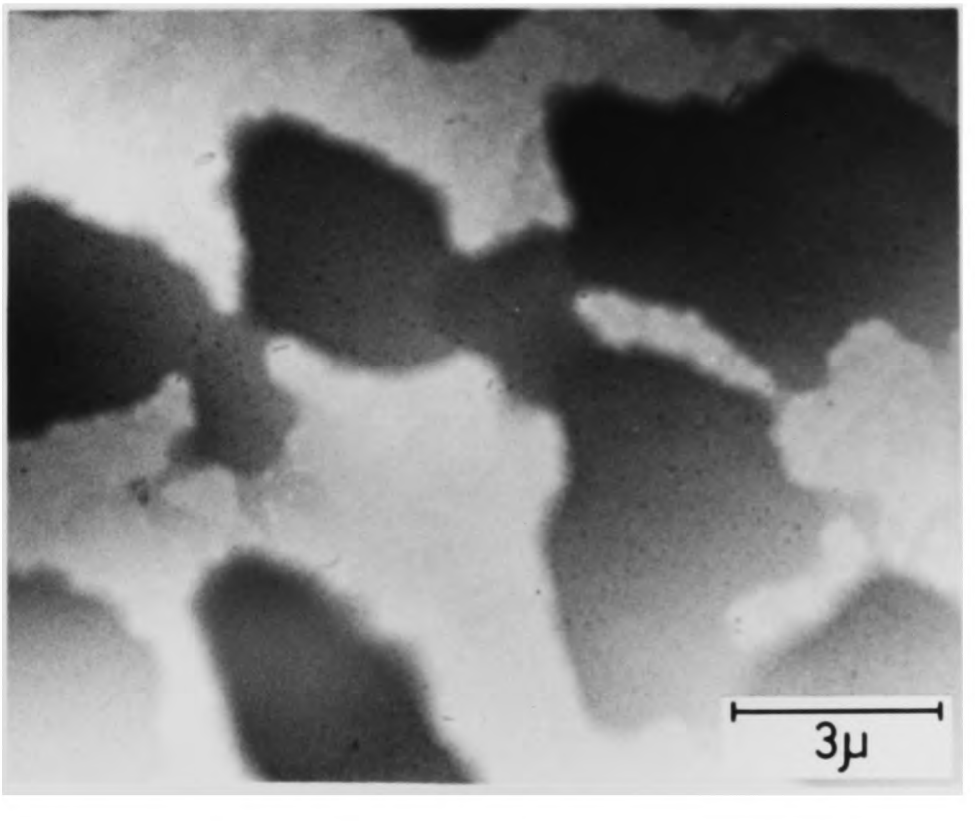
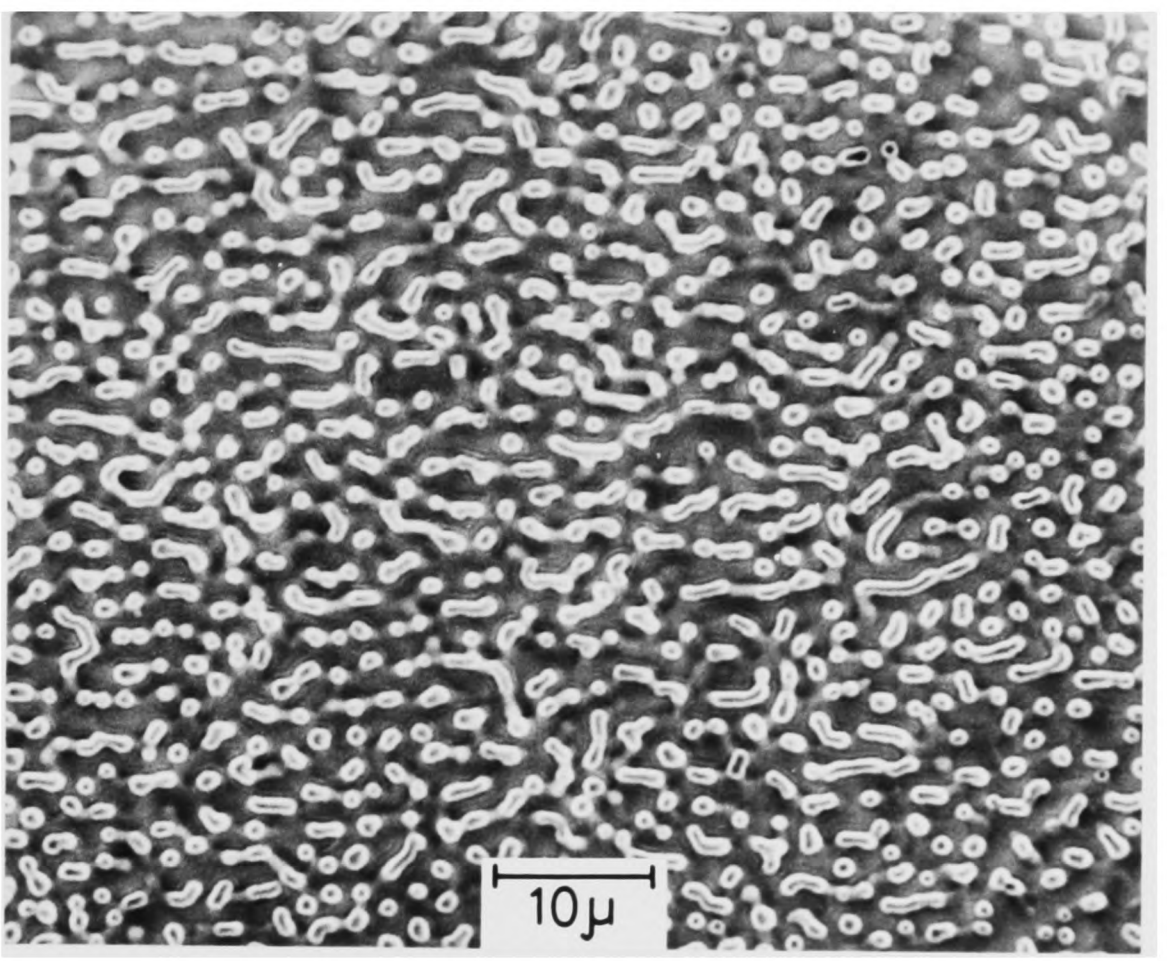
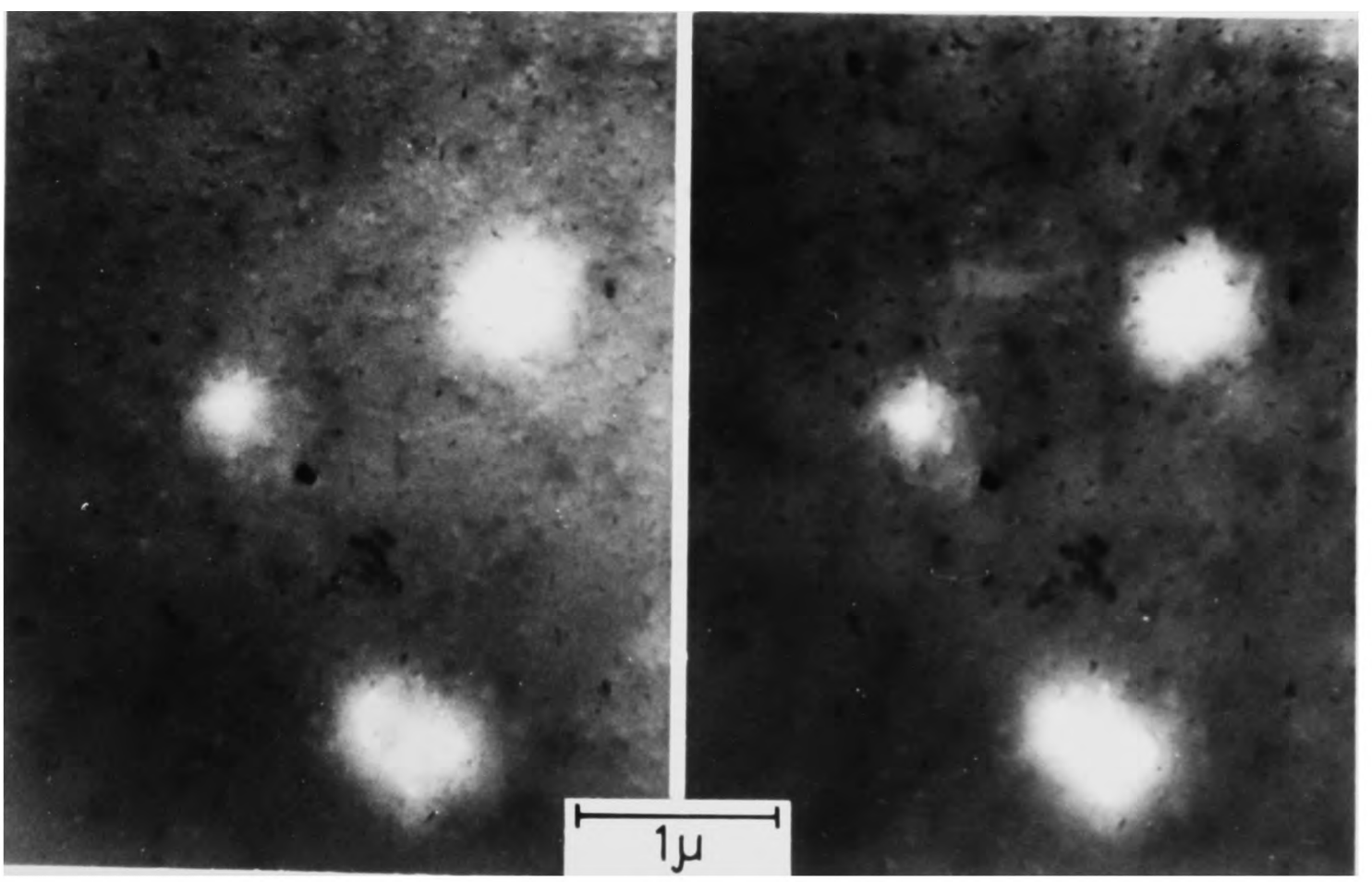

3μ

Fig 2.6 Si film with channelled structure, after initial growth centres had overlapped. (Optical micrograph)

Fig 2.7 Uneven Si film (uppermost) with array of fine particles at film/substrate interface. (Transmission electron stereomicrographs)


10μ


1μ

such a structure with a deposit thickness of ~ 1000 Å. Use of the TEM again showed that the films contained only a small number of dislocations and virtually no stacking faults. This is illustrated in fig 2.7 by a pair of transmission electron stereomicrographs of a film ~ 1400 Å thick. The film and substrate are delineated by a boundary constituted of an array of fine particles of the type already found in fig 2.5. The stereo-pair is arranged so that the deposited film appears uppermost, and the top surface has faintly discernible topographical features. By chance, the substrate beneath the film also contains a layer of impurity particles which took no part in the film growth, and were presumably introduced during the original melt-growth of the substrate material.

The film shown in fig 2.7 still contains deep pits, which penetrate most of its thickness. In general, films did not become smooth and uniform until several thousand Å of Si had been deposited.

A sublimation deposition run was also carried out in the presence of 5×10^{-7} torr H_2, to investigate its effect on growth centre formation. It was found that there was little significant change in growth centre shapes, and there was no mass spectrometric evidence for any Si/H_2 reaction, since during the run SiH_4 was absent to $< 10^{-10}$ torr. This is especially significant, since there was apparently little interaction of the H_2 with even the Si source, which was at a relatively high temperature near the melting point of the material.

2.5.2) Nucleation Behaviour

The optically observable growth centres were always found to occur in a number density which had apparently saturated at an extremely early stage in the growth, and did not change until coalescence eventually took place. Measurements were made upon a series of Si films deposited under different conditions (section 2.3), and the saturation number

density of centres (N_s) was found to depend upon growth conditions in a regular manner, as illustrated by the data given in table 2.1. The values marked * were obtained in a previous study by the author (Cullis, 1968).

Table 2.1

Substrate Temperature (^oC)	Saturation Number Density ($\times 10^6$ cm^{-2})	Deposition Rate ($\times 10^{-3}$ Å sec^{-1})
* 800	25 ($\pm$5)	30 ($\pm$1)
845	14 ($\pm$1.5)	30 ($\pm$1)
880	15.5 ($\pm$1)	60 ($\pm$2)
* 880	10.1 ($\pm$0.3)	30 ($\pm$1)
* 880	9.2 ($\pm$0.3)	25 ($\pm$0.8)
* 880	8.1 ($\pm$0.3)	20 ($\pm$1)
* 880	6.7 ($\pm$0.5)	15 ($\pm$1)
* 880	5.0 ($\pm$0.3)	10 ($\pm$0.6)
* 880	2.7 ($\pm$0.3)	4 ($\pm$0.7)
945	6.2 ($\pm$0.3)	30 ($\pm$1)
*1000	3.9 ($\pm$0.3)	30 ($\pm$1)

For a constant substrate temperature (T) of 880^{o}C, N_s increased as the deposition rate (R) increased. Fig 2.8 shows $\log_{10} N_s$ plotted against $\log_{10} R$, and it can be seen that a straight line is obtained, of slope 0.64 ($\pm$0.08). This relationship may be expressed

$$N_s = A R^{0.64} \qquad (2.1)$$

where A is a constant.

For deposition at a constant rate of 3×10^{-2} Å sec^{-1}, N_s decreased as the substrate temperature increased. Fig 2.9 shows $\log_{10} N_s$ plotted against T^{-1}, and a straight line is obtained, of slope 1.21 ($\pm$0.08) $\times 10^4$. This relationship may be expressed

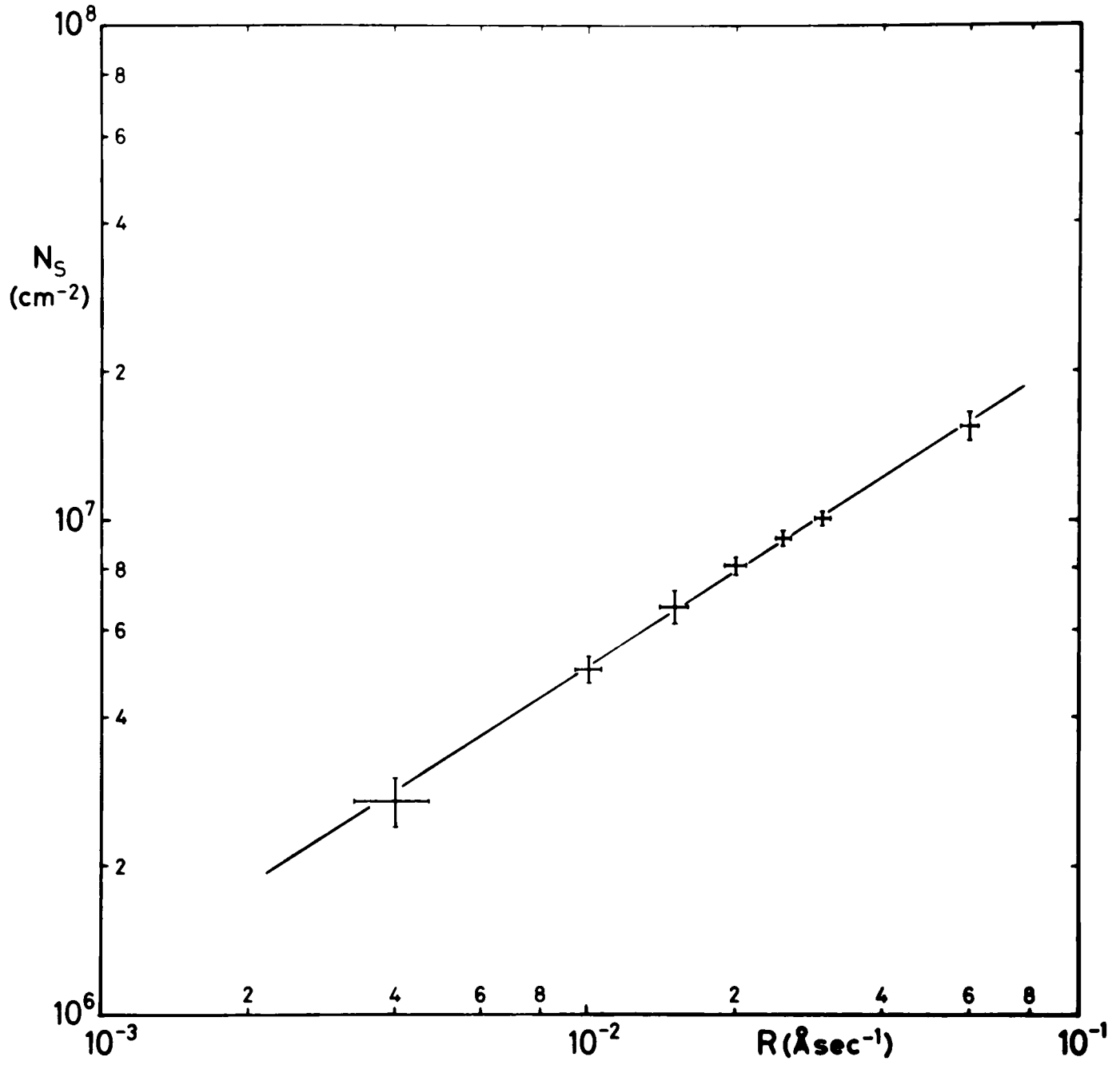
$$N_s = B \exp\left[\frac{1.21 \times 10^4}{kT}\right] \qquad (2.2)$$

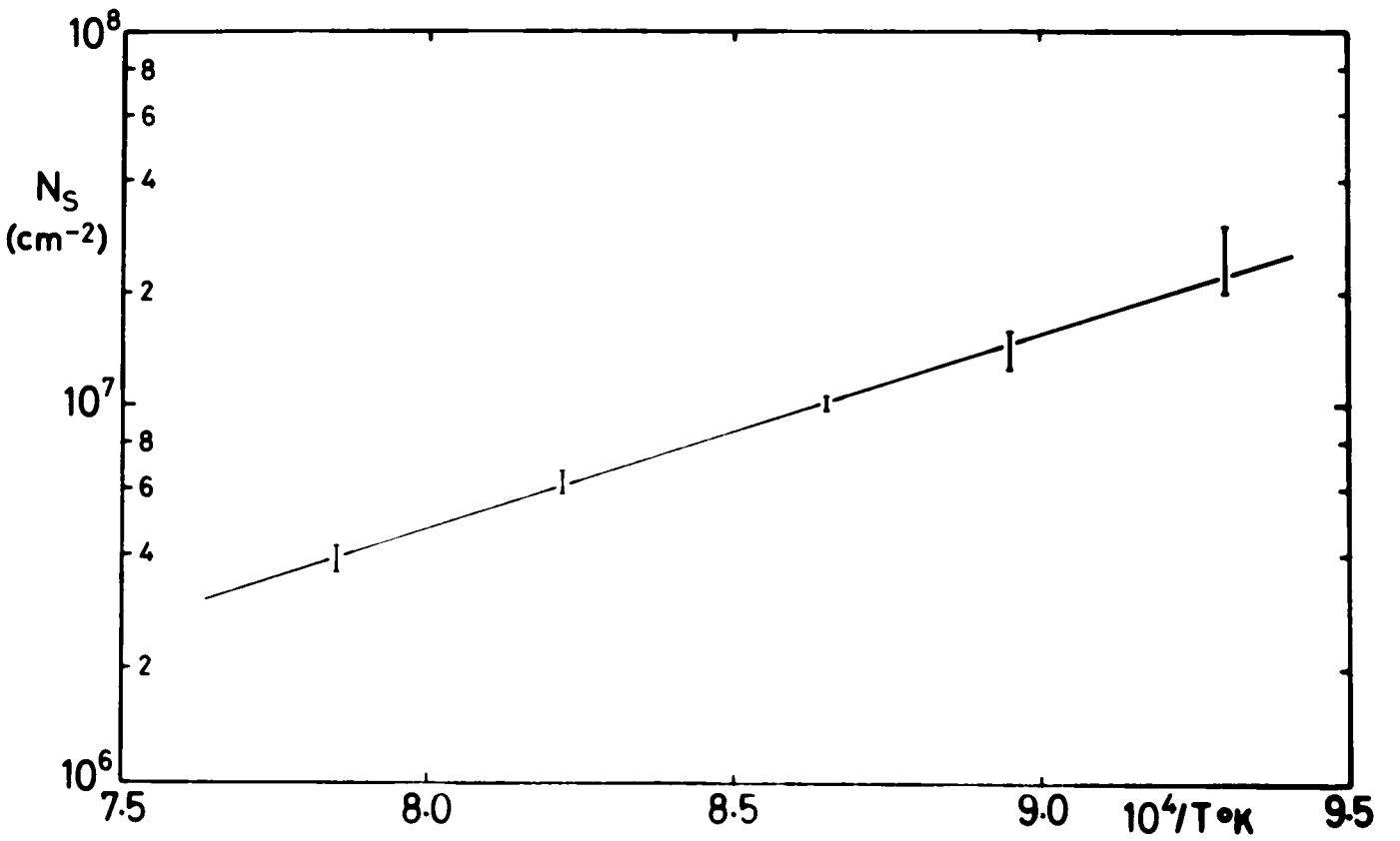
where B is a constant, k is Boltzmann's constant.

If the relationships expressed in eqs 2.1 and 2.2 may be applied

Fig 2.8 The variation in saturation number density of Si growth centres for changes in deposition rate, at a constant substrate temperature of 880°C.

Fig 2.9 The variation in saturation number density of Si growth centres for changes in substrate temperature, at a constant deposition rate of 3×10^{-2} Å sec^{-1}.


10^8
8
6
4
N_S
(cm^{-2})
2
10^7
8
6
4
2
10^6
2
4
6
8
2
4
6
8
10^{-3}
10^{-2}
$R(Å sec^{-1})$
10^{-1}


10^8
8
6
4
N_S
(cm^{-2})
2
10^7
8
6
4
2
10^6
7.5
8.0
8.5
9.0
$10^4/T°K$
9.5

simultaneously over the ranges of R and T used in the experiments, then they may be combined to give

$$N_s = C R^{0.64} \exp\left[\frac{1.21 \times 10^4}{kT}\right] \qquad (2.3)$$

where C is a constant. It is possible to evaluate C from the experimental results by two independent procedures. Fig 2.8 may be extrapolated to $\log_{10} R = 0$, giving N_s when $R = 1$ atom cm^{-2} sec^{-1} and $T = 1153^{o}K$. Similarly, fig 2.9 may be extrapolated to $T^{-1} = 0$, giving N_s when $T = \infty^{o}K$ and $R = 1.5 \times 10^{13}$ atoms cm^{-2} sec^{-1}. Eq 2.3 may now be solved to give C in each of these separate situations, and it is found that the two values obtained differ by only a factor of ~ 3, giving a mean value of $C \simeq 10^{-6}$. This close agreement, between the two independent determinations, gives confidence that the two sets of experimental results are related in a consistent manner. The way in which eq 2.3 may be interpreted in terms of nucleation theory will be discussed in the next section. A brief review of selected experimental nucleation studies by other investigators is given in Appendix B.

2.6) Correlation of Present Results with Nucleation Theory

The results presented in section 2.5.2 will first be analysed using current nucleation theory, assuming that this is directly applicable to the present system. The experimental results will be compared with those of Joyce et al (1967), and to facilitate this comparison, the theory developed by these workers will initially be used. Reference should be made to Appendix A for the development of the theoretical approach, and here the first object will be to determine which of the theoretical alternatives should be used.

2.6.1) Correlation with the Theory of Joyce et al (1967)

It should first be noted that the experimental values of N_s vary in a regular manner with both R and T (figs 2.8 and 2.9). Therefore eq A.17, which is for incomplete condensation, cannot be applicable in the present circumstances, since it exhibits no R dependence. This implies that the Si/(111)Si system must be treated as one of initially complete condensation, which is not unexpected since the adsorbate binding energy (Si - Si) is relatively large.

The exact nature of the dependence of N_s upon R may be used to determine the number of Si atoms constituting the smallest stable nucleus. Depending upon whether this is 2, 3 or 4, the theory proposed by Joyce et al predicts that one of eqs A.18, A.19 or A.20, respectively, should apply. A fundamental difference between these equations lies in the power law dependence of N_s with respect to R, which should be, respectively $\frac{1}{2}$, $\frac{2}{3}$ or $\frac{3}{4}$. It has been experimentally shown in the present case that a power law of $\frac{2}{3}$ is closely obeyed (eq 2.3), and therefore eq A.19 is appropriate

$$N_s = \left(\frac{N_o}{\nu_o^2}\right)^{\frac{1}{3}} R^{\frac{2}{3}} \exp\left[\frac{E_2 + 2E^*_{sd}}{3kT}\right] \qquad (A.19)$$

where N_o is the number density of substrate surface sites for adatoms, ν_o is an adatom vibration frequency and E_2 is the internal binding energy of a diatomic nucleus. This indicates that in the present Si/(111)Si system, the smallest stable nucleus contains 3 Si atoms (i.e. the critical nucleus is an atom pair). This result is also expected in terms of orientation effects, since the rotational symmetry of a Si single crystal about [111] is three-fold. Simple reasoning then indicates that surface binding sites should form a triangular array, especially favourable to the formation of 3 - adatom units (but, see section 2.7.2).

The similarities between the experimental and theoretical relationships (eqs 2.3 and A.19) are readily apparent. The energetics

of the nucleation processes may be investigated, and E^*_{sd} determined, by equating the exponential energy terms, so that

$$\frac{E_2 + 2E^*_{sd}}{3k} = 1.21\ (\pm 0.08) \times 10^4$$

or
$$E_2 + 2E^*_{sd} = 3.1\ (\pm 0.2)\ \text{eV} \qquad (2.4)$$

It is difficult to estimate the magnitude of E_2, since the nature of the binding between a pair of adatoms is uncertain. However, following Joyce et al (1967), as a first approximation it will be taken to be the thermochemically determined Si - Si bond energy of 2.0 eV. By substitution into eq 2.4 it is then found that E^*_{sd} (the activation energy for surface diffusion of Si on (111) Si) becomes 0.55 ($\pm$ 0.1) eV. This should be compared with the value of 2.5 eV determined by Joyce et al, who used SiH_4 pyrolysis for Si deposition. Another determination by Abbink et al (1968), who used a non-chemical deposition technique and a completely different method of analysis, yielded a value for E^*_{sd} of 0.2 eV. The reason for the large range of values obtained for this parameter is not yet clear, although it may be connected with variations in surface contaminants, differences in deposition technique or inadequacies in the theoretical treatments.

If it is assumed that there are no preferred atom sites on the (111) Si surface so that $N_o \simeq 10^{15}\ \text{cm}^{-2}$, and $\nu_o \simeq 10^{13}\ \text{sec}^{-1}$, then the constant $(N_o / \nu_o^2)^{\frac{1}{3}}$ of eq A.19 is approximately two orders of magnitude too large compared with the constant C ($\simeq 10^{-6}$) of eq 2.3. This discrepancy suggests that the large growth centres observable with the optical microscope, and to which the above data refer, may nucleate at some kind of preferred site, e.g. impurity, geometrical, crystallographic, etc. A discrepancy regarding the constant C was also found for the pyrolysis of SiH_4 (Joyce et al, 1969a), amounting to approximately seven orders of magnitude. It is worthwhile noting that if the value of

$(N_o/\nu_o^2)^{\frac{1}{3}}$ calculated for no preferred atom sites is used as the constant C in eq 2.3, rather than the experimental value of $\sim 10^{-6}$, then the resulting values of N_s are appreciably larger. Moreover, these values correspond approximately to the number of extremely small centres observed by TEM to constitute the surface roughening structure between the larger growth centres. This suggests that the growth occurring between the large centres may correspond to nucleation on non-preferred sites, while the large centres correspond to nucleation on preferred sites. However, it is emphasized that there are other factors which may contribute to the complexity of the situation, and an alternative possible explanation will be discussed later.

2.6.2) Correlation with the Theory of Logan (1969)

There have recently been more detailed treatments of nucleation processes, and these are described in Appendix A. The work of Logan (1969), in particular, includes many desirable features, and his final expressions are also closely similar to those of Stowell (1970). In fact, Logan obtained eq A.19 of Joyce et al as a special case, for a 3-atom smallest stable nucleus, valid only under restricted conditions. A more generally applicable relationship was formally identical to eq A.21

$$N_s = 0.4\left(\frac{N_o^2}{\nu_o^3}\right)^{\frac{1}{5}} R^{\frac{3}{5}} \exp\left[\frac{E_2 + 3E^*_{sd}}{5kT}\right] \qquad (A.21)$$

Now, the present experimental results (eq 2.3) showed that N_s depends upon R raised to the power of $0.64\ (\pm 0.08)$. Therefore, eq A.21 is as applicable as the relationship derived by Joyce et al, since it exhibits an R power law of 0.6, which is within the limits of accuracy of the results. To investigate the system energetics using this new relationship we proceed as before, and from eqs 2.3 and A.21

$$\frac{E_2 + 3E^*_{sd}}{5k} = 1.21\ (\pm 0.08) \times 10^4$$

or $$E_2 + 3E^*_{sd} = 5.2\ (\pm 0.3)\ \text{eV} \qquad (2.5)$$

Once again, if it is assumed that E_2 is 2.0 eV (following Joyce et al, 1967), eq 2.5 shows that E^*_{sd} becomes 1.1 ($\pm$ 0.1) eV. This is double the value previously obtained using eq A.19, although both are physical possibilities. It is interesting to note that if the results of Joyce et al (1967) from the pyrolysis of SiH_4 experiments are fitted to eq A.21, it is found that E^*_{sd} takes the higher value of 3.2 eV. The various experimentally determined values of E^*_{sd} are summarized in table 2.2.

Table 2.2 (values in eV)

	Joyce et al	Cullis	Abbink et al
Eq A.19	2.5	0.55	
Eq A.21	3.2	1.1	
Other			0.2

If it is accepted that Logan's theoretical analysis is a valid description of nucleation processes, it is possible to extract more information about the system energetics. Whichever of eqs A.19 and A.21 is applicable to the present Si/(111)Si system, the analysis showed that there is an overriding condition which must be fulfilled. This relates to pair stability with respect to single atoms, and it was shown by Logan that the pair lifetime (τ_2) must have an upper limit placed upon it. Above this value, his initial assumption of a quasi steady state number of pairs becomes invalid, and if unrestricted, τ_2 could become large enough to imply that pairs are actually stable. In terms of Logan's dimensionless parameter λ (see Appendix A), which measures pair stability, the necessary limiting condition may be written (Logan, 1969)

$$\lambda \ll 1 \qquad (2.6)$$

where $$\lambda = (K_o R)^{\frac{1}{2}} \tau_2 \qquad (2.7)$$

in which K_o is a generalized collision rate constant, given by

$$K_o = 3\left(\frac{\nu_o}{N_o}\right) \exp\left[\frac{-E^*_{sd}}{kT}\right] \qquad (2.8)$$

and $$\tau_2 = \nu_o^{-1} \exp\left[\frac{E_2 + E^*_{sd}}{kT}\right] \qquad (2.9)$$

Logan also showed that if eq A.19 is valid, there is the simultaneous limitation $\lambda \gg 10^{-2}$ which implies that the only acceptable value of λ must be $\sim 10^{-1}$. Alternatively, if eq A.21 is valid, the simultaneous limitation is now $\lambda < 10^{-2}$, so that there is no conflict with the overall condition $\lambda \ll 1$. For present purposes, to conform with the limitations placed upon both theoretical expressions (if there is no preference for either one), the general limiting condition will be written

$$\lambda \leqslant 10^{-1} \qquad (2.10)$$

Then, from eqs 2.7, 2.8 and 2.9

$$\left(\frac{3\nu_o R}{N_o} \exp\left[\frac{-E^*_{sd}}{kT}\right]\right)^{\frac{1}{2}} \nu_o^{-1} \exp\left[\frac{E_2 + E^*_{sd}}{kT}\right] \leqslant 10^{-1}$$

or $$2E_2 + E^*_{sd} \leqslant kT\left(\ln \frac{\nu_o N_o}{R} - 5.7\right) \qquad (2.11)$$

This inequality may be used to independently investigate the relative magnitudes of E_2 and E^*_{sd}, while previously derived results relied upon a preconceived approximation for E_2. R and T must be chosen such that, under the conditions then specified, adatom pairs are unstable and triplets form the smallest stable nuclei. In the present case, the values $R = 1.5 \times 10^{13}$ atoms cm^{-2} sec^{-1} (3×10^{-2} Å sec^{-1}) and $T = 1153^oK$ (880^oC) are self consistent in this respect, since as has been shown, a comparison with theory indicates that the smallest stable nuclei contain 3 Si atoms. However, although it may initially appear that N_o and ν_o should be taken as $\sim 10^{15}$ cm^{-2} and 10^{13} sec^{-1} respectively, a difficulty arises from the fact that the predicted value of the constant $(N_o/\nu_o^2)^{\frac{1}{3}}$ of eq A.19 does not agree with its experimental value. Since the reason for this discrepancy remains uncertain, the results of the application of inequality 2.11 must be interpreted with caution, although these results are not a sensitive function of N_o or ν_o. Using the above values of R, T, N_o and

ν_o, the inequality gives

$$2E_2 + E^*_{sd} \leqslant 2.8 \text{ eV} \qquad (2.12)$$

Combining this with the result of the present Si/Si studies, as expressed in eq 2.4, it is found that

$$E_2 \leqslant 0.9 \text{ eV} \quad \text{and} \quad E^*_{sd} \geqslant 1.1 \text{ eV} \qquad (2.13)$$

Similar relations are obtained by using alternative eq 2.5.

The striking feature of these results is that they do not permit the adoption of the previously given values of E_2 and E^*_{sd}. These relied upon an assumed value for E_2 of 2.0 eV (the normal Si - Si σ - bond energy), but it is now indicated that the real pair binding energy may be considerably lower than this. While the actual permitted range of < 0.9 eV, predicted by inequalities 2.13, should be treated with caution, arguments will be presented in section 2.7.2 to support the use of a value for E_2 which is below 2.0 eV.

It is interesting to apply inequality 2.11 to the results of Joyce et al (1967), when SiH_4 pyrolysis experiments indicated that $E_2 + 2E^*_{sd} = 7.05$ eV. One is then led to the conclusion that $E_2 \lesssim$ zero eV while $E^*_{sd} \gtrsim 3.5$ eV, and although there are uncertainties in the derivation of these limitations, the situation is clearly most unexpected. In order to investigate these anomalous conclusions, since inequality 2.11 applies a limitation related to adatom pair stability, it is relevant to determine the actual pair lifetime (τ_2), using the values of E_2 and E^*_{sd} (2.0 eV and 2.5 eV respectively) proposed by Joyce et al. Now, τ_2 is given approximately by eq 2.9, and if $\nu_o = 10^{13}$ sec^{-1} and T = 1173°K (900°C), τ_2 becomes $\sim 10^6$ secs. This enormous period of time is vastly greater than even the duration of an experimental run, so that adatom pairs should be exceedingly stable, in clear contradiction of other fundamental assumptions. However, the present author feels that this anomaly may be produced by peculiarities in the system energetics, and that these may possibly be explicable in terms of

complexities in the SiH_4 pyrolysis reaction.

The value of τ_2 derived from the measurements of the present investigation depends upon which of eqs A.19 or A.21 is used in the analysis, and upon whether either E_2 is assumed to be 2.0 eV or inequality 2.11 is applied. However, a typical predicted value would be in the range from ~ 1 sec down to $< 10^{-4}$ secs, although a value at the lower end of this range would probably be the most physically realistic.

2.7) Discussion

In this section, the experimental results presented earlier will be discussed, with emphasis placed upon features which have not been well understood. The general concept of a 'real' Si surface will be introduced (as detailed in Appendix C), and correlations will be made with the results of Joyce et al (1967, 1969b). Finally, the structure of the growing Si film will be discussed in relation to possible electronic device applications.

2.7.1) The Number Density Discrepancy

A curious feature of the Si/Si experimental results is the unexpectedly low range of values of N_s given by all sets of optically observable growth centres. It has already been suggested that this could be produced by nucleation on preferred sites (section 2.6.1), although this is difficult to substantiate in practice. Carbon impurity is unlikely to be directly involved, since Joyce et al (1969b) showed that while this contaminant influenced growth centre shape, if substrates were partially cleaned by initial treatment at a high temperature, the growth centre N_s values remained constant. A related suggestion was based on the idea of Si nucleation at minute holes in the initial surface oxide film. However, this was made virtually untenable by Watts et al (1968), who

grew Si on a (100) Si substrate using the SiH_4 pyrolysis technique. After the initial induction period, corresponding to removal of surface oxide, growth centres were formed in the usual way, but then the deposition conditions were abruptly changed and a second set of growth centres, commensurate with the new growth conditions, were formed immediately. Therefore, since no oxide was thought to be present during the second nucleation process, oxide could hardly influence the growth.

Another possible type of preferred site is that which may be produced by a step edge. However, if such sites were involved, growth centres should have occurred with substantial interalignment, and this was definitely not observed. Clustered vacancy 'complexes' could also provide special sites. However, this possibility would introduce conflicts with the observations of Watts et al, since final removal of an oxide film should produce a temporarily high number density of vacancies, due to the surface reaction then taking place. If the vacancies affected nucleation, then N_s values obtained at this stage would not be expected to correlate numerically with those obtained later, produced by nucleation long after all oxide had been removed. Again, this is contrary to the experimental observations.

Since the concept of nucleation at preferred sites is not easily linked with the experimental observations, some special Si surface processes which may occur will now be discussed. Logan (1969) showed that N_s varied inversely with respect to K_o, the adatom collision rate constant. Therefore, if K_o were increased by the nature of surface processes, the theoretically predicted values of N_s would be depressed, and the discrepancy with experiment accordingly reduced. One possibility is that activated adatoms may translate over distances which are greater than the surface intersite spacing (a_s). To determine information about the real 'long jump' distance (ℓ), it is necessary to have an experimental value for the Si

surface self diffusion coefficient, D_s. Abbink et al (1968) determined a minimum value, but this was based on the assumption that $\ell = a_s$. Gjostein (1967) correlated experimental surface diffusion results for a range of FCC metals (Cu, Ni, Fe etc), and by considering adatom entropies of migration found that $\ell = 4.7\, a_s$. If it is assumed that this result has relevance to the surface self diffusion of Si, it implies that Si adatoms may make 'long jumps' across the surface, significantly greater in extent than a_s. The actual value of ℓ for Si is uncertain, and will largely depend upon the intrinsic stability of the reorganized surface, as described next.

The intrasurface bonding arrangement of a real Si surface probably involves substantial odd electron pairing (see Appendix C). This implies that an activated adatom, migrating across the surface, will experience a somewhat weakened attraction towards available bonding sites, so that it will travel further than predicted by the 'ideal' surface model. The extent of diminution of surface attraction, and hence the actual magnitude of ℓ, will then depend upon the stability of the intrasurface bonding.

There is another issue of possible importance. The addition of a Si adatom on to a Si surface introduces at least a perturbation into the original structural arrangement. An adatom bound to a resonance stabilized surface could disrupt the delocalized π - orbitals over a relatively large area. The effect would provide an adatom with an 'area of influence' which could signal the atom's presence to another which was nearby, but not necessarily adjacent. The force between the two adatoms should be attractive, since as their 'areas of influence' overlap, the total surface disruption probably decreases giving an accompanying decrease in free energy of the system.

The effect upon surface processes of 'long jump' distances for adatoms, coupled with the possession of 'areas of influence', would yield

an increased collision rate constant, K_o. As described above, the theoretically predicted values of N_s would then be in closer agreement with experiment. However, the magnitude of the correction produced in this way is uncertain, and it is difficult to estimate the extent to which special surface processes are involved.

The properties of real Si surfaces may introduce still more effects, such as the channelling of adatoms along preferred directions, and the provision of more than one type of binding site. However, there are so many unknown factors that it is not easy to estimate their importance.

2.7.2) Energy Considerations

Certain determinations of E^*_{sd} given in section 2.6 relied upon the assumption that E_2 was the normal Si - Si 6-bond energy. However, if surface binding sites are atoms with unsatisfied bonding potential, in the 'ideal' model (top layer in fig 3.28, see Appendix C), the unmodified bond distance (r) within an adatom pair would be a factor of 1.64 greater than the normal Si - Si sp^3 6-bond distance (r_o). Now, the bond energy can be approximated as a Morse function M(r)

$$M(r) = E'\left\{\exp\left[-2a_o(r - r_o)\right] - 2\exp\left[-a_o(r - r_o)\right]\right\} \qquad (2.14)$$

where E' is the normal bond dissociation energy, and a_o is a parameter fitted empirically. If r_o = 2.34 Å, E' = 2.0 eV and following Taloni and Haneman (1968) $a_o \simeq 2$ $Å^{-1}$, the elongated pair bond has an energy of only ~ 0.2 eV. If the bonds binding the pair to the surface are strained, although they would be weakened, the actual value of E_2 should be increased by a shortening of the intrapair spacing. Clearly, a compromise situation of lowest total energy would be the result where E_2 would be substantially above the extremely low minimum value of 0.2 eV, but nevertheless, below the full value of 2.0 eV. Pair binding in relation to the two 'real' surface models discussed in Appendix C would probably be analogous,

although a weakening of the binding could occur in the Haneman model due to the surface height disregistries. If these general ideas are extended and applied to the bonding of a 3-atom nucleus to a Si surface, similar problems are encountered, since the atoms constituting the nucleus are too closely spaced to occupy normal surface lattice sites.

In this section, arguments have been given which suggest that E_2 should be less than the Si - Si σ-bond energy. This gives additional support to the analysis of the author's results presented in section 2.6.2, where this possibility was also proposed, based on considerations of nucleation theory. If a value of E_2 of < 2.0 eV is adopted, then the appropriate values of E^*_{sd} given in table 2.2 would be accordingly increased. Inequality 2.11 may be used to estimate the magnitude of this correction, as suggested in section 2.6.2, although uncertainties in the theoretical analysis render the acceptance of preferred values for E_2 and E^*_{sd} rather speculative at the present time. However, quite apart from these considerations, it is clear from the wide range of values of E^*_{sd} (table 2.2) determined using various experimental techniques in combination with several different theoretical treatments, that there may be other important factors, of which account has not yet been taken.

2.7.3) Impurity Effects

Joyce et al (1969b) have shown that the shape of their geometrical Si growth centres was in some way influenced by the contaminants (principally carbon - containing), present upon the Si substrate surfaces. In the present experiments, the optically observable growth centres were generally irregular in shape. It is suggested here that the nature of the observed Si film growth may depend upon the state of aggregation of carbon - containing surface impurities. Based on this idea, if the impurity is in a non-aggregated form, it may pin advancing Si growth

steps in a much more regular manner than when it is transformed into particles of aggregate (e.g. β-SiC).

When Si deposition on to an unpreheated Si substrate is initiated, using the ideas given above, if the impurity remains non-aggregated, it could distribute itself fairly evenly along step edges surrounding growth nuclei, and restrain their motion across the surface in a uniform manner. This would lead to the formation of regular growth centres, extending only slowly over the surface and therefore constrained to grow vertically up from it. Also, impurities which migrated up on to the centres themselves from the substrate surface, could be continually swept by advancing steps to growth centre facet intersections, where they would accumulate and possibly be incorporated into the deposit. Indeed, unintentional acid etching of geometrical centres, produced by Joyce et al in their experiments, showed on one occasion that a skeletal structure of the intersections remained after the acid attack (Booker, private communication). This indicates that the centres may well have contained materials other than Si.

If impurity on the substrate surface becomes aggregated during deposition, advancing step fronts surrounding growth centres would be pinned by the particles so produced. However, the steps would bulge out between the pinning sites to give an irregular structure, so that the centres could rapidly lose any initial overall geometrical shape. Since fine particles were observed during the present experiments in the interfacial region between grown films and their substrates, it seems possible that this may be the effect responsible for producing the irregular growth centre shapes. Also, if aggregate particles were formed during deposition on clear substrate surface between the growth centres, these particles could eventually act as preferential nucleation sites. These could then yield a background film structure of minute

centres, which might correspond to the tiny centres, observed using TEM, in films grown by the author. An alternative possible explanation for the presence of these centres was given earlier in section 2.6.1, based on theoretical nucleation ideas, but while it is difficult to make a definite choice between them, the author favours the approach suggested in this section.

The suggested regimes outlined above predict, on the basis of experimentally observed growth centre shapes, that aggregation of impurities should be greater on unpreheated substrates in the author's experiments than in those of Joyce et al. It is not easy to put forward a definite explanation for this, but it could be related to the Si deposition technique. For instance, in the pyrolysis of SiH_4 experiments, the presence of many radical species e.g. $\cdot SiH_3$, $:SiH_2$, etc on the surface could hinder aggregation by reducing carbon-containing impurities to isolated molecules containing very stable C-H bonds. However, in the author's experiments, the deposited Si atoms may actually react with such impurities to give β-SiC particles during deposition. The author attempted to investigate this point by performing vacuum sublimation of Si under a partial pressure of 5×10^{-7} torr H_2, to determine whether the gas induced any growth centre shape changes. However, although no significant change in the form of the centres was observed, it is likely that H_2 molecules cannot easily be broken down on a Si surface, due to their very great stability, so that this experiment may not have been a suitable test (see section 2.5.1).

The effect of substrate pretreatment at a high temperature prior to growth will be described in the next chapter. However, if only impurity effects are considered, one might expect that aggregation of impurities would be promoted by such a heat treatment. This is in accord with the findings of the author (chapter 3), that after substrate pretreatment at

1250°C, the Si films grew by a pinned layer mechanism, and the pinning particles were large enough to be identified as SiC (Ditchfield and Cullis, 1970). Also, it is consistent with the results of Joyce et al (1969b), who found that less regular centres were produced in their system for pretreatment temperatures of ⩽ 1200°C.

2.7.4) Silicon Film Structure

The Si films grown during the previously described experiments were of high quality, since they contained relatively few crystallographic defects. One significant feature was the presence of fine impurity particles at the film/substrate interface, but since these did not penetrate far into the film, they did not, themselves, cause much disturbance. However, as discussed in section 2.7.3, it is likely that this impurity is responsible for inhibiting the lateral extension of the initial growth centres over the surface. Due to this, such a film would require to attain a mean thickness of several thousand Å before becoming reasonably smooth and uniform. While this would probably be satisfactory in many electronic device applications, it is not a generally desirable feature for film growth, and would obviously cause difficulties if very thin films were required. This problem could be at least partially overcome by the growth of Si films under conditions which would give the highest possible number density of growth centres, so that these would very rapidly overlap one another by expansion over the surface. The experimental results indicated that this could be achieved by film growth at high deposition rates and low substrate temperatures. However, deposition conditions could not be changed without limit, since e.g. at very low substrate temperatures the film crystal quality would be degraded.

As stated earlier, for given deposition conditions, the rate of which growth centres overlapped did vary somewhat from run to run.

Therefore, it seems that there may have been some random change in the amount of impurities initially present on substrate surfaces. This suggests that if it were possible to completely remove this surface contamination prior to growth, any subsequently formed Si growth centres should spread rapidly over the surface to give a uniform Si film more quickly than would otherwise be the case. Such cleaning pretreatment should provide the additional advantage of improving film perfection, since the experimentally observed fine particles should no longer be present. Therefore, a series of experiments was carried out, in which substrate surfaces were cleaned by pretreatment at a high temperature in UHV (Joyce et al, 1969b). These experiments are described in the next chapter.

2.8) Summary

The investigation presented here has been concerned with the UHV sublimation of Si on to unpreheated (111) Si substrates. After an initial induction period, thought to correspond to the removal of surface oxide, optically observable irregular Si growth centres were produced, indicating that initial growth had been by nucleation. With continuing Si deposition, such centres increased in size and eventually overlapped to give a film which had a channelled structure, and which contained few crystallographic defects.

The experimentally observed variation in growth centre saturation number density (N_s) was determined as a function of deposition rate (R) and substrate temperature (T). It was found that

$$N_s \simeq 10^{-6} R^{0.64} \exp\left[\frac{1.21 \times 10^4}{kT}\right]$$

This equation was correlated with relationships theoretically derived by Joyce et al (1967) and Logan (1969). It was deduced that:

a) the form of the rate term indicated that the smallest

stable nucleus contained 3 Si atoms;

and b) assuming the adatom pair binding energy (E_2) to be 2.0 eV, the system energetics showed that the activation energy for surface diffusion of Si (E^*_{sd}) was ~ 0.55 eV (Joyce et al), or 1.1 eV (Logan).

However, an extension of Logan's theoretical treatment yielded a useful limiting relationship, which related the energy parameters to one another, and indicated that E_2 may be lower than previously assumed, so that E^*_{sd} may be higher than either of the values given above. This possibility was supported by arguments based upon models of the (111) Si surface.

The constant term in the above equation was approximately two orders of magnitude smaller than the theoretically predicted value. Although this may seem to be a large discrepancy, it is very much less than the analogous discrepancy observed by other investigators for similar semiconductor systems. Various possible explanations for this behaviour were discussed, including the occurrence of special surface processes and nucleation at preferred sites.

The possible effects of impurities present on the surface were related to the observed film growth characteristics. The findings suggested that:

a) impurities impeded the motion of the edges of growth centres across the substrate surfaces, so that the centres were constrained to increase in thickness with continuing Si deposition;

and b) the state of impurity aggregation may have had a decisive effect upon the shapes of growth centres so produced.

CHAPTER 3 THE GROWTH OF SILICON ON SILICON - PREHEATED SUBSTRATES

		Page
3.1)	Introduction	54
3.2)	Experimental Details	54
3.3)	The Silicon Substrates	56
3.4)	Deposition in UHV	57
3.4.1)	Standard Preheated Substrates	57
3.4.2)	Initial 'In Situ' Gas Polish	59
3.5)	Particle Microanalysis	62
3.5.1)	The Particle Energy Loss Spectrum	62
3.5.2)	Composition of the Particles	64
3.6)	Effect of Contaminating Gases	65
3.6.1)	Carbon monoxide and Dioxide	66
3.6.2)	Methane and Ethylene	66
3.6.3)	Oxygen	67
3.7)	Discussion	68
3.7.1)	General Surface Step Interactions	68
3.7.2)	Processes at Single Steps	72
3.7.3)	Silicon Film Growth	76
3.7.4)	Effect of Contaminating Gases	80
3.8)	Summary	82

3.1) Introduction

The state of a Si substrate surface can be a decisive factor in determining the form of subsequent Si film growth. An important feature of growth on substrates directly heated to the deposition temperature, concerns the influence of impurities (especially carbon) upon growth centre formation (chapter 2). There are several methods by which impurities may be removed from a substrate surface, and one of importance which has been studied by other workers is treatment at a relatively high temperature prior to deposition (see section 2.2). In this chapter, the use of this technique, and the effect that it has upon film growth will be described and discussed. Investigations of the possible use of 'in situ' gas polishing will also be described, together with the effect of contaminating gases deliberately admitted during film growth. Further, an illustration will be given of the use of transmission electron energy loss analysis, by which it is possible to microanalyse particles which are too small to be examined by other more conventional techniques.

3.2) Experimental Details

The experiments to be described concern the deposition of Si on to Si substrates which had been preheated in UHV at temperatures of up to 1250°C prior to deposition. During such a procedure, the substrate and associated assemblies evolved relatively large quantities of gas (principally CO_2). To minimize pressure rises, a substrate was first outgassed at a dull red heat and, after a suitable time, was rapidly heated to the high temperature. The ambient pressure then rose, and as it passed 10^{-7} torr, the substrate was cooled to the outgassing temperature while the pressure returned to less than 10^{-8} torr. This heating procedure was often repeated twice to accumulate the required period at the pretreatment temperature,

and during the last such cycle the ambient pressure usually remained below 3×10^{-8} torr.

During some experiments it was necessary to admit gases into the vacuum chamber through the leak valve. All of these were British Oxygen Corporation research Grade X gases, usually 99.9 - 99.99% purity, except H_2 which was 99.99% high purity grade. Impurity levels were checked mass spectrometrically. Before entering the chamber, each gas could be passed through a cold trap to remove residual water vapour. The trap temperature was as low as could conveniently be obtained without condensing a particular gas, e.g. freezing methanol for ethylene.

Some deposited Si films were studied by means of the TEM using surface replicas, which were either directly or indirectly obtained. Direct replication involved shadowing the film surface with Pt/carbon at a shallow angle (15°), backing this layer with ~ 300 Å of carbon, dicing the replica and removing all of the underlying Si by dissolution in acid, using a reagent that produced only a minimum of bubbling (12% HF (40%) + 25% HNO_3 (conc) + 63% $CH_3 \cdot CO_2H$ (glacial)) (Abbink et al, 1968). The small remaining pieces of the replica were floated on water, and scooped out with TEM specimen grids, on which they were to be examined. This technique proved difficult, though it gave better results than the indirect method, in which a plastic replica of the Si surface, which could be dissolved in acetone, was itself replicated again using Pt/carbon shadowing.

Particles in the Si films have been studied using transmission electron energy loss analysis (Ditchfield and Cullis, 1970). The instrument employed consisted of a Siemens Elmiskop 1 transmission microscope, with a Möllenstedt electron lens below the final image screen (Metherell, 1971). A fine line in the final image was selected with a 15μ slit, and electrons which passed through were dispersed in energy by

the lens to produce an energy spectrum which could be recorded on a photographic plate (fig 3.1). The spectrum was obtained in graphical form by scanning the plate using a recording microdensitometer. The features of the spectrum were specifically related to the material producing the image focused on the analyser entrance slit, so that when the image of a particle was moved to this position, it could be identified if it was sufficiently electron transparent.

3.3) The Silicon Substrates

The state of a substrate surface immediately prior to deposition is of great interest. If a substrate received the standard pretreatment at 1250°C for 10 min in the apparatus, but was then removed for examination before deposition, optical microscopy revealed few surface structures. However, when the TEM was used, thickness fringe contrast showed the presence of uniform arrays of very fine surface steps in certain regions. These steps were often straight over relatively large distances. Other surface areas showed little direct evidence for the existence of steps, although the presence of unresolved minute steps was revealed where they interacted with occasional included foreign particles, which caused them to become bunched and to be deflected (fig 3.2). This indicated that the steps had been moving across the surface, and the direction of the motion was deduced from the manner in which they were deflected by the particles which had pinned their advance. If the direction of step motion was taken as lying in the (111) plane and being perpendicular to the direction of the step edge, then the steps mostly moved in one of the ⟨112⟩ directions. The absolute sense of the observed motion was obtained by comparison with the orientation of the crystallographic Thompson tetrahedron, deduced from transmission electron diffraction (TED) patterns (Cullis and Booker,

Fig 3.1 Diagram showing the manner in which a Möllenstedt lens system disperses electrons in energy due to its large chromatic aberration. B - edges of box-shaped electrode at earth (anode) potential, C - cylindrical electrodes connected to negative EHT.

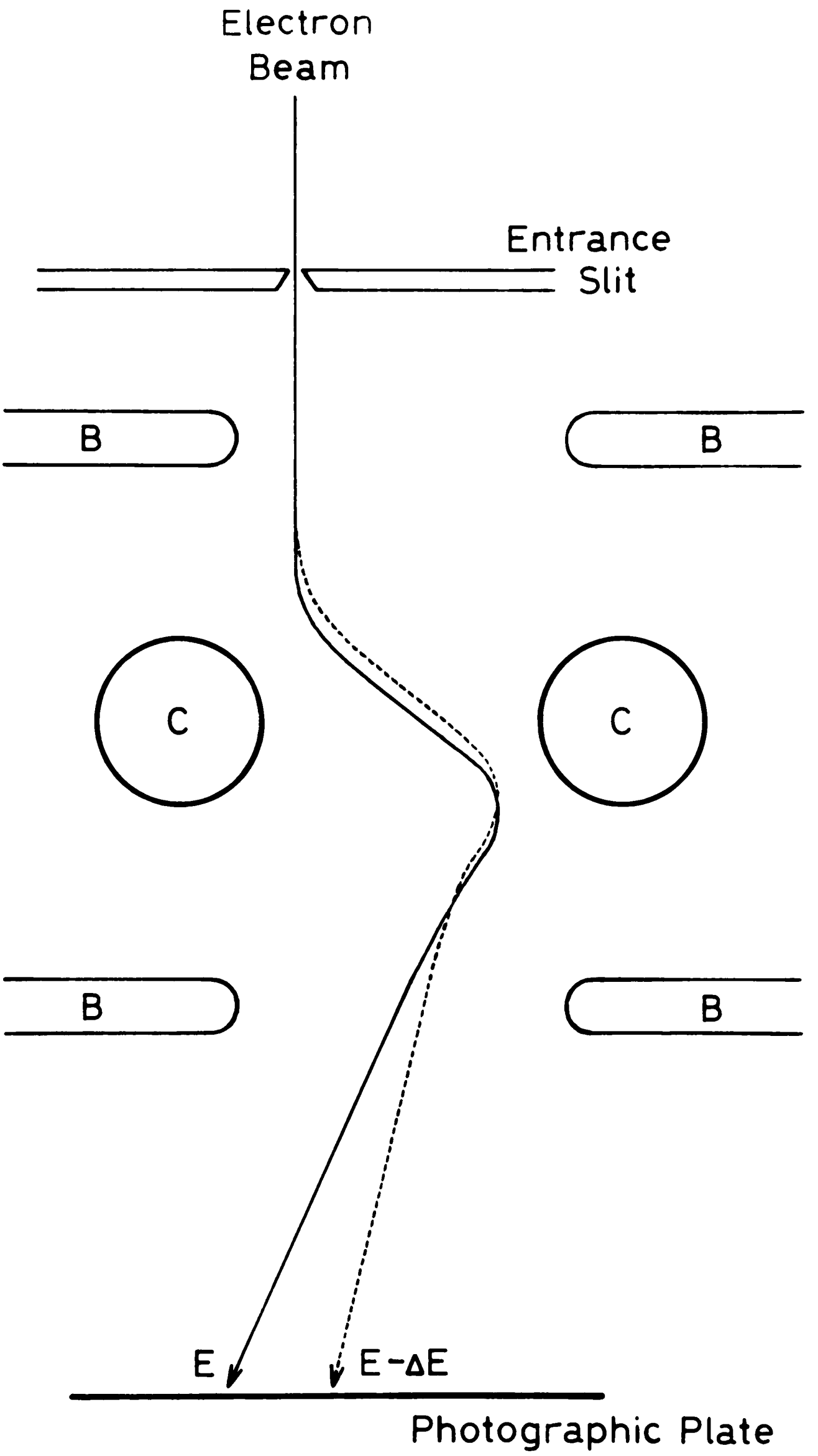
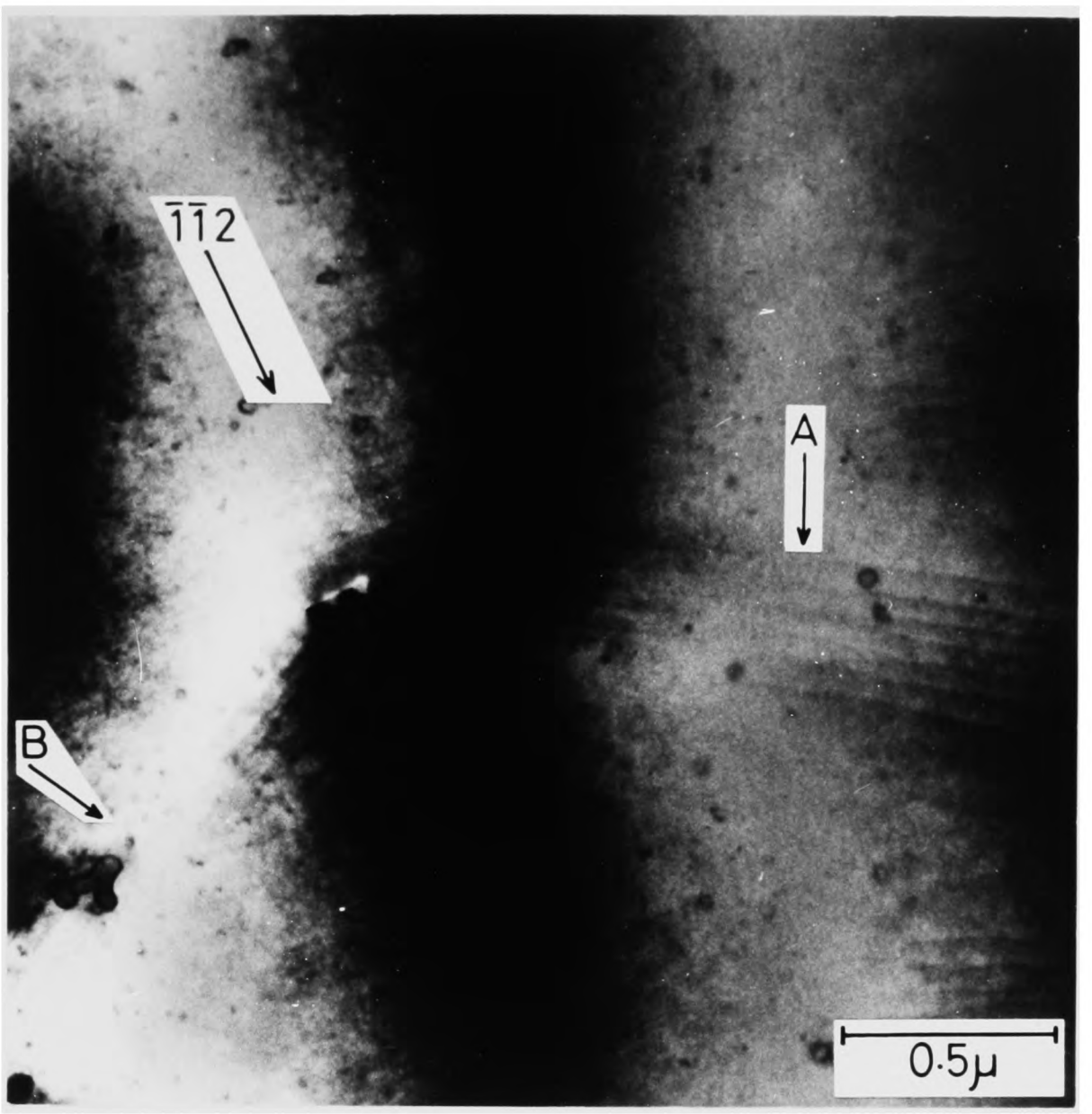
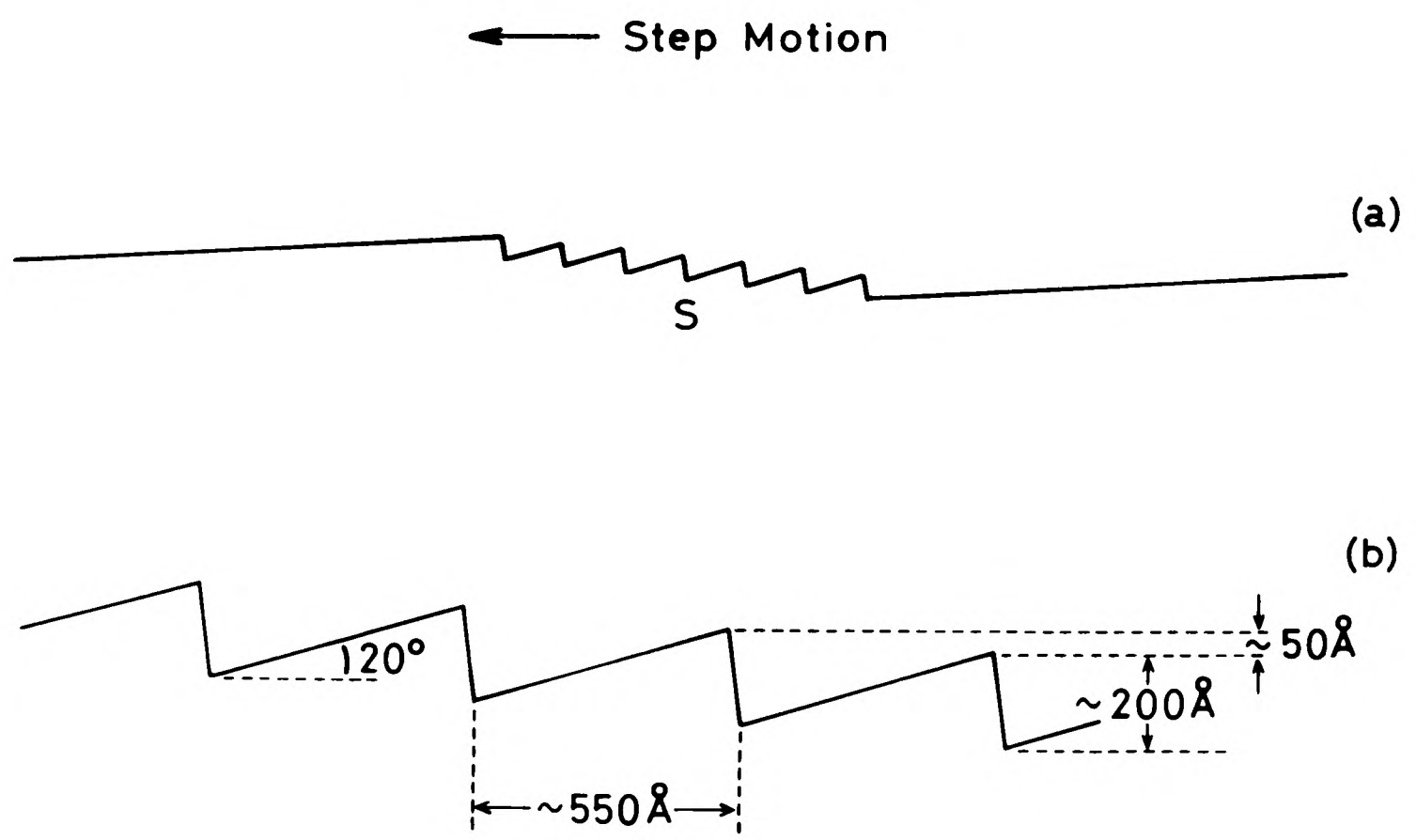

Electron
Beam
Entrance
Slit
B
B
C
C
B
B
E
E-ΔE
Photographic Plate

Fig 3.2 Si sublimation steps moving in [$\bar{1}\bar{1}$2] type direction on (111) Si substrate: note new directions for deflected steps at A and B. (Transmission electron micrograph, thickness fringe contrast)

Fig 3.3 a) Diagram showing profile through surface in direction of A (fig 3.2); note that individual atomic steps group into superbunches of the type S.

b) Diagram of steps superbunch S illustrated in fig 3.2(a) at higher magnification, showing approximate dimensions.


$\bar{1}\bar{1}2$
A
B
0·5μ


Step Motion
(a)
S
(b)
120°
~50Å
~200Å
~550Å

1971a). This showed that the step motion occurred along the $[\bar{1}\bar{1}2]$, rather than the $[11\bar{2}]$ direction, using the notation given in fig 3.28.

While only weak TEM thickness fringe contrast was given by undeflected surface steps, those deflected by particles were much more widely spaced and gave stronger contrast. This showed that the deflected steps, which generally travelled in $\langle 110 \rangle$ directions (A and B in fig 3.2), did not have a simple 'staircase' configuration, but exhibited a 'saw-tooth' profile (fig 3.3). Since the thickness extinction distance for 100 kV electrons in Si using a $2\bar{2}0$ reflection is ~ 750 Å, it was possible to estimate the slope of the shallowly inclined, leading step risers. This indicated that they were $\sim 20^{\circ}$ from the (111) plane, i.e. close to the orientation of $\{123\}$ planes. The slope of the trailing inclined risers was much steeper, and could not be similarly estimated, although they were probably nearly perpendicular to the (111) plane. The slope of the surface between the individual step bunches was mostly around 2°.

One substrate was examined by TEM after heating to 1250°C for only 3 min. It was found that this was also covered by similar surface steps, although they were even finer and correspondingly harder to detect. Also, no substrate showed any evidence for the presence of significant numbers of surface impurity particles.

3.4) Deposition in UHV

3.4.1) Standard Preheated Substrates

When substrates were heated to 1250°C for 10 min, and then the temperature lowered to 880°C and deposition commenced at $\sim 5 \times 10^{-2}$ Å sec^{-1}, individual growth centres, observed on unpreheated substrates, no longer resulted. Growth took place by the extension of layers of Si atoms across the surface (Cullis and Booker, 1971a). Optical microscopy revealed a

wave-like surface structure (fig 3.4), while TEM showed these wave fronts to be terraces of steps which were the boundaries of the layers growing over the surface. The layers were held back in many places at pinning sites, which mostly proved to be impurity particles several hundred Å across, situated at the bottom of relatively deep pits, often hexagonal with edges along ⟨110⟩ directions, in the grown film. The particles were analysed, as described in the next section, and identified as SiC.

If deposition was carried out for 3 hr (layer thickness 600 Å), the resulting step terraces were mainly bowed. Few straight steps were present and there was no obvious single direction of growth (figs 3.5 and 3.6). However, when growth was continued for 15 hr (layer thickness 3000 Å), the number density of pinning sites decreased, and many straight step terraces occurred (fig 3.7). The observations showed that the direction of step motion was now $[11\bar{2}]$, i.e. opposite to that of the 'sublimation' steps. On some occasions, the direction of step motion was $\sim 10^{\circ}$ from $[11\bar{2}]$, i.e. close to $[21\bar{3}]$. The profile of the steps was generally of the type shown in fig 3.3.

An important feature of the growth is that the Si films had a high crystallographic perfection. Stacking faults and dislocations were constantly looked for but virtually never seen in the TEM studies.

Increasing the Si deposition rate to 1 Å sec^{-1} at 880°C gave a film with a finer topographical pinning structure. Therefore, the film uniformity was somewhat improved, although TEM showed that the pits associated with pinning sites still penetrated deeply into the Si. No crystallographic defects were found in the film, but in some regions minute particles were included in the deposit.

When Si was deposited at $\sim 5 \times 10^{-2}$ Å sec^{-1} at the lower temperature of 750°C (the lowest temperature measureable with the pyrometer in use), while the mode of growth did not change, the shape of the step terraces

was no longer wave-like. They were then found to be arranged in straight arrays, with periodic angular disturbances resembling sections of triangles (fig 3.8). Pinning sites of the shape previously described were not observed.

The effect of recontaminating a preheated substrate surface was investigated by admitting air into the vacuum chamber, up to atmospheric pressure, after pretreatment at 1250°C had been carried out. After ~ 1 hr the apparatus was re-evacuated and baked in the usual way to obtain UHV. When 600 Å of Si was deposited at 880°C and $\sim 5 \times 10^{-2}$ Å sec^{-1}, the resulting film growth no longer produced uniform arrays of surface steps. Instead, the growth was irregular, and the film resembled an assembly of growth centres, of the type normally observed on unpreheated substrates (fig 3.9).

If a Si substrate was preheated to only 1160°C for 10 min immediately prior to standard deposition at 880°C, the main mode of growth was again by the extension of pinned layers over the surface. However, in certain localized regions, which probably contained residual impurity, the growth was greatly modified and reverted to the formation of very irregular growth centres (fig 3.10). At the edges of these regions there was a continuous transition between the two types of observed structure. This illustrates the role of the surface and its associated contaminants in determining the form of the film growth.

3.4.2) Initial 'In Situ' Gas Polish

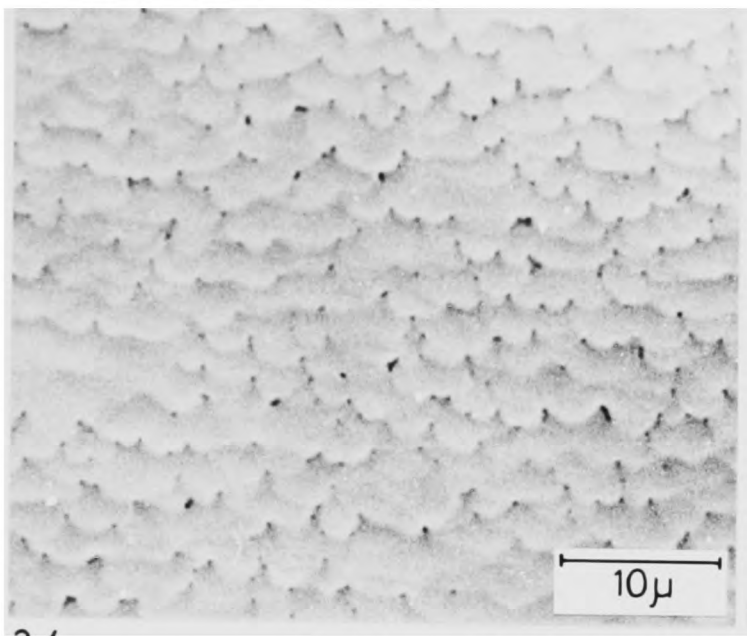
When substrates were cleaned by pretreatment at a high temperature in vacuum, it was shown that there were accompanying topographical changes i.e. bunched step formation (section 3.3). Subsequent growth took place by the addition of atoms to these steps, which were also then pinned by impurity particles on the surface. Further, it has already been found that as-received gas polished substrates had no surface steps detectable by direct

Fig 3.4 Si growth steps with pinning sites.
(Optical micrograph, phase contrast)

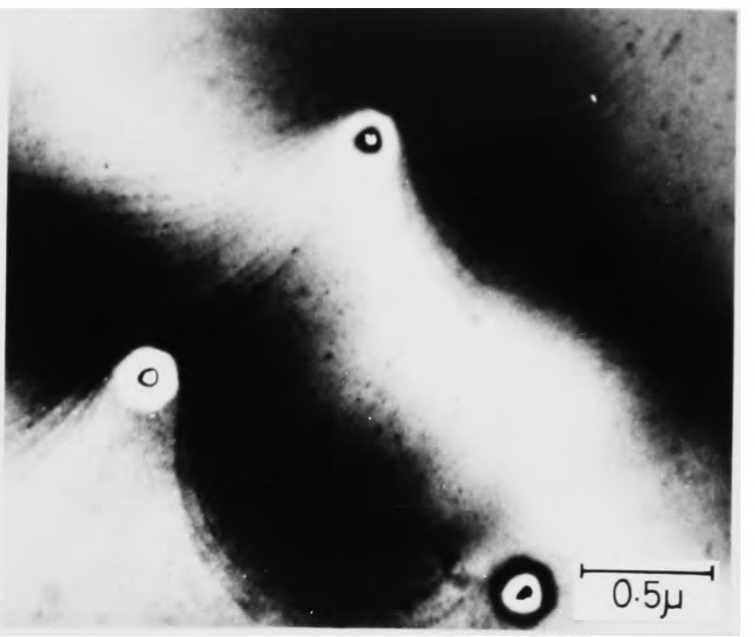
Fig 3.5 Si growth steps with pinning sites.
(Transmission electron micrograph, thickness fringe contrast)

Fig 3.6 Si growth steps with pinning sites.
(Transmission electron micrograph of Pt/carbon replica directly obtained from film surface)

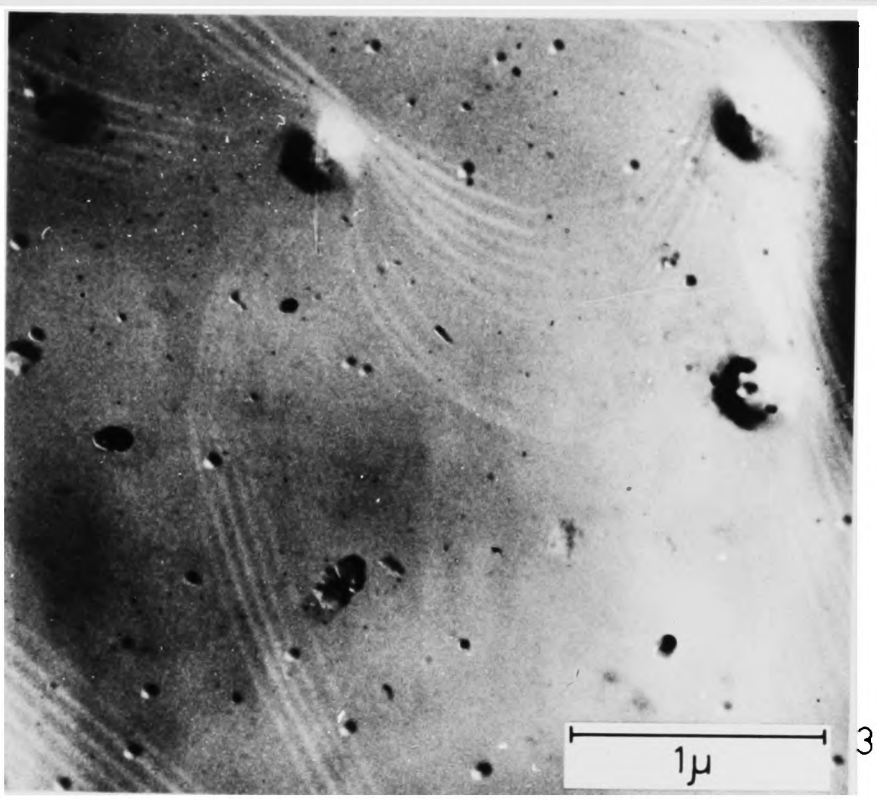
Fig 3.7 Si growth steps moving in $[\bar{1}\bar{1}2]$ and $[21\bar{3}]$ directions.
(Transmission electron micrograph, thickness fringe contrast)



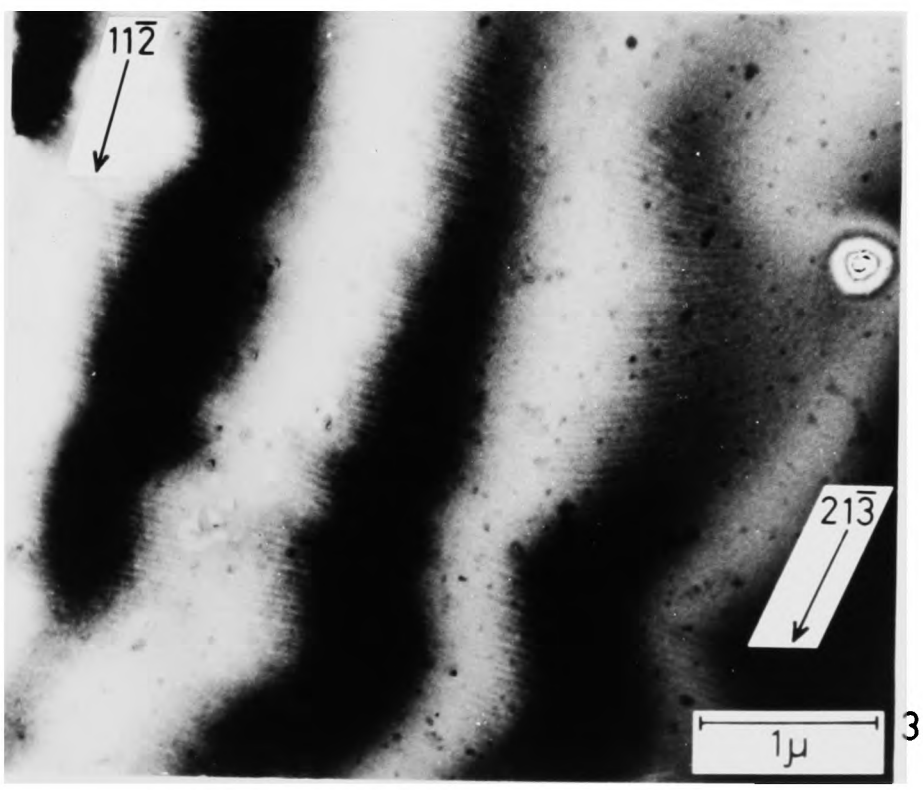
3·4



3·5



3·6

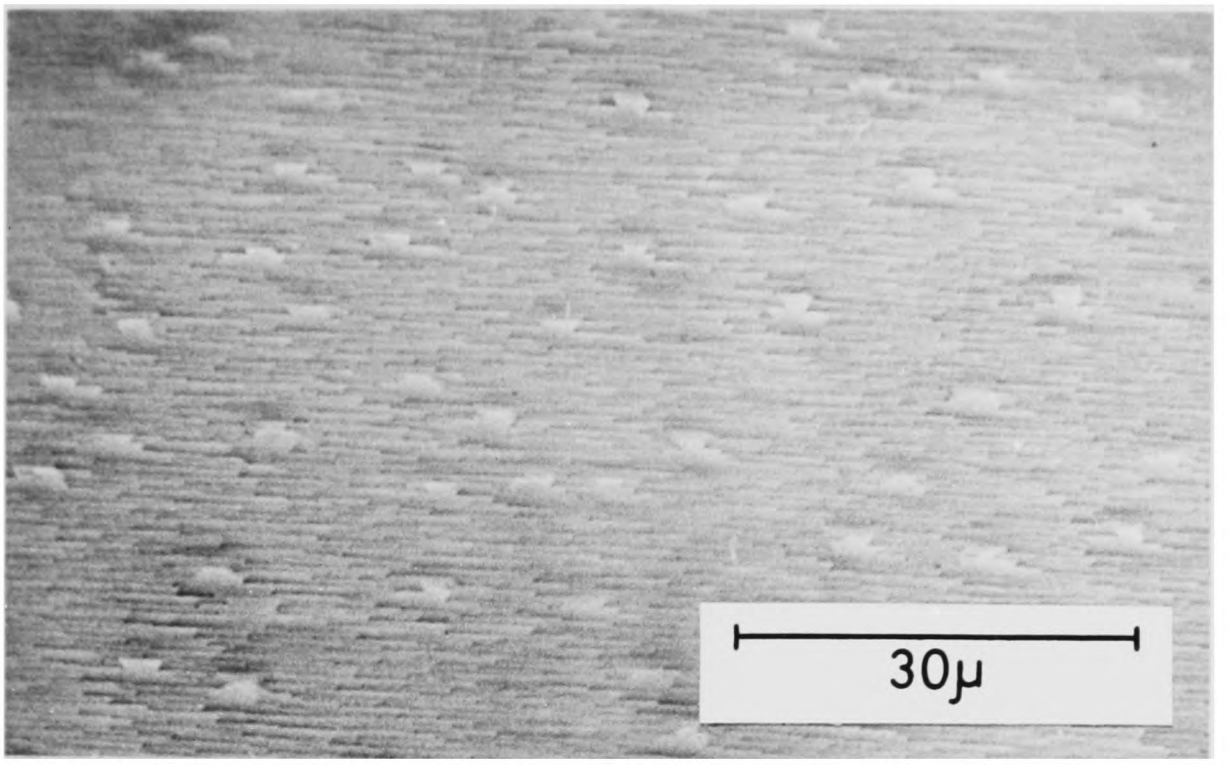


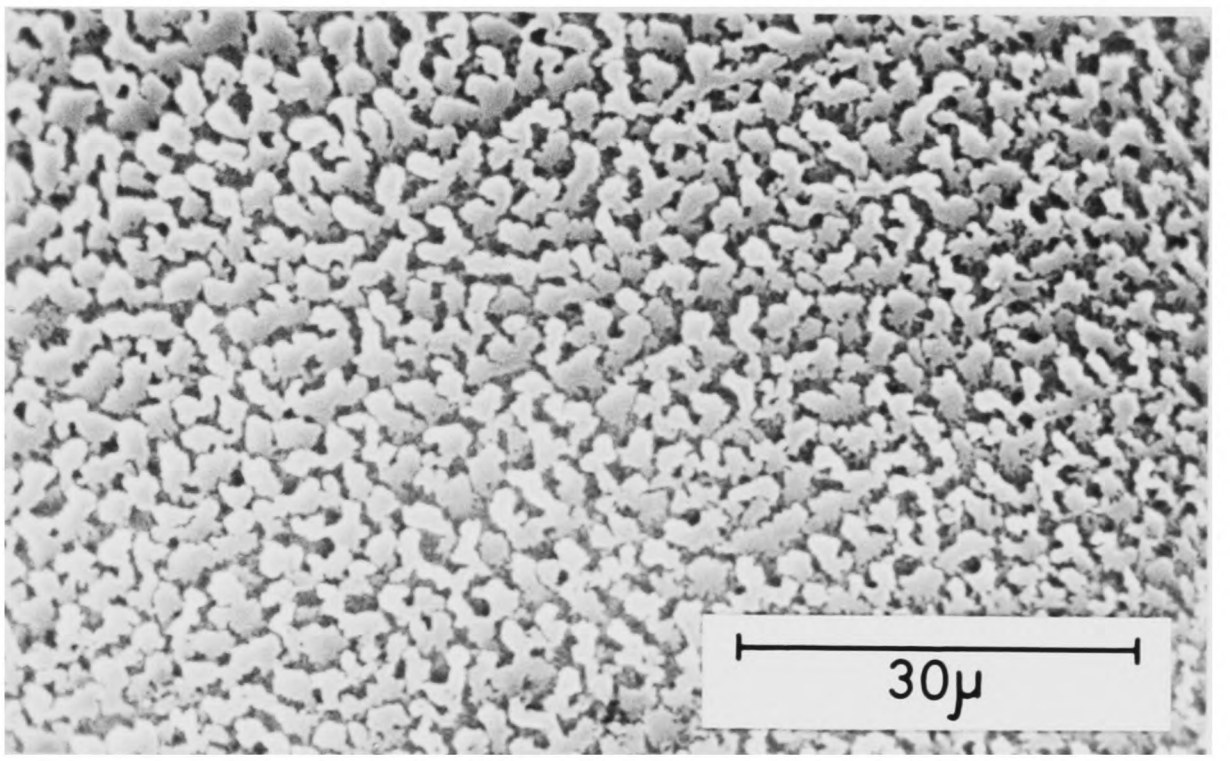
3·7

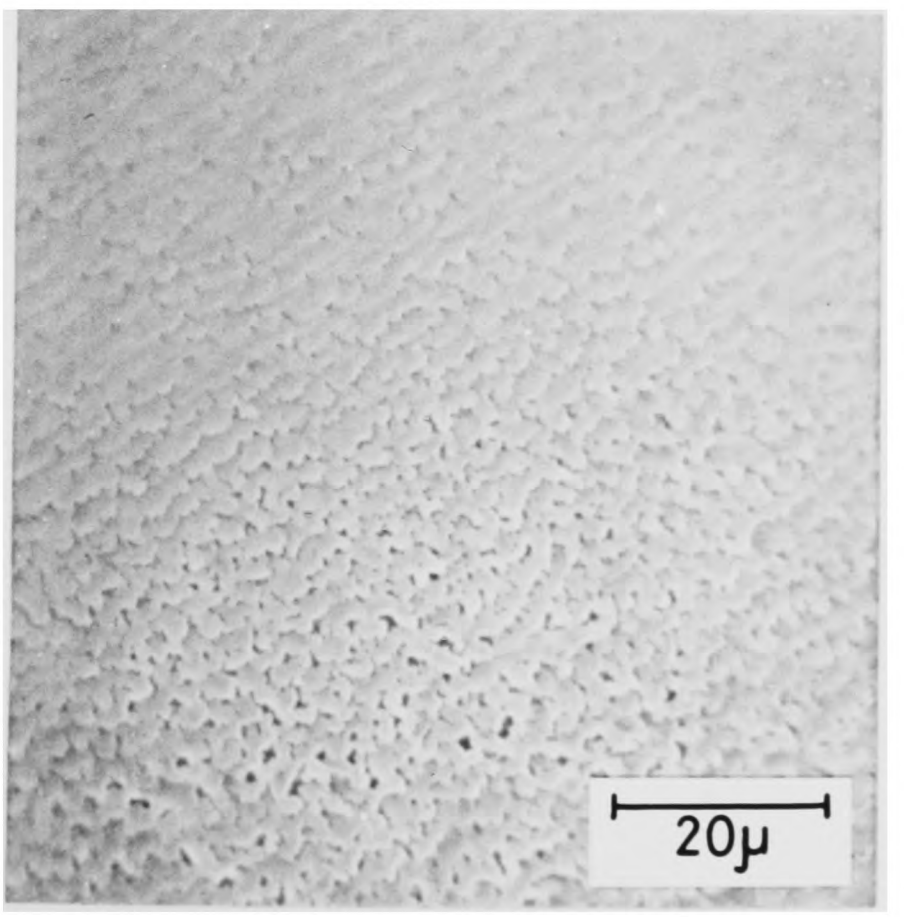
Fig 3.8 Straight Si growth steps produced by deposition at only 750°C. (Optical micrograph, phase contrast)

Fig 3.9 Irregular Si film growth after recontamination of substrate with air. (Optical micrograph, phase contrast)

Fig 3.10 Regions of different Si film growth after substrate pretreatment at only 1160°C: note transition from wave-like to irregular structure from top to bottom of figure. (Optical micrograph, phase contrast)


30μ


30μ


20μ

TEM (section 2.4), but clearly they were contaminated by exposure to air, before insertion into the vacuum deposition apparatus. This led to film growth by nucleation, but with the subsequent formation of large irregular growth centres. Now, a hypothetical ideal form of Si growth may be visualized as nucleation, leading to the extension of single monolayers over an otherwise featureless surface, with no impurities present to disrupt the process. Therefore, it was decided to attempt an 'in situ' gas polishing procedure, which would hopefully give relatively featureless, contamination-free substrate surfaces, in order to facilitate the growth of very uniform thin Si films.

High gas flow-rate processes at atmospheric pressure are not readily compatible with apparatus designed for work at UHV. Also, the highly corrosive compounds often used as gas polishing reagents (HCl, HBr), could not be passed through the vacuum apparatus, since the molecular sieve and diffusion pump fluid might have been severely degraded. Therefore, to make apparatus modifications unnecessary, gas polishing in H_2 with a small amount of H_2O vapour was investigated. The standard high purity H_2 was found to be wet to the extent of a few hundred ppm, and this was considered satisfactory for this preliminary work.

For the first experiment, the apparatus was set up in the normal manner, and baked to obtain UHV. Since it was considered desirable, if possible, to avoid further baking procedures, which could recontaminate a substrate, gas polishing with a low pressure of H_2 was first attempted. Therefore, after the diffusion pump had been switched off for 15 min, wet H_2 was admitted through the leak valve up to a pressure of only 1 torr. The rotary pump remained in operation to maintain a substantial gas flow-rate. In order to reduce direct sublimation from the substrate bar, this was heated to only 1150^{o}C for 10 min, and then allowed to cool with the gas still flowing. The apparatus was next re-evacuated, and with the

diffusion pump in operation, a chamber pressure of 10^{-8} torr was obtained in ~ 6 hr. The main residual gas was H_2. Si was then deposited on to the substrate held at 880°C, although extensive preliminary outgassing was found to be necessary, as the Ta substrate clips had absorbed large quantities of H_2. The ambient pressure during deposition was 6×10^{-8} torr, almost exclusively H_2. The resulting Si film, which had a mean thickness of ~ 600 Å, was found to consist of isolated irregular growth centres (fig 3.11a), while a portion of the Si substrate surface which had received no deposit exhibited a 'fern-like' etching structure (fig 3.11b).

The Si film and substrate surface structures produced in the first experiment were clearly undesirable, so that the use of more vigorous gas polishing conditions was next investigated. The H_2 pressure was increased to ~ 0.1 atm, and a Si substrate bar was held at 1240°C for 5 min. The bar was then removed from the apparatus for immediate study, since subsequent deposition at a useful working pressure would have been difficult to achieve, due to evolution of H_2 by the Ta substrate support clips. Indeed, these showed signs of partial degeneration. However, the surface of the substrate bar was found to have been well polished, with only occasional small triangular etching features (fig 3.12).

Since it was now likely that a useful substrate polish could be obtained, a full deposition run was undertaken. Also, the substrate bar was supported in W clips, since W absorbs H_2 to a very much smaller extent than Ta (Dushman, 1962). However, great difficulty was experienced in bending W sheet to the required configuration, without producing fractures. The actual gas polishing procedure was carried out under 1 atm of H_2, at a flow rate of 2 litres min^{-1}, the H_2 being vented through an outlet in the backing line. The substrate bar was heated to 1240°C for only 1 min, to remove a minimum of Si consistent with cleaning the surface. After the bar had been cooled in the H_2, UHV was re-established by a mild baking

Fig 3.11 'In situ' gas polish - first experiment

a) Irregular Si growth centres

b) Substrate surface structure

(Optical micrographs, phase contrast)

Fig 3.12 'In situ' gas polish - second experiment

Substrate surface structure

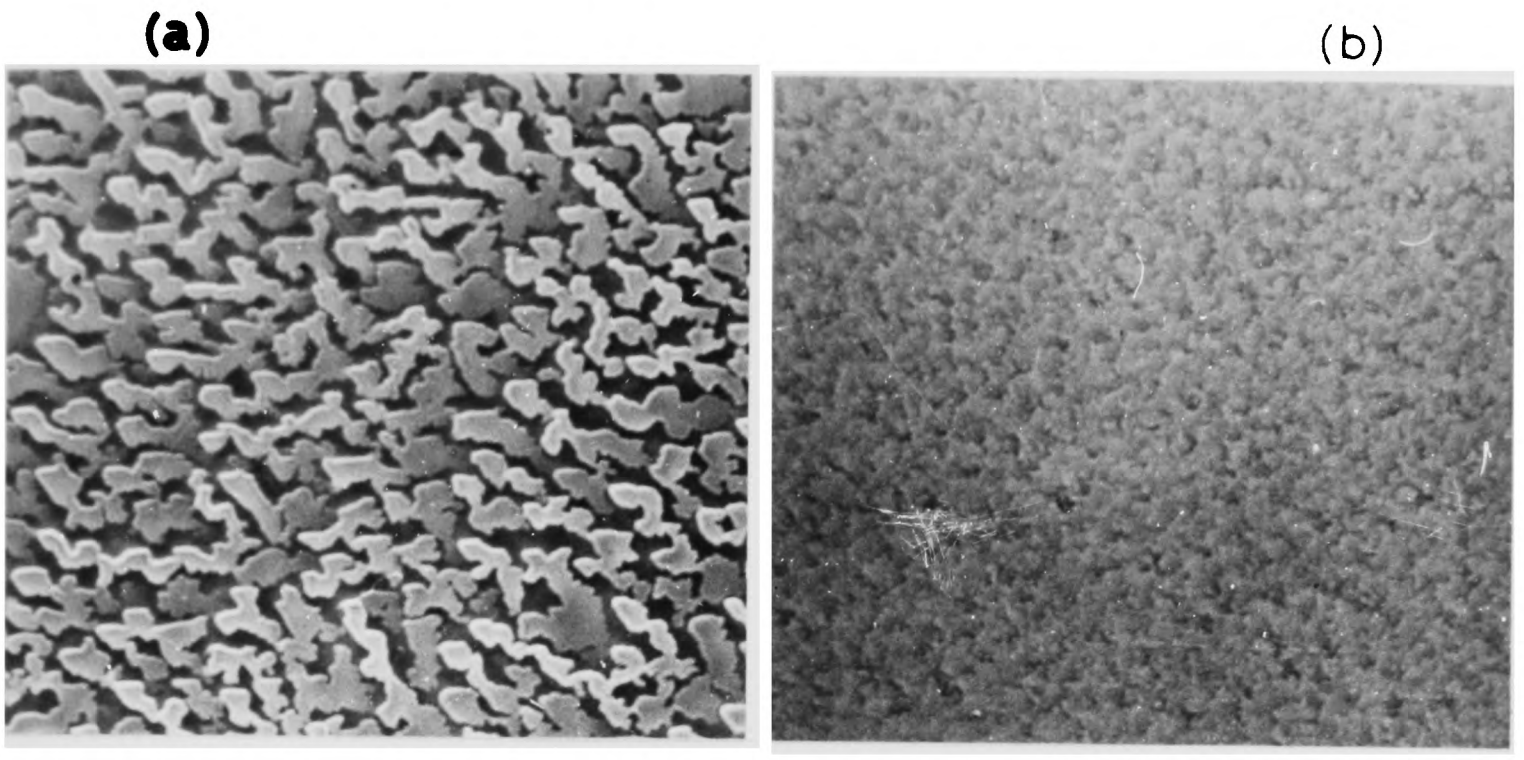
(Optical micrograph, phase contrast)

Fig 3.13 'In situ' gas polish - third experiment

a) Channelled Si film

b) Substrate surface structure

(Optical micrographs, phase contrast)


(a)
(b)
10μ
(a)
(b)

operation (sieve trap 100°C, UHV chamber 140°C) to give a base pressure of $\sim 3 \times 10^{-9}$ torr. Si was then deposited in the usual way, with no great outgassing problems, under an ambient pressure of $\sim 3 \times 10^{-8}$ torr; the residual gases were composed mainly of H_2. The Si film, which was equal in mean thickness to that of the first experiment, was found to have a channelled structure, resembling growth centres which had overlapped to a great extent (fig 3.13a). A portion of the substrate surface, which had received no deposit, was virtually featureless (fig 3.13b).

Both of these observations represent large improvements when compared with the results of the first experiment, and there is great promise of further possible advances if polishing conditions are optimized. However, this series of experiments was terminated here because of time constraints, coupled with various technical difficulties. These will be mentioned later, and several suggestions will be put forward in chapter 7.

3.5) Particle Microanalysis

3.5.1) The Particle Energy Loss Spectrum

When a Si film was deposited at 880°C on to a substrate which had been preheated in vacuum at 1250°C for 10 min, the growth was disrupted by impurity particles. Therefore, it was important to determine the constitution of these particles to identify the contaminant responsible. The particles were generally 100 - 1000 Å in diameter, and so were too small for analysis by selected-area transmission electron diffraction (SAED) or the electron microprobe technique. Therefore, transmission electron energy loss analysis was chosen, and the instrument used is described in section 3.2.

All materials introduce specific energy losses into a high energy transmitted electron beam, since this induces quantized plasmon oscillations

(collective electron excitations) in the sample. The probability of exciting surface plasmons increases with decreasing sample thickness (Ritchie, 1957), and in the present case, this would have been important for thicknesses of $\lesssim$ 65 Å. Therefore, since it was necessary to determine plasmon energies characteristic of the bulk material, particles of around 1000 Å diameter were studied. Undesirable overlap effects could have been another source of difficulty. However, the particles lay at the bottom of pits in the grown film, and since Si was removed from beneath them during the chemical specimen thinning, it was possible to find particles suspended in the Si matrix, but not overlapped by it.

To facilitate accurate positioning of the image of a particle over the analyser entrance slit, a fairly high microscope magnification was employed (4×10^4), and this gave a low energy loss spectrum intensity. To record the spectrum on a photographic plate, exposures of from 2 to 5 min were necessary, and since specimen drift then became a problem the image position was periodically re-adjusted. If the Si energy loss spectrum had been superimposed on that of a particle, subsidiary peaks would have been introduced at 17 eV and 34 eV, so that the spectrum would have been distorted. Figs 3.14 and 3.15 show the micrograph of a particle and its associated energy loss spectrum, respectively. The spectrum had a single well defined peak at 23.0($\pm$0.4)eV, with a half width of $\sim$ 10 eV. Even though the analyser was fitted with a vacuum cold trap and specimen anticontaminator, it was initially thought possible that carbon contamination might have accumulated on a particle during the long photographic exposure, giving a distorted spectrum. However, the 6.6eV plasmon peak given by amorphous carbon was never seen. Also, when a particle loss spectrum was recorded on a fast LN type plate in less than 1 min, although the signal/noise ratio was poorer than standard, the energy loss peak did not change in any way, indicating that carbon contamination was negligible

during the longer exposures.

3.5.2) Composition of the Particles

The energy loss spectrum of the particles was compared with spectra obtained from materials which were possible contaminants, in order to determine which was responsible for the layer pinning points.

It was initially considered that the particles might have been residual surface polishing materials, Al_2O_3 or ZrO_2. Accordingly, the energy loss spectra of these materials were obtained from the polishing powders themselves, which consisted of small crystallites with transparent edges. These spectra, which are shown in fig 3.16, indicated that the polishing materials were unrelated to the contaminant particles.

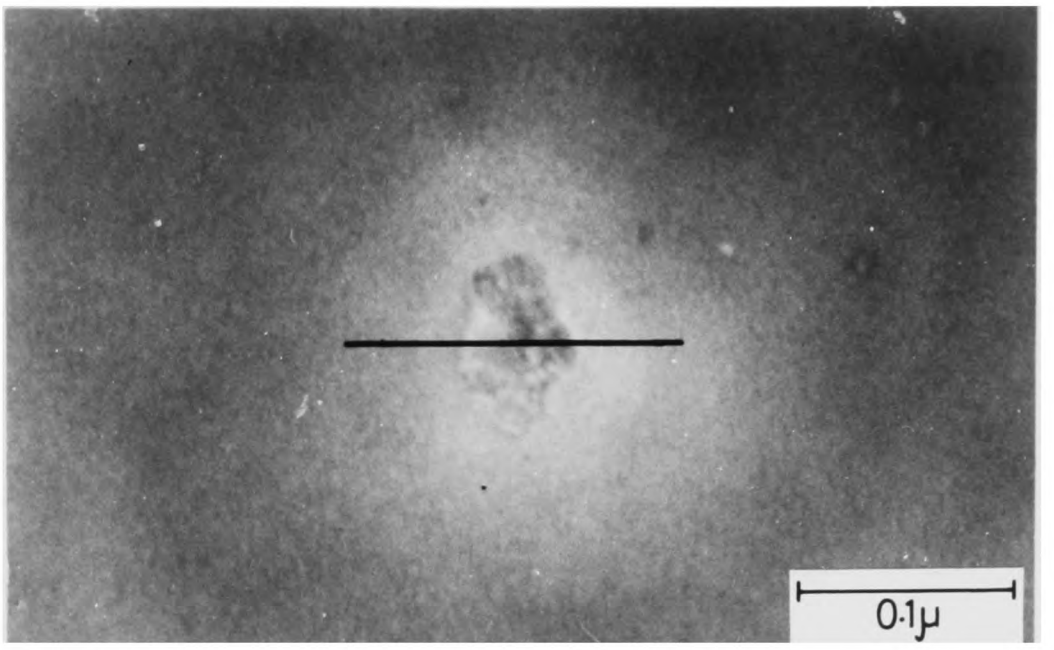
The possibility of Fe or Ta contamination was also considered. It has been postulated that Fe may be associated with the production of Si(111) - 7 x 7 LEED patterns (e.g. Thomas and Francombe, 1970), and high temperature preheated surfaces would certainly give this pattern (Charig and Skinner, 1969). Also it seemed possible that Ta might have migrated on to substrate bars, from the clips in which they were supported. Therefore, each of the two elements was fused with a Si substrate bar, under conditions similar to those of a standard high temperature pretreatment procedure. The resulting Ta and Fe silicides gave loss spectra with peaks at 16·2 eV and 21·5 eV respectively (fig 3.17), and neither of these corresponded to the spectrum of the particles.

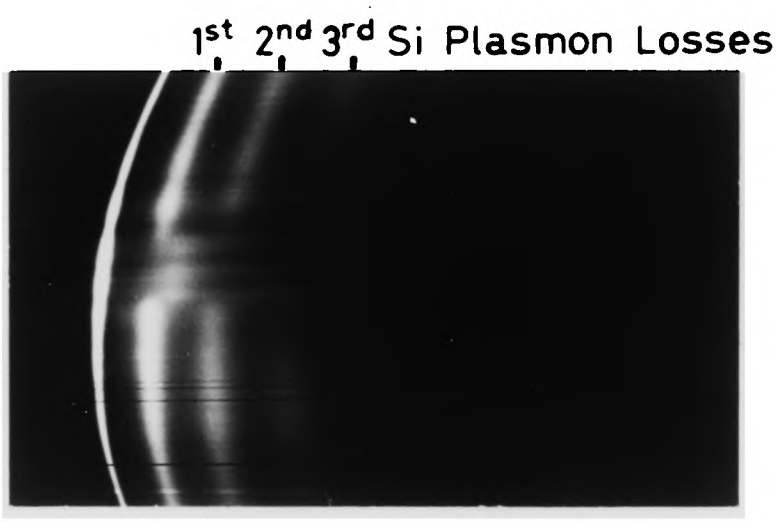
It was thought to be just possible that particles of residual SiO_2 could have been present on substrate surfaces, although Joyce et al (1967) had shown that this contaminant would probably have been removed as volatile SiO prior to deposition, by reaction with Si itself. Nevertheless, the energy loss spectrum of thermally produced SiO_2 was obtained, and it exhibited a double peak structure (15.5 eV and 22.8 eV, fig 3.18). Obviously, this did

Fig 3.14 Impurity particle at bottom of pit in Si film. Line marks position of energy loss analyser entrance slit. (Transmission electron micrograph)

Fig 3.15 (Top) Typical analyser spectrum illustrating the way in which electrons, having passed through the entrance slit, were dispersed in energy. After the zero loss electrons, the first, second and third characteristic plasmon losses produced by the Si matrix can be seen. In the central region, these losses are no longer visible where the slit passed across the image of a particle which gave its own specific displaced energy loss.

(Bottom) Microdensitometer trace across the plasmon loss produced by an impurity particle. Note that the peak (23.0 eV) is well defined.


0·1μ


1st 2nd 3rd Si Plasmon Losses

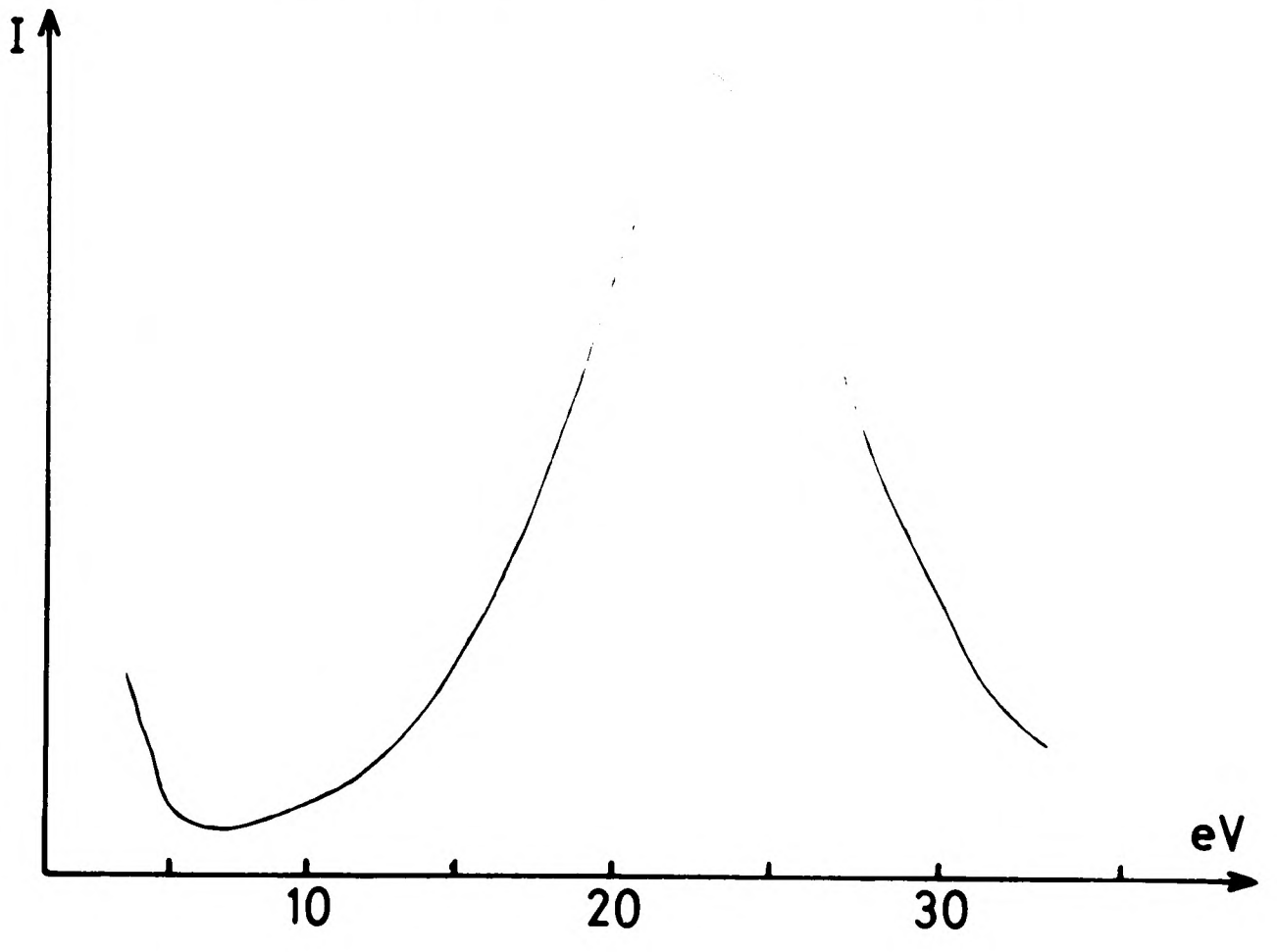
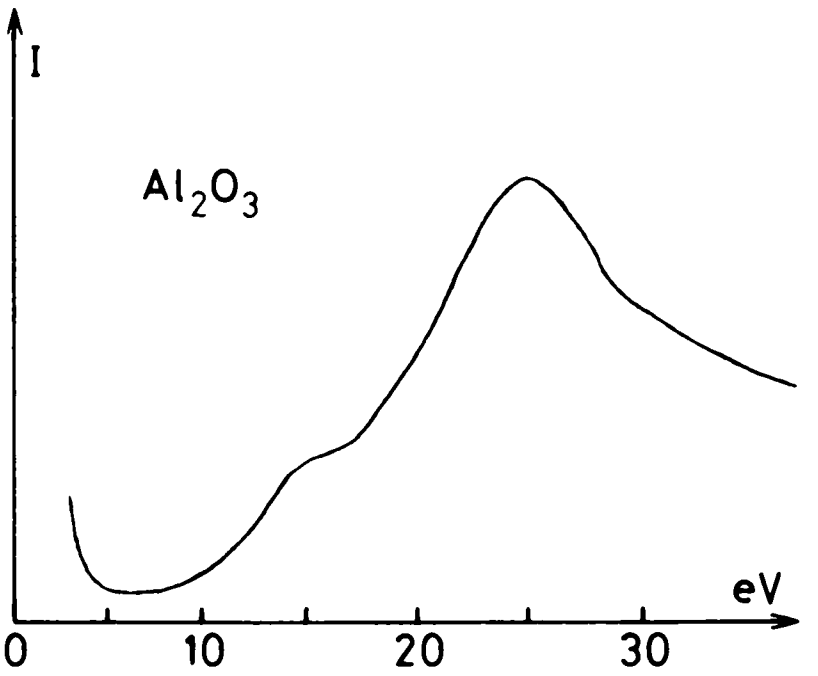

I
eV
10
20
30

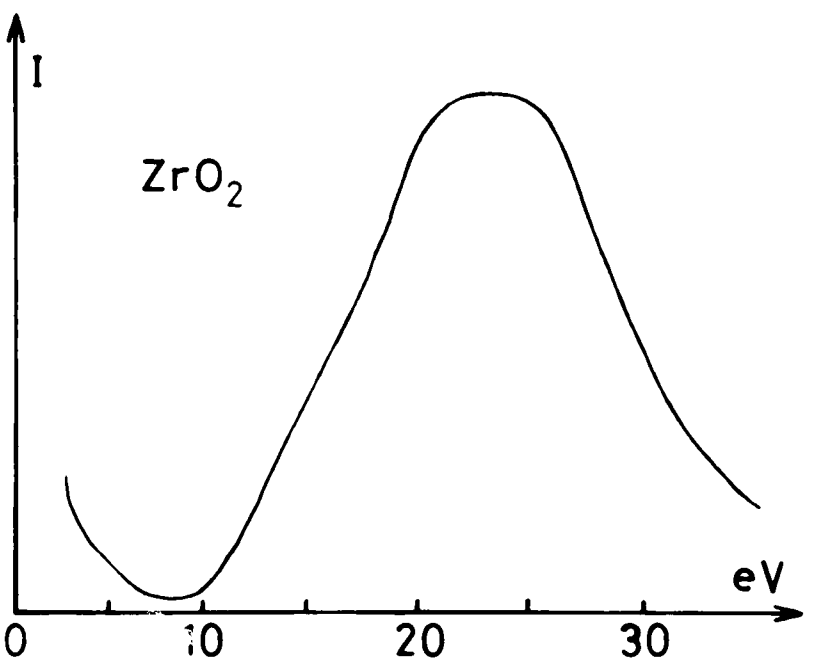
Fig 3.16 Loss spectra of polishing compounds:

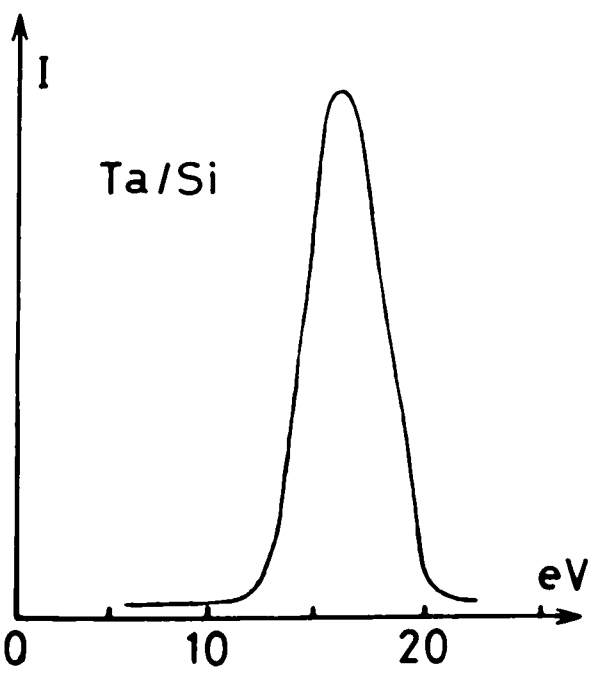
Al_2O_3 - double peak structure

ZrO_2 - peak with broad top

Fig 3.17 Loss spectra of compounds produced by fusion of Ta and Fe with a Si bar - peaks at 16.2 eV and 21.5 eV respectively


I
Al_2O_3
eV
0
10
20
30


I
ZrO_2
eV
0
10
20
30


I
Ta/Si
eV
0
10
20

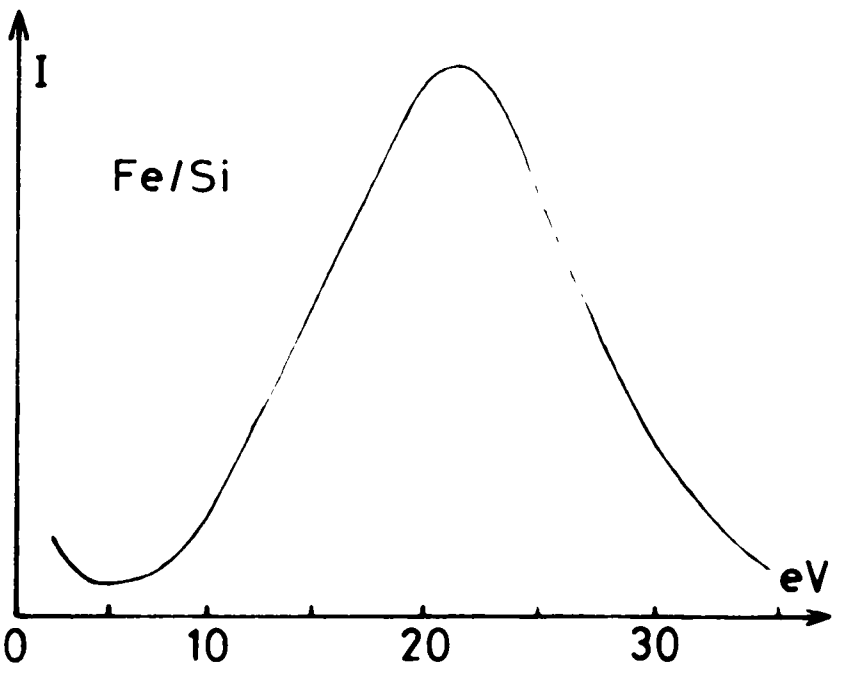

I
Fe/Si
eV
0
10
20
30

Fig 3.18 Loss spectrum of SiO_2 - double peak structure

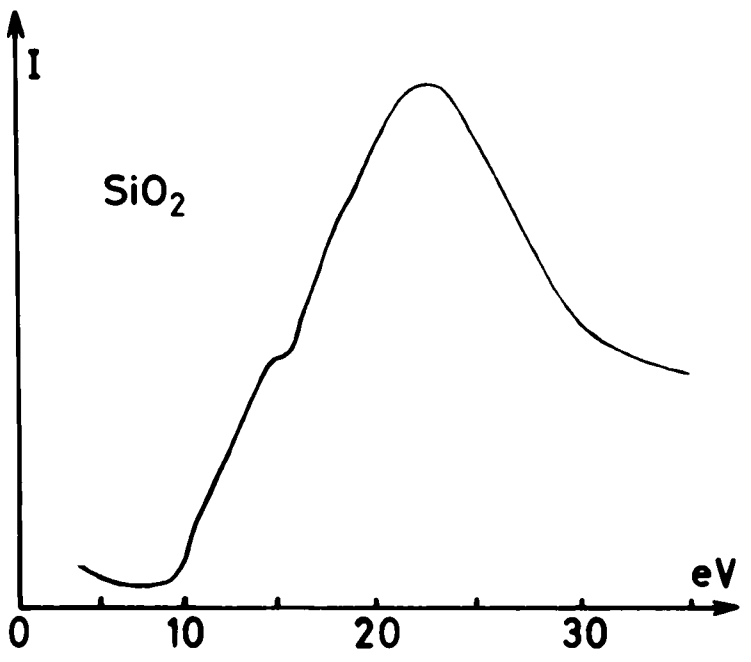
Fig 3.19 Loss spectrum of amorphous carbon - double peak structure

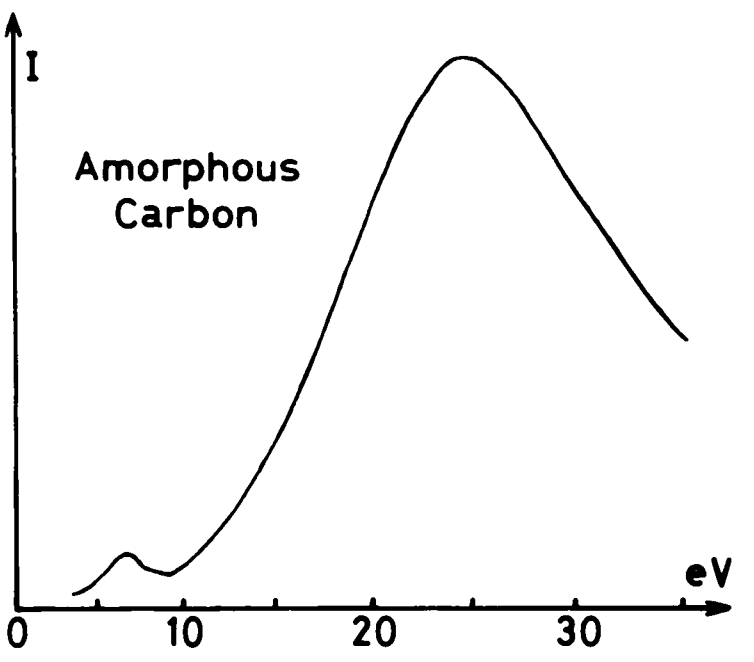
Fig 3.20 Loss spectra of SiC:

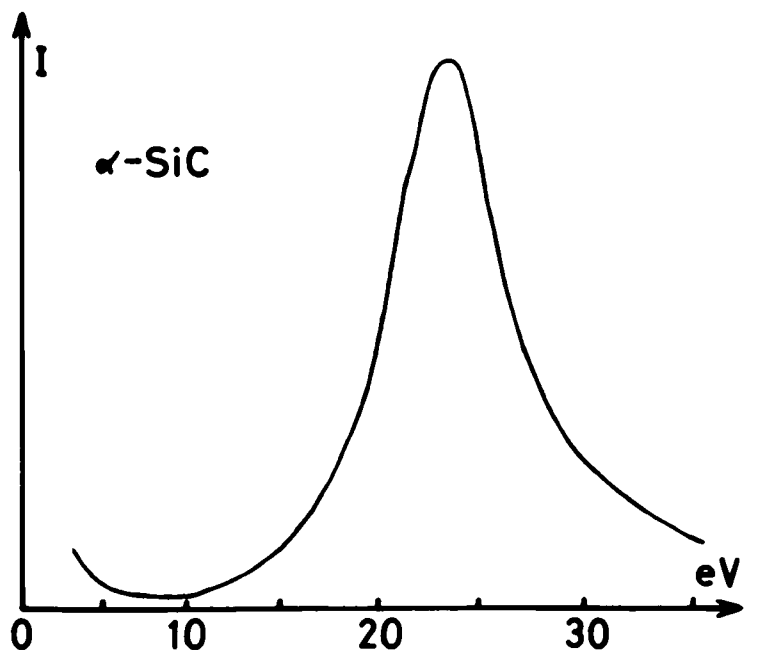
α - SiC - peak at 23.5 eV

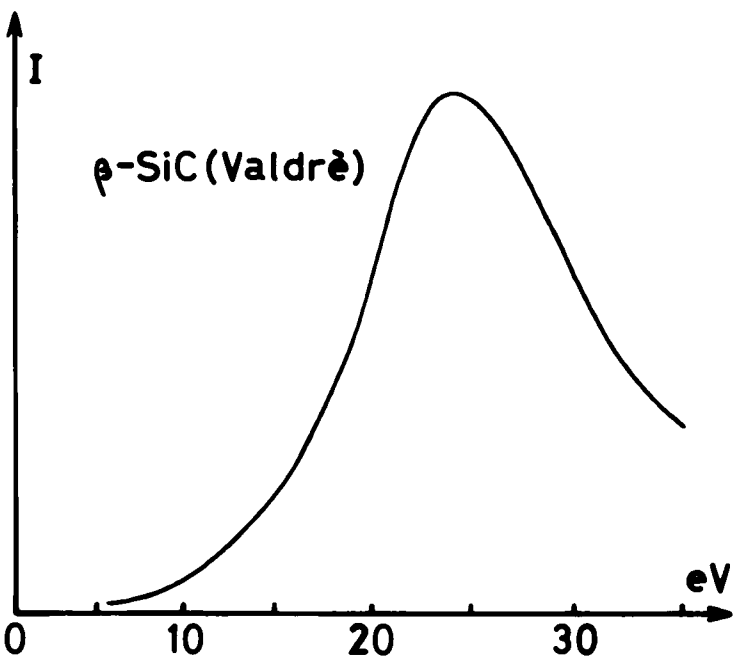
β - SiC (produced in Valdrè hot stage) - peak at 24.2 eV

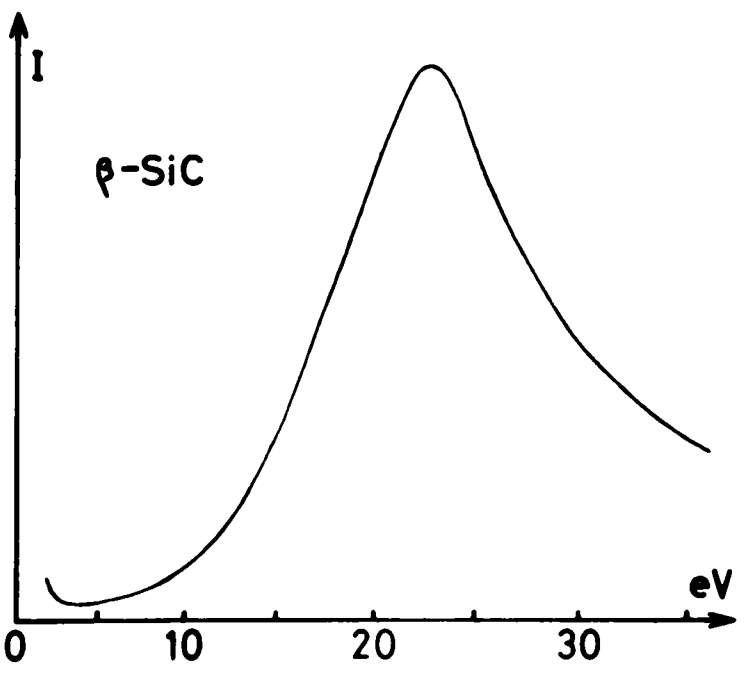
β - SiC (pure, chemically vapour grown) - peak at 22.8 eV


I
SiO2
eV
0
10
20
30


I
Amorphous
Carbon
eV
0
10
20
30


I
α-SiC
eV
0
10
20
30


I
β-SiC (Valdrè)
eV
0
10
20
30


I
β-SiC
eV
0
10
20
30

not correspond to the loss spectrum of the particles.

The remaining possible source of contamination was carbon. Fig 3.19 shows the energy loss spectrum of amorphous carbon which exhibited peaks at 6.6 eV and 24.5 eV. Since the unknown particles did not yield a double loss peak structure, they were not composed of amorphous carbon. However, the high temperature pretreatment of substrates prior to deposition would probably have caused carbon to combine with Si to give SiC. Therefore, the energy loss spectra of both α- SiC and β - SiC were determined (fig 3.20). The sample of the former consisted of a fine powder, and gave a single loss peak at 23.5 eV. One specimen of β - SiC had been formed directly in a thinned Si specimen using a Valdrè TEM hot stage, and gave a loss peak at 24.2 eV. However since the residual gases present in the TEM during the preparation were unknown, it is possible that the β - SiC may have been contaminated with e.g. Si_3N_4. Therefore, another sample of pure chemically vapour grown β - SiC was obtained and found to give a single loss peak at 22.8 eV.

These SiC spectra, especially that of the pure β - SiC, are closely similar to the spectrum of the particles. Therefore, by this process of elimination, carbon is identified as the contaminant which caused the formation of pinning sites in the Si films grown on preheated substrates.

3.6) Effect of Contaminating Gases

In a series of runs, contaminating gases were deliberately admitted to the vacuum chamber during Si deposition, to investigate their effect upon film growth. The substrates, which had been preheated at 1250°C for 10 min, were held at 880°C, and Si films were deposited at 5×10^{-2} Å sec^{-1} up to a mean thickness of ~ 600 - 800 Å. Except where stated, the impurity gas was introduced up to the desired pressure ~ 15 sec prior to initiation of deposition. In this way, initial interaction of the gas with the cleaned substrate surface was minimized.

The low Si deposition rate was retained for two reasons. First, the structure of such films grown under good vacuum conditions ($\sim 10^{-8}$ torr, with residual CO_2 and CO), was well characterized (section 3.4.1). Second, the effect of contaminating gases was expected to be greater, and therefore more easily recognized than at higher deposition rates.

3.6.1) Carbon Monoxide and Dioxide

The effect of each gas upon Si growth was investigated at pressures of 10^{-7} and 10^{-6} torr. The sequence of changes observed is shown in fig 3.21. At a pressure of 10^{-7} torr, both gases disturbed the film pinning structure, causing the pinning points to become somewhat enlarged. At 10^{-6} torr, CO had a relatively large effect by inducing the film to break up, giving isolated Si growth centres of the type seen on unpreheated Si substrates. At this gas pressure, CO_2 had notably less influence upon the growth, since the Si film still displayed a continuous pinning structure, although it was rather less regular than that produced in the absence of gas. When this CO_2-induced structure was examined by TEM, it was found that the surface had many step terraces as expected. However, there were also numerous particles included in the film, presumably produced by reaction of the CO_2 with Si, (fig 3.22).

3.6.2) Methane and Ethylene

When CH_4 was introduced at a pressure of 10^{-7} torr, subsequent optical microscopy revealed no significant changes from the usual Si film pinning structure. In contrast, ethylene at this pressure induced relatively large structural alterations (fig 3.23a). When the ethylene pressure was held at 10^{-6} torr, the Si growth was severely affected, with the production of a very irregular film structure which appeared, optically, to incorporate an array of uniformly spaced point-like regions of disturbed

material (fig 3.23b). TEM showed that these regions contained polycrystalline particles of β-SiC. A TED pattern from such a film is given in fig 3.24, and the β-SiC rings show clear evidence for the existence of a preferred orientation, matching that of the Si. Micrographs A and C were taken using the β-SiC diffraction 'spots' indicated, and the corresponding carbide crystallites are readily visible. Micrograph B shows the Si matrix, and although there were only a small number of crystallographic defects, the material had a curious mottled structure. Sometimes stacking faults occurred adjacent to β-SiC crystallites, and one of these is circled in the micrograph. The diffraction pattern also indicates that the Si film contained twinned regions, and in particular, spots of the type labelled D were produced by 30^{o} rotational twins.

Parts of the substrate surface exposed to 10^{-6} torr of ethylene, but which received no Si deposit, showed evidence for attack by the gas.

3.6.3) Oxygen

The effect of an ambient pressure of 10^{-7} torr O_2 during Si deposition was the production of a film pinning structure, with possibly somewhat fewer pinning sites than would be expected in the absence of the gas, (fig 3.25a). However, a dramatic improvement in the film structure occurred for deposition in the presence of 10^{-6} torr O_2, since the resulting Si film had no remaining pinning sites, and surface steps were very fine and straight (fig 3.25b). No crystallographic defects were observed using TEM (fig 3.26), although certain regions did contain some included particles. A section of the substrate surface which had received no Si deposit showed a faint wave-like etching structure under the optical microscope.

To test whether the O_2 exerted a beneficial action by cleaning

Fig 3.21 Si films grown in -

a) UHV (10^{-8} torr)

b) CO_2 (10^{-7} torr)

c) CO_2 (10^{-6} torr)

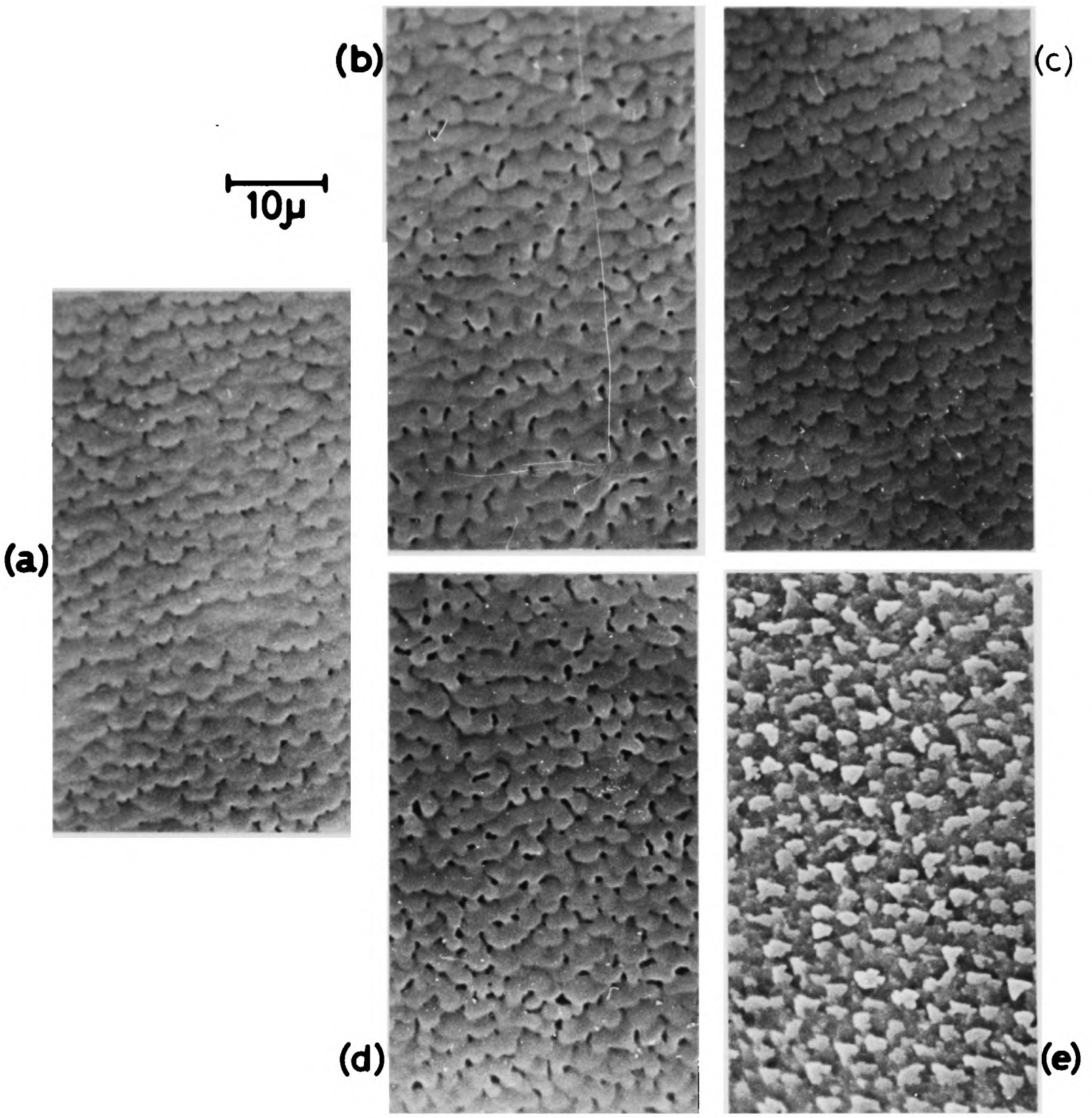
d) CO (10^{-7} torr)

e) CO (10^{-6} torr)

(Optical micrographs, phase contrast)

Fig 3.22 Si film grown in CO_2 (10^{-6} torr)

(Transmission electron micrograph)


(a)
(b)
(c)
(d)
(e)
10μ

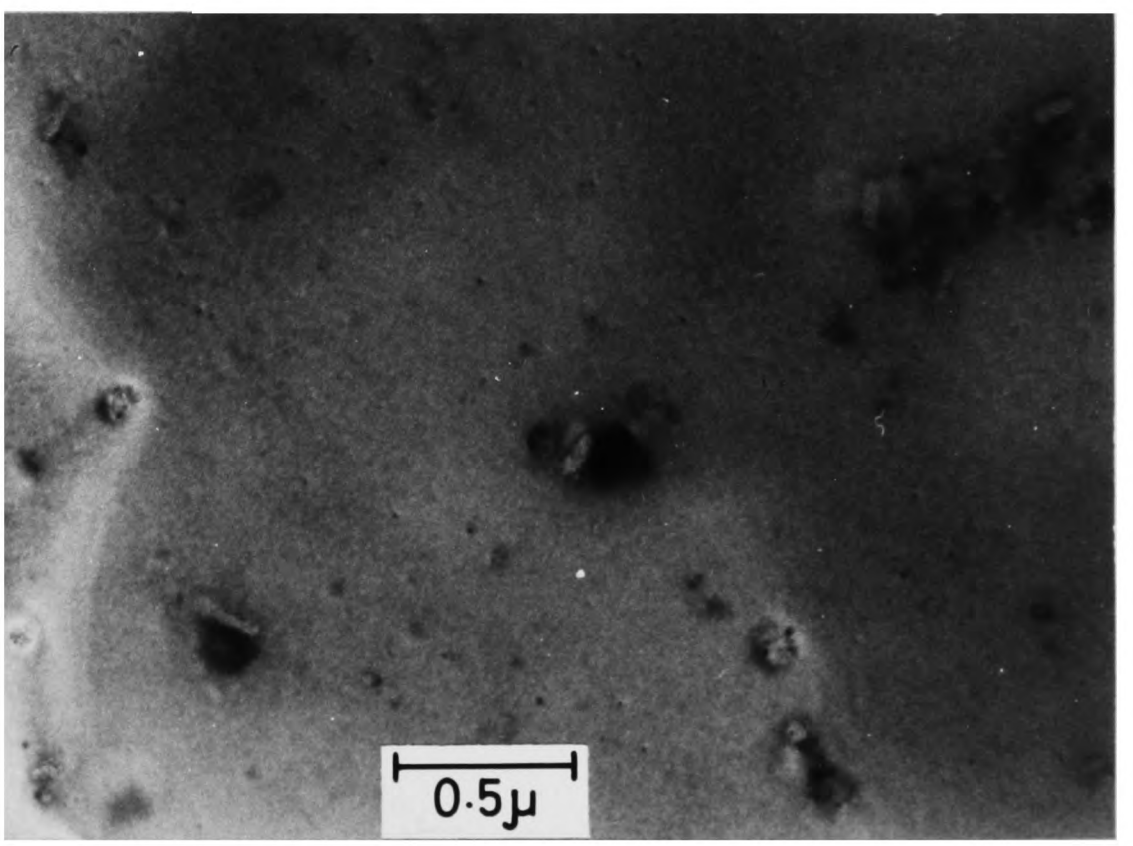

0·5μ

Fig 3.23 Si films grown in ethylene -

a) at 10^{-7} torr

b) at 10^{-6} torr

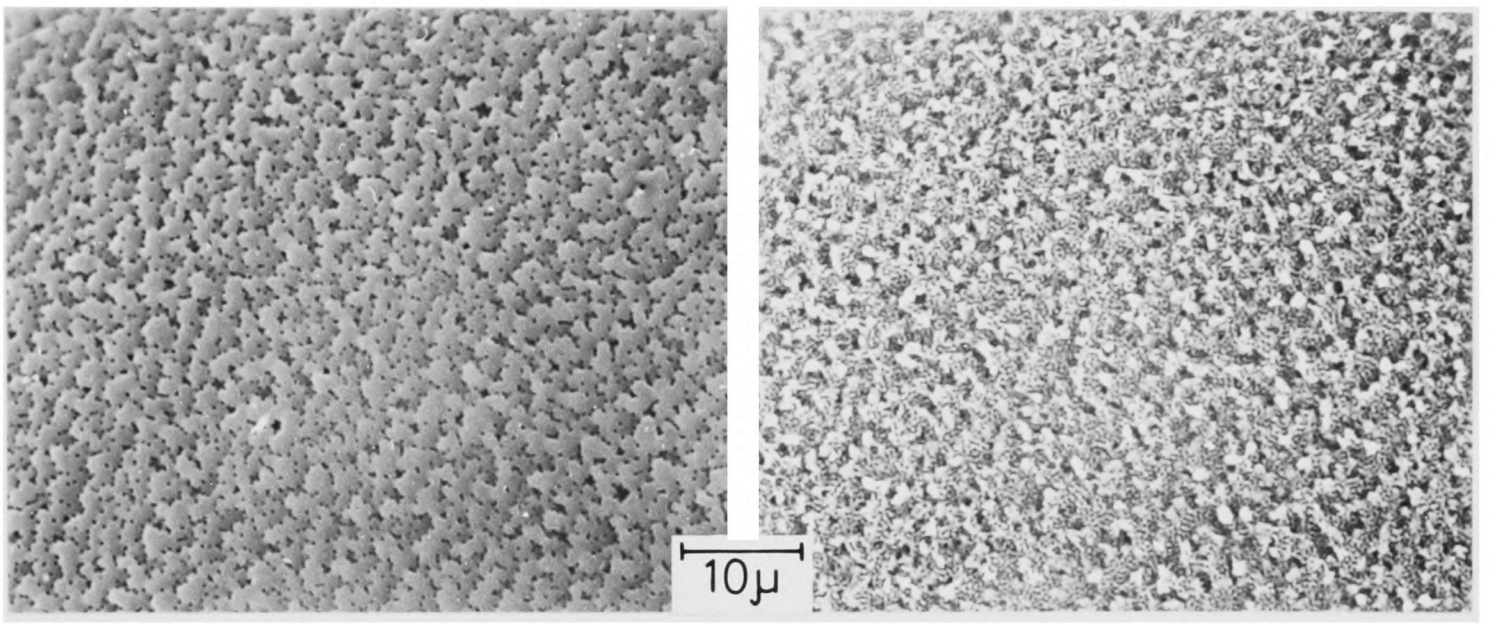
(Optical micrographs, phase contrast)

Fig 3.24 Si film grown in ethylene at 10^{-6} torr.

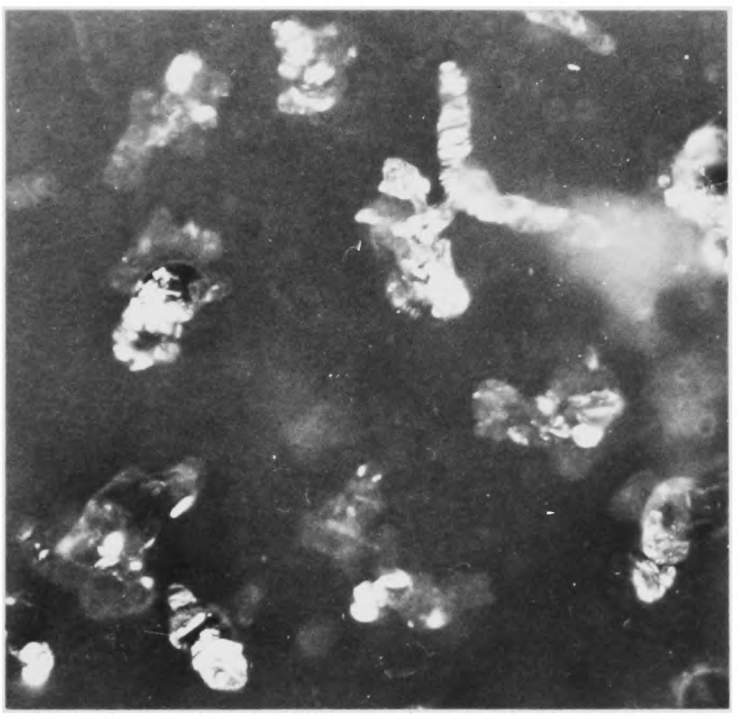
TED pattern showing Si spots (e.g. 220 type from matrix (B) and 30° rotationally twinned material (D)) and β - SiC rings (giving evidence for preferred orientation in 220 ring at A). Also shown are images recorded using 'spots' labelled A, B and C. Note different β- SiC crystallites visible in A and C, and also stacking fault (circled in B) in Si matrix adjacent to β - SiC inclusion. (Transmission electron micrographs, dark-field)

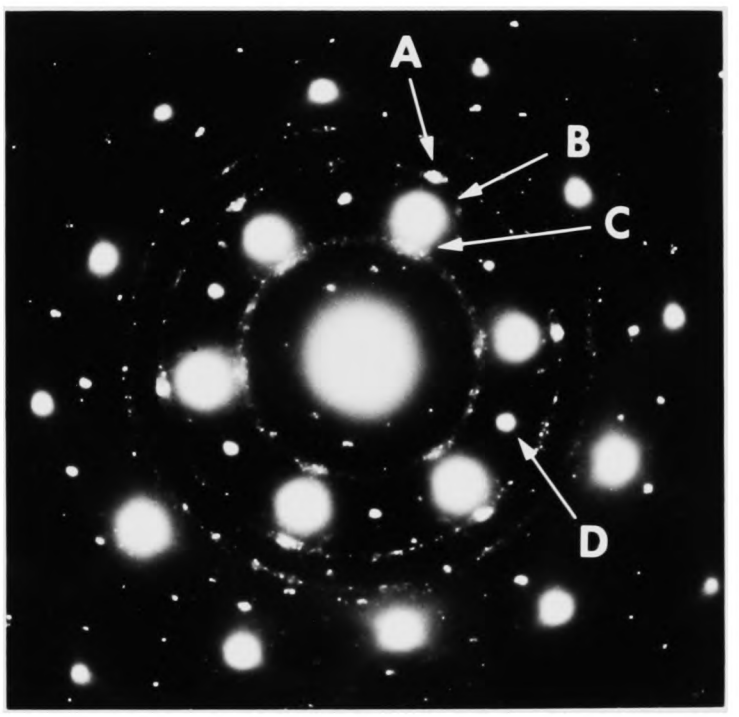
a

b

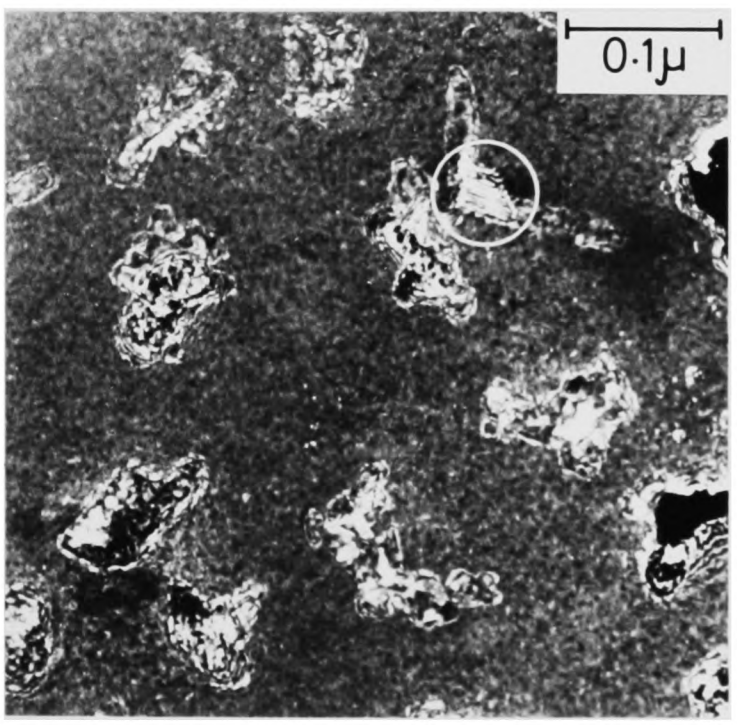


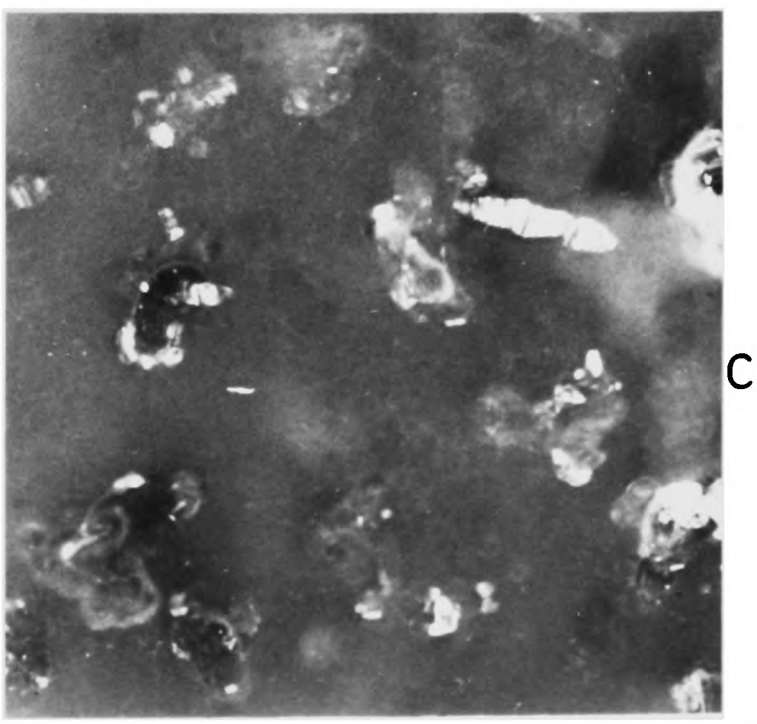
A





B





C

Fig 3.25 Si films grown in O_2 -

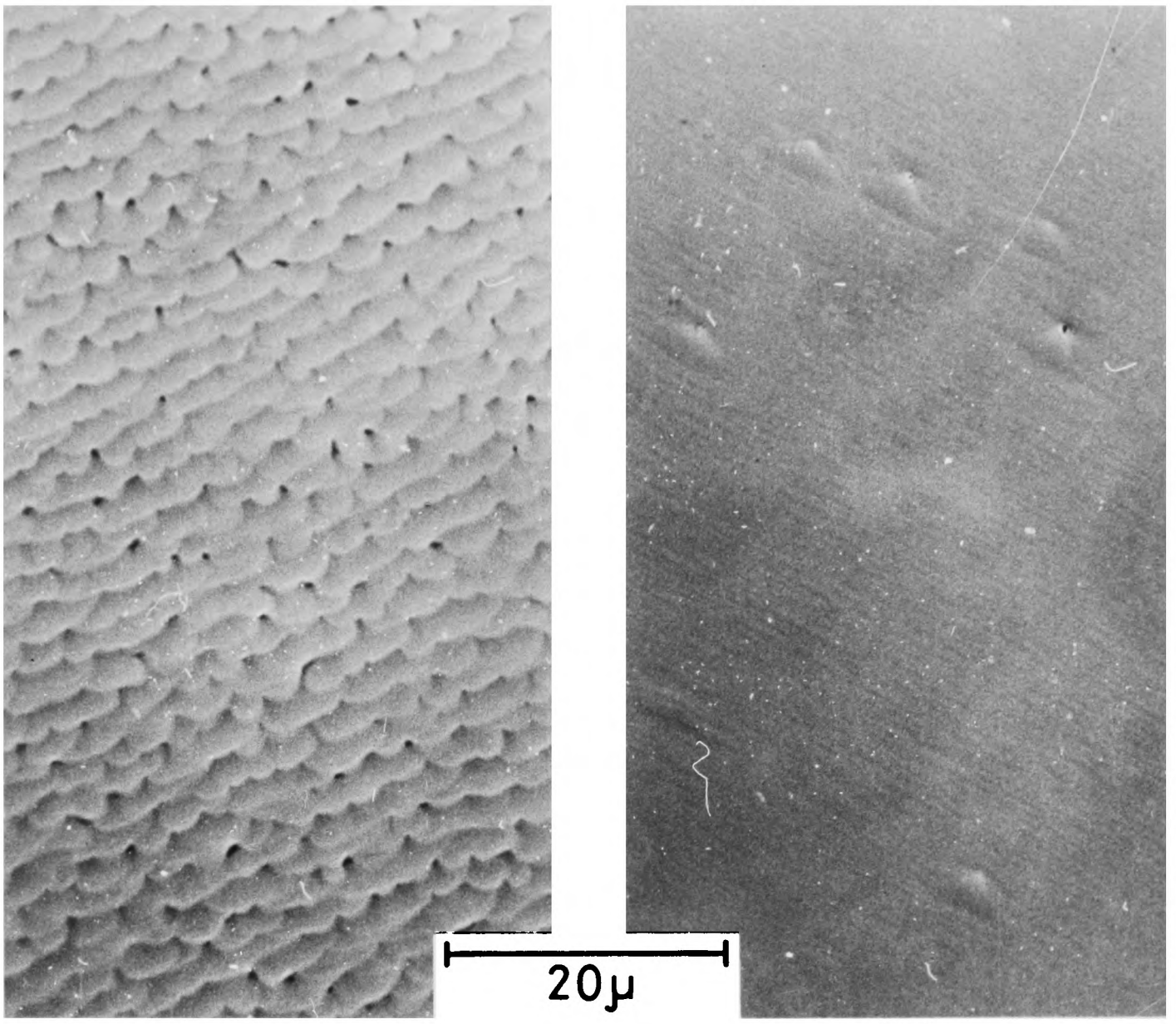
a) at 10^{-7} torr

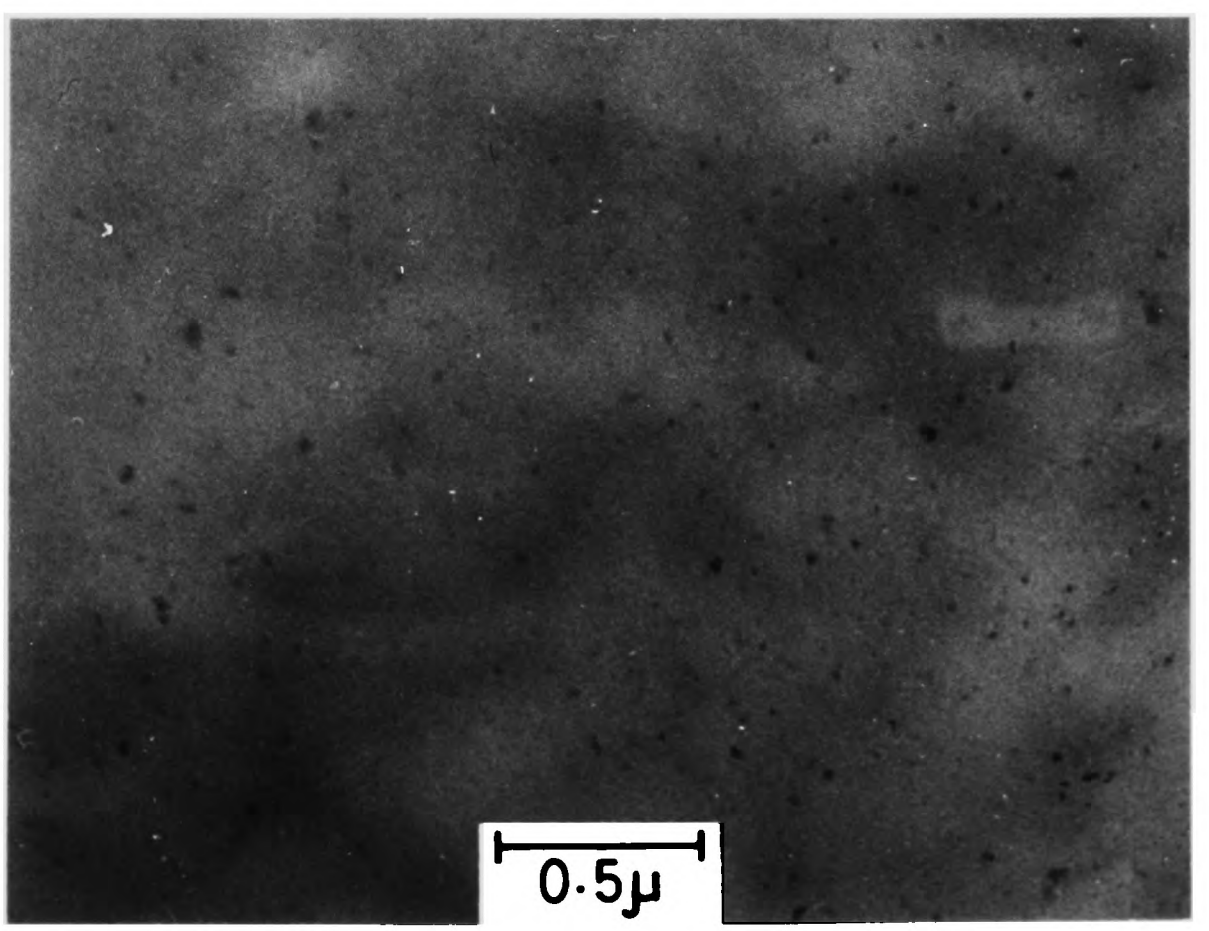
b) at 10^{-6} torr

(Optical micrographs, phase contrast)

Fig 3.26 Si film grown in O_2 at 10^{-6} torr

(Transmission electron micrograph)


20μ
(a)
(b)


0·5μ

the substrate surface, after the initial 1250°C vacuum pretreatment, one substrate was heated at 880°C for 45 min with an ambient pressure of 10^{-6} torr O_2. After this period, the O_2 feed was turned off and Si deposition was carried out under a standard 10^{-8} torr vacuum. The resulting film exhibited a pinning structure, similar to that shown in fig 3.25a.

3.7) Discussion

3.7.1) General Surface Step Interactions

The usual Si surface cleaning procedure used during the present work was substrate pretreatment at 1250°C for 10 min in vacuum. It was found that surface steps were generated, and that these had been in a state of motion at the high temperature. Now, calculations by Hirth (1965) indicate that, in general, low index surfaces of close packed lattices do not roughen significantly at temperatures below the crystal melting point. However, while these considerations might also be expected to apply to strongly bonded diamond lattice materials such as Si, imperfections initially present on real surfaces may critically affect the situation. In the case of interest here, the surfaces of the Si substrate bars were up to 2° off the ideal (111) orientation. Under these conditions, monatomic steps could initially be present in high densities, with spacings of only 100 Å. When such a bar is heated, these steps would move across the surface as Si atoms are lost to the vapour, and more steps could be generated by sources which require a minimum of energy for activation, e.g. topographical features, crystallographic defects, etc. (Hirth and Pound, 1957). However, the manner in which these steps subsequently behave depends upon factors such as the microscopic kinetics of their motion, impurity effects, etc.

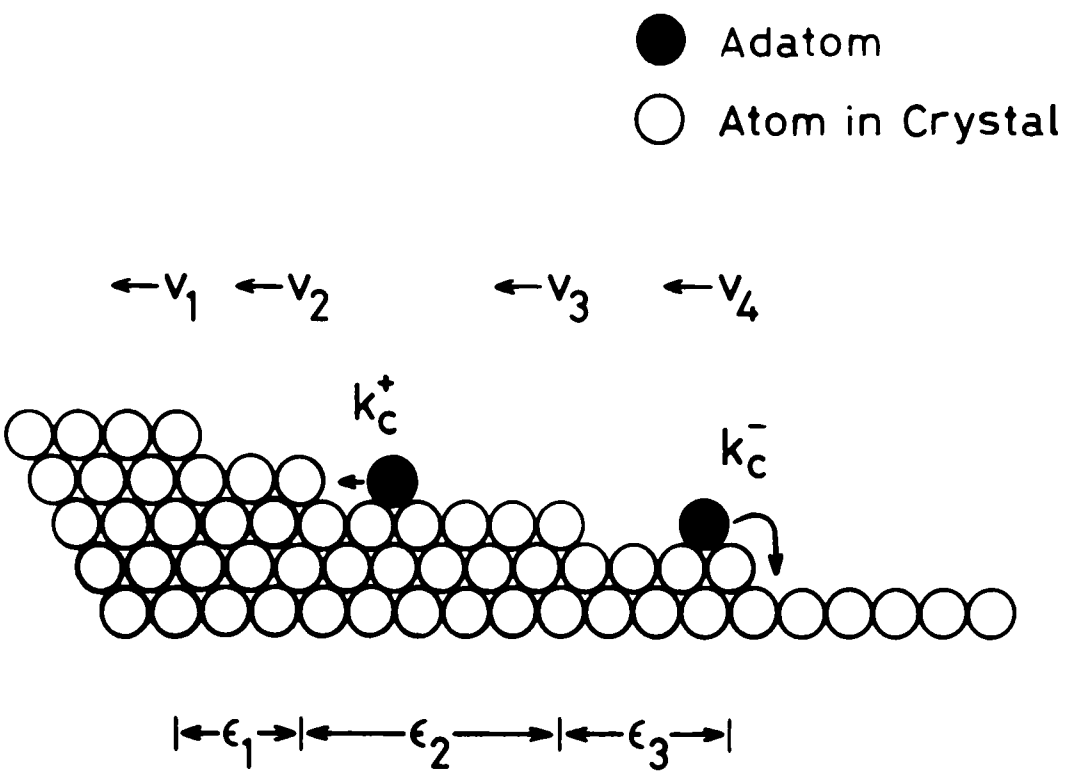
The kinematic theory of surface step motion, based on simple adatom

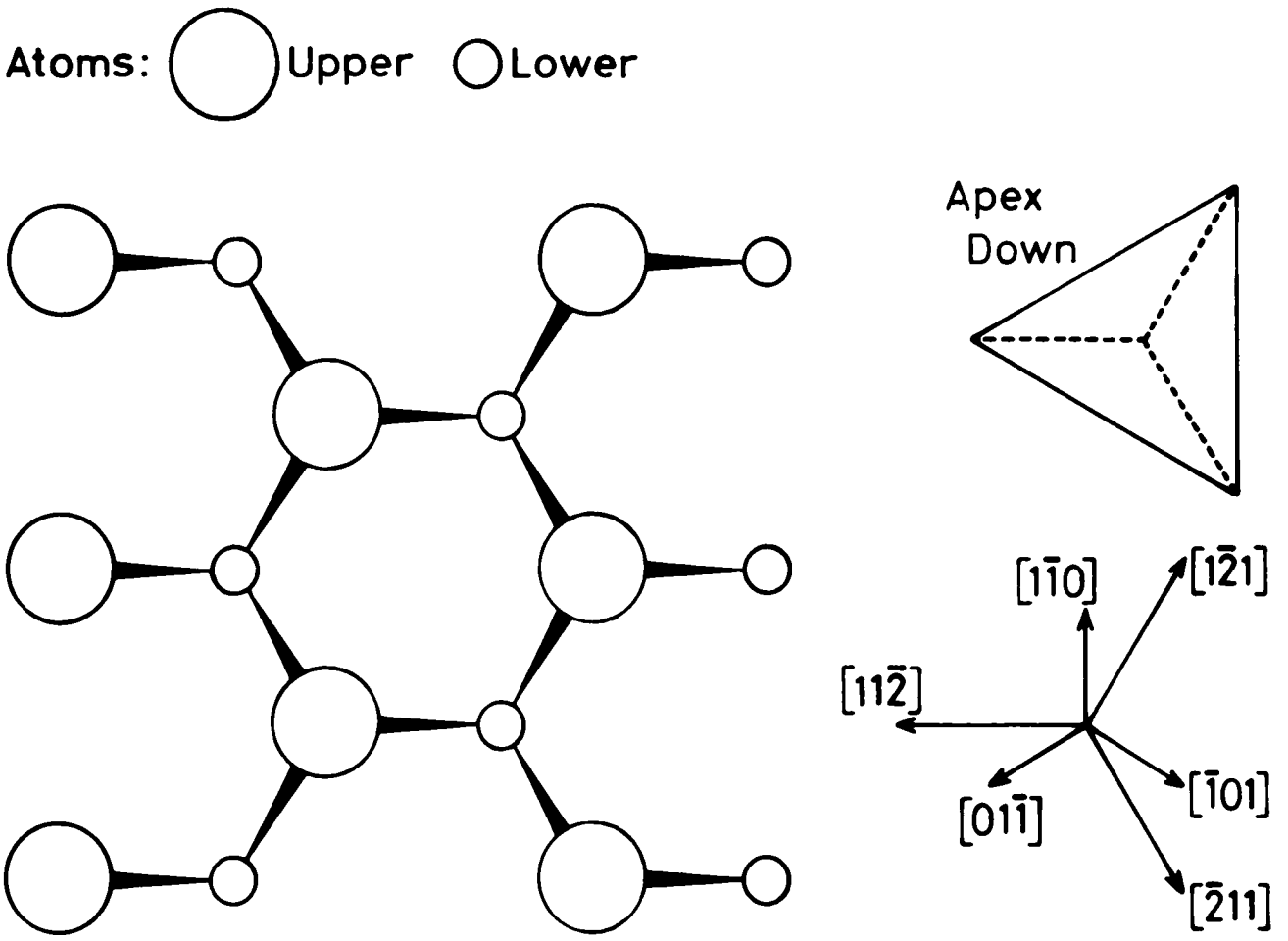
diffusion concepts, was initially developed by Frank (1958) and extended by Mullins and Hirth (1963). If the velocity (v) of a given step in an array depends only upon the distance (ϵ) to either of the adjacent steps (fig 3.27), then the overall motion is dependent upon the sign of $dv/d\epsilon$. If $dv/d\epsilon > 0$, there will be an overall divergence of the steps, although for a finite array, pairwise interaction of steps will start at the rear of the array, and spreading of steps at the front. If $dv/d\epsilon < 0$, any step which has ahead of it a spacing ϵ greater than the spacing of the steps behind it, will move with a lower velocity than the trailing steps, causing a pile-up and macroscopic bunch formation. No single steps move through such a bunch, and also the average step spacing in the bunch will decrease with time.

Many factors can influence the sign of $dv/d\epsilon$. The simplest ideas of step/adatom equilibria indicate that the velocity of a given step will increase monotonically with increasing distance to either of the adjacent steps, i.e. $dv/d\epsilon > 0$. Therefore, ideally there should be no tendency for macroscopic step bunch formation. However, impurity effects may make $dv/d\epsilon < 0$, while if the steps interact with one another in certain ways, the differential may change its sign accordingly. Schwoebel and Shipsey (1966) and Schwoebel (1969) considered how steps might interact in either an attractive or repulsive sense, by taking into account details of the rate constants for capture and detachment of adatoms. They found that the step motion for both growth and sublimation depended only upon the capture rate constants, where these may be written k_c^+ and k_c^- for the processes illustrated in fig 3.27. Then, under physically realistic conditions, it was shown that i) if $k_c^+ > k_c^-$, the step system of fig 3.27 tends to develop steps of more uniform spacing, ii) if $k_c^- > k_c^+$, individual steps may coalesce into bunches, and iii) if $k_c^+ = k_c^-$, the steps neither coalesce nor form a uniform array. The predictions of condition (iii)

Fig 3.27 Diagram showing surface steps with velocities v_{1-4} and spacings ϵ_{1-3}, and also illustrating adatom capture processes with rate constants k_c^+ and k_c^-

Fig 3.28 Diagram showing plan view of Si (111) double layer of atoms. The [111] direction projects upwards out of the page, and the other directions in the plane are shown together with the associated orientation of a Thompson tetrahedron


Adatom
Atom in Crystal
$\leftarrow v_1$ $\leftarrow v_2$ $\leftarrow v_3$ $\leftarrow v_4$
k_c^+
k_c^-
ϵ_1
ϵ_2
ϵ_3


Atoms: Upper Lower
Apex
Down
$[1\bar{1}0]$
$[1\bar{2}1]$
$[11\bar{2}]$
$[\bar{1}01]$
$[01\bar{1}]$
$[\bar{2}11]$

are qualitatively analogous to those of the simple condition $dv/d\epsilon > 0$ of the earlier theory.

During the present experiments, it was found that a (111) Si substrate surface heat treated at 1250°C was covered with steps of various sizes. In regions where steps were not directly detected using TEM, the presence of unresolved minute steps was revealed when they were pinned by occasional foreign particles (fig 3.2). The steps began to pile up and therefore became detectable, somewhat before they encountered a particle, presumably due to an interaction of their adatom diffusion fields. The pinning action of the particle caused the formation of large deflected step bunches, with a profile approximately that shown in fig 3.3. Using the kinematic theory of step motion, Frank (1958) predicted that such bunches, with large discontinuities at their trailing edges, could form in the case $dv/d\epsilon > 0$, (this is mathematically analogous to shock wave formation in aerodynamics). The large bunches rapidly decayed, since they were found only near to pinning particles. The general behaviour, including the rapid decay of artificially formed bunches, indicates that only the smallest steps (i.e. monolayer edges) should be stable, and this implies $dv/d\epsilon > 0$ using the kinematic approach. This is the result expected for a clean surface. In surface regions where apparently isolated fine steps were detected using TEM thickness fringe contrast, these may have been a temporary residue of the decay of the artificially produced large step bunches. Alternatively, they may have been the result of a limited bunching produced by localized impurities, and this will be discussed later.

If the concepts of Schwoebel and Shipsey are applied, the general absence of spontaneous step bunching implies that $k_c^+ \geq k_c^-$. This is a physically realistic situation, since when an adatom is captured by a step-face from the terrace above, there should be at least as much and

possibly more bond breaking in the transition state, when compared with adatom capture from a site in front of the step.

Joyce et al (1969b) also found that when a (111) Si surface is heat treated at 1250°C under clean conditions, there is no spontaneous roughening. However, Joyce (private communication) has shown that the presence of contaminants (especially carbon) caused such a surface to roughen even at temperatures substantially below 1250°C. There are several possible explanations. If many large impurity particles were initially present, extensive step pinning could produce many bunched arrays. If these were formed at a rate greater than that of their decay, the surface would roughen. Alternatively, a non-uniform distribution of a tight binding impurity could induce surface roughening. For example, carbon forms very strong Si-C bonds, and it will be shown in the next section how such an impurity may retard step motion. Using this concept, step motion would be more retarded in regions with large impurity concentrations, so that steps from neighbouring regions would approach the retarded steps and form bunches. These would persist for periods depending upon the rate of redistribution of the impurity, or its rate of diffusion into the bulk crystal. Yet another possible explanation is based upon the concept of a time-dependent impurity concentration, e.g. produced by contaminants incident from the gas phase. Under these conditions Frank (1958) showed that step bunching could once again occur.

Attention will now be given to the surface step arrays formed during Si film growth upon preheated substrates. It was shown in section 3.4.1 that 600 Å Si films grown at 5×10^{-2} Å sec^{-1} and a substrate temperature of 880°C exhibited a growth step structure pinned in many places by SiC particles. It is difficult to discuss step interactions in such a disturbed system. However, Abbink et al (1968) observed that their deposited Si films had a similar structure, and using a high resolution

shadow replica technique, found that steps of monolayer height moved away from the base of advancing bunches. This implies that growth steps are unstable with respect to bunching, and the kinematic theory of step motion then gives $dv/d\epsilon > 0$. If the treatment of Schwoebel and Shipsey is applied, it is found that $k_c^+ \gg k_c^-$. Both of these results are identical to those obtained by observations of sublimation steps, and this indicates that the surface processes are completely complimentary, as would be expected.

In section 3.4.1 it was also shown that thicker (3000 Å) Si films had less pinning sites, which led to the formation of much straighter bunched step arrays. Using the conclusions already obtained concerning growth step propagation, it is likely that while bunches continually decayed, new ones were formed by pinning sites at a rate sufficient to maintain the observed bunch population. It is germane to note that the risers of the bunch trailing edges were much steeper than those at the front. Under these circumstances, the kinematic theory predicts that $dv/d\epsilon > 0$, in agreement with the results given above.

3.7.2) Processes at Single Steps

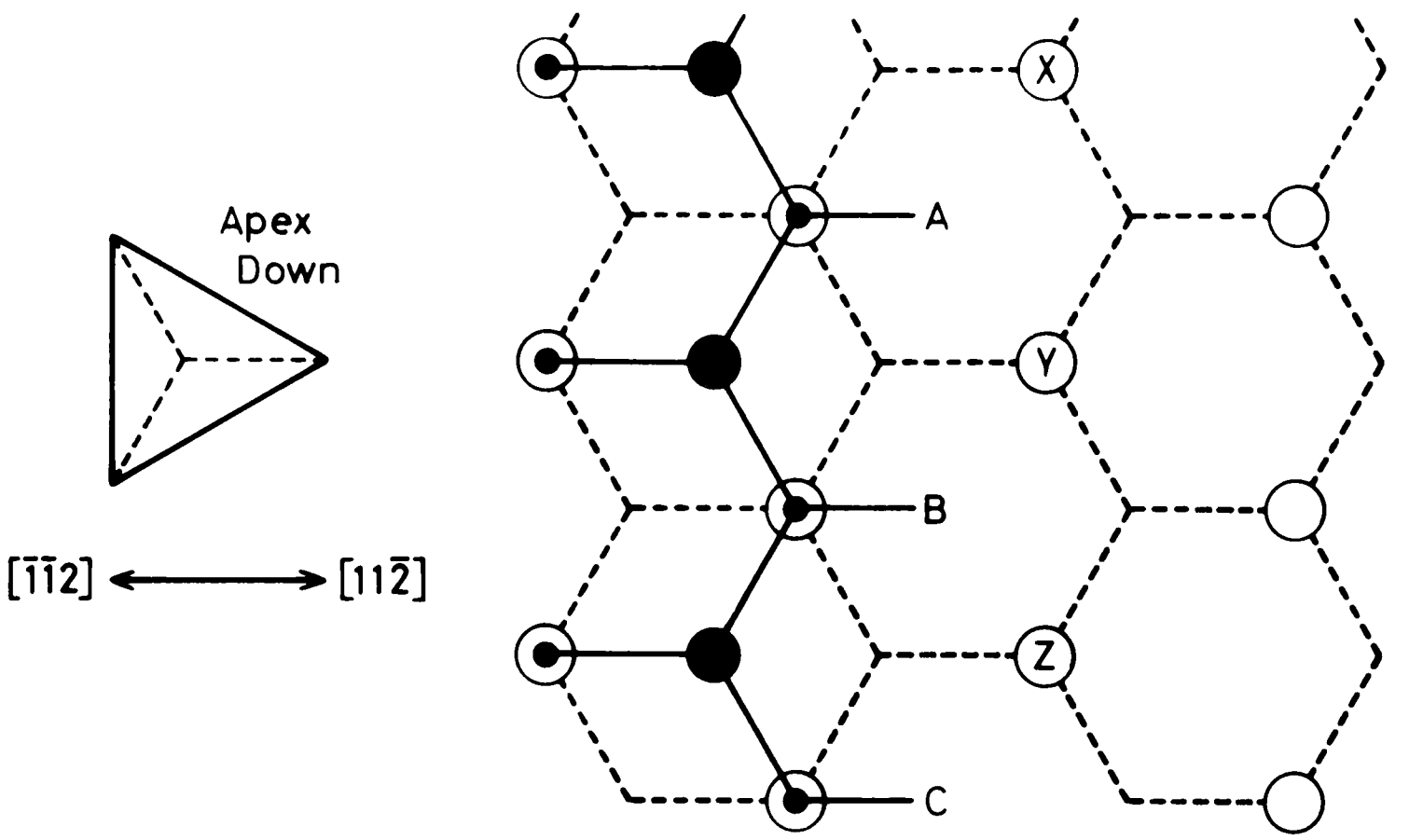
The experimental results presented earlier showed that the smallest, undisturbed, straight Si sublimation steps moved in a $[\bar{1}\bar{1}2]$ direction, while straight, bunched Si growth steps moved in the opposite direction, i.e. $[11\bar{2}]$. If it is assumed that straight monolayer growth steps would also propagate in a $[11\bar{2}]$ direction, these observations are consistent with the hypothesis that straight steps, of the same configuration, are produced by both growth and sublimation processes.

By studying atomic models, it is possible to understand the relative stabilities of surface steps, using ideas developed by Billig (1956) and Frank et al (1958). Fig 3.28 shows a plan view of a Si (111) plane (a double layer of atoms), together with the associated orientation

of a Thomson tetrahedron and the corresponding crystallographic notation used in the text. The [111] plane normal is a triad rotation axis, and therefore, while the $[11\bar{2}]$ direction is equivalent to $[\bar{2}11]$ or $[1\bar{2}1]$, and the $[\bar{1}\bar{1}2]$ direction is equivalent to $[2\bar{1}\bar{1}]$ or $[\bar{1}2\bar{1}]$, these two sets of directions are different from one another. Figs 3.29a and b show two different steps which would face in non-equivalent $\langle 112 \rangle$ type directions on a (111) Si surface. Consider first the step in fig 3.29a under conditions of crystal growth. Atoms would then be incident upon both (111) terraces, and the step would move to the right of the diagram (in a $[11\bar{2}]$ type direction), as adatoms joined its face. Now, if an adatom is simply attached by any of the dangling bonds A B C etc it will only be singly bonded, and therefore, its stability should be little greater than when it is attached to an open (111) surface site. However, if two adatoms collide at the step face to form a pair, such that one is bonded at A and the other at X, then they will each have formed two bonds, leading to considerable co-stability. It is then relatively easy for the step to move forward, along its entire length, by half a lattice translation in a $[11\bar{2}]$ type direction, since the two kink sites formed each provide a pair of dangling bonds to bind each subsequent adatom. For example, if an adatom becomes bonded to the step at Y, it also forms a bond with the atom already present at A. Therefore, once kink sites have been nucleated at the step face, they should rapidly move along the step by the attachment of adatoms. When these kinks have moved a large distance, they would have produced a straight step awaiting the nucleation of new kinks for further growth.

The behaviour of the complimentary step shown in fig 3.29b under growth conditions is different. When adatoms strike this step, each one may form two bonds immediately, e.g. at K and L, M and N, etc. Therefore, each is quite stably bound, and these may then bind further adatoms which,

Fig 3.29 Diagrams a) and b) show steps which face in non-equivalent ⟨112⟩ type directions on a (111) Si surface


Apex
Down
[$\bar{1}\bar{1}$2] ⟷ [11$\bar{2}$]
X
Y
Z
A
B
C
Atoms
Lowest → Highest
Sublimation ⟷ Growth
[11$\bar{2}$] ⟷ [$\bar{1}\bar{1}$2]
Apex
Down
R
S
T
K
L
M
N

in turn, would also be doubly bound involving dangling bonds R, S, T etc. Therefore, such a step may grow forward relatively rapidly in a $[\bar{1}\bar{1}2]$ type direction, by addition of single adatoms at any positions along its length. In this situation, kink sites do not provide favourable bonding positions for lateral growth along the step, so that there is no special tendency for the step to become straight.

By a comparison of the two systems outlined above, it is evident that if growth steps are observed to be straight over relatively large distances, then they should be the set moving in a $[11\bar{2}]$ type direction, as was found experimentally. The reason why these steps are especially stable, is related to the fact that they move forward more slowly than the other steps travelling in a $[\bar{1}\bar{1}2]$ type direction. This latter set do not require the growth rate limiting nucleation of kink sites for forward motion. Therefore, the steps moving in a $[\bar{1}\bar{1}2]$ type direction grow forward rapidly, and in the absence of pinning sites would eventually disappear, leaving behind steps moving slowly in a $[11\bar{2}]$ type direction. This process is completely analogous to facet formation on e.g. melt grown crystals, when the fast growing planes effectively 'propagate out of the crystal'.

These conclusions are substantiated by the observation that Si film growth at the low temperature of 750°C produced only straight step edges (fig 3.8), principally of one orientation, while there were no curved steps related to those observed for deposition at 880°C. At the lower temperature, steps moving in a $[\bar{1}\bar{1}2]$ type direction could be nearly perfect sinks for adatoms so that they would 'grow out' extremely rapidly, whereas steps travelling in a $[11\bar{2}]$ type direction would still require adatoms to be incident at kink sites if they were to be captured. In this way, low temperature growth could exaggerate the differences between the two alternative types of surface step.

If attention is transferred to Si (111) surface steps produced by

removal of Si atoms through sublimation, analogous considerations apply. A step of the type shown in fig 3.29a must initially lose an edge atom to form two kink sites. Such an atom is triply bound, and therefore this process requires a large activation energy. However, after it has occurred, the kink sites formed may move along the step edge relatively easily, since only doubly bonded Si atoms must then be removed. Therefore, since the rate of motion in a $[\bar{1}\bar{1}2]$ type direction of this sublimation step is controlled by the rate of kink site formation, such a step would tend to remain straight.

Conversely, a sublimation step shown in fig 3.29b is bounded by only doubly bonded atoms. These may be removed from any position along the step exposing other doubly bonded atoms, so that the step motion does not depend upon an initial, high activation energy, rate-controlling process. Therefore, sublimation steps moving in a $[11\bar{2}]$ type direction show no special tendency to remain straight, and travel faster than the alternative steps discussed above. Once again, the fast moving steps tend to be removed, leaving slower moving straight sublimation steps travelling in a direction of the type $[\bar{1}\bar{1}2]$, as was observed experimentally.

Abbink et al (1968) grew Si films in UHV, and claimed to have observed straight monolayer Si growth steps propagating in a $[\bar{1}\bar{1}2]$ type direction. While they noted that this was difficult to interpret in terms of an atomic model, they failed to separately specify the system of crystallographic axes used. This does not inspire confidence in the arguments employed, and it seems possible that there may have been some inconsistency in their notation.

It is instructive to examine the effect of impurity atoms upon step motion. Carbon is a tight binding impurity, since Si-C bonds are stronger than Si-Si bonds. Therefore, if carbon atoms are present on a (111) Si surface from which Si is being removed by sublimation, and it

'poisons' the kink sites of straight steps moving in a [$\bar{1}\bar{1}$2] type direction, it may severely retard their motion, since kink formation is probably the rate-limiting process for Si atom removal. The effect of such an impurity on single sublimation steps moving in a [11$\bar{2}$] type direction could be less pronounced, since kink site formation should be unimportant in this case. It might be expected that tight binding impurities would influence growth step motion to a smaller degree, since the contaminant could then be simply incorporated into the Si film. However, much depends upon the form in which the impurity is present, e.g. the extent of aggregation.

3.7.3) Silicon Film Growth

In the previous chapter, it was shown that Si deposition on to (111) Si substrates, heated directly in UHV to growth temperatures around 880°C, produced film growth by nucleation leading to growth centre formation. However, the experiments described in this chapter showed that if such a substrate was heated to 1250°C in vacuum prior to deposition, the grown Si film had a pinned layer structure. Each pinning point started as a small SiC particle on the substrate surface. The particle inhibited film growth in its immediate vicinity by impeding the progress of Si growth steps, which were the edges of Si layers growing over the surface. This caused a pit to form in the film around the particle as growth proceeded. These pits often became several thousand Å deep before the SiC particles were grown over, and the pits disappeared.

This change in growth characteristics with substrate pretreatment is analogous to that found by Joyce et al (1969b), who used SiH_4 pyrolysis for Si deposition. They found that when a Si substrate was heated to 1250°C in UHV the surface was cleaned, and in particular, both carbon - and oxygen - containing impurities were removed. They specifically proposed that a carbon contaminant (possibly free carbon or SiC) was responsible

for three dimensional growth centre formation on unpretreated substrates, and that when this was removed by the heat treatment, possibly by dissolution into the bulk Si of a substrate, two dimensional growth became possible. Since this growth occurs by the lateral motion of surface steps, they speculated as to their origin. It was concluded that the steps could have been initially present on the surface due to misorientation with respect to the (111) plane, and that possibly they were poisoned by contaminants on unpreheated substrates. Alternatively, it was proposed that the steps could have been produced during initial growth by two dimensional nucleation. This possibility was considered most likely since studies of nucleation kinetics gave consistent growth centre N_s values for various substrate pretreatment temperatures approaching 1250°C.

Nevertheless, during the present experiments, the author found that Si substrates which had been subjected to the high temperature pretreatment, were covered with surface sublimation steps of various sizes (section 3.3). Their origin has already been discussed (section 3.7.1), and it seems that at least monolayer steps could be a general feature of such preheated surfaces, except under exceptional circumstances. These might include requirements such as the initial preparation of a substrate almost exactly at (111) surface orientation, the absence of surface defects which could become step sources, etc.

The above discussion indicates that, in the present series of experiments, the high temperature pretreatment served both to clean substrate surfaces and to produce an active surface step arrangement. However, it is important to note that when Si growth takes place on a surface covered with such steps of the slow growing type, even in quite high densities, the growth mechanism should still be nucleation. This is a consequence of the fact that the slow growing steps require a nucleation of kink sites for forward growth, in a manner analogous to Si nucleus

formation on an open, step-free surface. Therefore, the steps would not be expected to act as sinks for adatoms to an extent which would preclude growth by nucleation. Presumably also, if e.g. monotomic steps of the slow growing kind were present on unpreheated surfaces, initial Si growth by nucleation would not depend upon a complete poisoning of these steps by, possibly, a carbon contaminant. However, of course, the contaminant would be expected to influence subsequent growth, and could lead to macroscopic growth centre formation by inhibiting the lateral extension of centres over the surface. This conclusion is supported by the observation that air recontamination of a preheated substrate caused later film growth to give three dimensional growth centres. These general considerations indicate that initial nucleation processes may not necessarily be critically sensitive to either the surface step density (provided the steps are of the slow growing kind), or the extent of surface contamination. This is the experimentally observed situation.

The reason why the Si growth step motion on preheated substrates should be disrupted by impurity particles is not completely clear. The particles were shown by electron energy loss analysis to be SiC, so that they may have been formed from residual carbon which was not removed, for instance, by dissolution into the bulk Si substrate during the high temperature pretreatment. However, when preheated substrates were examined by TEM prior to Si deposition, very few surface particles were found. Therefore, it seems possible that any residual SiC may have been present as minute particles (say 10 - 20 Å in diameter). During subsequent initial Si film growth, these might have been carried slowly forward by advancing growth steps, until particles collided and formed completely immobile aggregates, which could act as step pinning centres.

The relationship between pinned layer growth and that by irregular growth centre formation, is illustrated by Si deposition after substrate

pretreatment at only 1160°C. Both types of growth took place simultaneously in different areas, and it is likely that growth centre formation occurred where contaminants remained in sufficiently high concentration after the lower temperature pretreatment. The regions surrounding the centres showed a continuous transition between the two growth structures. This suggests that the irregular edges of observed centres were produced by many bunches of Si layer steps bulging out between numerous pinning sites. The shapes of Si growth centres, and their possible relationship to the state of aggregation of surface impurities, was discussed in the last chapter.

In order to grow thin and uniform Si films, it is necessary to eliminate step pinning effects, which led to the generation of uneven surface topography. It is possible that changing the Si deposition conditions may alter e.g. the sensitivity of advancing growth steps to pinning particles, which might be incorporated into the film more quickly under favourable circumstances. However, when the deposition rate was increased by a factor of 20 (i.e. to 1 Å sec^{-1}), it was found that pits surrounding the pinning sites still penetrated deeply into the film. It is also possible that the initial heat treatment of the substrate could be optimized in some way to remove all impurities. Joyce et al (1969b) observed no significant pinning structure in films grown by SiH_4 pyrolysis on preheated substrates, although this may be due to the chemical reaction with accompanied deposition. Different substrate cleaning pretreatments have been proposed by other workers, e.g. Bedair and Smith (1969) investigated the use of pulsed laser bombardment.

In the present work, an initial 'in situ' gas polishing procedure at high temperature in H_2 (with a trace of H_2O vapour) was tested as a possible treatment for the production of clean and uniform substrate surfaces. Progress was made towards developing this technique, although

the fact that the best Si film did not become continuous during initial growth probably indicates that impurity effects were still important. While the actual polishing conditions could certainly be further optimized, since the substrate bar cooled from the high temperature while the H_2 was still flowing, any impurities in the gas stream could have adsorbed on to the surface. Therefore, the gas purity probably requires improvement before the best results can be obtained. Furthermore, the experimental apparatus could usefully be modified to facilitate the polishing process, as detailed in chapter 7.

The results of Si deposition in the presence of O_2 gas, which is discussed in the next section, are relevant to the growth of uniform Si films.

3.7.4) Effect of Contaminating Gases

Both CO and CO_2 are residual gases commonly found in UHV systems. Results presented earlier showed that these can both have undesirable effects upon Si film growth, in the pressure range 10^{-7} to 10^{-6} torr, under the deposition conditions employed. CO_2 was found to be considerably less detrimental than CO, and this is consistent with their physical properties. CO_2 is a very stable molecule in which carbon has a high oxidation state. All the carbon 2s and 2p electrons are involved in the molecular bonding. However, CO, which readily forms co-ordination complexes with many elements, has a 'lone pair' of electrons strongly directed away from the carbon atom, opposite the molecular bond. These electrons could show a strong tendency to interact with the 'dangling bonds' projecting from a Si surface.

The negligible effect upon Si film growth exhibited by CH_4 is understandable in terms of the very great stability associated with its molecular structure. In contrast, ethylene (C_2H_4) is very reactive since it contains a π-bond between the two carbon atoms. This allows the

molecule to form complexes with certain transition elements, and should also permit strong interactions with a Si surface. Indeed, Joyce et al (1969b) used the gas to recontaminate cleaned Si surfaces with carbon, in controlled experiments. Therefore, it is not surprising that the gas was pyrolysed during Si deposition in the present experiments, with the formation of SiC. Evidently, the film strains produced by this material sometimes induced the generation of stacking faults in the Si. Also, some regions of the Si film were found to be rotationally twinned with respect to the substrate, and this is analogous to the twinning observed by Booker and Joyce (1966), which was a result of carbon contamination in films grown by SiH_4 pyrolysis. The severe nature of the contamination produced by the ethylene is emphasized by the presence of the unusual 30° rotational Si twins.

The apparently beneficial effects of O_2 upon film growth were not entirely expected. When the gas had been present at 10^{-6} torr during deposition, the resulting Si film was of particularly high quality, with great uniformity due to the absence of layer pinning sites. The film exhibited no obvious etching structure, although regions of the substrate which had received no deposit showed evidence for some attack. Since exposure of a substrate to O_2 prior to deposition did not produce a comparable improvement in layer quality, this suggested that the gas did not necessarily clean impurities from the substrate surface. Instead, it appears that the gas may have either reduced the ability of impurity particles to disturb step motion, or caused disturbances to be rapidly removed. However, Si films grown in the presence of O_2 may contain more lattice vacancies than otherwise expected, since O_2 can induce vacancy formation by removal of surface Si atoms to give volatile SiO. Also, due to this loss of Si, it is difficult to estimate the exact thickness of the deposited film. Therefore, it would probably have been advisable

to remove O_2 from the vacuum chamber, as soon as a satisfactory film structure had been obtained.

3.8) Summary

The effects of cleaning (111) Si substrates by heating them at 1250°C in UHV were examined, and it was found that arrays of straight surface steps were produced which moved across the surface in a [$\bar{1}\bar{1}2$] type direction. If Si deposition at 5×10^{-2} Å sec^{-1} was initiated upon such a surface at 880°C, the direction of step motion reversed as growth took place. However, the steps were pinned in many places by impurity particles, so that bunches were formed which then bowed out between the pinning sites to give wave-like terraces. The pinning sites ultimately produced pits in the grown film, which could be up to several thousand Å deep. The particles responsible for these disturbances were analysed by transmission electron energy loss analysis, and found to be SiC. Details of the film growth depended upon exact growth conditions, e.g. step terraces became very straight for growth at 750°C. If a preheated substrate was contaminated by exposure to air before deposition, subsequent growth occurred by optically observable growth centre formation. Since substrate surface condition prior to deposition was such an important factor in determining the nature of film growth, the possibility of initial 'in situ' gas polishing with H_2 (plus a trace of H_2O vapour) was investigated. While the technique is difficult to carry out with apparatus intended for vacuum work, progress was made towards the attainment of improved film perfection, although procedures need further optimization. The effect of contaminating gases present during film growth was also studied, and it was found that CO and ethylene produced more severe undesirable film disturbances than CO_2 or CH_4. O_2 had an apparently beneficial effect upon growth processes, and

led to the formation of films with improved uniformity.

The nature of both sublimation and growth step motion across substrate surfaces was analysed using the kinematic approach, and the concept of directional capture rate constants for adatoms at steps was introduced and discussed. Further, the individual atomic processes involved in step motion were considered, and related to observed step characteristics. It was concluded that,

a) in the absence of pinning effects, the step motion was generally that expected for a clean surface;

and b) the presence of surface steps of the most stable type did not preclude the possibility of subsequent film growth by a nucleation mechanism.

The possible origin of impurity particles (usually SiC) present on substrate surfaces was also examined, since their formation was most undesirable due to their ability to disrupt subsequent film growth. In fact, using standard preheated substrates, it would have been necessary to deposit a Si film a substantial fraction of a micron in thickness to obtain a completely uniform structure, free from surface step pinning sites.

The effects produced by the various impurity gases were also discussed, and the film growth modifications which they inroduced were found to be generally in accord with their chemical reactivities.

CHAPTER 4 THE GROWTH OF GERMANIUM ON SILICON

	Page
4.1) Introduction	85
4.2) Review of Literature	85
4.3) Experimental Details	88
4.3.1) Film Deposition	88
4.3.2) Film Examination	90
4.4) Morphology of Germanium Films	91
4.5) Nucleation Behaviour	93
4.5.1) Experimental Results	93
4.5.2) Theoretical Interpretation	94
4.6) General Crystallographic Structure of Germanium Films	95
4.6.1) Conventional TEM Examination	95
4.6.2) Examination of Films in Profile	98
4.7) Discussion	99
4.7.1) Initial Film Growth	99
4.7.2) Film Structure and Composition	101
4.8) Summary	105

4.1) Introduction

Ge and Si occupy Group IV in the periodic table, and share many common properties. They both have the diamond lattice structure and are miscable in all proportions, though Ge has a much lower melting point than Si. In the present work, the epitaxial growth of Ge on Si has been studied over a range of temperatures almost up to the melting point of the former. The initial growth will be interpreted partially in terms of nucleation theory, although certain unexpected features prevent a complete correlation. An important feature of the Ge/Si system is the atomic mismatch between the two lattices, and this produces many film characteristics such as strains and crystallographic defects. In particular, an interfacial dislocation network relieves much of the mismatch, and emphasis will be placed upon the determination of its various properties, although a basic structural analysis and discussion of TEM contrast behaviour will be deferred until chapter 6.

4.2) Review of Literature

The structure of Ge films grown on Si substrates has not been studied by many workers. Ito and Takahashi (1968) grew such films by vacuum evaporation of Ge on to (111) Si substrates, and with a deposition rate of 100 Å sec^{-1} RHEED showed that the perfection of the deposit improved as the substrate temperature was increased in the range 330 - 930°C. When films were grown at 13 Å sec^{-1} and 850°C, TEM showed that irregular triangular growth centres were formed, and that as the mean deposit thickness was increased, the centres overlapped to give a channelled structure. Parallel fringes of 90 Å spacing were also observed using a $2\bar{2}0$ type reflection, with unspecified deviation from the Bragg position. It was claimed that these were ideal images of misfit dislocations at the interface, and not a

Moiré effect. The electrical and photoelectrical characteristics of Ge - Si p - n heterojunctions were also studied, and interpreted in terms of dense interfacial states generated by dangling bonds. These effectively produced a double Schottky barrier, which had been proposed earlier (Kimura et al, 1966).

Other workers have also measured and discussed the electrical characteristics of such heterojunctions. Nunoshita et al (1969) fabricated Ge - Si n - n heterojunctions by chemical vapour deposition, and by extending available theory were able to explain the observed conduction properties. They also found such junctions to have high speed switching characteristics, since the current was carried by electrons (the majority carrier), and the switching time was thought to be only ultimately limited by their dielectric relaxation time in the Ge, $\sim 10^{-10}$ sec.

Fujimoto and Yamaguchi (1968) examined Ge films deposited at 850°C by chemical vapour decomposition on to Si substrates, and used an X-ray analytical technique to show that films of $> 1\mu$ in thickness contained substantial quantities of Si, introduced from the substrates. In their films, two reasonably distinct alloy regions were formed. Up to 0.4μ from the 'interface' the film contained $\sim 70\%$ Si, while beyond this an alloy region contained $\sim 55\%$ Si.

Pashley (1970) has recently reviewed epitaxial growth in many other systems. A number of workers have carried out theoretical analyses concerning heteroepitaxial phenomena, and have made predictions about interfacial properties and film structures. Frank and van der Merwe (1949) originally made a theoretical study of the conditions under which hetero-epitaxial growth would give rise to dislocations at the interface. These were first observed in the TEM some years ago, by Matthews (1961) in the PbS/PbSe system, and by Delavignette et al (1961) between $CrBr_3$ and unknown crystals. Van der Merwe (1963) considered theoretically the case of an

interface with mismatch in only one direction, and developed the concept of 'critical misfit'. For a given film thickness, this is the misfit below which the deposit should strain to fit the substrate, without the formation of interfacial dislocations - pseudomorphism. These ideas were extended by van der Merwe (1970), and also by Jesser and Kuhlmann-Wilsdorf (1967) who treated the case of isolated hemi-spherical nuclei on a flat substrate.

Evidence for initial pseudomorphic growth was obtained by Matthews (1966), who studied the deposition of Au on several FCC metals. For very thin deposits on Pt and Pd (misfits 3.9% and 4.8% respectively), the density of interfacial dislocations was low, indicating that the misfit was partially accommodated by elastic strains. However, in the Au/Ag system (mismatch 0.18%), no interfacial dislocations were observed for Au film thicknesses of $\lesssim 250$ Å, and this appears to be a case of complete pseudomorphism. Other examples of this type of growth have also been reported (e.g. Jesser and Matthews, 1967 and 1968 a,b), and recent work by Vincent (1969) is of special importance. He deposited Sn on SnTe substrates, and found that the average amount of mismatch accommodated by lattice strain, in the observed Sn growth centres, decreased as the centre size increased. However, the strain did not increase in a uniform manner, but oscillated with centre size between a low value and a critical limit, as discreet mismatch dislocations were introduced at the interface.

Film deposition studies by 'in situ' TEM techniques were devised by Bassett (1960) and developed by other workers including Pashley and colleagues (see e.g. Pashley, 1965). The formation of lattive defects has been observed during film growth, often using Moiré fringe effects. In particular, the phenomenon of growth centre coalescence in relation to initial double-positioning and defect formation has been studied, especially during the growth of metals on non-metallic substrates. Important

experiments have recently been carried out by Honjo and Yagi (1969) and Yagi et al (1971). Their work included the use of direct, high resolution cinematography, and when PbSe was deposited on to (001) PbS substrates, initial growth was by pseudomorphic layer formation. As the film thickness increased, misfit dislocations were gradually introduced into the interface, and since they were shown to be of edge character, it was deduced that the mechanism operating involved climb motion. When Pd was deposited on to (111) Au, initial growth was by the formation of pseudomorphic growth centres. At a critical size, misfit dislocations were introduced from the edges of the centres by glide along the interface, since this was a slip plane. To illustrate the differences between the two mechanisms of dislocation motion just mentioned, Au was simultaneously deposited on to two neighbouring Pd crystals in (001) and (111) orientations. As growth proceeded, misfit dislocations moved rapidly into the interface of the (111) region from edges of growth centres by glide motion. However, growth centres in the (001) region remained relatively devoid of interfacial dislocations, since climb motion, requiring a higher activation energy, would have been involved. Mechanisms for production of interfacial dislocations are reviewed by Matthews(1967).

4.3) Experimental Details

4.3.1) Film Deposition

The construction of a suitable contamination-free source of Ge vapour, for use in these experiments, was not easy. If a disc of Ge was simply placed in the standard source holder beneath the electron gun (section 1.2.3), the whole disc became molten before satisfactorily high deposition rates could be achieved. This was a consequence of the lower melting point of Ge, compared with that of Si. Therefore, to obtain low

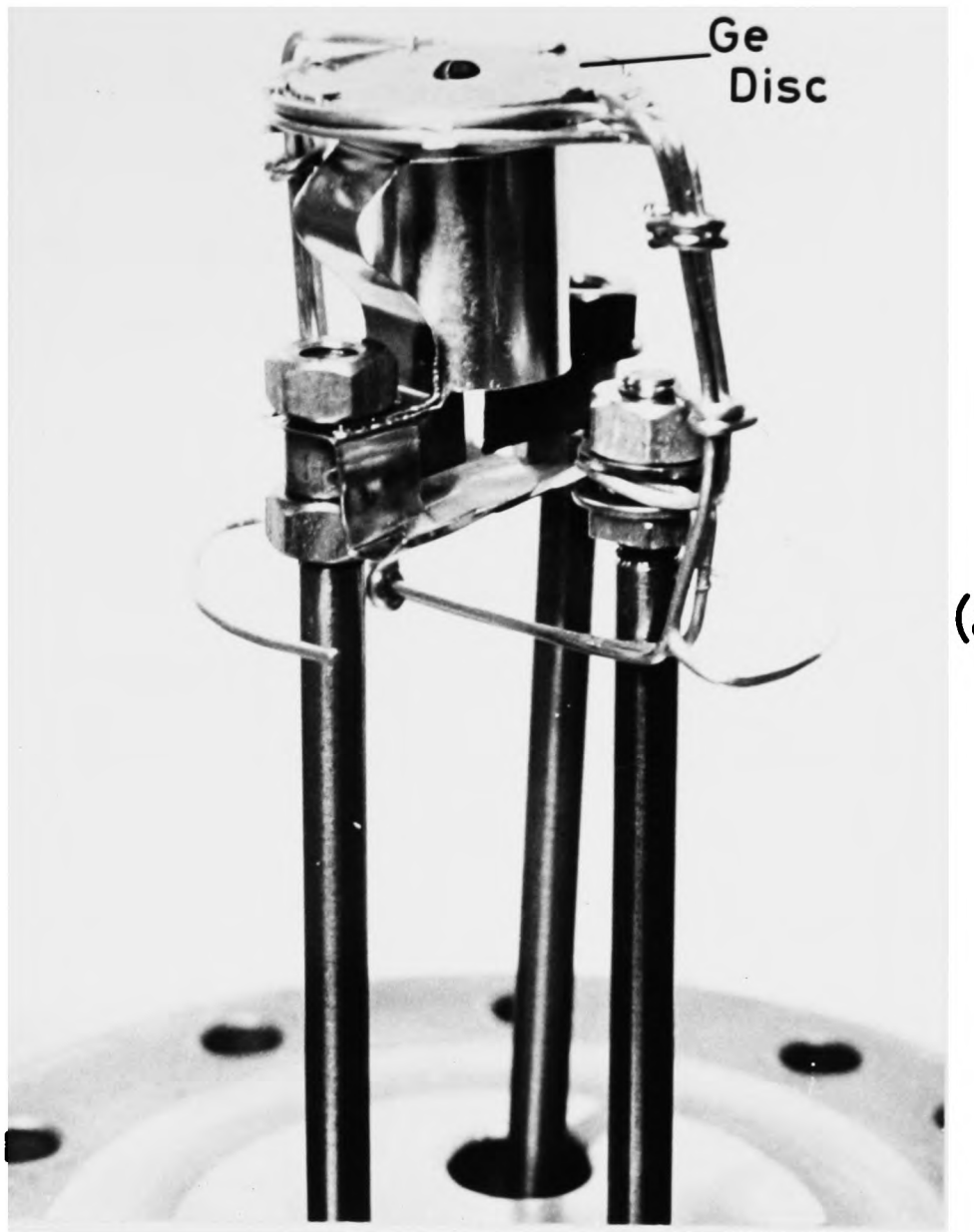
deposition rates in the region of 10^{-2} Å sec^{-1}, the holder was modified as shown in fig 4.1a, to remove as much heat as possible from the edges of a Ge source disc. When in operation, this inhibited the expansion of a central molten zone as electron beam current was increased, so that the liquid Ge droplet could be heated to a temperature significantly above the melting point. Heat was removed from the disc by the Mo wire assembly shown, and conducted away by the supporting electrical lead-through.

For many experiments higher Ge deposition rates were required, and so a resistance heated wire basket source was developed to hold a molten droplet of the material. To minimize contamination of the Ge, W wire was used to construct the basket, since molten Ge did not appear to wet this metal easily. This reduced the area of contact between them and restricted the amount of W dissolved by the melt. Also, when in operation, the Ge showed little tendency to creep along the current lead-in wires. The W basket with its Ge charge was held by Ta tapes, which were bolted to electrical lead-throughs in a vacuum flange (fig 4.1b). The source arrangement was surrounded by Ta shields, which screened substrate bars from hot wires leading to the basket, since these could have acted as minor secondary indirect sources of Ge. Also, because the source was required to operate in an inverted position above the Si substrates, the Ge had to be premelted into its W basket. This was carried out in a separate vacuum system at $\sim 10^{-5}$ torr, and sufficient Ge was added to ensure that, during a subsequent run, there would be no significant change in the amount of material in the basket during deposition. This enhanced the operational stability of the source.

A heating current of $\sim$25A was consumed by the source at a low voltage, to produce Ge temperatures of $\sim 1100^{\circ}C$. The power was supplied by a Variac and low voltage transformer. Deposition rates of up to ~ 3 Å sec^{-1} were obtained at substrates held ~ 3 cm below the basket.

Fig 4.1a Ge disc heated by electron bombardment from the back. Edges of disc in close contact with holder, which was constructed of relatively thick Mo wires

Fig 4.1b Resistance heated wire basket source of Ge. Source surrounded by Ta shields (see text). Stainless steel lead-throughs by-passed by Cu wires to aid conduction



(a)



(b)

While it is appreciated that W contamination of the deposited Ge was a possibility, its presence was not detected during subsequent TEM examination of the grown films.

The two Ge sources described above were not treated as simple point sources, for the purpose of calculating deposition rates. In fact, the rate monitor unit (section 1.2.4) was modified, so that it would provide information concerning the variation of deposition rate in a direction perpendicular to the edge of a substrate bar. This allowed an accurate determination of the deposition rate at a position on a substrate bar, in terms of the measured rate at a corresponding position at the edge of the adjacent monitor slide. Such distance corrections typically involved allowances of $\sim 5\%$. Two slots were cut in the back of the Ta holder covering the glass slide, which collected deposited Ge for measurement. After a run was completed, the two strips of Ge film deposited on the back of this slide made possible a determination of film thickness as the required function of distance from the edge of the neighbouring substrate bar. Thicknesses were measured as usual, with a Tolansky interferometer, after the slide had been covered with a reflective Al layer. Since the time taken for deposition was known, deposition rates could be evaluated.

4.3.2) Film Examination

Although most TEM studies were carried out on specimens prepared in a conventional manner, as detailed in the first part of section 1.5.1, it was considered desirable, if possible, to examine some Ge films in profile. The specimen preparation technique then used was that developed by Pettit and Booker (1971), and the reader is referred to that paper for details. Briefly, however, a section was cut from a substrate bar, which had a Ge film on one side, and the piece removed was next stuck with

adhesive (often araldite) between larger flat pieces of Si, so that the film was facing inwards. The 'sandwich' was then mechanically polished down to a thickness of $\sim$0.025 mm, and a small part of it incorporating a section of the bonded junction was then mounted on a supporting metal washer. This specimen was next thinned using an ion beam (second part of section 1.5.1), until a region adjacent to the remaining Ge film was perforated, whereupon the complete specimen (with its washer) was transferred to the TEM for examination.

4.4) Morphology of Germanium Films

When Ge films were deposited at rates from 10^{-2} up to 10 Å sec^{-1} on to (111) Si substrates at temperatures in the range 750 - 920°C, growth centres were always formed, indicating that initial growth had been by nucleation. For a substrate temperature of 840°C and a deposition rate of $\sim 10^{-2}$ Å sec^{-1}, centres were triangular and orientated in the same sense with edges along $\langle 1\bar{1}0 \rangle$ directions, though they were of non-uniform thickness with a channelled structure. As the mean film thickness increased in the range 400 - 900 Å, the centres grew larger and eventually overlapped giving a Ge film with a worm-like or channelled structure (fig 4.2).

Unless otherwise stated, all substrate bars were preheated to 920°C (the highest deposition temperature employed) in UHV for 10 mins prior to deposition, to standardize surface conditions. Nevertheless, it is known that pretreatment at 1250°C cleans Si surfaces (see chapter 3), and when Ge was deposited on to substrates after such a procedure, the films obtained were very similar to those already described, again indicating that initial growth had been by nucleation. However, there was a very small amount of Ge growth between the observed growth centres,

suggesting that a little of the Ge may have been trapped at substrate surface steps, present after the pretreatment (fig 4.3). While this observation is interesting, such a feature was considered to be undesirable, especially in relation to subsequent nucleation studies (section 4.5), since Ge adatom migration processes would have been disturbed. Therefore, the 1250°C pretreatment was not generally used.

If the substrate temperature was held at 840°C and the Ge deposition rate was increased towards 10 Å sec^{-1}, the growth centres remained triangular in shape. However, with higher substrate temperatures, sometimes hexagonal centres occurred. SEM observations (fig 4.4a) showed that a narrow denuded zone often surrounded individual centres, and this probably accounted for the double boundary often seen around centres in optical micrographs (see e.g. fig 4.3). By tilting the specimens to high angles in the SEM, the angles between facets and the (111) surface could be directly measured (fig 4.4b). Results of determinations from many different micrographs showed that the facets on the triangular centres were usually inclined at $\sim 30^{\circ}$ to the substrate surface, so that they were close to $\{311\}$ type planes, since the centres were orientated in the appropriate sense (section 4.6.1). Also, for the hexagonal centres, the analogous three facets were close to $\{311\}$ type planes, while the other three were close to $\{110\}$ type planes. These results should be compared with previous observations of triangular Si growth centres on both Si and Ge substrates (respectively Booker and Joyce (1966), and Takeishi et al (1967)), when in each case, the inclined site facets were found to be $\{311\}$, rather than $\{1\bar{1}\bar{1}\}$ type planes.

Fig 4.2 Individual Ge growth centres grew larger and overlapped giving a film with a channelled structure for increase in film mean thickness. (Optical micrographs)

Fig 4.3 Slight Ge growth between large centres on Si substrate cleaned by pretreatment at 1250°C. (Optical micrograph)

Increase in Film Thickness ⟶

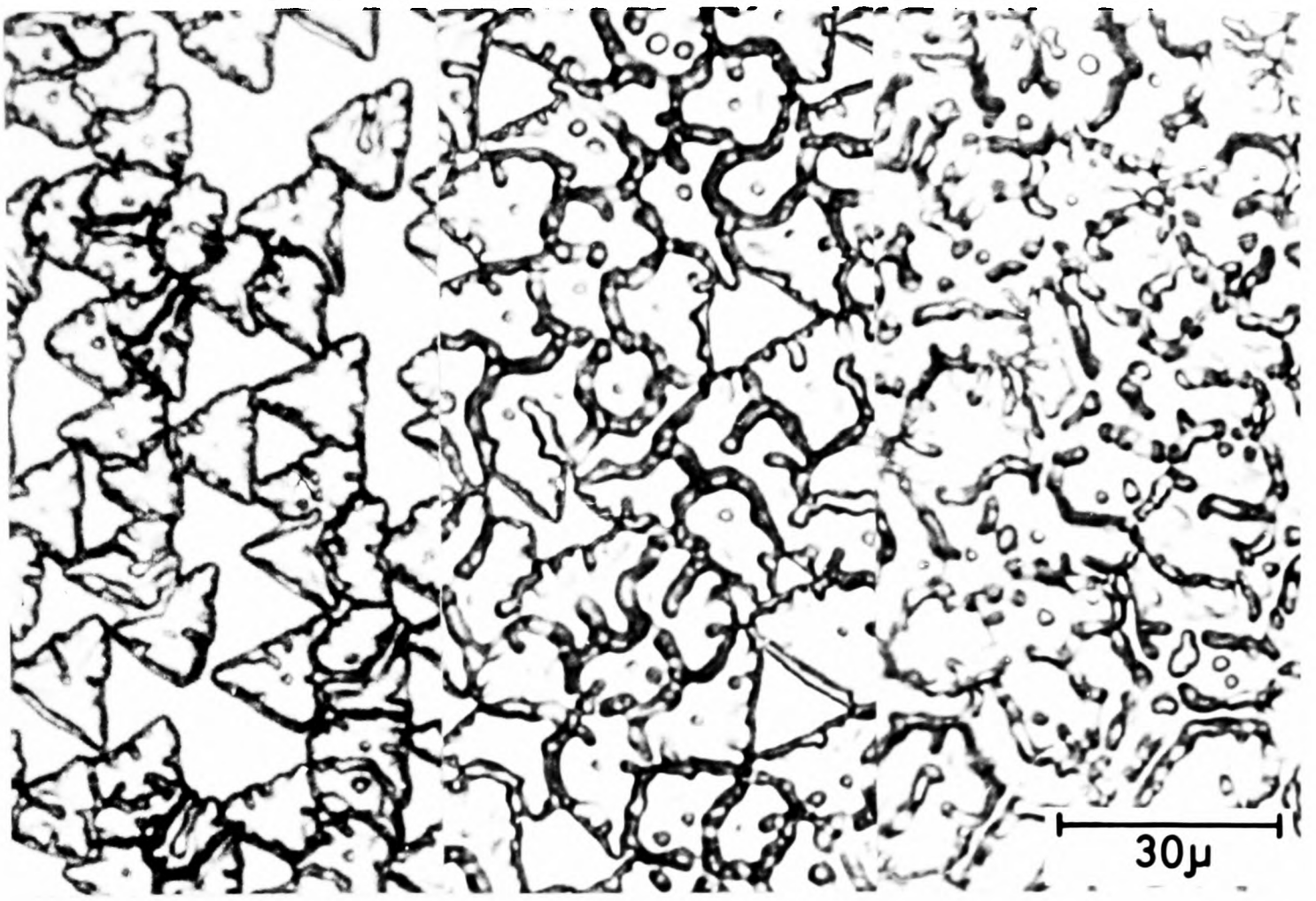
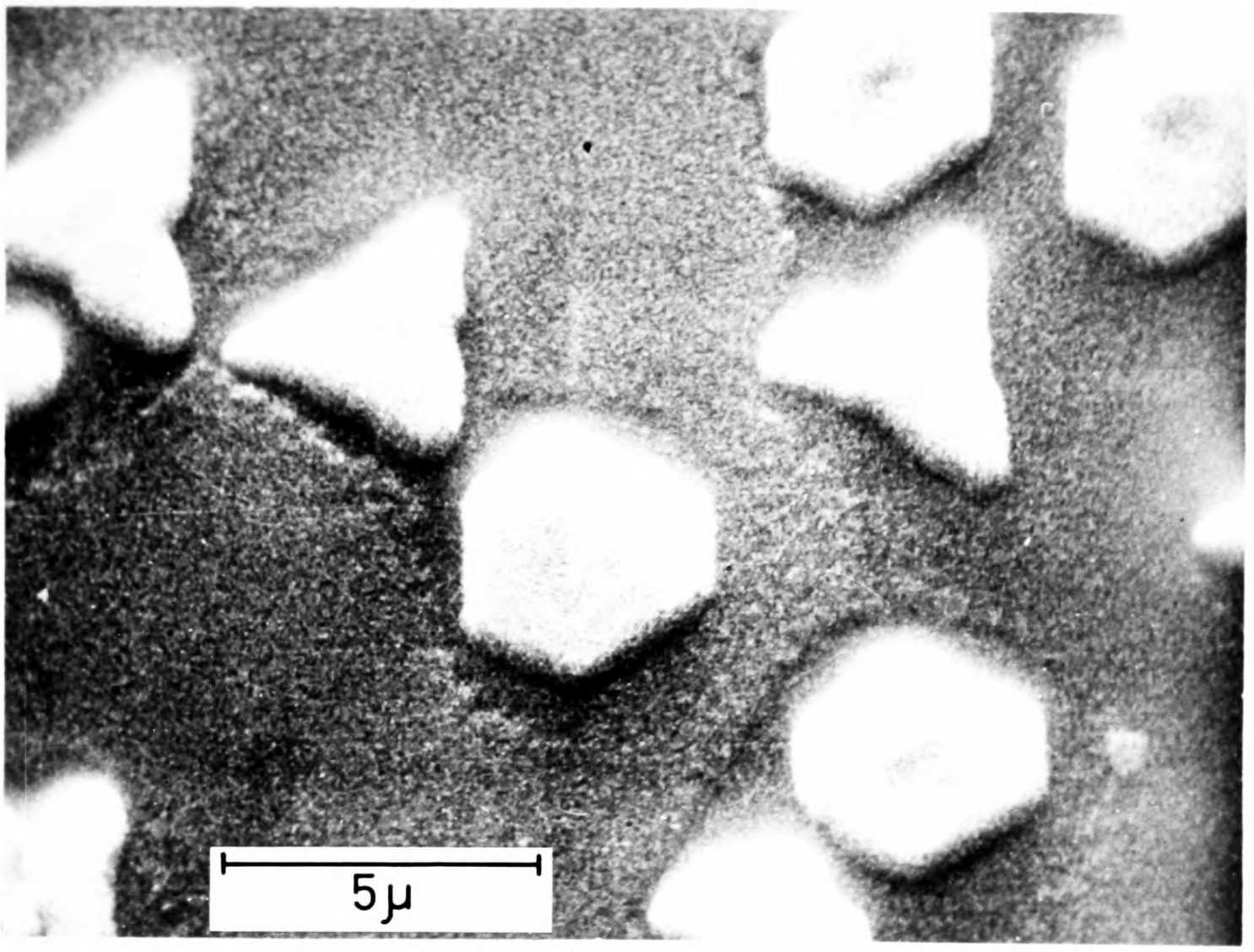
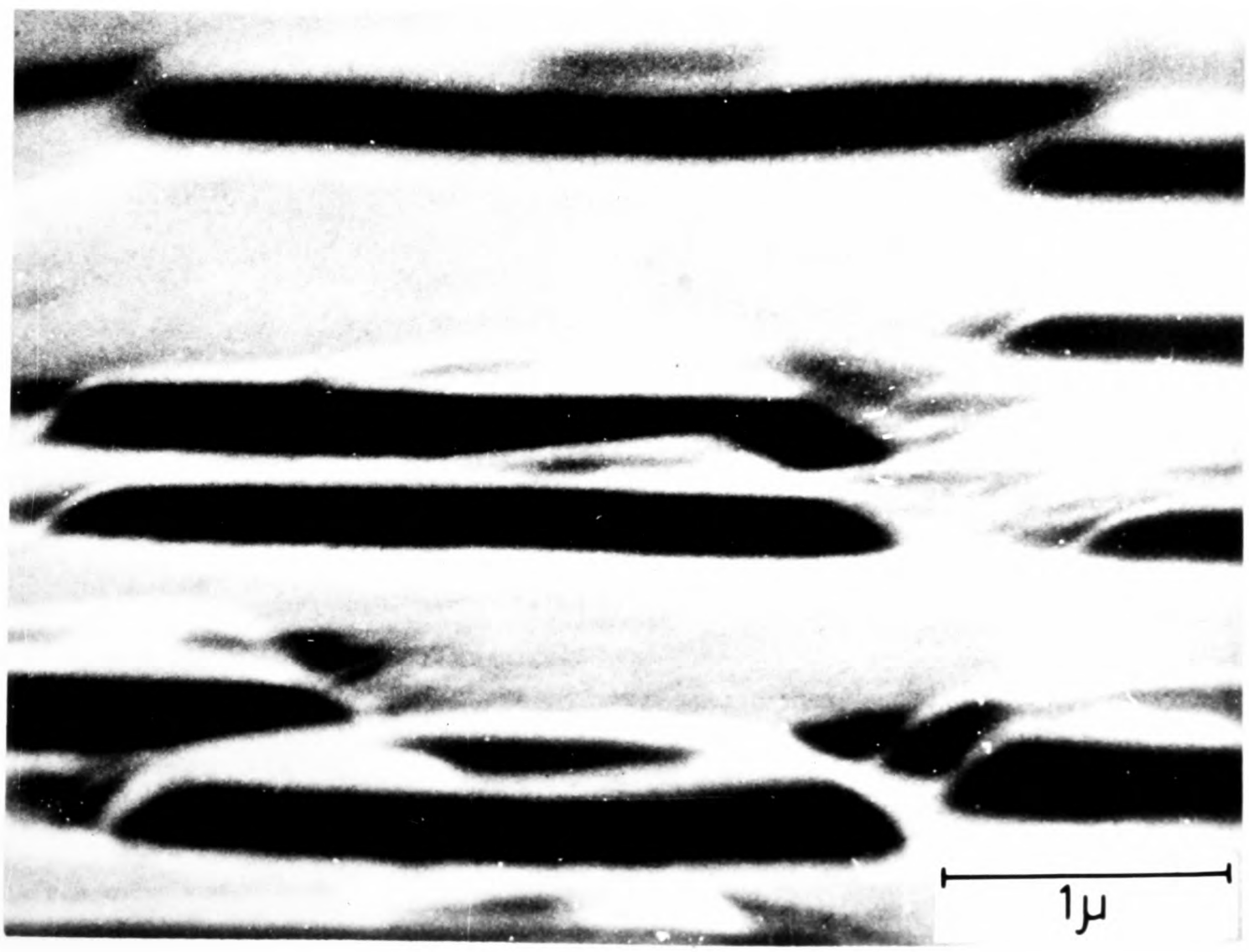




Fig 4.4a Ge growth centres surrounded by narrow denuded zones. (Scanning electron micrograph)

Fig 4.4b Ge growth centres tilted to a high angle. (Scanning electron micrograph)


5μ


1μ

4.5) Nucleation Behaviour

4.5.1) Experimental Results

The saturation number density (N_s) of Ge growth centres formed on the (111) Si substrates varied with deposition conditions. Fig 4.5 shows the effect of changing deposition rate (R), with a constant substrate temperature (T) of 840°C. To determine whether the observed behaviour was consistent with present nucleation theory (Appendix A), measurements were made of N_s values, over ranges of R and T (table 4.1).

Table 4.1

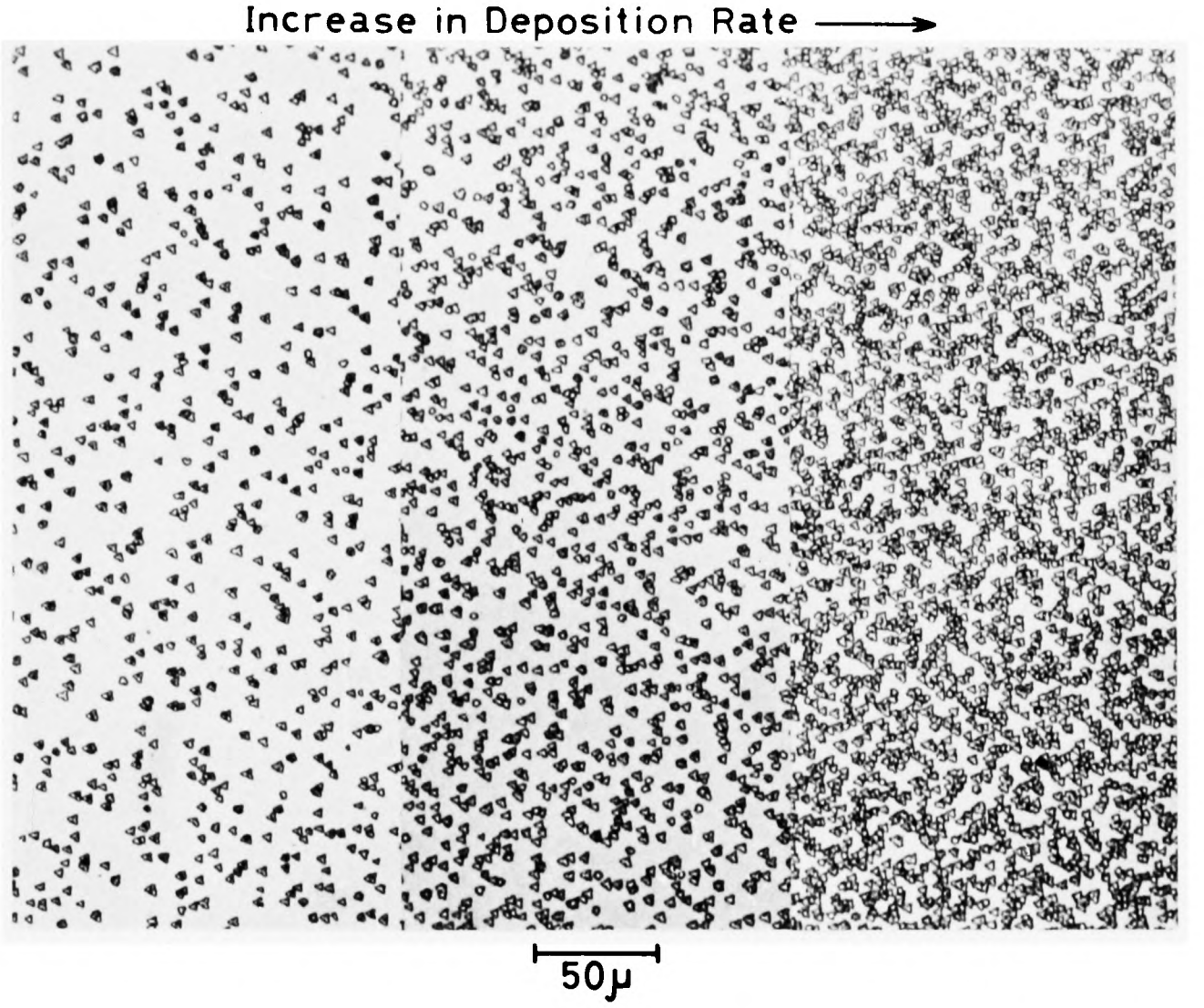
Substrate Temperature (°C)	Saturation Number Density ($\times 10^6$ cm^{-2})	Deposition Rate ($\times 10^{-2}$ Å sec^{-1})
750	29.8 ($\pm$0.8)	75 ($\pm$5.0)
840	4.42 ($\pm$0.1)	195 ($\pm$6.0)
840	3.51 ($\pm$0.1)	155 ($\pm$6.0)
840	2.56 ($\pm$0.15)	99 ($\pm$6.0)
840	2.04 ($\pm$0.05)	31.6 ($\pm$1.6)
840	1.78 ($\pm$0.05)	25.1 ($\pm$1.8)
840	1.51 ($\pm$0.06)	21.8 ($\pm$1.7)
840	1.24 ($\pm$0.06)	16.6 ($\pm$1.7)
840	2.48 ($\pm$0.05)	16.7 ($\pm$0.7)
840	2.10 ($\pm$0.06)	12.5 ($\pm$0.8)
840	1.66 ($\pm$0.06)	9.4 ($\pm$0.8)
920	2.41 ($\pm$0.1)	75 ($\pm$5.0)

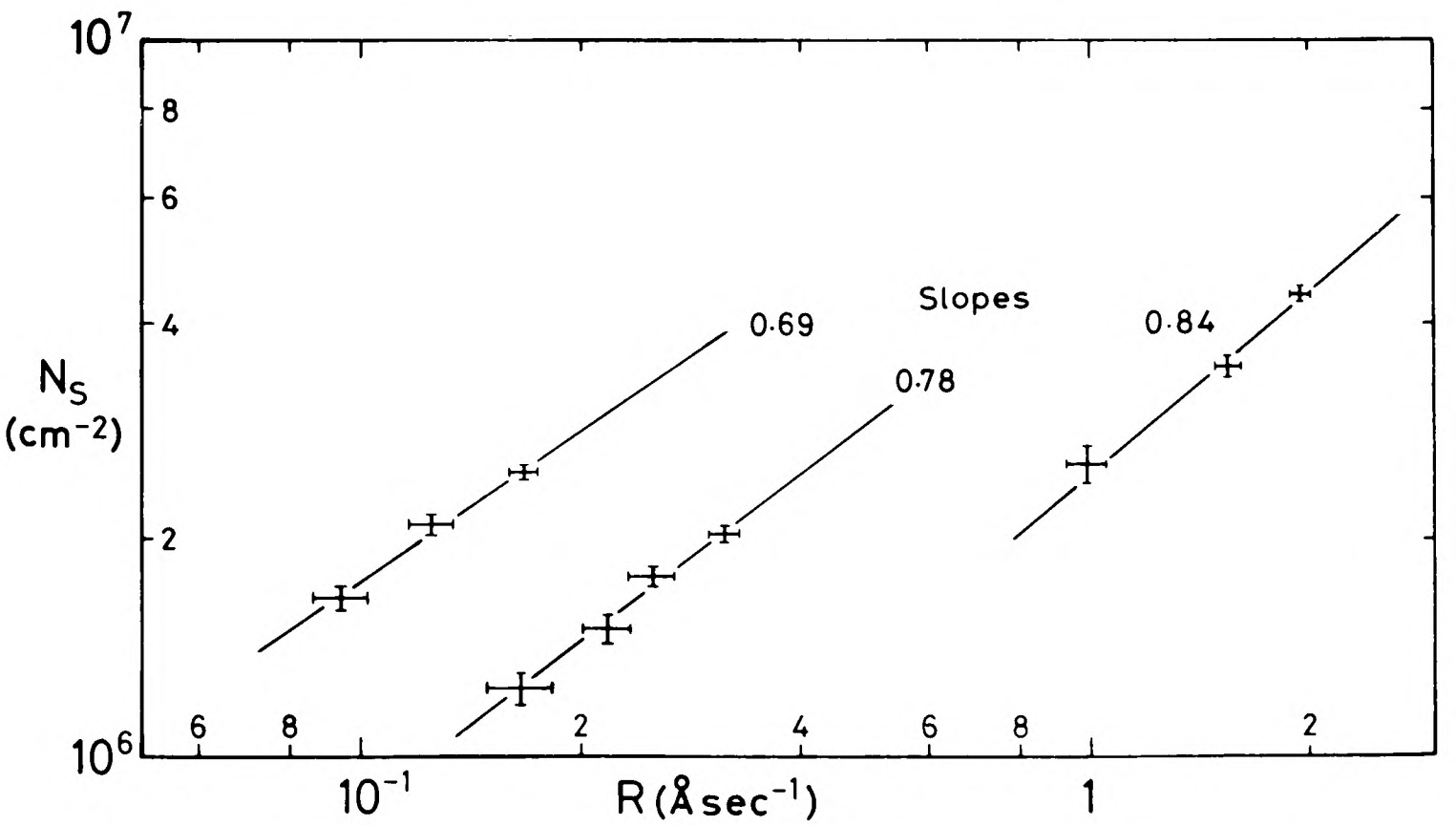
Fig 4.6 shows $\log_{10} N_s$ plotted against $\log_{10} R$ for constant T (840°C). The experimental points fall on three separate, and fairly well defined straight lines - an unexpected result. The three separate sets of data corresponding to the individual lines were obtained from three different substrate bars, used during three different experimental runs. Therefore, it appears that there was some unanticipated difference between deposition on the various substrate bars, for which no allowance has been made. The various possibilities are discussed in section 4.7.1.

When comparisons are made between one substrate bar and another,

Fig 4.5 Increase in number density of Ge growth centres with increase in deposition rate (Optical micrographs)

Fig 4.6 The variation in saturation number density of the growth centres for changes in deposition rate, at a constant substrate temperature of 840°C. The three individual lines correspond to data obtained from three separate substrate bars.


Increase in Deposition Rate
50μ


10^7
8
6
4
2
10^6
N_S (cm^{-2})
Slopes
0.69
0.78
0.84
6
8
10^{-1}
2
4
6
8
1
2
R (Å sec^{-1})

the corresponding values of N_s are displaced by approximately constant factors. Consequently the slopes of the individual lines are very similar, and yield a mean slope of ~ 0.77. The accuracy of this determination is not as great as it would have been if all the data could have been fitted to a single line, but nevertheless, at constant T, an approximate general relationship may be given,

$$N_s = X R^{0.77} \qquad (4.1)$$

where X is a different constant for each individual substrate bar.

Measurements concerning the variation of N_s with T at constant R (7.5×10^{-1} Å sec^{-1}) were, of necessity, carried out using different substrate bars during separate experimental runs. The results are provided in table 4.1 for only illustrative purposes, and it can be seen that there is a general decrease in the value of N_s as T increases. However, for an accurate numerical comparison, it would be necessary to obtain the value of X for each individual bar. Since the manner in which this constant may be evaluated is uncertain, this was not attempted during the present investigation.

4.5.2) Theoretical Interpretation

The variation of N_s with R at constant T, for a given substrate bar, is quite uniform. If it is assumed that this has significance for the initial Ge film growth behaviour, the variation may be tentatively interpreted in terms of nucleation theory. From eq A17 given by Lewis and Campbell (1967), it is evident that if the Ge/Si system were one of initially incomplete condensation, no variation of N_s with R would be expected (Appendix A). This is the opposite of the observed situation, so that over the range of R studied, the re-evaporation of Ge should be negligible. Given this situation, it might be expected that one of eqs A18, A19 or A20, developed by Joyce et al (1967), could be applicable.

These treat the cases of different possible smallest stable nuclei, and by comparing the theoretical R dependencies of N_s with the experimentally determined relationship eq 4.1, it is found that eq A20 is in closest agreement, since it predicts that $N_s \propto R^{0.75}$.

The derivation of eq A20 is based upon the assumption of a four atom smallest stable nucleus. Therefore, it indicates that the smallest stable group of Ge atoms on a (111) Si surface may be of this size. It is of interest that eq A20 also predicts that, as T increases, so N_s should decrease. This type of dependence was observed experimentally in a qualitative manner, although an accurate comparison with theory cannot be made for the reason already given.

4.6) General Crystallographic Structure of Germanium Films

4.6.1) Conventional TEM Examination

Initial TEM examination confirmed that the Ge films grew with the epitaxial relationship (111)Ge//(111)Si, and $[1\bar{1}0]$Ge//$[1\bar{1}0]$Si as expected. The triangular growth centres were orientated such that shallow {311} type planes were available for inclined facet formation.

When specimens were examined such that there was a substantial positive deviation from an operating Bragg reflection, it was found that the Ge films contained a high density of crystallographic defects. Fig 4.7, which was taken with an operating $2\bar{2}0$ type reflection, shows that a continuous network of misfit dislocations, similar to those observed for metal films (e.g. Matthews, 1966), occurred over the entire Ge/Si interface. Stereomicrographs confirmed that such networks lay in a plane in the position of the interface (Cullis and Booker, 1970). They would ideally consist of arrays of edge dislocations (section 4.7.2), and their detailed structure and TEM contrast behaviour will be described in

chapter 6. Many stacking faults had grown up from the interface through the Ge films, on inclined $\{1\bar{1}\bar{1}\}$ type planes. Numerous inclined dislocations were also seen, together with some singledislocations a small distance beneath the interface, in the Si substrate. Much of this structure is evidence for the large film strains present during growth.

When specimens were examined with only a small deviation from the Bragg angle of the operating reflection (strong-beam conditions), the dislocation network image no longer resembled the actual crystallographic structure of the network. The specimen shown in fig 4.7 was somewhat bent due to residual film strains, and as a small region of it approached the Bragg reflecting position, it can be seen that the misfit dislocation network image distorted to give parallel fringes. Fig 4.8 shows a similarly bent specimen, which was orientated in one area so that the [111] foil normal lay on the axis of the microscope. In this region each $2\bar{2}0$ type reflection with a diffraction vector (g) in the (111) plane was strongly excited, and a hexagonal dislocation fringe pattern was produced. However, on moving away from this [111] pole so that only one $2\bar{2}0$ type reflection was operating, only one set of parallel fringes resulted. The formation of this dislocation network fringe image will be considered in detail in chapter 6, and here it is sufficient to note that it was, effectively, a Moiré pattern. Indeed, it was disturbed by underlying foil defects in a manner expected for Moiré fringes (Hirsch et al, 1965), e.g. there were fringe displacements across inclined stacking faults, while fringe terminations were produced by inclined dislocations.

An important feature of the growth concerns changes which occurred in the misfit dislocation networks with variation of deposition conditions. At low deposition rates and high substrate temperatures (e.g. 10^{-2} Å sec^{-1} and $920^{\circ}C$ respectively), the dislocation spacing was observed to be much larger than the 96 Å spacing, predicted theoretically for ideal mismatch

between Ge and Si (see section 4.7.2). However, as the deposition rate was increased and the deposition temperature reduced (e.g. towards 3 Åsec^{-1} and 750°C respectively), the resulting dislocation spacing decreased towards the theoretical value. For a series of seven separate experimental deposition runs carried out over the appropriate range of conditions, giving films with mean thicknesses from ~ 300 - 700 Å, the experimentally determined variations are shown in figs 4.9a and b. The range-bars passing through the experimental points on the graphs do not represent measuring inaccuracies, but indicate the localized changes in network spacings which were observed to occur. The general behaviour of the network spacings was interpreted in terms of a variation in alloying between the Ge and Si, as described in section 4.7.2. A related observation concerns the regularity of the misfit dislocation networks. It was observed that while the networks of smallest spacing had a reasonably uniform structure, those of large spacing exhibited a somewhat degraded regularity. In fact, fig 4.7 shows an example of a rather irregular network. Since only the large spacing networks exhibited this non-uniform structure, it is considered that its presence may be associated with interdiffusion between the Ge and Si as also discussed later.

An exceptional example of the interaction between the two elements was observed after Ge had been deposited at the low rate of 10^{-2} Åsec^{-1} on to a Si substrate held at 920°C (near the melting point of Ge). The surface between the growth centres, which were widely spaced, exhibited a terraced step structure (fig 4.10). Even part of the substrate which had received no direct deposition showed significant surface roughening, so that evidently the Ge had diffused over the whole of the surface. Also, it appears that as Ge diffused into the Si substrate surface, it produced a fairly uniform change in lattice parameter, without inducing the formation of strain-relieving defects. Because of this, the accumulated

Fig 4.7 Crystallographic defects in Ge films -

A Interfacial misfit dislocation network

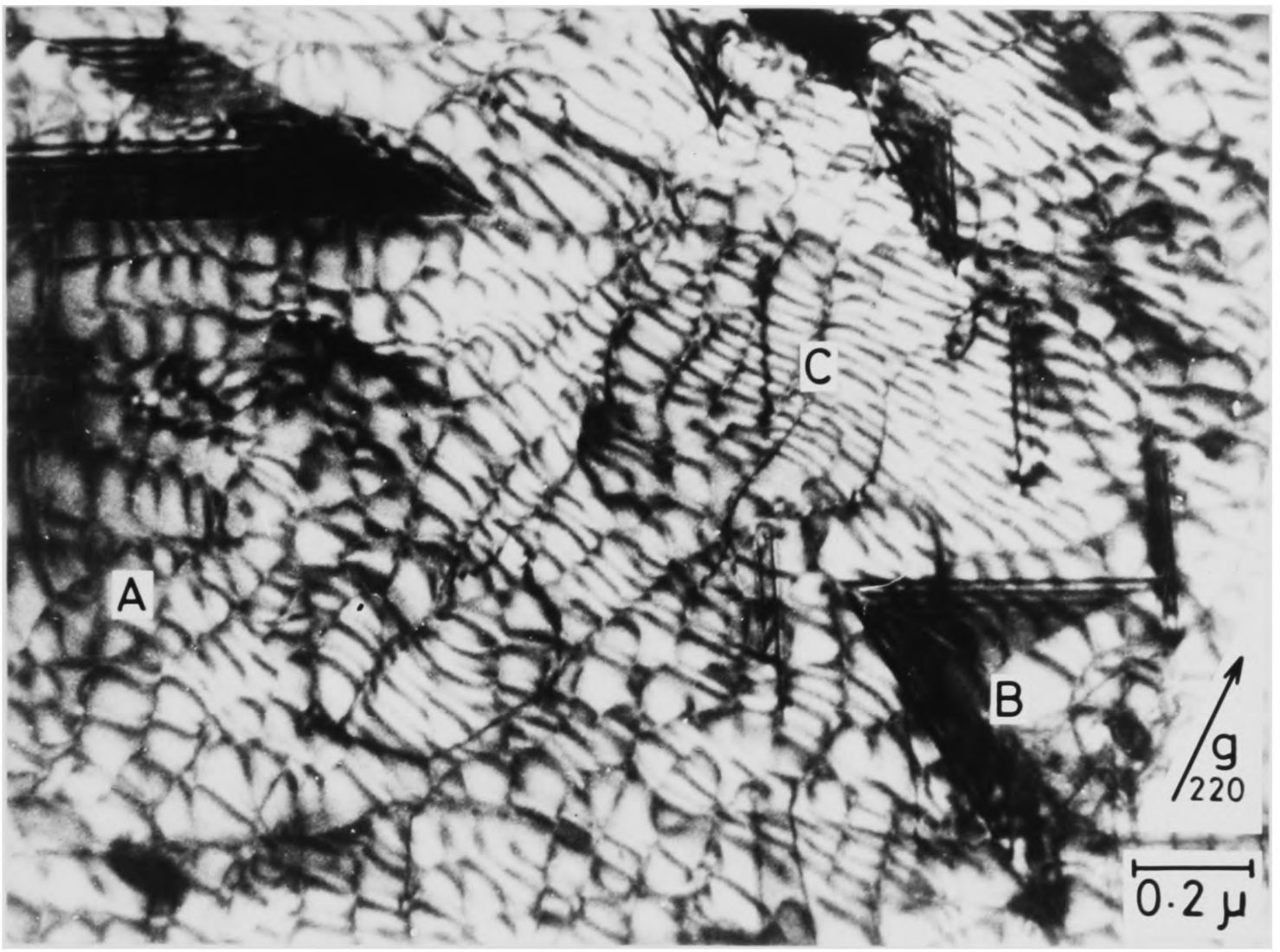
B Inclined stacking faults

C Fringe image of interfacial network

(Transmission electron micrograph, bright-field)

Fig 4.8 Interfacial dislocation fringe image. Hexagonal pattern in [111] pole region with fringes due to single 220 type reflections radiating from it.

(Transmission electron micrograph, bright-field)


A
C
B
g
220
0·2 μ

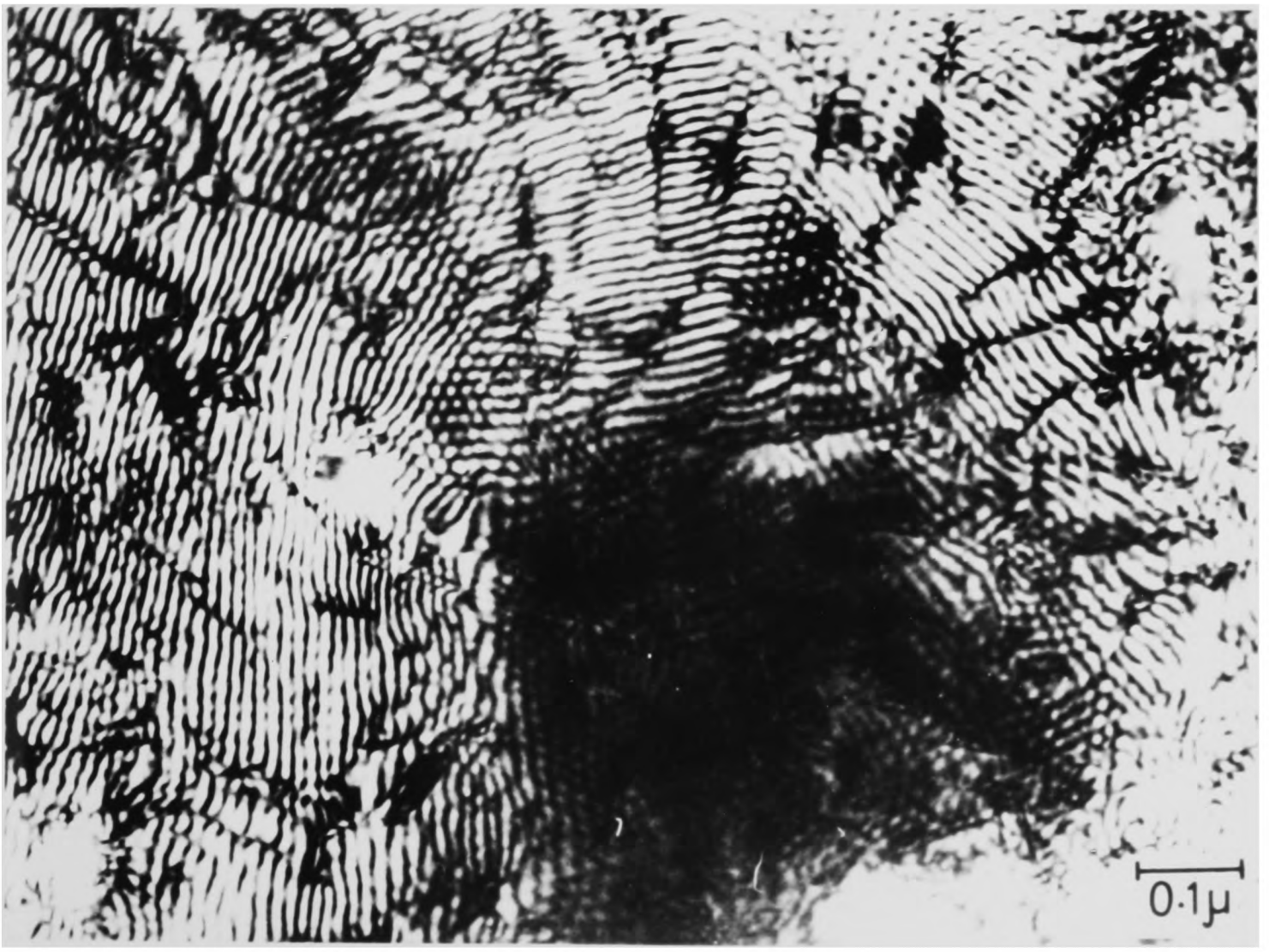
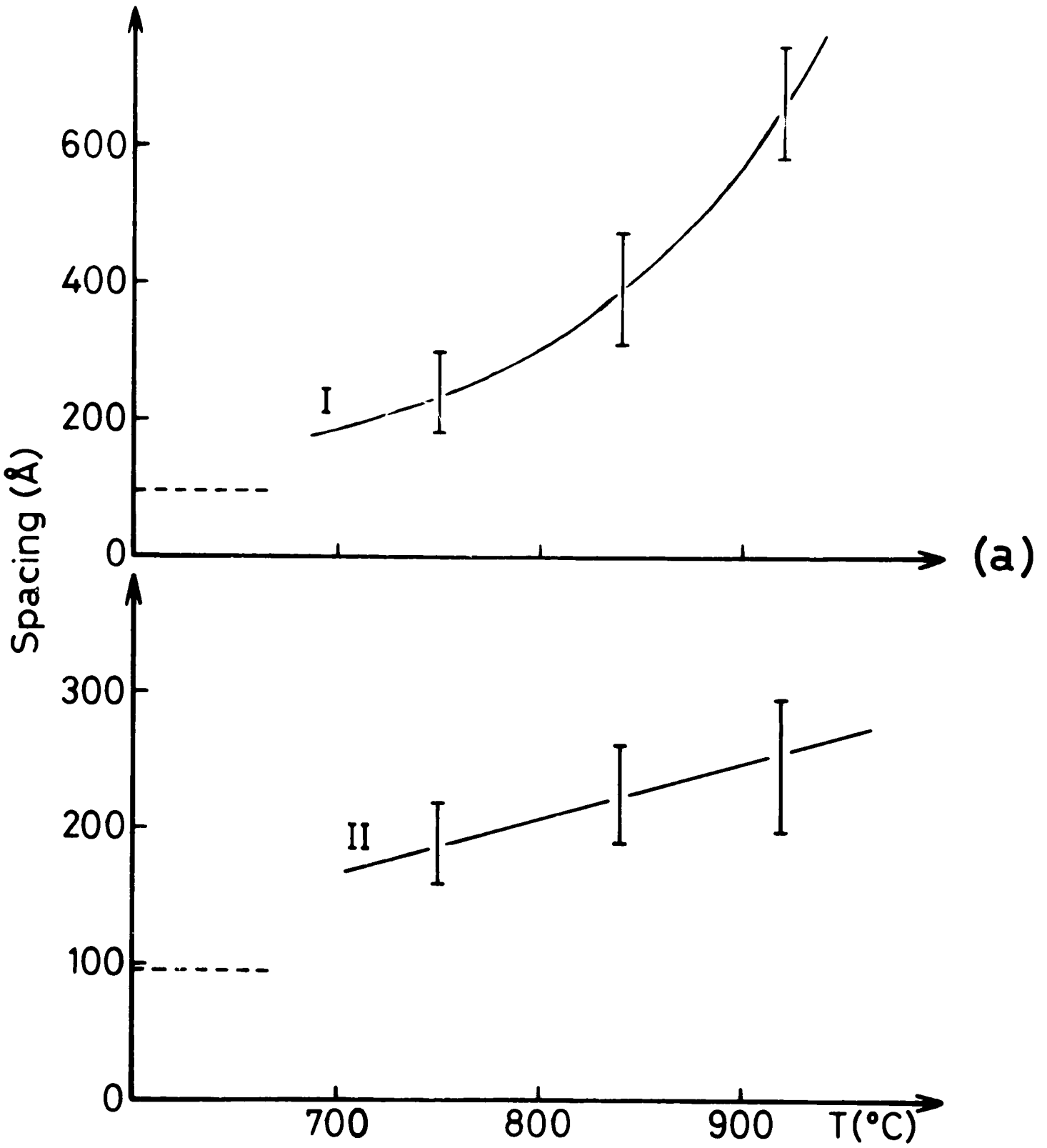

0·1μ

Fig 4.9 Variation in spacing of interfacial misfit dislocations with deposition conditions (theoretical ideal 96 Å, dashed lines)

a) variation with substrate temperature for deposition rates of 2×10^{-2} Å sec^{-1} (curve I) and 2 Å sec^{-1} (curve II)

b) variation with deposition rate for a substrate temperature of $840^{\circ}C$


600
400
200
0
Spacing (Å)
I
(a)
300
200
100
0
II
700
800
900
T(°C)

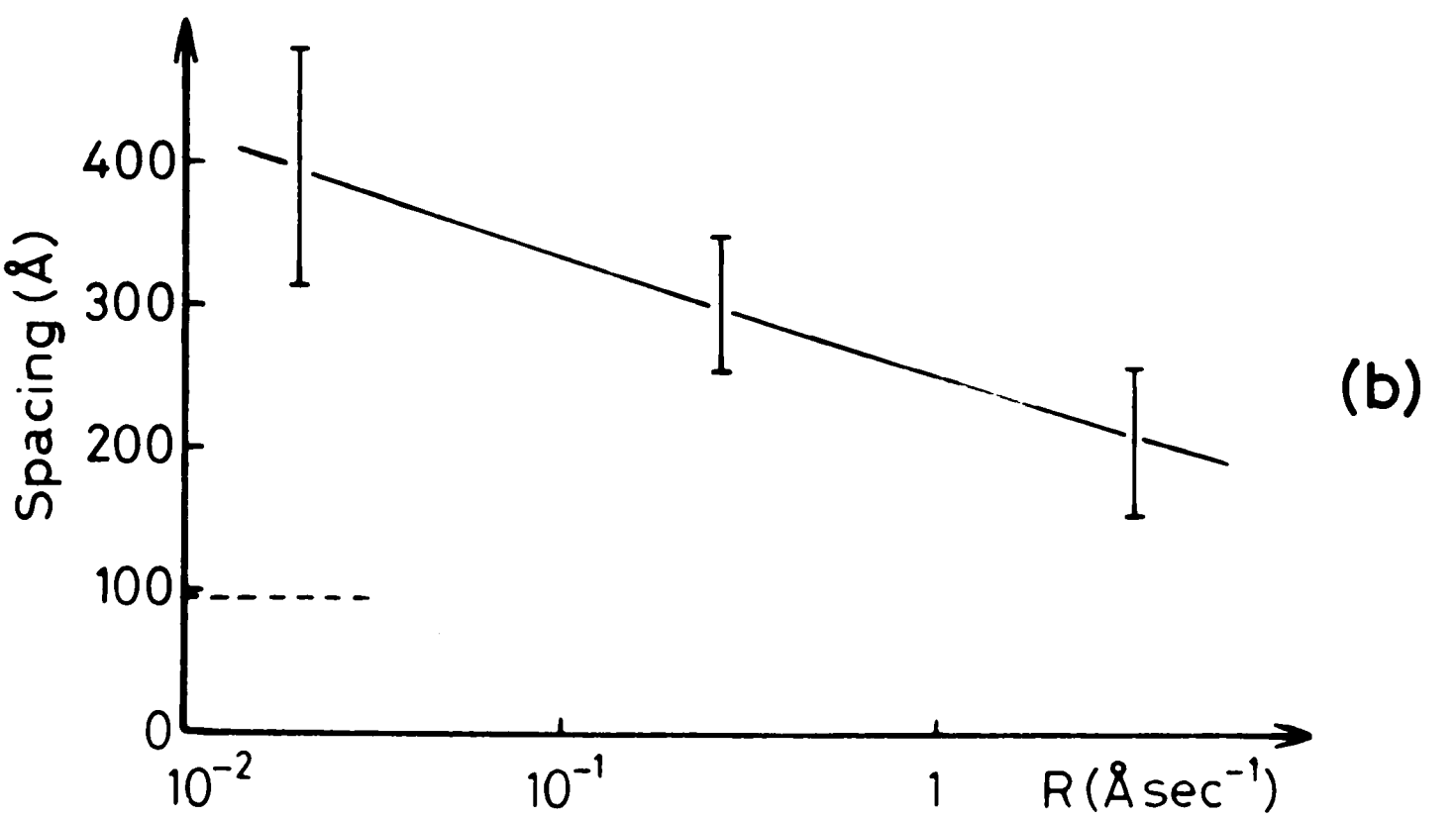
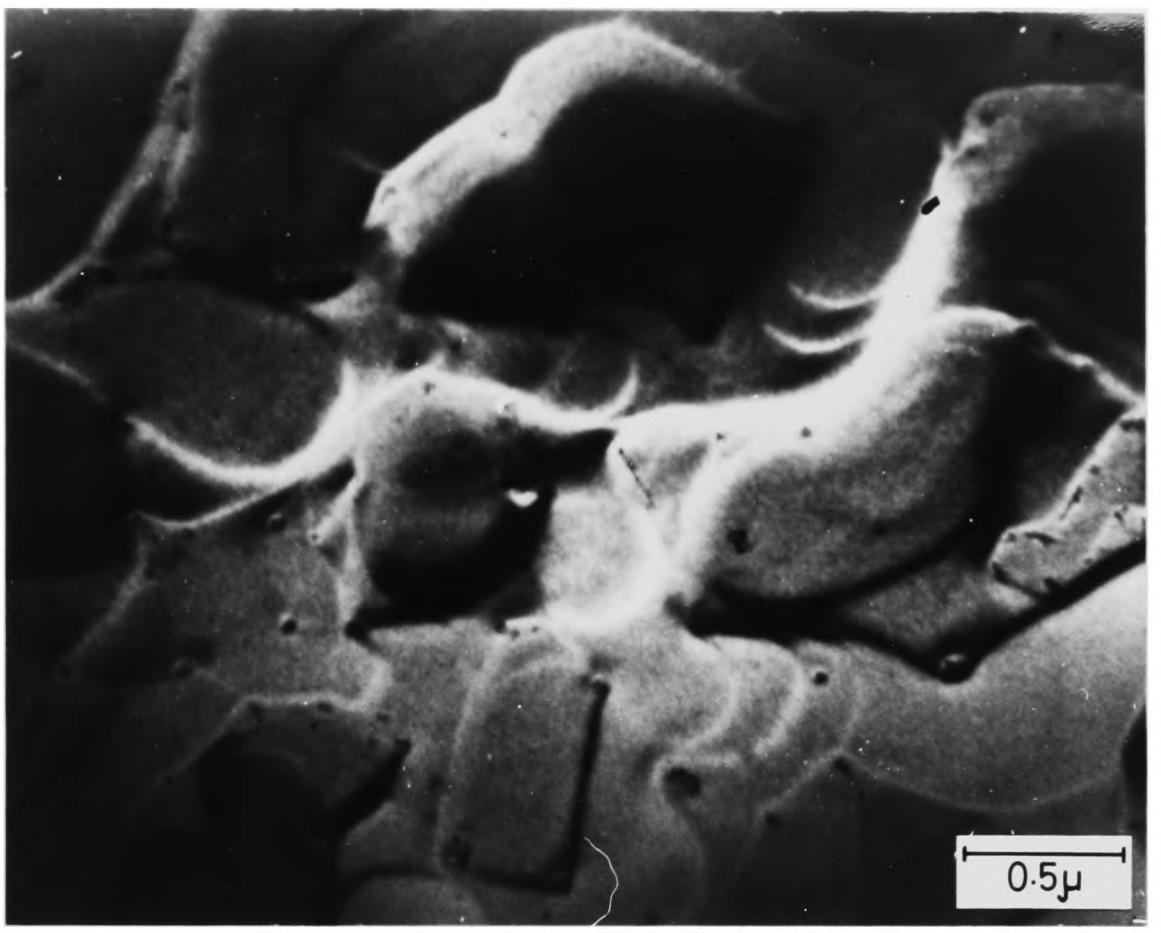
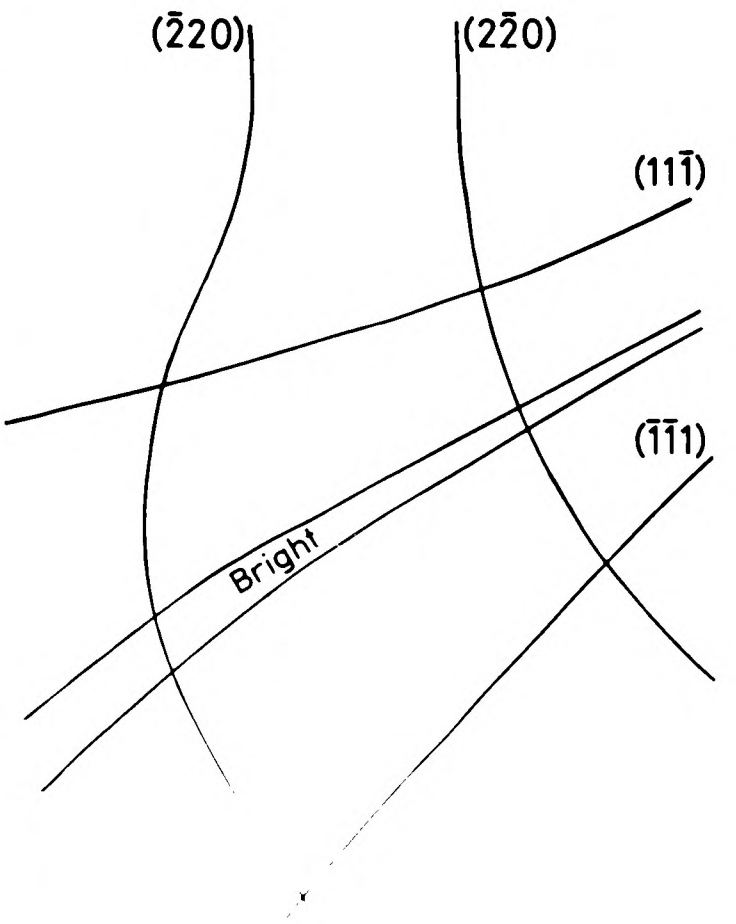

400
300
200
100
0
Spacing (Å)
10^{-2}
10^{-1}
1
R (Å sec^{-1})
(b)

Fig 4.10 Substrate surface between growth centres, after Ge deposition at 2×10^{-2} Å sec^{-1} with a substrate temperature of 920°C.
(Transmission electron micrograph, bright-field)

Fig 4.11 [112] pole region crossed by band of enhanced electron transmission - illustrated by diagram.
(Transmission electron micrograph, bright-field)


0·5μ

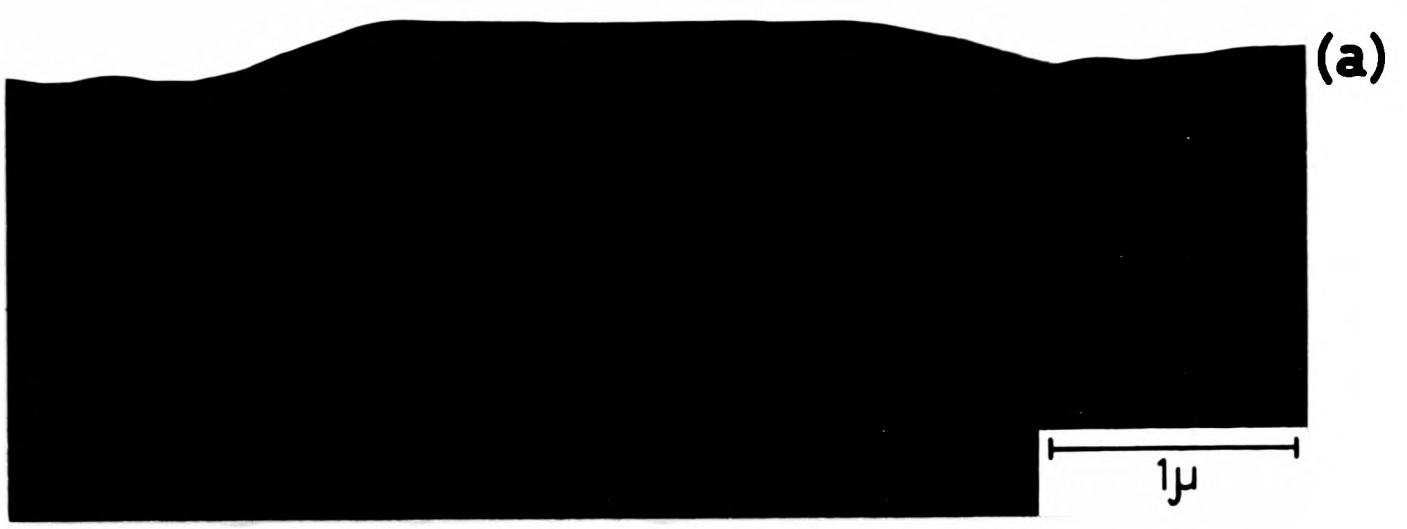

5μ


(2̄20)
(22̄0)
(11̄1̄)
(1̄1̄1)
Bright

surface strain induced some regions of relatively thick TEM specimens to bend simultaneously in two directions, i.e. to become dome-shaped. This type of bending is not usually seen with Si specimens because of their rigidity, and it enabled a demonstration to be given of the anomalous transmission expected for 100 kV electrons, at the symmetry position for 111 systematic diffraction (Fowler and Marton, 1965). Fig 4.11 shows an array of bend contours associated with a [112] type pole, taken in bright field, and a region of enhanced transmission can be seen across the centre, following the symmetry position for the 111 type contour. This contrast effect is peculiar to elements having the diamond lattice, and Humphreys et al (1971) have explained it using structural arguments. They showed that its presence is related to the fact that, unlike simple FCC and BCC elements, the centre of symmetry of the Si diamond lattice does not coincide with an atomic position, but lies mid-way between an atom pair. Due to this atomic arrangement, electron Bloch wave scattering in the [111] direction is modified so that the above image contrast feature is produced. In fact, diffraction by (111) planes of diamond lattice materials should resemble positron diffraction by the planes of simple metals.

4.6.2) Examination of Films in Profile

Some Ge films were subjected to TEM examination in profile, for which specimens were prepared by the ion thinning technique given in section 4.3.2. Silhouettes of 'edge-on' Ge growth centres were frequently observed, and these clearly showed the shallowly inclined side facets which were present (fig 4.12a). However, the facet inclinations may have been somewhat modified by ion erosion, so that angle measurements from such micrographs were not reliable. When specimens had received longer periods of ion beam bombardment the centres were sometimes thin enough to give transmission using 100 kV electrons. There was, then, often evidence


(a)
1μ


(b)
2μ

that they contained numerous inclined defects, as was expected from observations on conventionally thinned specimens.

A most unexpected difficulty arose during the preparation of such TEM 'edge-on' specimens. In the course of the final ion beam thinning, in many cases a thin strip of Si substrate material, adjacent to the Ge film, was found to have remained very thick, even though the bulk of the Si behind it had been removed. This was very unfortunate, since the Ge film also then remained too thick for TEM examination. If ion beam thinning was continued, the specimen was often destroyed before this edge region had been reduced to a satisfactory thickness. Fig 4.12b shows such a thick edge, and the sharpness of its profile seems quite remarkable. The reason for the presence of this undesirable feature is not certain, but it may be produced by transfer of material from other regions of the specimen, under the action of the ion beam. While the profile thinning technique is still under development, using carefully controlled conditions, good Si specimens have been produced (Pettit and Booker, 1971).

4.7) Discussion

4.7.1) Initial Film Growth

It was deduced from experimental observations that initial Ge film growth took place by a nucleation mechanism. The observed growth centre saturation number densities, obtained from individual (111) Si substrate bars, exhibited a smooth variation with changes in Ge deposition rate. The nature of this variation was tentatively interpreted in terms of a 4-atom smallest stable Ge nucleus. This should be compared with the case of Si nucleation on (111) Si substrates, for which there was deduced to be a 3-atom smallest stable nucleus. Taken together, these two results suggest that in the respective Ge/Si and Si/Si systems, Ge nuclei

had a smaller stability than Si nuclei of the same size. This occurred despite the fact that Ge deposition was generally carried out at higher rates than Si deposition, which would give the Ge nuclei an apparent increase in stability with respect to their Si counterparts.

The above observations are consistent with the fact that Ge-Ge and Ge-Si single bonds are both less stable than corresponding Si-Si single bonds. Therefore, Ge nuclei on a Si surface would be expected to be somewhat less stable than their Si counterparts. A 4-atom Ge nucleus could well have a tetrahedral configuration, formed by the migration of a Ge adatom on to the centre of a 3-atom triangular arrangement.

A prominent feature of the nucleation data presented in section 4.5.1 was the large and unanticipated fluctuations in absolute N_s values between growth centres formed upon different substrate bars. The reason for this variation is uncertain. A possible clue to an explanation is the observation that the distribution of Ge nuclei on the (111) Si substrates was not entirely uniform; see e.g. fig 4.5. Several important theoretical models for initial nucleation processes incorporate the concept of adatom diffusion zones around nuclei, giving a decreased probability of further nucleation in their vicinity (e.g. Lewis and Campbell (1967) and Stowell (1970): see Appendix A). Indeed, such behaviour has been experimentally observed for certain systems; e.g. Joyce et al (1969a) found that the spatial distribution of Si growth centres on (100) Si substrates was more tightly peaked than the Poisson distribution, expected for completely random nucleation. Fig 4.5 shows that Ge growth centres in the present system had a marked tendency to occur in non-uniform groupings.

These considerations indicate that there may have been preferred Ge nucleation sites on the (111) Si surfaces, which were of a somewhat variable nature. Since previous Si nucleation experiments on similar (111) surfaces showed no evidence for the presence of such unusual sites

(Joyce et al (1967) and chapter 2), it appears that they may be specific to the Ge/Si system. The presence of such sites could be associated with the extensive Ge/Si alloying, the existence of which will be discussed in the next section. Interdiffusion of Ge and Si at an early stage of film growth could disturb a substrate surface and exert an influence upon nucleation processes. However, in the absence of further experimental data, this reasoning is rather speculative.

4.7.2) Film Structure and Composition

The ideal mismatch (f) between a Ge film and its Si substrate (lattice parameters a_1 and a_2 respectively) may be written

$$f = \frac{a_1 - a_2}{a_2} \qquad (4.1)$$

Substituting $a_1 = 5.6575$ Å and $a_2 = 5.4307$ Å, it is found that $f = 0.0418$, i.e. 4.18% mismatch at room temperature. Since the thermal coefficient of expansion of Ge is greater than that of Si (Filyand and Semenova, 1968), the mismatch will be somewhat larger at film growth temperatures. When the film and the substrate meet across a (111) plane with no rotational misalignment, the strain would ideally be relaxed by a hexagonal array of edge dislocations, lying along $\langle 11\bar{2} \rangle$ type directions, as described in section 6.3.1. The dislocation Burgers vectors would be of the type $\frac{a}{2}[1\bar{1}0]$, with an ideal dislocation spacing (D_d) given by eq 6.8. Using the room temperature lattice parameters, $D_d \simeq 96$ Å. Also, parallel Moiré fringes produced using TEM Bragg reflection hkl under strong-beam conditions (see section 6.3.3) would have a spacing (D_m) given by eq 6.5. For $2\bar{2}0$ type reflections, $D_m \simeq 48$ Å.

During the experiments reported here, dislocation networks were always observed to be present at film/substrate interfaces, and both structural and fringe images could be obtained using the appropriate TEM conditions. However, measured values of D_d were always found to be much

larger than the ideal value of 96 Å, as shown in fig 4.9. Now, a change in the dislocation spacing indicates that there is a corresponding change in the amount of lattice mismatch to be accommodated, if residual film strains may be excluded from consideration. The magnitude of the lattice mismatch is linked directly to the nature of the substrate and its overgrowth, and therefore it is proposed that the films were in general alloys between Ge and Si. Since mixtures of these two elements obey Vegard's law (Johnson and Christian, 1954), the greater the Si content of the film, the greater would be the reduction in mismatch between the film and the substrate. This interpretation is physically reasonable, since the extent of the alloying would be expected to be greatest at low deposition rates and high deposition temperatures, when interdiffusion should be most pronounced. In fact, use of these growth conditions gave the largest values of D_d, as expected. Also, these findings are supported by the earlier work of Fujimoto and Yamaguchi (1968) on the Ge/Si system, where it was shown by the use of an X-ray analytical technique that the deposited films had a large Si content. In the present work D_d varied between ~150 Å and 700 Å, depending upon deposition conditions. This implies that the film alloy constitution varied over the range of ~ 65% Ge : 35% Si to 15% Ge : 85% Si, respectively.

The use of dislocation spacing data as an approximate indication of the extent of Ge/Si alloying, requires that most of the mismatch should be accommodated by the interfacial dislocations, and not be present as large residual lattice strains. Van der Merwe (1963) derived an expression for the critical film thickness (h_c) beyond which misfit dislocations should be rapidly introduced (in the absence of an energy barrier), so that the above approximation would be valid. Following van der Merwe

$$h_c = - \frac{a_1(1-2\nu)}{2\pi(1-\nu)^2(1+G_1/G_2)f} \ln \frac{4\pi f G_2}{G_o e(1-\nu)\ (1+G_2/G_1)} \qquad (4.2)$$

where ν is the mean Poisson ratio of film and substrate, G_1, G_2 and G_o are the shear moduli of the film, substrate and interface respectively and e has its usual significance. If $\nu \simeq 0.21$, $G_2 = 8.0 \times 10^{11}$ dynes cm^{-2} and $G_1 = G_o \simeq 7.4 \times 10^{11}$ dynes cm^{-2}, then as the effective film/substrate mismatch (at room temperature) varied from 2.7% to 0.6% in accord with the previously proposed film alloy composition range, h_c varied from ~ 30 Å up to 250 Å. Note also that the lattice mismatch at deposition temperatures was inevitably larger than that quoted here (due to thermal expansion differences), so that the values of h_c would be further depressed. Now, since mean film thicknesses were between 300 Å and 700 Å, and the actual growth centres were much thicker still (due to incomplete surface coverage), the interfacial dislocations should have accommodated most of the mismatch and the above approximation is acceptable.

It is also of interest to decide the mechanism by which such large proportions of Si could have been introduced into the Ge films. It is likely that the most important alloy formation mechanism involved surface diffusion processes, which probably rapidly incorporated Si directly into deposited films throughout their growth period. It is possible that the 'denuded zones', sometimes observed around growth centres, could have been produced by such diffusion and alloying. Nevertheless, solid state diffusion across interfaces may also have been important, and it is possible to estimate its magnitude using published diffusion data. The solid state diffusion coefficient of Si in Ge may be approximated by the Ge self diffusion coefficient (D), which at 750°C is $\sim 1.9 \times 10^{-14}$ cm^2 sec^{-1} (Widmer and Gunther-Mohr, 1961). The deposition of ~ 300 Å of Ge at 3 Å sec^{-1} required a time (t) of ~ 100 sec, and therefore, the characteristic diffusion length, $(Dt)^{\frac{1}{2}}$, would have a value of ~ 140 Å under these conditions. This is a substantial fraction of the film thickness, and indicates that solid state diffusion of Si from the substrate could have had a significant effect

upon film alloy composition, especially since all other films were grown under conditions more favourable to interdiffusion.

In previous work on the Ge/Si system, Ito and Takahashi (1968) did not consider the possibility of a reduction in film/substrate mismatch by alloy formation (section 4.2). Therefore, it is probable that the $2\bar{2}0$ type TEM fringe image observed by these workers was produced by a Moiré effect, and that the misfit dislocation spacing in their films was ~ 180 Å, and not 90 Å as claimed by them. The larger spacing would be in reasonable agreement with the data in fig 4.9, under the prevailing deposition conditions.

During film growth in the present experiments, the mechanism by which misfit dislocations were introduced was probably by glide along the interface from the edges of growth centres. This was possible since the (111) growth plane was also the primary diamond lattice slip plane. It is likely that the process required only a relatively small activation energy, in accordance with the observations of Yagi et al (1971). If the films had become continuous before the introduction of misfit dislocations (which was never observed in the present system), other mechanisms would have been involved, such as those proposed by Matthews (1967). Furthermore, since solid state diffusion of Si across the heterojunction was shown above to have been an important process, the film/substrate mismatch must have changed accordingly during the growth. Therefore, misfit dislocation networks, once formed, would have been subjected to continually changing forces. Thus, under conditions of enhanced alloying, it is not unexpected that such a network should be somewhat irregular, as was observed experimentally.

Throughout the present work, films produced by Ge deposition have sometimes been referred to as Ge films, even though they may have had a substantial, and possibly dominant Si content. This description was, therefore, used only for simplicity when knowledge of the exact film

composition was unimportant.

4.8) Summary

Ge films up to 900 Å in thickness were deposited at rates of from 10^{-2} up to 10 Å sec^{-1} on to (111) Si substrates held at temperatures in the range 750 - 920°C. The thinnest films were observed to be composed of growth centres, which were usually triangular, but sometimes hexagonal in shape. This indicated that initial growth had been by nucleation. However, although a tentative comparison of experimental data with theoretical models indicated that a smallest stable nucleus may have been composed of four Ge atoms, certain unexpected irregularities in the data did not permit a more comprehensive analysis. After further Ge deposition, the growth centres were observed to have spread laterally and joined together, to give a film with a channelled structure.

When the deposited films were examined using the TEM, it was confirmed that the epitaxial relationship was (111)Ge//(111)Si with $[1\bar{1}0]$Ge//$[1\bar{1}0]$Si. The films were found to contain a large number of crystallographic defects, including dislocations and stacking faults present on inclined $\{1\bar{1}\bar{1}\}$ type planes. Some of the most prominent defect structures were continuous networks of misfit dislocations, which occurred over each entire Ge/Si interface. However, the observed dislocation spacing in such networks was always considerably larger than the ideal theoretical spacing (96 Å), and was found to vary with deposition conditions. This was interpreted in terms of interdiffusion between the Ge and Si during growth, yielding films which were, in general, alloys between these two elements.

CHAPTER 5 THE GROWTH OF SILICON ON INSULATORS

		Page
5.1)	Introduction	107
5.2)	Review of Literature	107
5.2.1)	Silicon on Sapphire	108
5.2.2)	Silicon on Spinel	112
5.2.3)	Silicon on Other Single Crystal Insulators	113
5.3)	Experimental Details	114
5.4)	Results - Silicon on Sapphire	117
5.4.1)	The Sapphire Substrates	117
5.4.2)	Silicon Films Grown at 900°C	117
5.4.3)	Silicon Films Grown at 1100°C	120
5.5)	Results - Silicon on Other Insulators	121
5.5.1)	Silicon on Diamond	121
5.5.2)	Silicon on β - Silicon Carbide	123
5.6)	Discussion	124
5.6.1)	Silicon on Sapphire	124
5.6.2)	Silicon on Diamond	127
5.6.3)	Silicon on β - Silicon Carbide	129
5.7)	Summary	130

5.1) Introduction

When electronic devices are fabricated in an epitaxial Si film, it is often necessary to electrically isolate them from the substrate upon which the film was grown. For Si substrates, this is usually achieved by reverse biasing an appropriately positioned p - n junction. However, leakage capacitative coupling with the substrate may then impose an upper limit upon device operation frequency, and this is clearly undesirable. The isolation difficulty could be avoided by the formation of devices in Si films grown directly on electrically insulating materials. Nevertheless, the choice of possible substrates is somewhat restricted by considerations including material availability, crystallographic mismatch and thermal coefficient of expansion differences. The growth of Si on sapphire, which is a readily available material, has been studied by a number of workers. However, due to difficulties in thinning the sapphire, comparatively little work has been carried out using direct TEM studies of the Si films whilst still attached to their substrates, especially at an early stage of growth. The present chapter is concerned with investigations of this nature, in which sapphire substrates were thinned using the ion beam method. The work was further extended to a preliminary study of Si growth on the insulators diamond and β-SiC, which have certain desirable thermal properties.

5.2) Review of literature

A review of many studies concerning the growth of Si single-crystal films on insulators has been given by Filby and Nielsen (1967). More recently, Cullen (1971) has reviewed epitaxial Si film growth by chemical vapour deposition on sapphire and spinel substrates.

5.2.1) Silicon on Sapphire

Much work has been directed towards the preparation of sapphire substrates, with a surface perfection satisfactory for subsequent Si growth. Substrates have been mostly cut from bulk sapphire crystals, mechanically polished and then chemically treated to remove residual surface damage. Liquid polishes such as phosphoric acid (Scheuplein and Gibbs, 1960), and molten vanadium pentoxide (Faktor et al, 1967) have been tested, with varied degrees of success, and it is thought that a residue of the polish may generally be left on the surface. Accordingly, high temperature vapour polishing techniques have been developed, and pretreatment in H_2 has given especially good results, as shown by Manasevit and Simpson (1964) and Robinson and Mueller (1966). Experiences with anhydrous HCl have been mixed (e.g. Chu et al, 1965), while polishing with both Si vapour (Reynolds and Elliot, 1966) and SiH_4 (Filby, 1966) has also been attempted. Further, Tamura and Nomura (1967) and Manasevit et al (1968) deposited Si upon sapphire substrates with as-grown surfaces, and obtained relatively good results.

Both chemical vapour decomposition and vacuum evaporation have been used for Si deposition. Manasevit et al (1965) used SiH_4/H_2 and $SiCl_4/H_2$ vapour deposition techniques, and by the TEM study of film surface replicas found that growth centres were present, indicating initial growth was by nucleation. Similar results were obtained by Bicknell et al (1966), who also used $SiHCl_3$ reduction. Both groups of workers compared their respective deposition techniques. Bicknell et al used RHEED to show that their films contained a high density of crystallographic defects. Also, a TEM study of parts of a layer detached from one of their substrates, showed that microtwins and stacking faults were the most prevalent defects. A detailed X-ray and TEM replica study by Nolder et al (1965) showed that there were far fewer twin defects in SiH_4 -grown material than in $SiCl_4$ deposits.

For Si deposition by UHV evaporation, Weisberg and Miller (1968) showed that the use of oxygen-free Si source material was desirable to obtain Si films of the best quality. Naber and O'Neal (1968) investigated the use of sapphire substrates which had been subjected to various pretreatments. As expected, growth on mechanically polished surfaces was particularly poor, while if the surfaces were etched 'in situ' with Si vapour at a high temperature prior to deposition, subsequent growth was very much improved. However, Yasuda and Ohmura (1969) claimed that the state of the sapphire substrate surface was not important for Si deposition by evaporation. For films grown at 1000 - 1100°C on H_2-fired substrates, they found using TEM replica techniques that initial growth led to the formation of Si growth centres. RHEED showed that the centres occurred in four different rotational twin orientations. As the films became thicker, and the growth centres overlapped, one pair of twins could no longer be detected, and finally, for film thicknesses > 800 Å only a single orientation was observed. For films grown at only 950°C two orientations could be detected even in relatively thick deposits. Linnington (1970, 1971) used the TEM to study the structure of thick Si films grown on sapphire substrates, and employed the ion beam thinning technique for specimen preparation. He observed a high density of planar film defects (mostly microtwins) and dislocations, while he was unable to detect any structure specifically associated with the interface. Also Chang (1971) investigated the low temperature growth of Si on sapphire of various orientations using LEED.

The orientation relationships for epitaxial Si on sapphire have been studied by many workers (e.g. Manasevit et al 1965; Nolder and Cadoff, 1965; Bicknell et al, 1966). Some of the general relationships found to exist are $(111)_{Si} // (0001)_{Al_2O_3}$, both $(111)_{Si}$ and $(110)_{Si} // (11\bar{2}0)_{Al_2O_3}$, $(001)_{Si} // (1\bar{1}02)_{Al_2O_3}$ and $(111)_{Si} // (11\bar{2}4)_{Al_2O_3}$. These have been summarized

by Manasevit et al (1968), who also showed that multiple relationships, e.g. for $(11\bar{2}0)_{Al_2O_3}$, are produced when a small change in sapphire orientation would lead to special stability for one or other of the Si overgrowths. Directional relationships associated with these combinations have also been determined. The $(111)_{Si}$ // $(0001)_{Al_2O_3}$ combination is especially complex since it appears that both $[1\bar{1}0]_{Si}$ // $[11\bar{2}0]_{Al_2O_3}$ and $[11\bar{2}]_{Si}$ // $[11\bar{2}0]_{Al_2O_3}$ can occur (Chu et al, 1965). This is in agreement with the results of Yasuda and Ohmura (1969) who observed rotationally twinned initial Si growth centres of both orientations on (0001) sapphire, although those with $[1\bar{1}0]_{Si}$ // $[11\bar{2}0]_{Si}$ were preferred for subsequent film growth. The factors determining the observed orientation relationships have been investigated by Nolder and Cadoff (1965), who proposed that Si may substitute for Al in surface sites with the formation of Si-O bonds. The propagation of substrate symmetry elements into the Si film has also been shown to be a useful concept by Porter and Wolfson (1965) and Bicknell et al (1966). Using this idea, together with considerations of the relative density of Si and Al atoms at the interface, Larssen (1966) was able to theoretically derive several of the experimentally observed relationships.

In assessing the electrical properties of Si films on sapphire substrates, the majority carrier mobility has often been used as an indication of quality, since this is highly dependent upon film crystallinity. However, a major complication in the growth is autodoping of the Si films with Al vapour-transported from the substrate as Al_2O. It has been proposed that this may be produced either by reaction of the substrate with incident Si (Bicknell et al, 1966), or specifically for vapour deposition, by reaction of the substrate with H_2 (Manasevit et al, 1965). SiH_4 pyrolysis using helium carrier gas has been employed by e.g. Mercier (1970) to suppress the latter reaction.

For p-type (100) Si films, vapour deposited on H_2-fired ($1\bar{1}02$) sapphire substrates and with carrier concentrations between 1 and 5×10^{16} cm^{-3}, hole mobilities may vary from 50 $cm^2V^{-1}sec^{-1}$ in a 0.5μ thick film (Gottlieb et al, 1971) up to bulk Si mobilities around 300 $cm^2V^{-1}sec^{-1}$ in a 6μ thick film (Dumin and Robinson, 1968). The properties of the thinnest films are especially dependent upon deposition conditions, and by the use of an unusually high growth rate, Dumin et al (1970) have achieved a hole mobility of 100 $cm^2V^{-1}sec^{-1}$ in a 0.15μ thick film. While the hole mobility is generally little affected by p-type film heat treatment after deposition, the electron mobility of n-type films may be nearly doubled by e.g. thermal oxidation. For instance, Dumin and Robinson (1968) have found electron mobilities in excess of 550 $cm^2V^{-1}sec^{-1}$ for 2μ thick thermally oxidized (100) Si films, with electron concentrations from 10^{16} to 10^{17} cm^{-3}. Chang (1971) has recently measured near bulk Si hole and electron mobilities in 3-7μ thick Si films grown by vacuum sublimation.

Up to the present time, most of the devices fabricated in Si films on sapphire substrates have been of the junction diode and field-effect types. For example, Burns and Scott (1969) fabricated complementary MOS integrated circuits in 1 to 1.5μ thick Si, which exhibited signal delays of <1 nsec per gate. p-n Junction diodes were also prepared in high yield arrays by Miller (1967). Although bipolar transistors with both planar and vertical junctions have been fabricated, success has been somewhat limited, due to low minority carrier lifetimes of $\sim$ 1 nsec (Hart et al, 1967). These workers have attributed this to the high density of film crystallographic defects. However, recently Mueller (1970) and Dumin (1970) have reported that such lifetimes may be increased by an order of magnitude, by the use of impurity gettering techniques.

5.2.2) Silicon on Spinel

The use of spinel (in stoichiometric form $MgAl_2O_4$) as a substrate material has received less investigation than the use of sapphire, because spinel of suitable crystalline quality has only recently been commercially available. Nevertheless, spinel possesses several potential advantages over sapphire.

It has a cubic lattice, giving the possibility of a unique Si epitaxial relationship. Also, if a matching scheme superimposing three unit cells of Si over two unit cells of the non-stoichiometric spinel $MgO \cdot 3.3Al_2O_3$ is used, Manasevit and Forbes (1966) pointed out that the mismatch is only 1.9%, while it is even less for the stoichiometric product (the Si/sapphire mismatch depends upon orientation, and is generally much greater). Also Robinson and Dumin (1968) have found that Si grown on spinel is contaminated an order of magnitude less with Al from the substrate, as compared with Si on sapphire. Spinel substrates grown by flame fusion or flux growth techniques may be polished by high temperature H_2 etching to give a very high quality surface finish (Hart et al, 1967), although other procedures have been used. However, Cullen et al (1970) found that the H_2 treatment degrades the surface of Czochralski grown spinel substrates, and proposed that this may be due to variations in the stoichiometry of the material.

Si grown on $MgO \cdot 3.3Al_2O_3$ was first reported by Manasevit and Forbes (1965, 1966), who used both $SiCl_4$ and SiH_4 decomposition techniques. Although their spinel was of poor quality, they established the epitaxial relationships $(111)_{Si} // (111)_{spinel}$, $(110)_{Si} // (110)_{spinel}$, $(100)_{Si} // (100)_{spinel}$. Concurrent work was also carried out by Seiter and Zaminer (1965) and Seiter et al (1965). The structural perfection of such films was studied by Schlötterer and Zaminer (1966), who thinned epitaxial films using the ion beam machining technique and examined them in the TEM. They found that the

Si grown on (111) and (100) spinel contained many dislocations and stacking faults, together with various types of twin defects.

For (111) p-type Si (hole concentration between 1 and 5×10^{16} cm^{-3}) grown on flame fusion spinel, Cullen et al (1969) reported that the hole mobility increased rapidly from 110 $cm^2V^{-1}sec^{-1}$ at a Si thickness of 0.6μ up to 400 $cm^2V^{-1}sec^{-1}$ for a Si thickness of 3.1μ. This high hole mobility was thought to be due to strain effects in the Si, as predicted by Schlötterer (1968). Electron mobilities as high as $\sim$ 800 $cm^2V^{-1}sec^{-1}$ have been observed by Gottlieb et al (see Cullen, 1971).

MOS devices have been fabricated in Si films on spinel by Schlötterer (1968) with very good results. The determination of minority carrier lifetimes as great as 40 nsec in a 4μ gettered Si film by Cullen et al (1969) is especially promising for bipolar transistor applications.

5.2.3) Silicon on Other Single Crystal Insulators

The growth of Si films on quartz substrates has received comparatively little attention, partly due to the large difference in their thermal expansion coefficients. Bicknell et al (1964) grew Si films on mechanically polished quartz by H_2 reduction of $SiHCl_3$, and used RHEED to determine the epitaxial relationship $(001)_{Si} // (0001)_{quartz}$ and $[010]_{Si} // [01\bar{1}0]_{quartz}$. This leads to the possibility of three different types of Si rotational twin. While changes in Si deposition rate and film thickness appeared to have little effect upon the degree of film crystallinity, an increase in deposition temperature from 1000°C up to 1250°C apparently yielded an improvement. The Si films were studied in the TEM using both Pt/carbon replicas, and films stripped from their substrates. It was observed that Si growth centres were formed during the early stages of the growth, and that the films contained a high density of micro-twins and possibly stacking faults. The defect density increased

with film thickness. A speculative model for the interfacial bonding was also proposed by these workers.

Tallman et al (1966) studied the growth of Si on both the 'A' and 'B' faces of (0001) α-SiC, at between 1010 and 1270°C, using deposition by SiH_4 pyrolysis. Growth of the best crystalline quality occurred on the 'B' face (i.e. the carbon face (Brack, 1965)) although there was substantial rotational twinning. Two epitaxial relationships were found to be possible, both $(111)_{Si}$ // $(0001)_{SiC}$ with $[1\bar{1}0]_{Si}$ // $[01\bar{1}0]_{SiC}$ and $(110)_{Si}$ // $(0001)_{SiC}$ with again $[1\bar{1}0]_{Si}$ // $[01\bar{1}0]_{SiC}$. Continuous films contained many crystallographic defects, although active devices formed in these films grown on 'B' faces showed that the Si had reasonable electrical characteristics.

Epitaxial Si films have been grown on beryllium oxide (BeO) crystals by Manasevit et al (1966), since this substrate material has a potentially useful high thermal conductivity. They used both SiH_4 and $SiCl_4$ vapour deposition techniques, and determined various epitaxial relationships including $(111)_{Si}$ // $(0001)_{BeO}$ with $[1\bar{1}0]_{Si}$ // $[11\bar{2}0]_{BeO}$. The use of other single crystal insulating substrates for Si film growth has also been studied, e.g. thorium dioxide (ThO_2), zirconium sulphate ($ZrSO_4$) and lanthanum aluminate ($LaAlO_3$) by Chu et al (1965), and calcium fluoride (CaF_2) by Via and Thun (1962). Various attempts have been made to grow single crystal Si films on polycrystalline or amorphous insulating substrates, and these are detailed by Filby and Nielsen (1967).

5.3) Experimental Details

Single crystals of electrically insulating substrate materials were heated in UHV to the required deposition temperatures, by both conduction and radiation absorption, on a polished Si bar. The sapphire substrates, which were in the form of flat platelets, were heated directly on a flat

surface, while diamond and β-SiC substrates, which were in the form of 'three-dimensional' crystals, were heated in small depressions in the surface of the Si bar. The temperature of this bar, which was measured pyrometrically in the usual way, was also taken to be the temperature of the substrates. While it is appreciated that this may be inaccurate by a few tens of ^{o}C, this type of measurement is considered to be adequate for the present purposes, The substrate temperatures obtained are expected to be at least as accurate as those measured in different systems by other workers. For example, the sapphire substrates used by Yasuda and Ohmura (1969) were in contact with only another insulator (MgO), the temperature of which was apparently measured using a thermocouple. This procedure would seem to be unwise, since the real temperature of the sapphire could have been substantially different.

For these experiments, the Si heating bar was raised up above the position used for other depositions discussed in previous chapters, and was situated only 2 - 3 mm below the retractable shutter (section 1.2.4). Therefore, instead of casting a diffuse shadow over the substrates, retracting the shutter enabled several separate substrates, loaded together on to the same heating bar, to be fully exposed to the source in a sequential manner. In this way, it was possible to deposit Si films of different thicknesses during the same experimental run.

After deposition, sapphire substrates with their Si films were removed from the vacuum chamber, and cleaved into pieces with mm dimensions. These were then ivdividually sandwiched between two coarse TEM Cu grids, and the assembly was then thinned from the substrate side using the ion beam method (section 1.5.1). This procedure often required several hours to achieve perforation of the $\sim 2\mu$ thick sapphire in a few areas, beneath the Si film. The thinned regions were of quite uniform thickness where they were situated between the microscope grid bars, but the sapphire

remained at its original thickness where it had been shielded by these bars. This gave useful strength to the substrate foil which, together with its supporting grids, was ready for insertion into the TEM, after ~30 Å of carbon had been vacuum deposited on to it to minimize electrical charging problems.

Thinning of diamond substrates for TEM film examination produced special problems, resulting from the great hardness of this material in combination with the fact that some substrates were initially 0.75 mm thick. Such substrates were first stuck film downwards on to optically flat glass discs, using Tixo K20 adhesive, which gives a cyanomethacrylate polymer. Next the diamond substrates were ground down to a thickness of ~ 0.25 mm, using coarse (90μ) diamond grinding compound on a cast iron lapping plate. After this, successively finer grades of grinding compound were used (finishing with 6μ) to reduce the substrate thickness to ~ 0.025 mm. In the final stages, the specimen, on its glass disc, was held accurately parallel to the lapping plate using a suitable jig, since any misalignment at this point could obviously have had serious consequences. After the grinding was completed, the specimen was removed from its support by dissolution of the adhesive with hot dimethylformamide. The diamond was next mounted over a small hole in a non-magnetic stainless steel washer using another adhesive (e.g. collodion in amyl acetate), and thinned through towards the Si film from the substrate side using the ion beam method. Thinning rates were extremely low, but ~ 30 hrs of bombardment with a 150μA beam of 10 kV argon ions reduced the thickness enough to give a certain amount of electron transparency.

At present, partial success has been achieved using this diamond thinning procedure. Transmission has been obtained using the 1MeV TEM, although there were certain instrumental difficulties.

5.4) Results - Silicon on Sapphire

5.4.1) The Sapphire Substrates

The substrates were single crystal sapphire platelets, grown by vapour transport and of (0001) surface orientation. They were usually 0.5 - 3μ in thickness and had areas of up to $\sim$ 1 cm^2. The surfaces of some platelets were aluminized for examination with a Tolansky, multiple beam, optical interferometer, and this showed that they were step-free to the limits of resolution (i.e. no steps were present with a height of $\gtrsim$ 10 Å). TED studies of the thinner as-received substrates, with no Si deposit, showed that they gave sharp Kikuchi bands, indicating high crystallographic perfection. After such substrates had been thinned by the ion beam method, TEM examination confirmed this conclusion and showed that the platelets contained very few crystallographic defects. Occasional included particles were virtually the only features ever observed.

5.4.2) Silicon Films Grown at 900°C

When substrates with films deposited on one side were cooled from the deposition temperature, they gradually bent due to the difference between the thermal coefficients of expansion of Si and sapphire. The extent of the bending depended upon the film/substrate relative thicknesses. When a 1μ thick Si film was deposited upon a 0.5μ thick substrate, cooling induced them to roll up into a cylinder with a radius of curvature of $\lesssim$ 1 mm.

At an early stage of film growth TEM studies showed that separate Si growth centres were present. For a film deposited at 0.5 Å sec^{-1} up to a mean thickness of only $\sim$ 220 Å, the centres had lateral dimensions ranging upwards from a few hundred Å. This indicates that initial growth had been by nucleation, and that by the time of observation considerable coalescence of centres had taken place. Fig 5.1 is a dark field transmission electron micrograph showing such a film and taken using both

a $2\bar{2}0$ type Si reflection and $11\bar{2}0$ type sapphire reflection, which were strongly excited. The larger centres have a number density in the region of 10^9 cm^{-2}. Also, the substrate surface both between and beneath the centres exhibits a fine spotted structure, and this is considered to be evidence for a chemical reaction which occurred between the sapphire and deposited Si.

Since there is a large crystallographic misfit between the Si and the sapphire, the interfacial region between the two was carefully studied. However, in contradistinction to the Ge/Si system (chapter 4) where many misfit dislocations were found at the interface, in the present system no definite evidence was obtained for the presence of such strain relieving defects. Nevertheless, under certain conditions, weak periodic contrasts were observed in the TEM, and some of ~ 40 Å spacing are faintly visible in fig 5.1. A complicating feature is that these contrasts often extend to regions beyond the growth centres, where presumably there is no Si. However contrasts of ~ 70 Å spacing are shown in fig 5.2, and it is possible that these may be Moiré fringes. Also very faintly visible are fine and slightly irregular periodic contrasts of only ~ 30 Å spacing.

In TED studies, diffraction patterns were simultaneously obtained from the overlapping Si and sapphire. Fig 5.3 shows such a pattern obtained from a region similar to that of fig 5.1. The principal diffraction spots are labelled, and it should be noted that many spots are produced by double diffraction effects. The information provided by fig 5.3 is sufficient to confirm directly that the epitaxial relationships are $(111)_{Si} // (0001)_{Al_2O_3}$ together with $[1\bar{1}0]_{Si} // [11\bar{2}0]_{Al_2O_3}$.

Further TEM studies revealed that the centres shown in fig 5.1 were composed of essentially equal proportions of two 60° rotational twins, each with $[1\bar{1}0]_{Si} // [11\bar{2}0]_{Al_2O_3}$. In order to distinguish these twins in the microscope, it was necessary to employ Bragg reflections with $\underline{g}$ vectors not

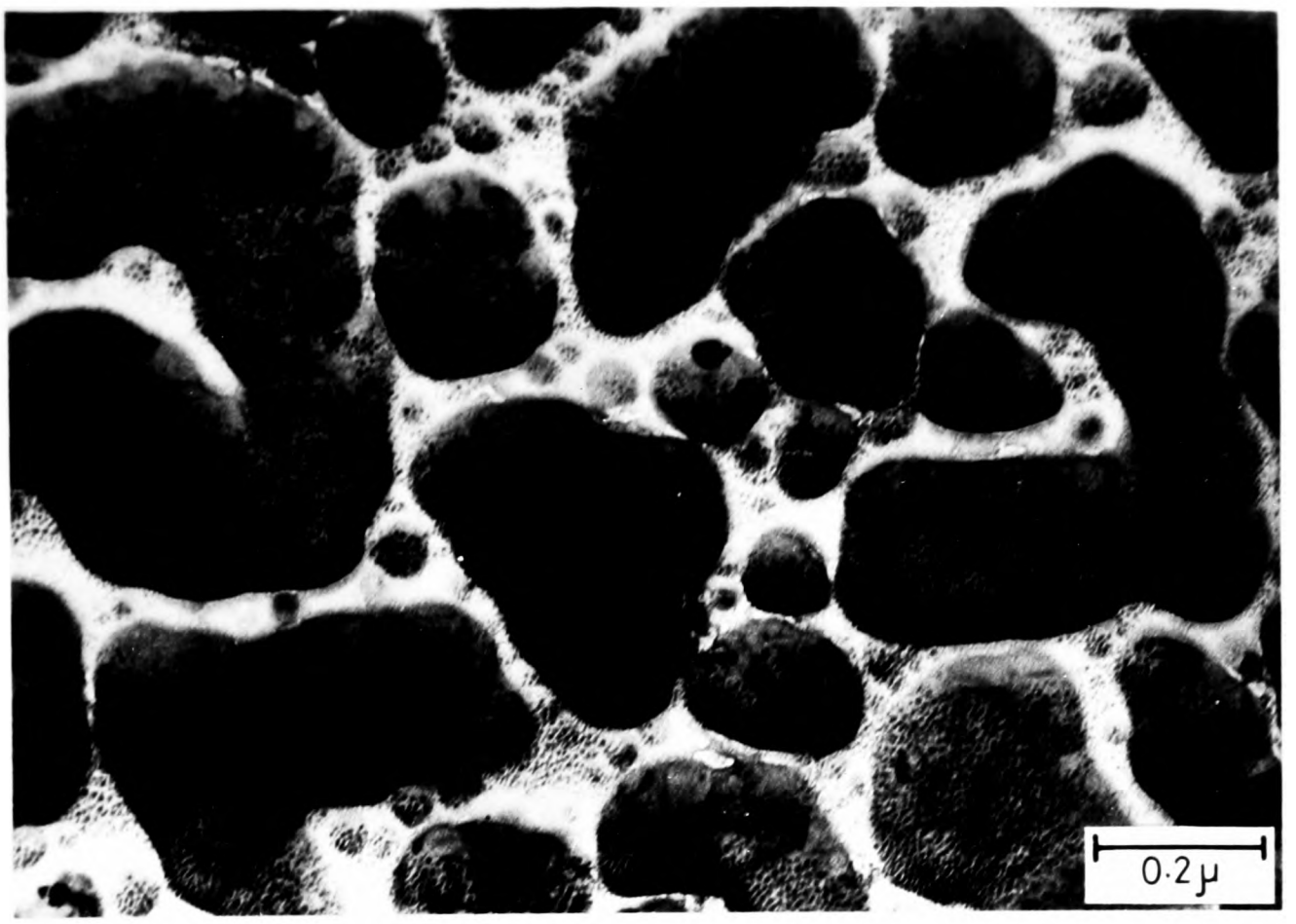
parallel to the foil plane, such that rotationally displaced inclined Si planes were involved. Accordingly, fig 5.4a shows a high resolution pair of bright-field micrographs, taken from the same specimen area, with adjacent, 60° displaced, $11\bar{1}$ type twin reflections. Fig 5.4b is a diagram showing the usual Si single crystal Kikuchi bands around a [111] pole, together with a pattern containing extra superimposed $11\bar{1}$ type bands, which would be produced in the presence of 60° rotational twins. The various regions composed of the two different twins in fig 5.4a can clearly be seen, and the dark regions in each case are those which actively diffracted intensity out of the main electron beam. Detailed observations showed that the smallest centres were composed exclusively of either one of the two twins. This indicates that the initial film growth was subject to a double positioning of the nuclei (Dickson and Pashley, 1962), that is, the initial nuclei occurred in either of two equivalent, though non-identical, rotational orientations. Also, although larger growth centres, formed by coalescence, did not seem to exhibit pronounced geometrical shapes, where they were bounded by straight edges, these were often parallel to $\langle 1\bar{1}0 \rangle$ type directions in the Si.

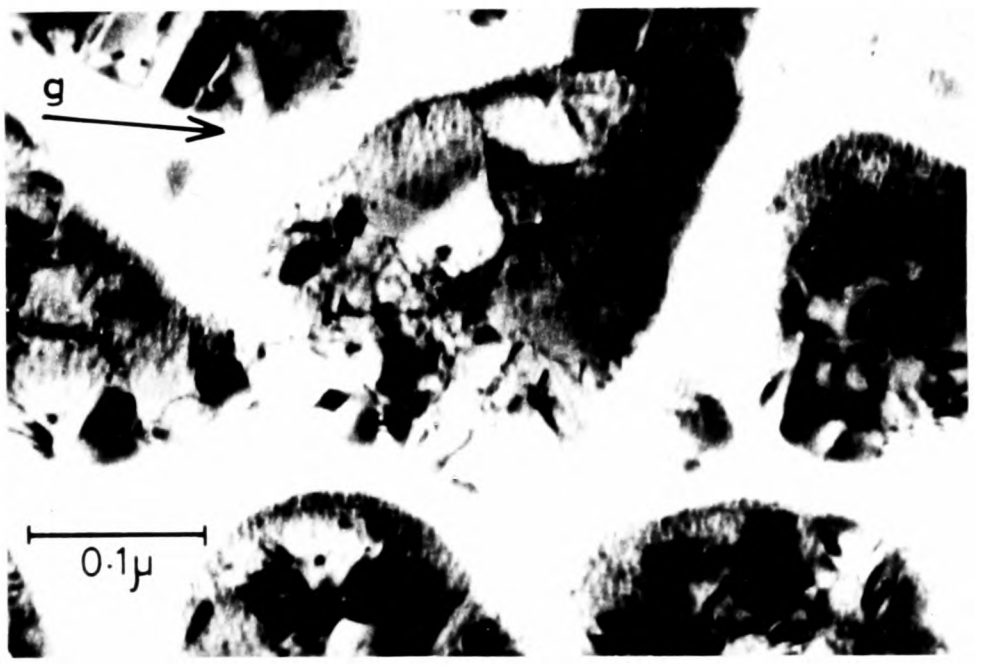
When a Si film was deposited at a substrate temperature of 900°C and at 0.5 Å sec^{-1} up to a thickness of $\sim 0.11\mu$, coalescence of growth centres had proceeded to give a film with a channelled structure. Fig 5.5 shows such a film, and the dark/bright striations visible in some regions indicate that inclined microtwins were the prevalent form of defect, apart from the 60° rotational twins. TED showed that the film contained crystallites with a spread of orientations of $\sim \pm 5^{\circ}$ around the preferred relationship $[1\bar{1}0]_{Si} // [11\bar{2}0]_{Al_2O_3}$. When Si deposition was carried out to give a film with a mean thickness of $\sim 0.33\mu$, the film was found to have a more coarse channelled structure (fig 5.6). This indicated that it would be necessary to deposit substantially more Si, in order to obtain uniform

Fig 5.1 Si growth centres on sapphire substrate. Note mottled background structure and that fringes are faintly visible in some regions. (Transmission electron micrograph, dark-field using both $2\bar{2}0$ (Si) and $11\bar{2}0$ (sapphire) reflections)

Fig 5.2 Si growth centres on sapphire substrate. Note fringes perpendicular to $\underline{g}$ vectors of operating reflections. (Transmission electron micrograph, same conditions as fig 5.1)

Fig 5.3 Typical transmission electron diffraction pattern obtained from a region such as that in fig 5.1. Shows both Si ($2\bar{2}0$ type) and sapphire ($11\bar{2}0$ type) spots, together with spots of the type labelled A which were produced by double diffraction effects.


0·2μ


g
0·1μ

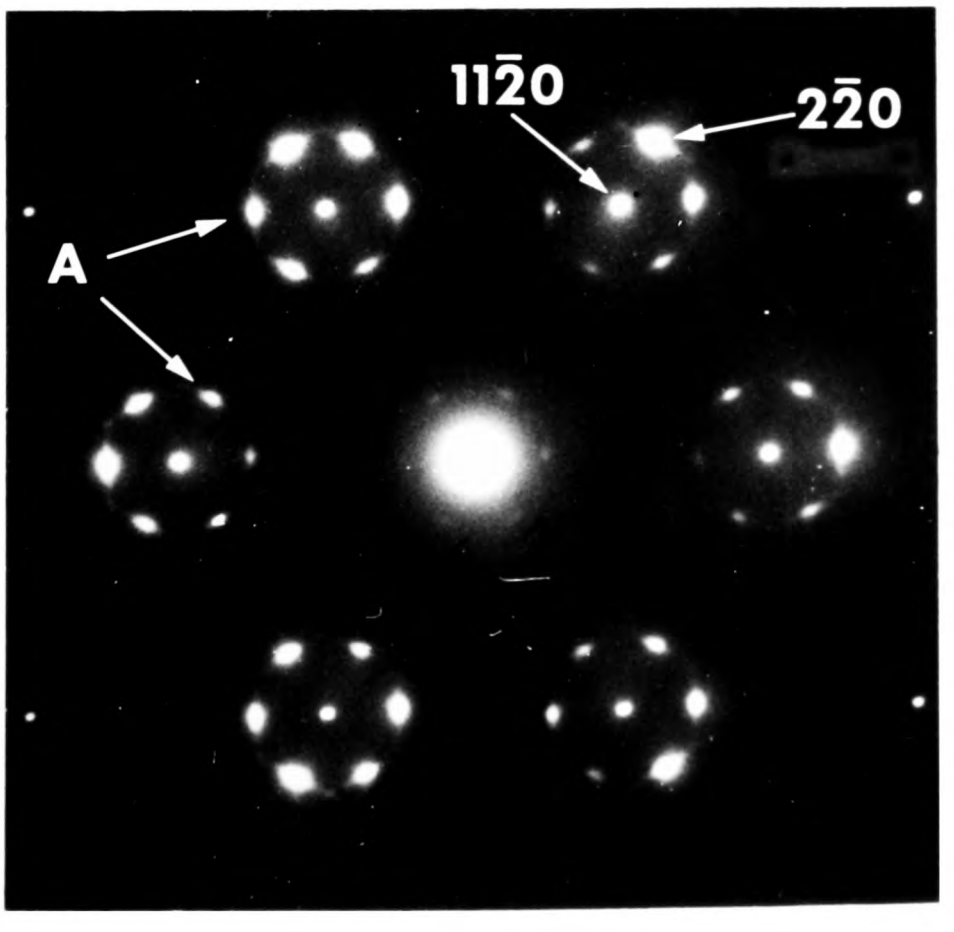
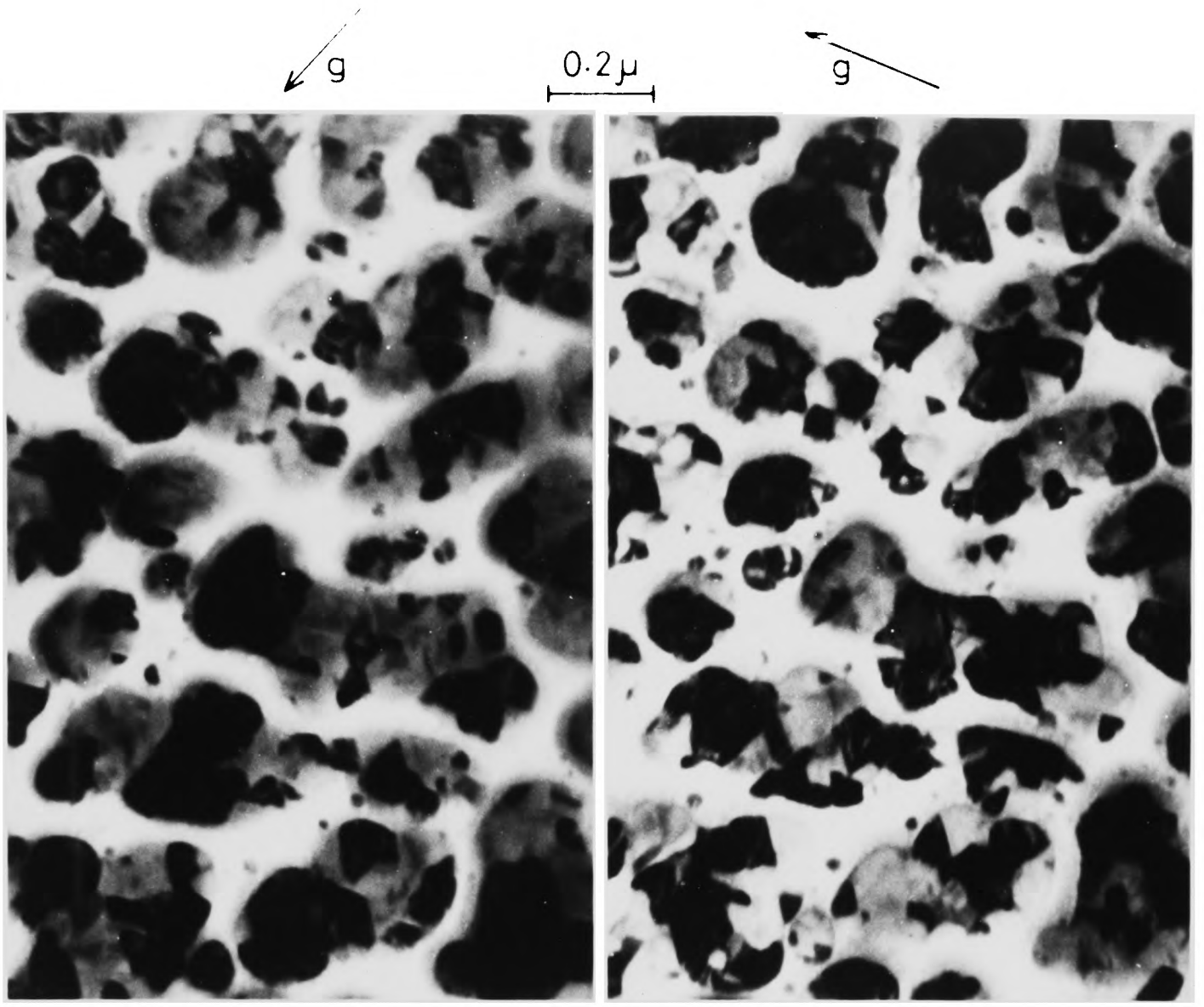
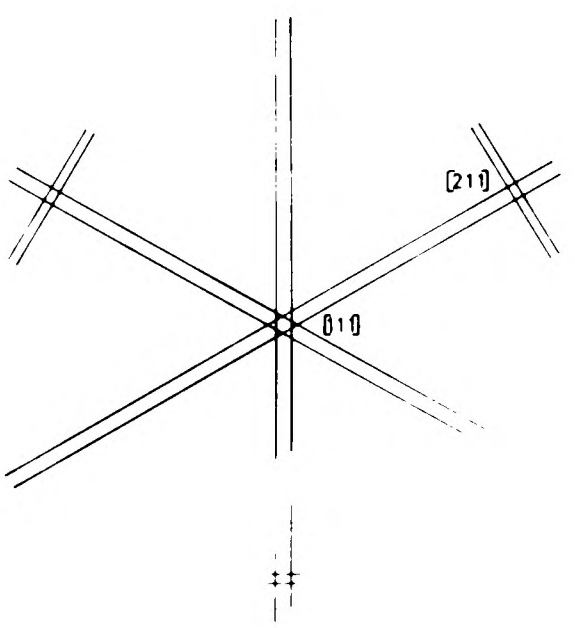

11$\bar{2}$0
2$\bar{2}$0
A

Fig 5.4a Si growth centres composed of two 60° rotational twins which give dissimilar contrast in the two micrographs. (Transmission electron micrographs of same specimen area, bright-field with different operating $11\bar{1}$ type twin reflections)

Fig 5.4b Diagrams illustrating the relationship between the TED patterns of 60° rotational Si twins A and B.


g
0·2μ
g


SINGLE CRYSTAL
[2 1 1]
[0 1 1]

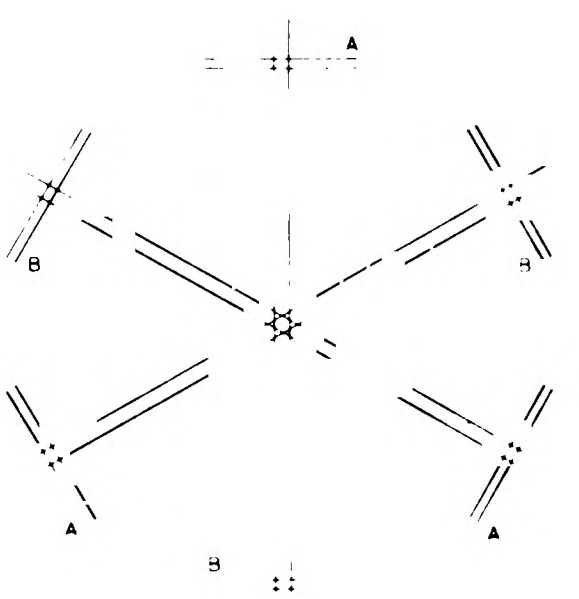
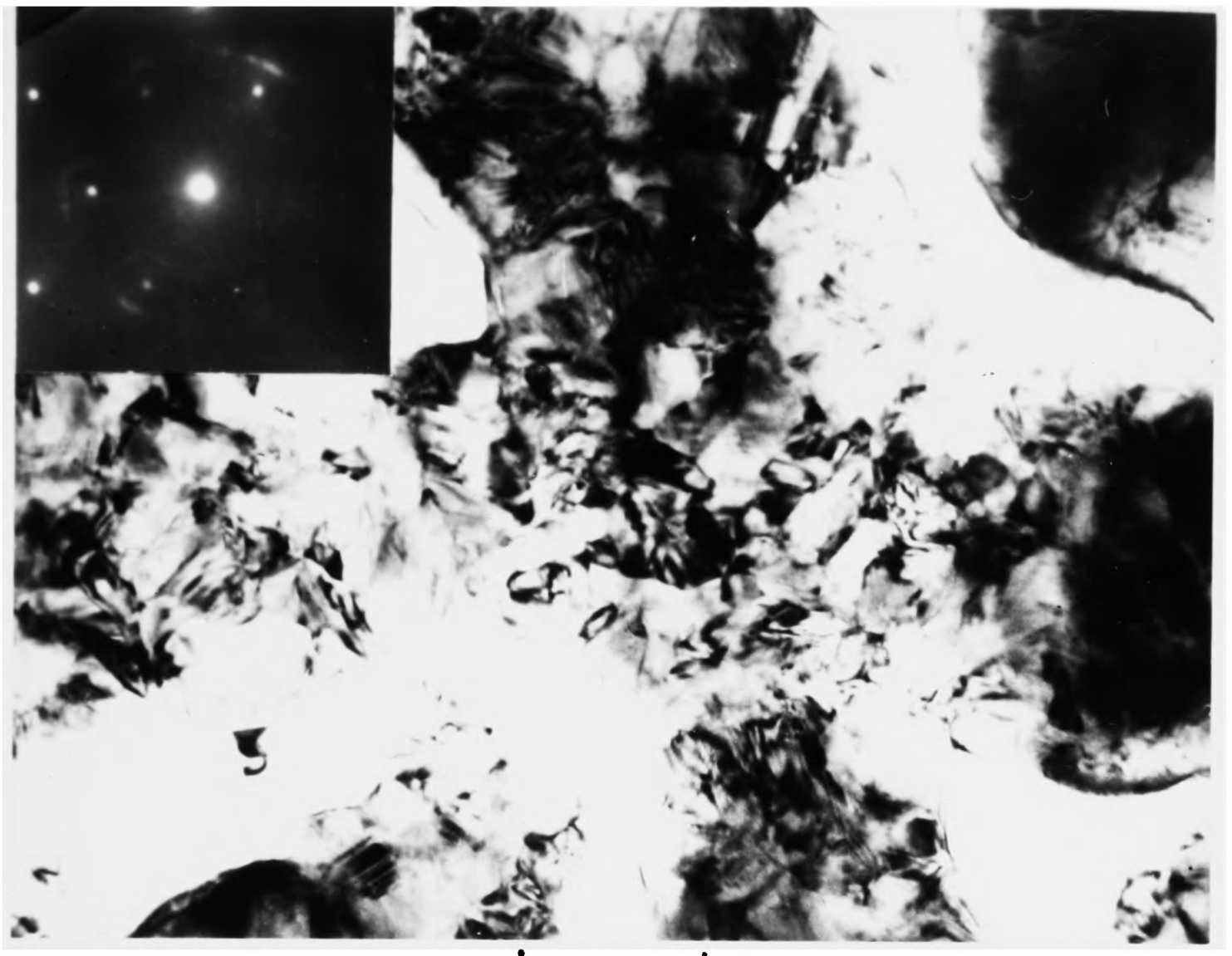

60° TWINS (A,B)
A
B
B
A
A
B

Fig 5.5 Si film ~0.11μ in thickness grown at 0.5 Å sec^{-1}; sapphire substrate temperature 900°C. TED pattern shows rotational spread in Si orientations. (Transmission electron micrograph, bright-field)

Fig 5.6 Si film ~0.33μ in thickness grown at 0.5 Å sec^{-1}; sapphire substrate temperature 900°C. TED pattern shows polycrystal rings. (Transmission electron micrograph, bright-field)


0·2μ

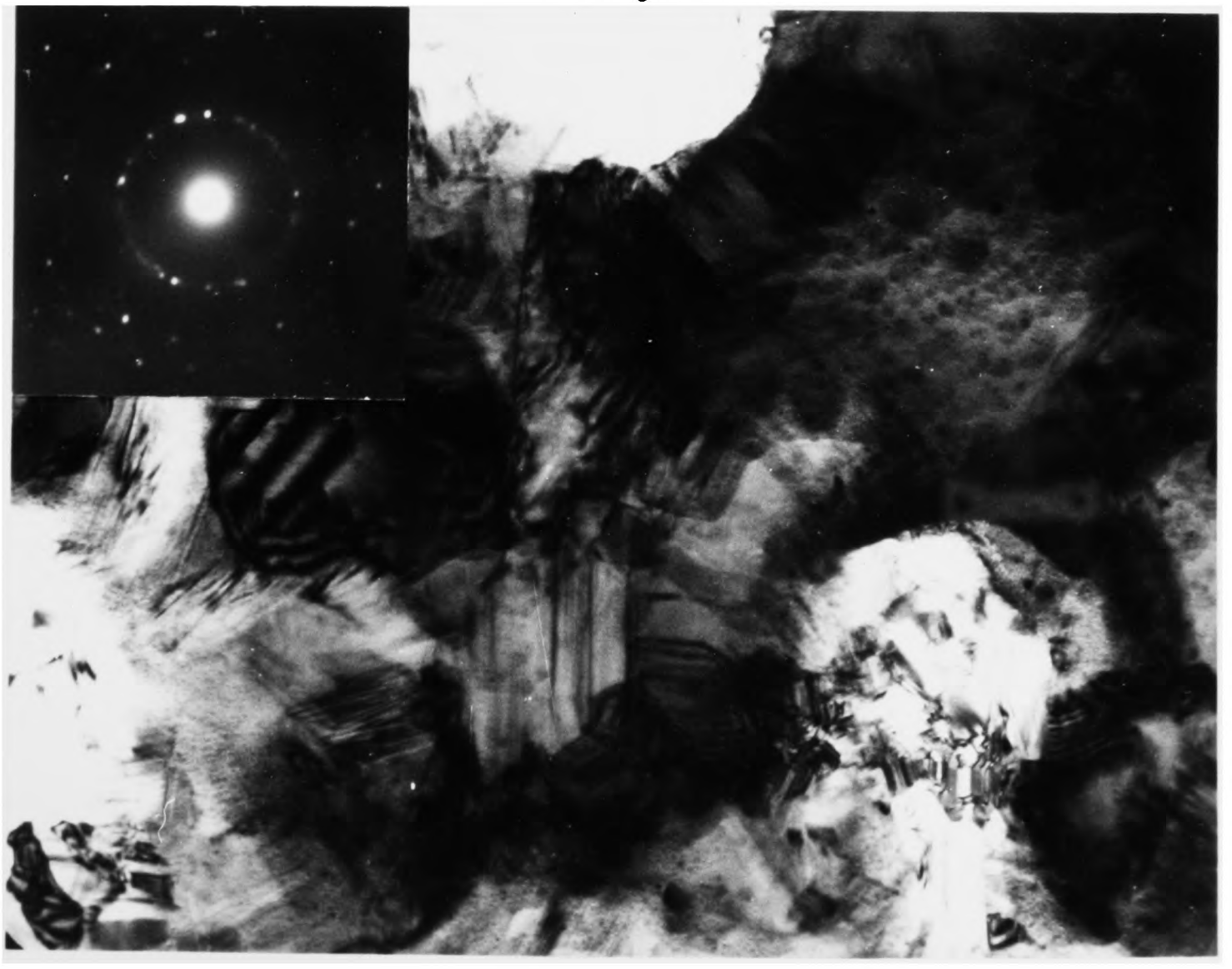
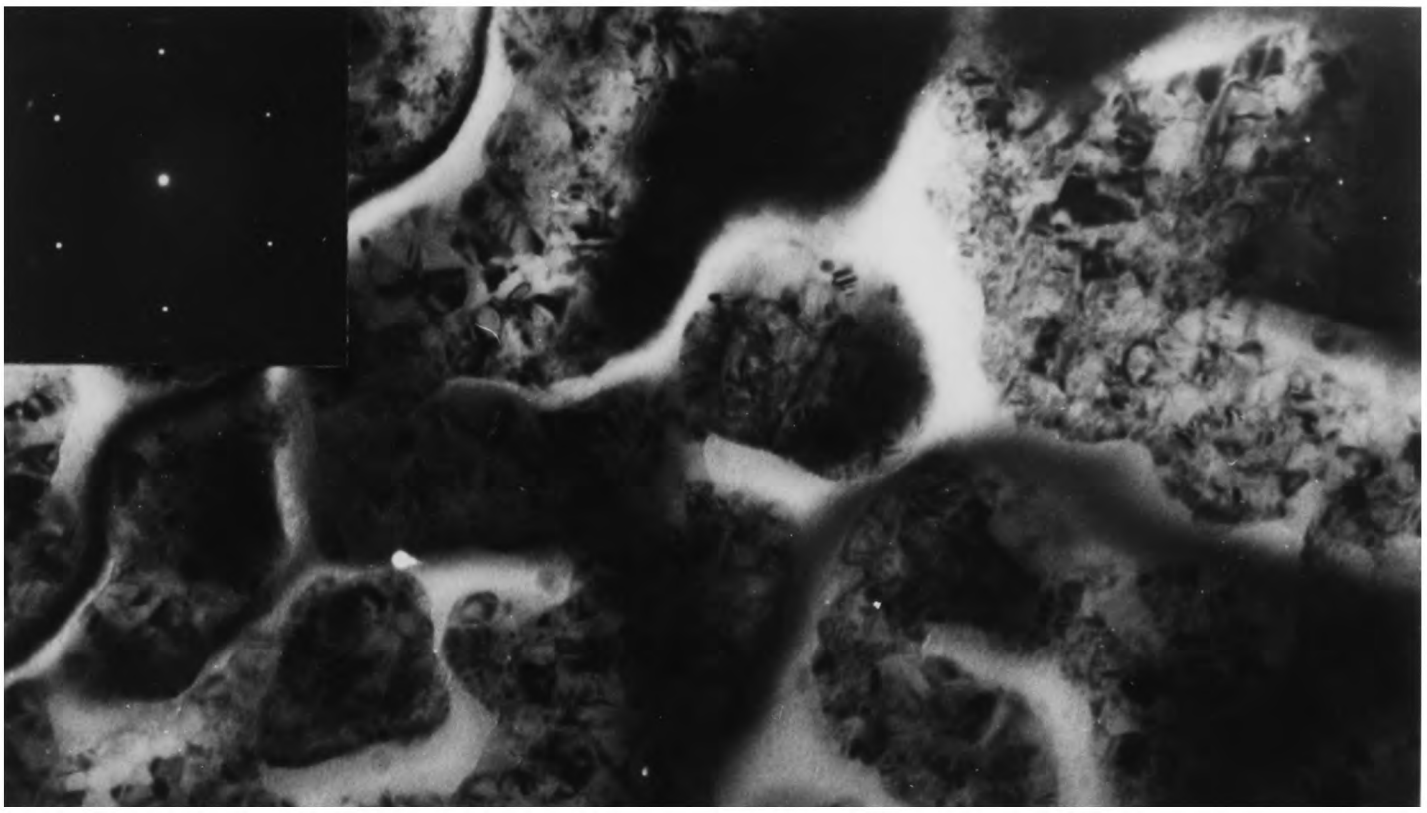
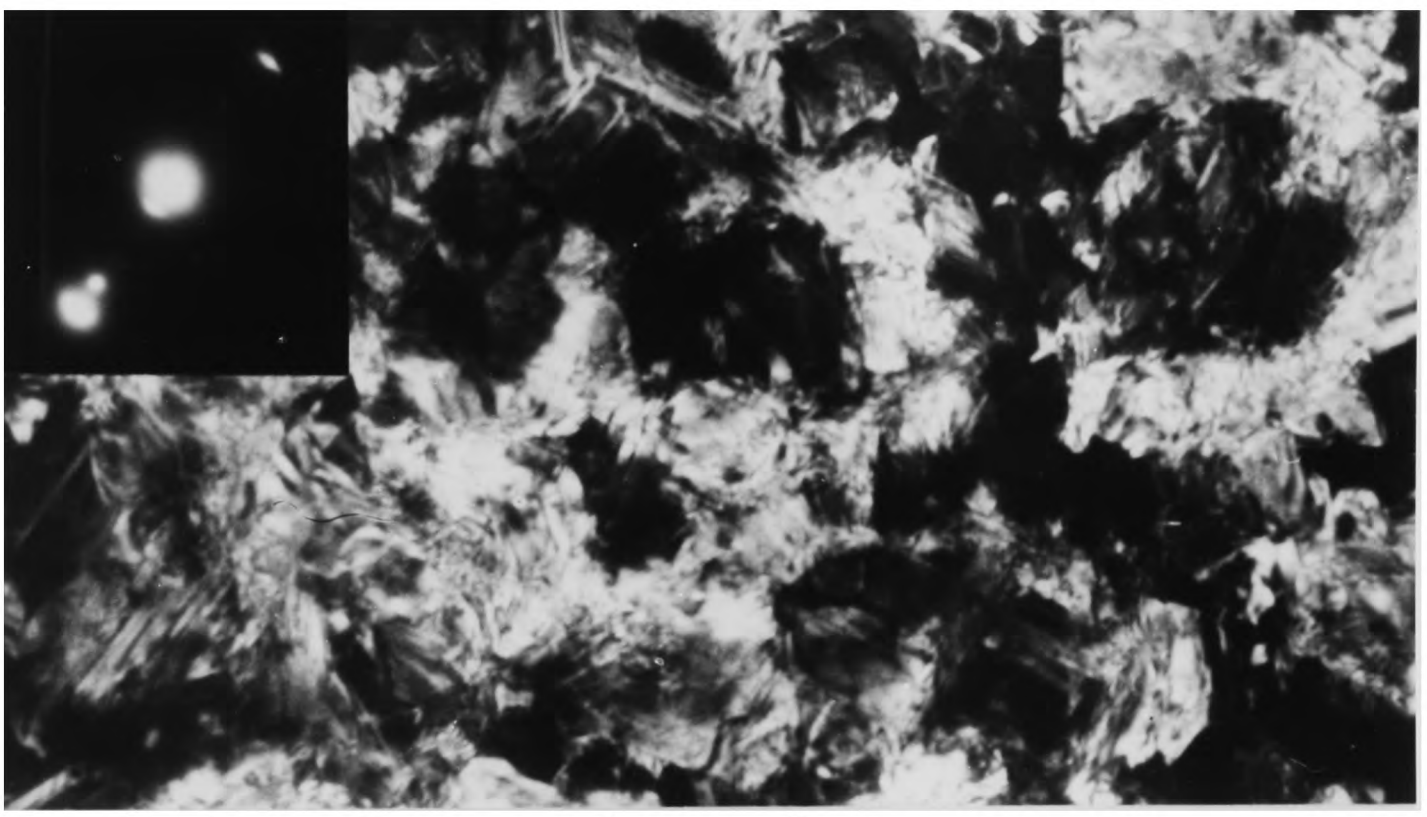


Fig 5.7 Si film ~ 300 Å in thicknes grown at 20 Å sec^{-1}; sapphire substrate temperature 900°C. Film contained many defects and small misorientations. (Transmission electron micrograph, bright-field)

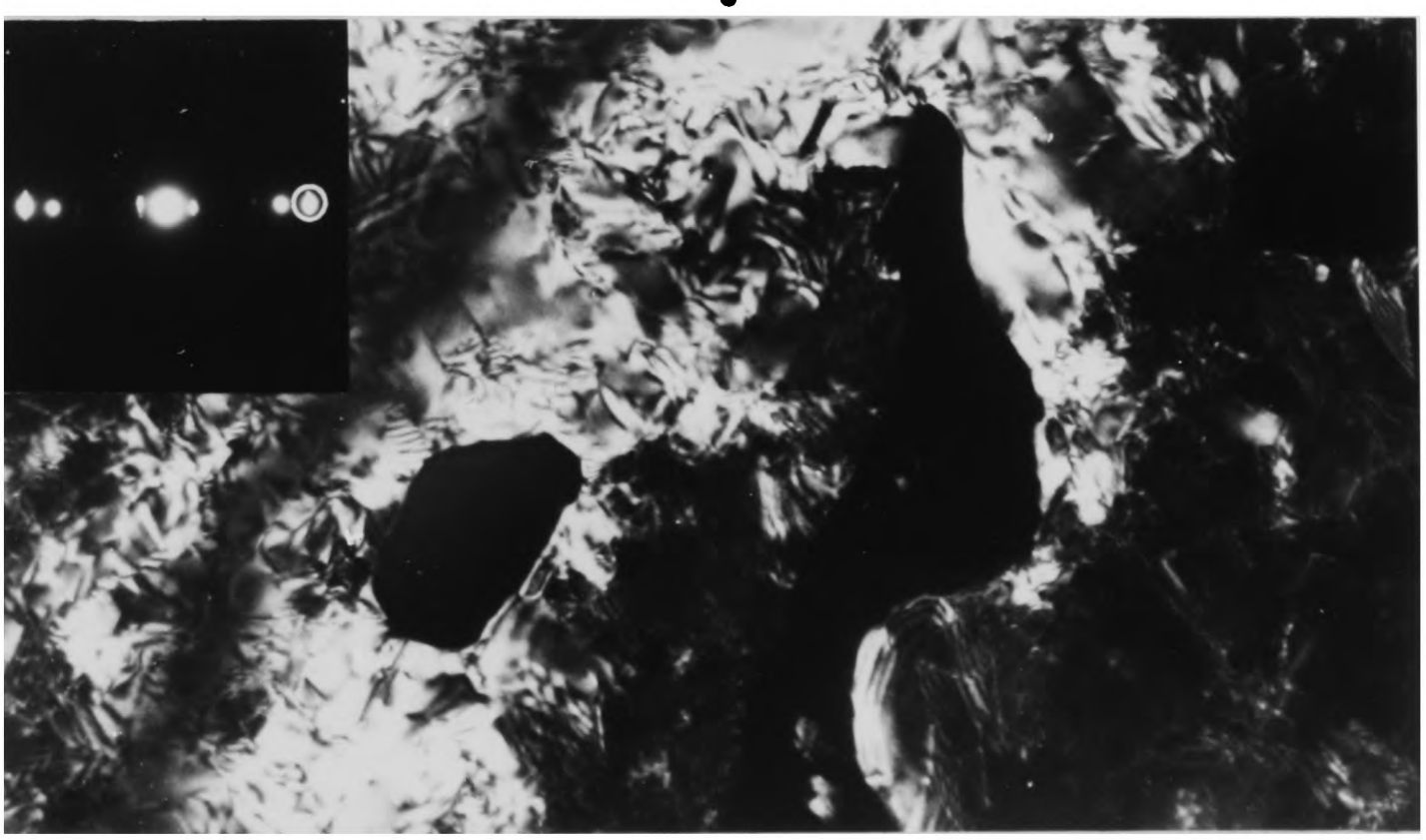
Fig 5.8 Si film ~ 0.15μ in thickness grown at 20 Å sec^{-1}; sapphire substrate temperature 900°C. Shows fewer channels than film in fig 5.7, though many defects present with small misorientations. (Transmission electron micrograph, bright-field)

Fig 5.9 Si film ~ 600 Å in thickness grown at 15 Å sec^{-1}; sapphire substrate temperature 1100°C. High density of planar defects. (Transmission electron micrograph, dark-field, Si $2\bar{2}0$ type reflection)





0·2μ



layers. However, TED showed that, at this stage, the film had become substantially polycrystalline, and possible reasons for this will be discussed in section 5.6.1.

Si films were also deposited at a rate of 20 Å sec^{-1}. For a mean deposit thickness of ~ 300 Å, initial growth centres had already apparently overlapped to give a film with a fairly fine channelled structure (fig 5.7). Substantial twinning had taken place, and the film contained a large number of defects.

A mottled background structure was observed, indicating that reaction of the Si with the sapphire substrate had probably taken place. However, this structure exhibited somewhat weaker contrast, compared with films grown at only 0.5 Å sec^{-1}, and therefore, it is likely that the reaction had proceeded to a rather smaller extent. TED showed that there was a small amount of film misorientation ($\sim \pm 5^{o}$) about the preferred relationship given above.

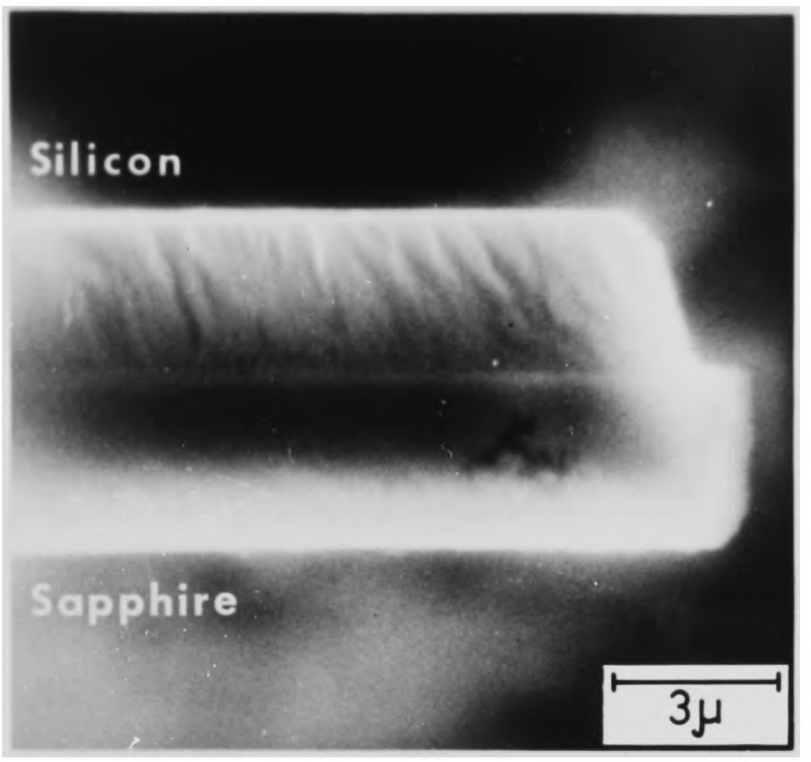
When a Si film was grown at 20 Å sec^{-1} up to a mean thickness of ~ 0.15μ, few channels remained in the deposit and it achieved more uniform coverage of the substrate. However, as shown in fig 5.8, the Si was not single crystal material, but was composed mainly of crystallites, which TED showed to have small rotations about the preferred epitaxial orientations.

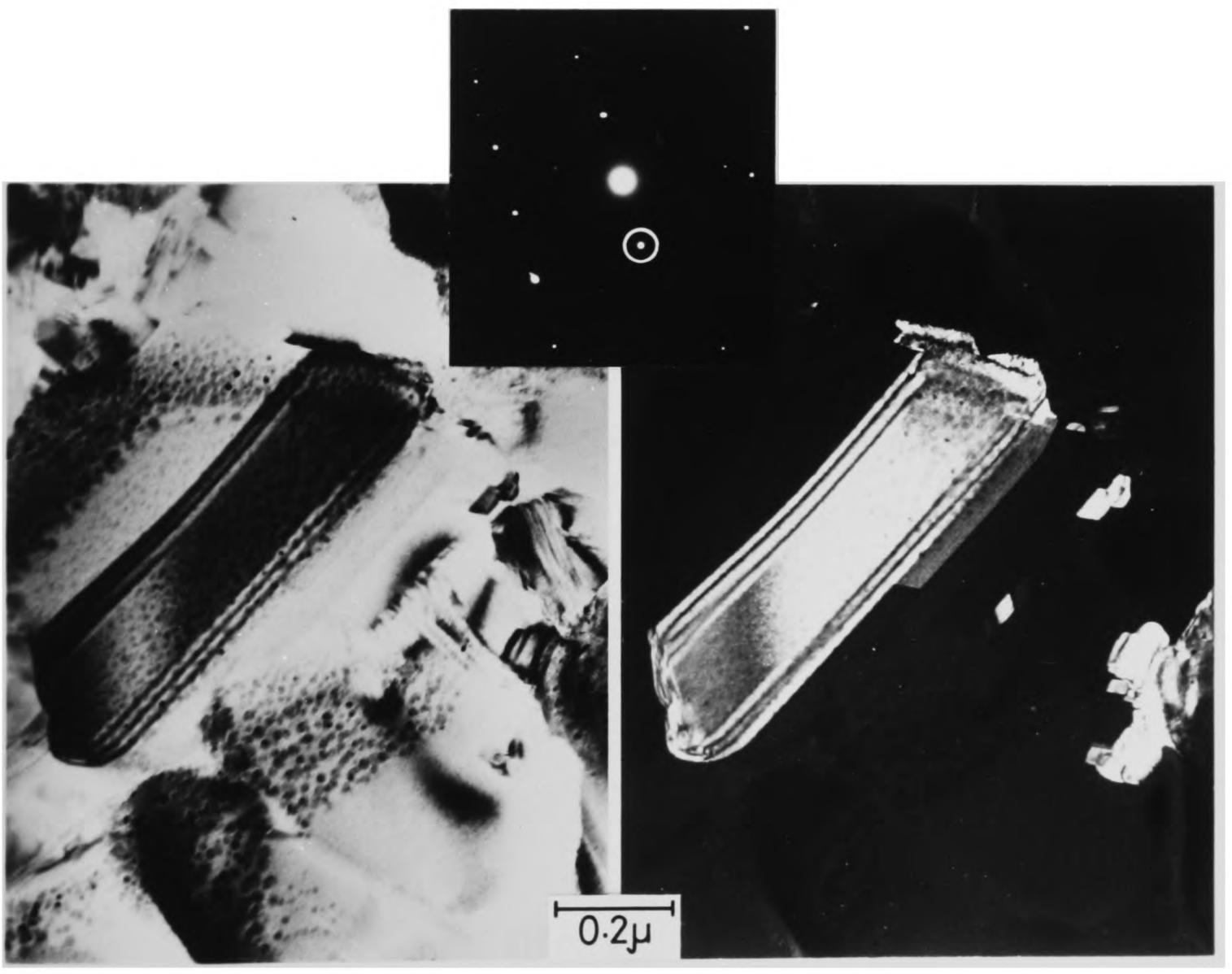
5.4.3) Silicon Films Grown at 1100°C

Si films were grown at a rate of 15 Å sec^{-1}. At a mean thickness of ~ 600 Å, the film covered most of the substrate and only relatively small channels remained. Nevertheless, as shown in fig 5.9, the Si contained an extremely high density of planar defects. These were probably both stacking faults and microtwin lamellae, although it was not always possible to distinguish between them since they would often be expected to give similar

Fig 5.10 Section through Si film ~ 2.9μ in thickness grown at 15 Å sec^{-1}, sapphire substrate temperature 1100°C. Note overall uniformity of film. (Scanning electron micrograph)

Fig 5.11 Similar film to that shown in fig 5.10. Note polycrystalline nature. (Transmission electron micrographs, bright-field (left) and dark-field)


Silicon
Sapphire
3μ


0·2μ

fringe profiles. Single dislocations were also observed. Bright field micrographs provided evidence for Si/sapphire interaction, since a mottled structure, of the type already described, was seen in the interfacial region. TED showed that the Si was present almost exclusively with the preferred epitaxial relationships.

When Si was deposited up to a total thickness of $\sim 2.9\mu$, film uniformity was very good. This was exemplified by SEM examination of a film grown on a sapphire substrate of almost identical thickness, as shown in fig 5.10. A similar film, grown on a thinner substrate, was examined by TEM and found to be substantially polycrystalline. Fig 5.11 gives both bright- and dark-field micrographs from the same specimen area, showing the crystallites present in the film. Some microtwin defects are also visible. Also, occasional narrow channels still penetrated through the Si, although it is not certain whether they extended down to the substrate surface.

5.5) Results - Silicon on Other Insulators

5.5.1) Silicon on Diamond

The substrates used during these experiments consisted of pieces of type IIA diamond with a thickness of 0.25 - 0.75 mm. The surfaces on to which Si was deposited were usually several mm^2 in area, and of (111) orientation prepared by cleavage. This was followed by treatment with boiling concentrated HCl, and then a mixture of 4 parts HNO_3(conc) + 1 part HF (40%) to remove residual mounting compounds, which had held the diamond during the initial cleavage. Final treatment was with boiling Analar methanol, after which the substrate surfaces were examined using the optical microscope. This showed that many very fine cleavage step arrays were present, although there were substantial, apparently flat regions between these steps.

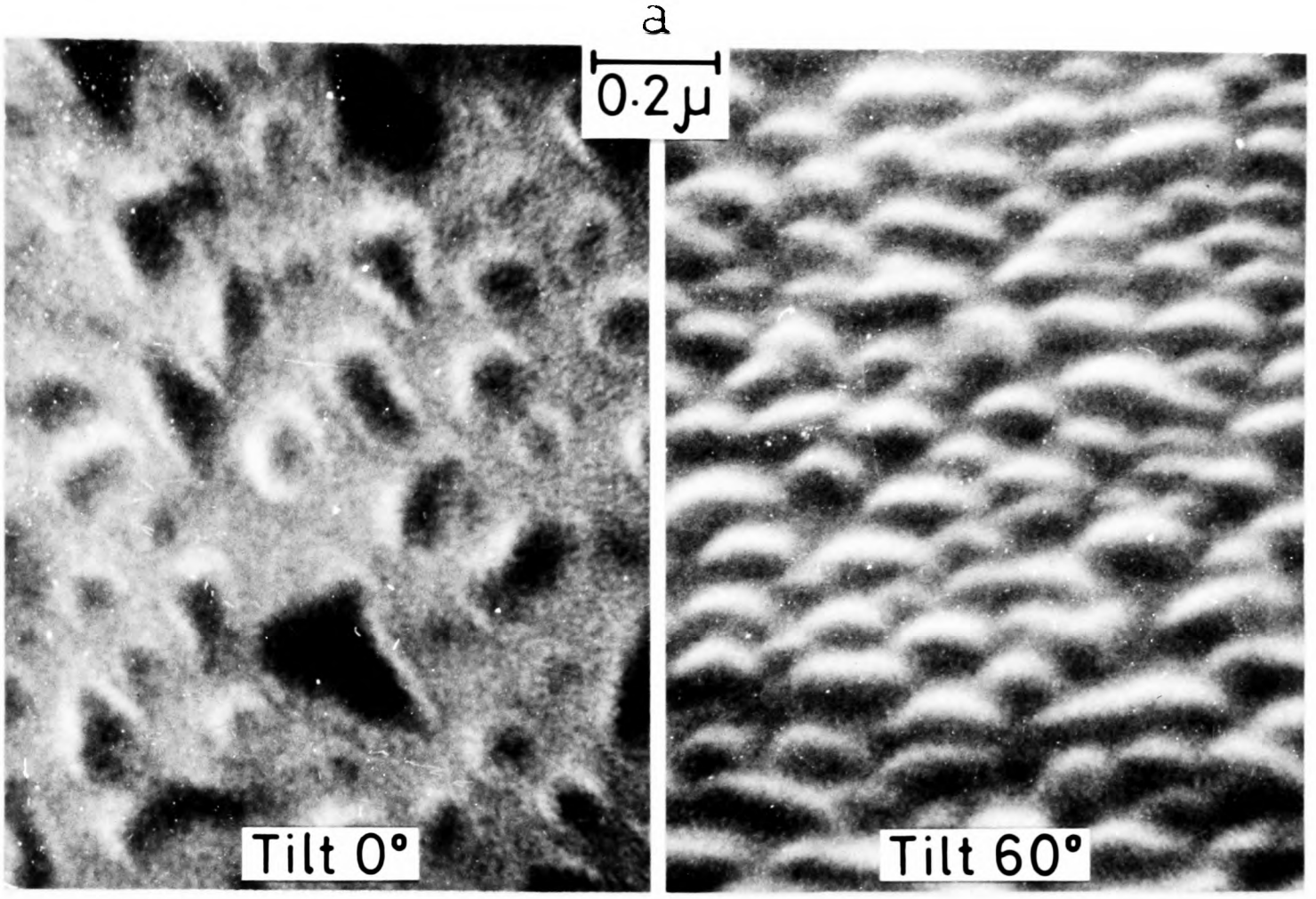
Only a small number of Si deposition runs were carried out due to difficulties experienced in subsequently preparing specimens for TEM examination. However, for a substrate temperature of $\sim 900^{\circ}C$, when Si was deposited at a rate of 1 Å sec^{-1} up to a mean film thickness of ~ 160 Å, subsequent SEM examination showed that separate minute growth centres were present in a number density of $\sim 4 \times 10^{9}$ cm^{-2}, and these are shown in fig 5.12a. The micrograph taken with 0° of specimen tilt illustrates that the centres were often approximately triangular in shape. These general observations indicate that initial Si film growth had taken place by a nucleation mechanism. When the Si deposition at 1 Å sec^{-1} was continued up to a mean thickness of $\sim 0.4\mu$, the film became continuous. Examination in the SEM (fig 5.12b) showed that the surface of the film was somewhat irregular, having a rough appearance. This suggests that the Si film may have contained separate crystallites, possibly with a range of orientations. General information about the crystallographic structure of the film was deduced from electron channelling patterns, obtained in the SEM from the film surface as described in section 1.6. Such a pattern is shown in fig 5.12b, and it exhibits a weak [111] pole. This indicates that the film had an overall preferred orientation identical to that of the substrate i.e. $(111)_{Si} // (111)_{diamond}$. The diffuseness of the bands further indicates that the film may have contained a high density of crystallographic defects, in accordance with the work of Davidson et al (1971) on channelling pattern contrast.

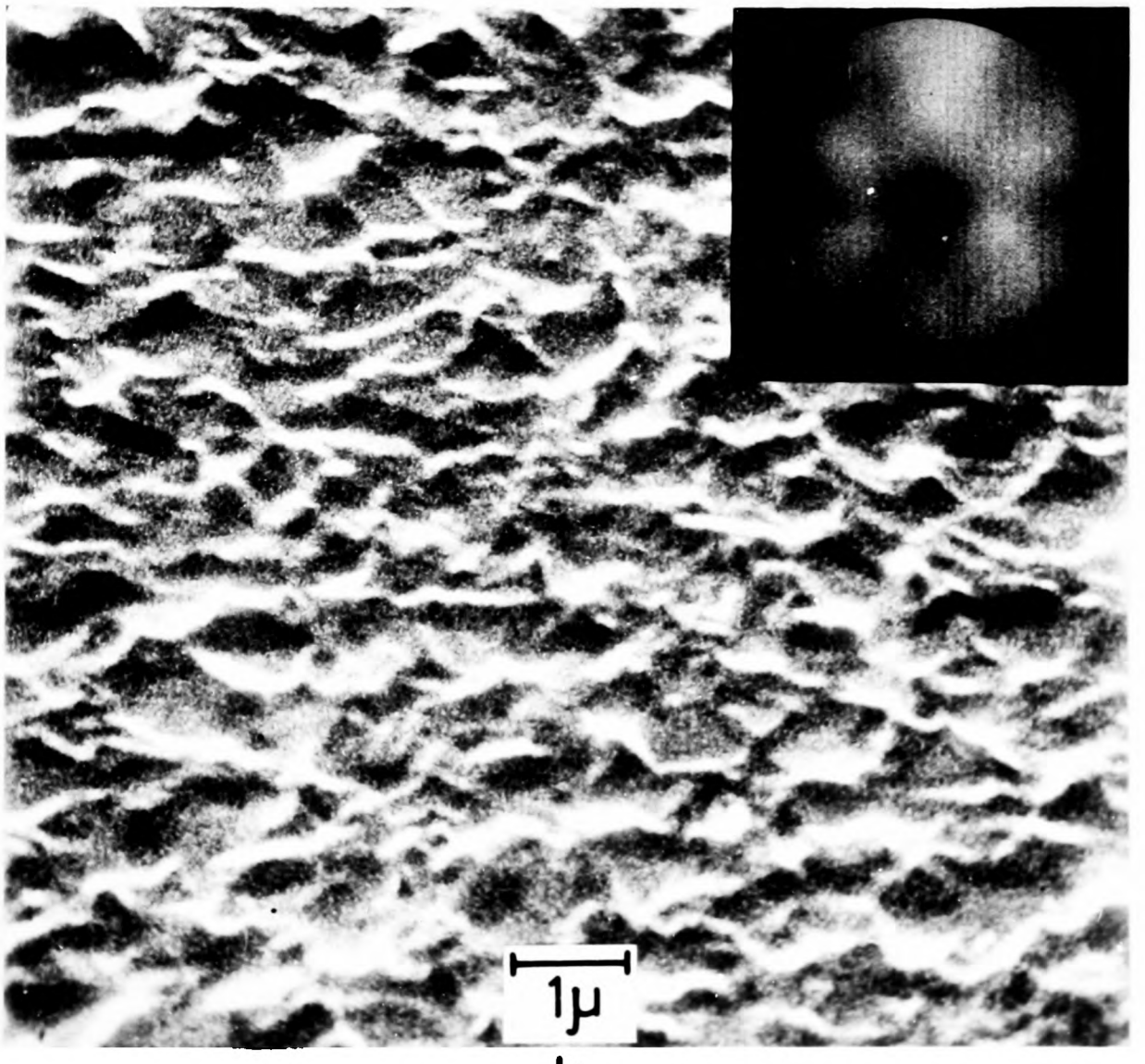
At the present time, only preliminary results are available from the TEM examination of substrates thinned by the procedure given in section 5.3, and these relate to the structure of the substrates rather than film/substrate combinations. Fig 5.13 shows the edge of a substrate which was transparent to 125 kV electrons. Curious fringe-like structures were present in the diamond, and their regularity varied along the edge.

Fig 5.12a Si growth centres on (111) diamond substrate. (Scanning electron micrographs)

Fig 5.12b Si film ~ 0.4μ in thickness on (111) diamond substrate. Note rough surface structure, though electron channelling patterns obtained from small areas (insert) gave evidence for retention of substrate orientation. (Scanning electron micrograph and channelling pattern)

a

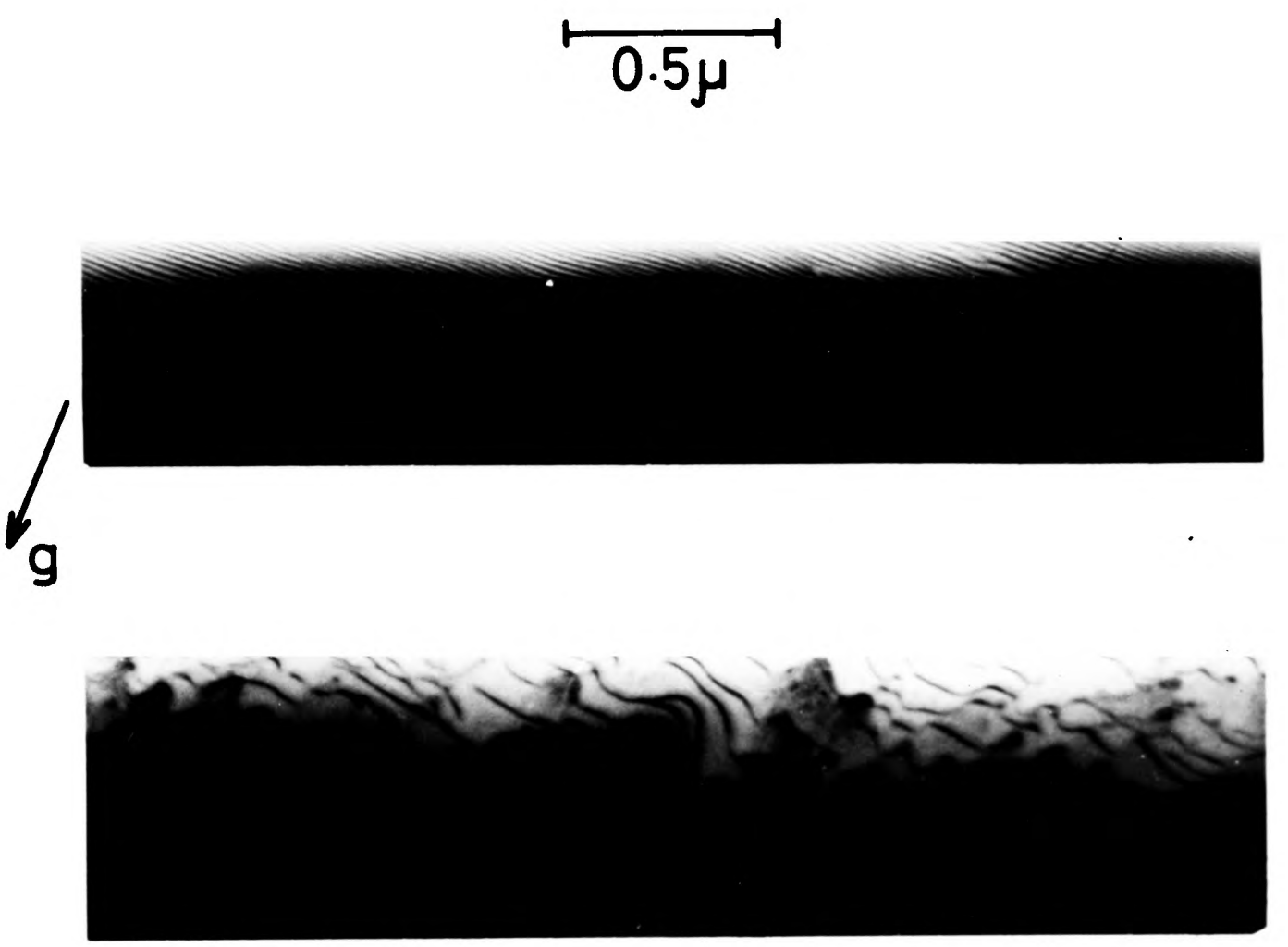


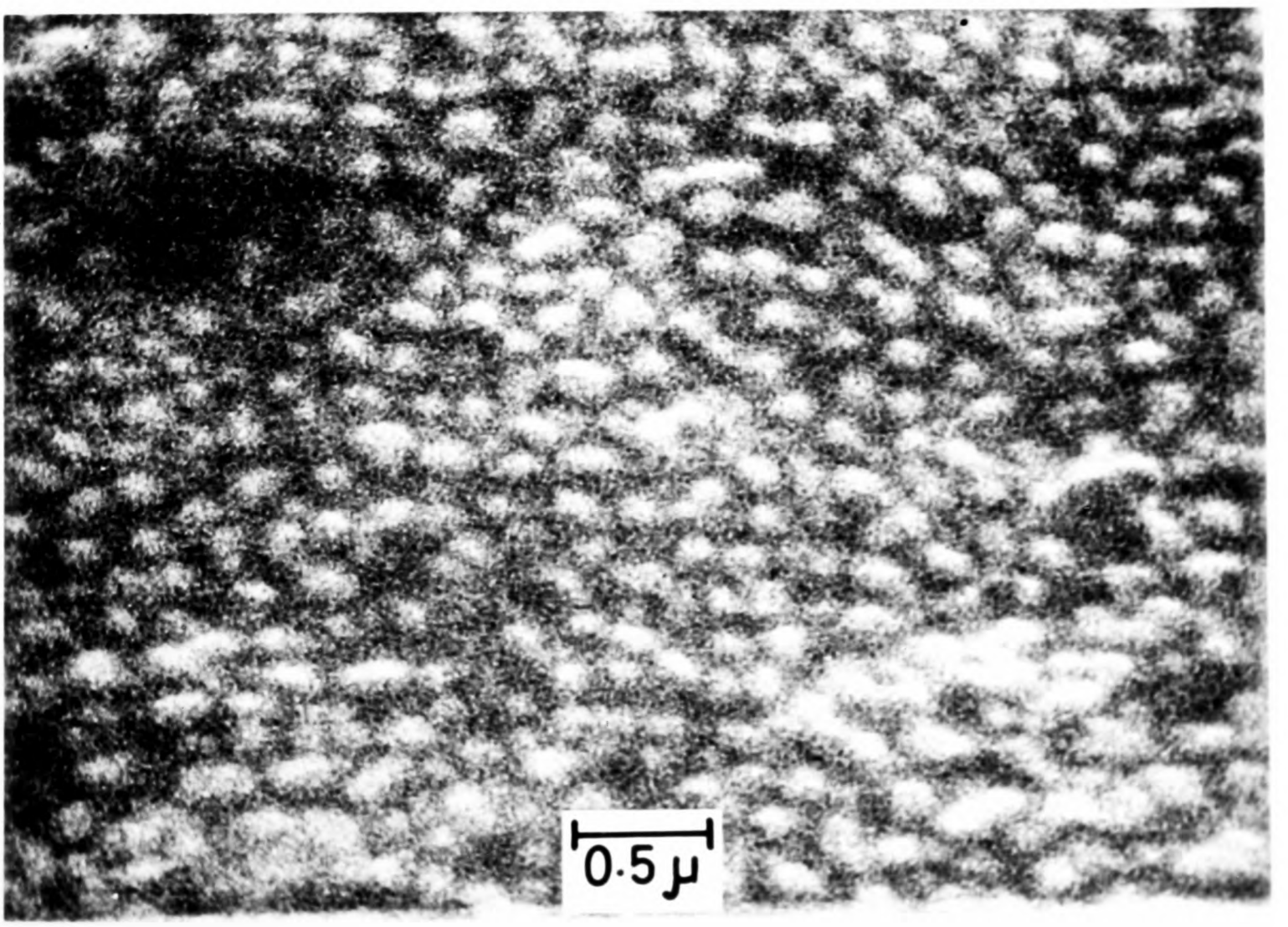


b

Fig 5.13 Fringe-like structures at edge of diamond substrate: illustrates variation in appearance from region to region. (Transmission electron micrographs, 125 kV, $2\bar{2}0$ type reflection, bright-field)

Fig 5.14 Si growth centres on (111) β - SiC substrate. (Scanning electron micrograph)


0·5μ
g


0·5μ

In one region they were straight and accurately parallel, although their direction did not depend upon the direction of the operating Bragg reflection g vector, indicating that they were not produced by a simple Moiré effect. Indeed, in another region they had a rather irregular structure, and their precise nature remains uncertain. Some preliminary investigations using the 1MeV TEM have been carried out. However, the few specimen areas which gave significant transmission showed no pronounced defect structures, and further studies are in progress.

5.5.2) Silicon on β-Silicon Carbide

Si deposition has so far been carried out on one β-SiC substrate. This was a single crystal overgrowth upon a subsidiary β-SiC base. The β-SiC had been grown from the vapour phase, and the surface upon which Si was deposited was as-grown, and had (111) orientation (confirmed using the Laue X-ray back-reflection technique). Final preparation before deposition consisted of treatment with various solvents, finishing with Analar methanol. Optical microscopy revealed that the surface was smooth, and free from topographical imperfections.

Si was deposited on to the substrate, held at a temperature of $\sim 900^{\circ}C$, at a rate of 1 Å sec^{-1} up to a mean thickness of ~ 160 Å. When the film was examined using the SEM, it was found that minute growth centres were present on the surface, and these are shown in fig 5.14. The centres occurred in a number density of $\sim 10^{9}$ cm^{-2}, and these observations are consistent with film growth having taken place by initial nucleation. It was not possible to determine whether the centres had geometrical shapes due to SEM resolution limitations.

5.6) Discussion

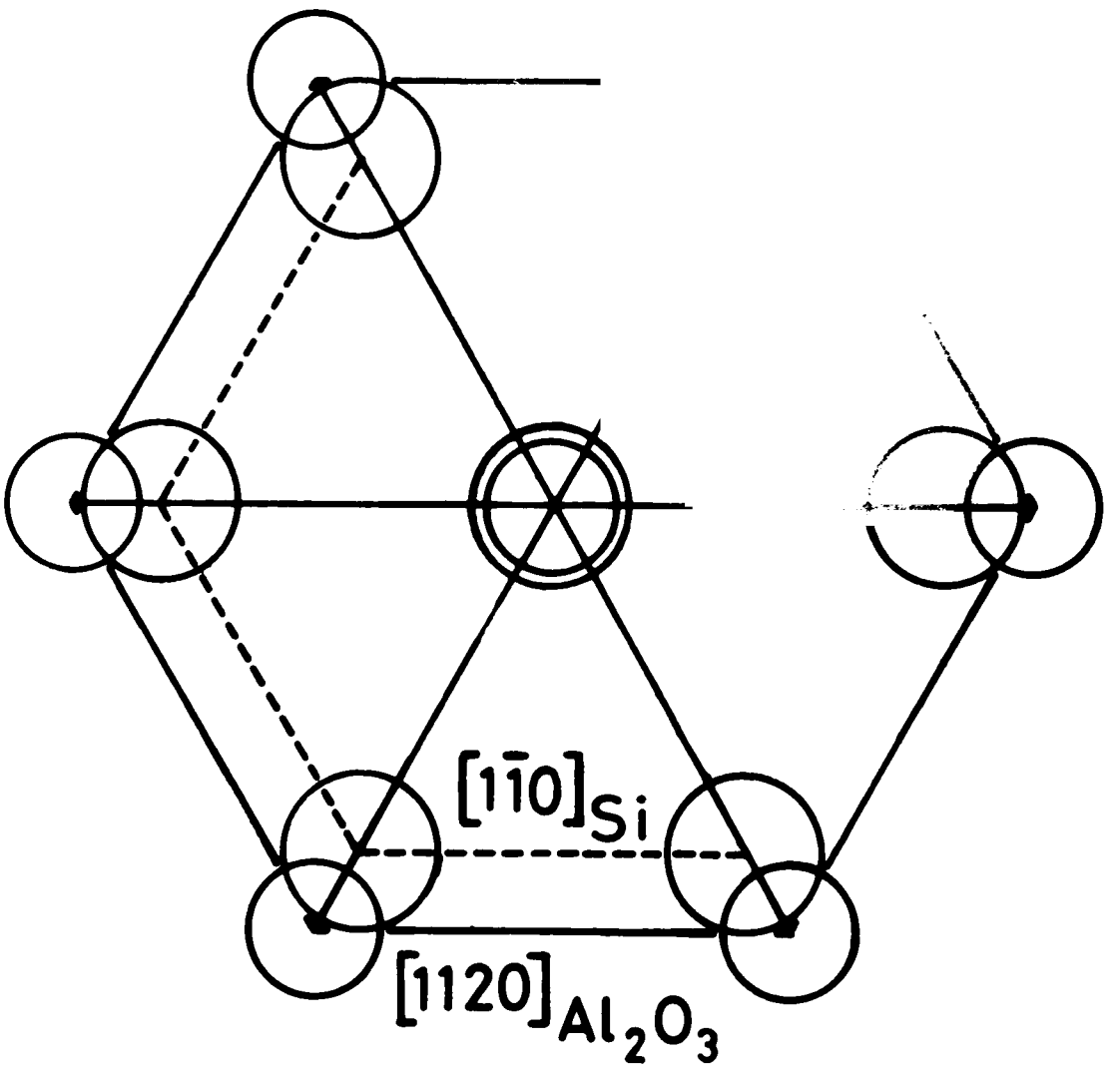
5.6.1) Silicon on Sapphire

Sapphire is potentially a most useful insulating substrate material for Si film growth, since it is readily available as large single crystals, with a high crystallographic perfection. However, it has a trigonal lattice, so that the mismatch with single crystal Si depends upon the relative orientations, and is generally quite large. Also, their thermal coefficients of expansion differ by a factor of approximately two; i.e. mean values, Si (400-600°C) 4.5×10^{-6} $^{o}C^{-1}$ and sapphire (20-1200°C) 9.5×10^{-6} $^{o}C^{-1}$ (Filby and Nielsen, 1967).

In principle, the (0001) face of a sapphire single crystal could be composed of either Al or oxygen ions. However, since substrates were exposed to air for long periods prior to deposition, it is likely that an Al face would be unstable with regard to oxidation, so that initial Si growth probably occurs upon the corresponding oxide face. A simple model may then be put forward to account for the observed Si epitaxial relationships. Following Larssen (1966), Si may be considered to enter vacant Al sites in the oxide surface, according to the scheme illustrated in fig 5.15, which shows how the relationship $(111)_{Si} // (0001)_{Al_2O_3}$ may be achieved. It is clear that the optimum fit is produced by arranging the layers to give the experimentally observed directional relationship $[1\bar{1}0]_{Si} // [11\bar{2}0]_{Al_2O_3}$. The misfit in the unit surface meshes is $\sim$ 19% (using room temperature parameters, and expressed as a percentage of $a_{Al_2O_3}$ (hexagonal axes)), and therefore, the match with the substrate of any initial epitaxial Si growth nucleus would change rapidly as it spread over the surface. Due to this, it is possible that the general propagation of sapphire symmetry elements into the Si is important for preserving the epitaxial relationships initially established.

Consideration of the mismatch between the Si $\{1\bar{1}0\}$ type planes

Fig 5.15 Diagram showing atomic model of (111) Si (large circles) parallel to (0001) sapphire (small circles - Al vacancies) (after Larssen, 1966).


$[1\bar{1}0]_{Si}$
$[1120]_{Al_2O_3}$

and the sapphire $\{11\bar{2}0\}$ type planes indicates that a misfit dislocation network of ~20 Å spacing might be expected (see derivation of eq 6.8). However, experimental observations did not provide evidence for the presence of such a network, although under some TEM diffraction conditions weak periodic contrasts were observed, with spacings from 30 - 70 Å (figs 5.2 and 5.3). It seems probable that these were Moire fringes, although their origin is uncertain. However, a mottled interfacial structure was usually observed, indicating that a reaction may have taken place between the Si and the sapphire. Indeed, regions of the substrate between initial growth centres exhibited a similar structure, giving support to this concept. Other workers have proposed certain possible reaction schemes (e.g. Bicknell et al (1966) suggested a reduction of sapphire to Al), but it seems likely to the present author that a probable reaction product was aluminium orthosilicate (Al_2SiO_5) formed by a reaction of the type

$$Si + 2Al_2O_3 \longrightarrow Al_2SiO_5 + Al_2O\uparrow$$

Therefore, this compound oxide could have been present as a residue at the interface, where it may have absorbed the Si/sapphire lattice mismatch, and therefore, prohibited the introduction of a misfit dislocation network. This may account for the observed interfacial structure, although the presence of such an oxide could complicate the otherwise simple Si/sapphire interface model discussed above.

Initial Si film growth was inferred to have been by nuclation, since the thinnest films examined were composed of separate growth centres. Their number density was in the region of 10^9 cm^{-2}, which is more closely in accord with the predictions of conventional nucleation theory than the observed number densities for Si growth centres on Si substrates (chapter 2), where substantially lower numerical values were obtained. Si films with mean thicknesses of only a few hundred Å, and which only partially covered their sapphire substrates, were found to be composed of two rotation twins,

each with a relationship of the type $[1\bar{1}0]_{Si}//[11\bar{2}0]_{Al_2O_3}$. This is in agreement with the model of fig 5.15, since Si has only three-fold symmetry about the [111] surface normal. This leads to the possibility of two distinguishable epitaxial orientations, inter-related by a 60° rotation about the [111] direction. It is interesting that 30° rotational twins, seen by Chu et al (1965), were not observed during the present experiments. It may be relevant that some earlier investigation techniques (e.g. X-rays and RHEED) yielded analyses from large specimen areas, and therefore, subsequent interpretation may have confused localized, and possibly contamination induced, effects with general orientation phenomena. The thin Si films were also observed to contain planar defects (microtwins and stacking faults), especially when deposited at the higher temperature of 1100°C. It is possible that some of these defects were produced when the films grew over Si/sapphire reaction products, such as Al_2SiO_5, on the substrate surface. The mechanism of formation could be similar to that proposed by Booker and Stickler (1962b) for stacking fault generation in epitaxial Si films on Si substrates.

As the Si film thickness was increased, TEM examination showed that misorientations had been introduced, first of a rotational nature and finally of a general character, giving an essentially polycrystalline defect structure. There are at least two possible reasons for this. Si growth centres would have had random lateral displacements on a sapphire surface due to the large crystallographic mismatch, so that when these centres eventually overlapped defects must have been produced, together with film strains. Therefore, the later the stage of coalescence, the greater the number of defects expected. However, there is another potentially serious source of defects. The thermal coefficient of expansion of sapphire is approximately twice that of Si, and therefore, when a film and its substrate were cooled from the deposition temperature, large differential strains were introduced. This is exemplified

by the fact that the sapphire platelets, used during the present experiments, often rolled up into narrow cylinders on cooling. Due to this, it is likely that while very thin Si films could elastically deform to relieve these strains, the thicker and more rigid films may have been unable to do so, with the resulting introduction of a large number of defects. It also seems possible that this process may have been affected by the physical bending of the substrate platelets during cooling.

Concerning use in electronic device fabrication, Si film uniformity is clearly a limiting factor. Although the film grown to a thickness of 2.9μ (at 1100^{o}C) had a very uniform profile (fig 5.10), TEM showed that it still contained some narrow channels, which could have had an undesirable effect upon devices constructed in it. Also, the polycrystalline character of the thicker films would probably degrade electrical carrier mobilities, leading to relatively poor device properties. Film uniformity may be improved by Si growth at higher deposition rates, when initial growth centres would be present in very high number densities, and hopefully overlap more quickly. This procedure might also minimize the Si/sapphire chemical reaction, although its effect upon general film crystallographic structure would have to be determined experimentally.

5.6.2) Silicon on Diamond

Diamonds are classified according to certain physical properties (Ditchburn and Custers, 1965), and in particular, photoconductivity is exhibited weakly by type I and relatively strongly by type II crystals. However, in the absence of optical stimulation, type II material is classified depending upon whether it is electrically insulating (type IIa) or semiconducting (type IIb). In addition, although most diamond exhibits a very high thermal conductivity, this is especially marked for type IIa material which, at room temperature, conducts heat five times better than

Cu. While this behaviour is not fully understood, it may be relevant that both types I and IIb diamond are thought to contain substantially more defects than type IIa, e.g. type I contains nitrogen impurity platelets (Berman, 1965). This thermal property would be potentially advantageous for devices fabricated directly in Si films grown on e.g. electrically insulating type IIa diamond substrates. Such devices could be operated at especially high power levels, since heat dissipation would be considerably enhanced. However, although Si and diamond have the same crystal structure, since the diamond lattice parameter is 3.567 Å, the Si/diamond lattice mismatch at room temperature is 34.4% (eq 4.1). Also, since the diamond thermal expansion coefficient (mean value (400 - 600°C) 3.5×10^{-6} $^{o}C^{-1}$ (Thewlis and Davey, 1956)) is somewhat less than that of Si, this mismatch would be exacerbated at a useful film growth temperature.

Due to the great resistance of diamond to chemical attack, in the present experiments, it was considered that the optimum (111) substrate surface preparation was by cleavage. Although such a surface was covered with steps, it would have been unwise to remove these by mechanical abrasion, since this would have produced severe surface damage on a fine scale (Driver et al, 1971), which could not then be removed by a convenient chemical method. It is also important that diamond is only metastable, except under very high pressure, and is known to transform to graphite in vacuum at temperatures at least as low as 1500°C (Evans and James, 1964). Since this transformation is initiated at the surface, it could have extremely deleterious effects on epitaxial growth, which is very sensitive to surface disturbances. Therefore, high temperature substrate 'cleaning' pretreatment would seem to be of dubious usefulness, and some care may also be necessary in choosing the optimum deposition temperature. In the present experiments this was 900°C, where it was hoped that the transformation

could be neglected.

Once again initial Si growth was by nucleation, giving a high number density of growth centres. These overlapped to give a fairly uniform rough film, which at least partially preserved the (111) orientation of the substrate up to a thickness of 0.4μ. This is an encouraging observation, when the large film/substrate mismatch is considered. However, the large number of Si film defects inevitably present would undoubtedly have an undesirable effect upon electronic devices fabricated in the film.

When grinding the back surfaces of diamond substrates to thin them for TEM examination, it is most important that the substrate should be orientated a few degrees away from the (111) plane for as long as possible. This increases the diamond removal rate markedly, due to the pronounced decrease in hardness away from the low index orientation (Driver et al, 1971). This effect was amply verified during the author's experiments.

Initial TEM observations showed that the diamond sometimes contained curious defects which gave periodic contrasts, distinct from simple Moiré fringes. It would be interesting to determine whether these defects specifically occur only in type IIa material, and whether they are associated, in any way, with its physical properties.

5.6.3) Silicon on β-Silicon Carbide

β-SiC has the zinc blende cubic lattice ($a = 4.358$ Å), and the room temperature mismatch with Si is 19.8% (eq 4.1). While this is large, it is not as great as the Si/diamond mismatch. However, β-SiC also possesses a special advantage as a substrate material for Si, since their thermal coefficients of expansion are quite similar (mean $\sim 4.5 \times 10^{-6}\ ^{o}C^{-1}$) between room and film growth temperatures (Filby and Nielsen, 1967). Due to this, there should be few extra strains introduced on cooling a film and its

substrate from the deposition temperature, and therefore, the quality of the resulting deposit may be improved.

Only preliminary investigations have so far been carried out, but these indicate that initial Si film growth occurs by nucleation, giving a high number density of growth centres. Since this is a system of strong film/substrate binding, it is to be hoped that such centres would spread quickly over the substrate, giving a uniform film at an early stage in the growth. More experiments are necessary to establish the Si/ β-SiC behaviour.

5.7) Summary

Si films were grown on insulating substrates, with the object of both obtaining fundamental information about the growth mechanism, and evaluating film structure with regard to possible use for electronic device fabrication. When Si was deposited on to (0001) sapphire substrates, it was observed that:

a) the thinnest films were composed of growth centres, indicating that initial growth had been by nucleation;

and b) while the centres grew with the epitaxial relationship $(111)_{Si} // (0001)_{Al_2O_3}$, they were found to be composed of essentially equal proportions of two 60° rotational twins, each exhibiting a directional relationship of the type $[1\bar{1}0]_{Si} // [11\bar{2}0]_{Al_2O_3}$.

These results agreed well with a theoretical model of the Si/sapphire interface. However, high resolution TEM studies provided no evidence for the presence of an interfacial network of misfit dislocations, but instead indicated that a reaction had taken place between the Si and the sapphire. A possible reaction product was thought to be aluminium orthosilicate.

Apart from the Si twins rotated about the interface normal, the most prevalent film defects were stacking faults and microtwins on inclined planes.

As Si films became thicker, small rotational misorientations were first observed to be introduced. However, films a substantial fraction of a micron in thickness contained misorientations of a more general nature, and ultimately became polycrystalline. The thickest film grown (2.9μ) had this structure, although it was quite uniform in thickness and only a few channels remained in the deposit. It was thought that electrical carrier mobilities would have been depressed by the severe film defects, and that the channelled structure would need to be eliminated before electronic devices could be successfully fabricated in the films.

Si films were also grown on (111) diamond and β-SiC substrates. Although the experiments were of a preliminary nature, they showed that initial growth was again by nucleation. Also, a 0.4μ thick Si film on diamond exhibited significant orientation retention, which is encouraging when the large film/substrate mismatch is considered.

CHAPTER 6 HIGH RESOLUTION TEM STUDIES OF CRYSTAL DEFECTS

		Page
6.1)	Introduction	133
6.2)	The TEM Weak-Beam Technique	134
6.3)	Observations of Dislocations at the Germanium/(111)Silicon Interface	136
6.3.1)	Nature of Ideal Dislocation Networks	136
6.3.2)	Basic TEM Contrast Behaviour	139
6.3.3)	Interfacial Fringe Images	142
6.3.4)	Observations Using Weak Beams	147
6.4)	Observations of Defects in Single Crystal Silicon	151
6.4.1)	Weak-Beam Observations of Dislocation Networks	151
6.4.2)	Weak-Beam Observations of Inclined Stacking Faults	156
6.5)	Discussion	157
6.5.1)	Threefold Dislocation Nodes	157
6.5.2)	TEM Image Contrast and Crystal Defects	161
6.6)	Summary	163

6.1) Introduction

During studies of epitaxial Ge films grown upon (111) Si substrates (chapter 4), it was found that a network of dislocations occurred at each film/substrate interface. These networks were produced to accommodate the cyrstallographic mismatch between the two materials, and the dislocations always had very small separations, sometimes as small as 150 Å. Accordingly, it was necessary to carry out transmission electron microscopy under conditions which would give narrow dislocation images, minimally displaced from the real positions of these defects. The weak-beam technique, developed by Cockayne et al (1969), was admirably suited to this purpose and has been used extensively in these investigations. Indeed, conventional strong-beam microscopy (using strongly excited Bragg reflections) generally gave images which were very different in form from the real structure of the underlying defects, and was, therefore, of only restricted usefulness. Use of the weak-beam technique enabled the interfacial dislocation networks to be studied in sufficient detail to determine the extent of dislocation dissociation, especially at their points of intersection (nodes). The manner in which the stacking fault image intensity changed for different weak-beam conditions was also studied, and various unusual features were observed.

Weak-beam observations were extended to defects in single crystal Si, so that a comparison with the Ge/Si system could be made. Both dissociated dislocations and large inclined stacking faults were studied, using several different Bragg reflections over a range of excitations from strong to weak.

6.2) The TEM Weak-Beam Technique

While the real width of a dislocation core in a crystalline material may be as small as ~ 5 Å, the corresponding TEM image contrast, observed using conventional strong-beam conditions, is usually a linear feature $\sim \frac{1}{5}\xi_g$ wide, where ξ_g is the extinction distance of the operating Bragg reflection. For Si, using 100 kV electrons, $\xi_{220} \simeq 750$ Å so that dislocation image widths may be as large as ~ 250 Å, which indicates that image contrast is produced by very small crystal lattice distortions. Also, the form of the contrast is often complex, and depending upon the exact diffraction conditions, it may be displaced from the real position of the dislocation in relation to other structures in the image. These prominent features of strong-beam dislocation images often render detailed interpretation difficult. For example, if a dislocation is dissociated, the images of the partial dislocations so produced, together with the ribbon of crystal stacking fault between them, would be expected to overlap if the splitting is small, and to produce a complex image. Also, if many dislocations are closely spaced, their images would tend to overlap and produce possibly confusing contrast effects.

The undesirably large image widths of dislocations observed using strong-beam conditions are directly related to the magnitude of ξ_g. However, for a finite deviation (s) from the exact reflecting position of the operating reflection, ξ_g must be replaced by an effective extinction distance ξ_g^w defined by

$$\xi_g^w = \xi_g/(1 + w^2)^{\frac{1}{2}} \qquad (6.1)$$

where $$w = s\xi_g \qquad (6.2)$$

As the magnitude of s is increased, the value of ξ_g^w decreases, and since dislocation image widths are now related to this parameter, they also decrease in a corresponding manner. This behaviour forms the basis for

the weak-beam technique (Cockayne et al, 1969), since s may be increased sufficiently to ultimately give dislocation image widths as small as ~15 Å. Using dark-field illumination, for large deviations the background intensity is extremely low, but the image contrast produced by the defect can be quite high. Nevertheless, due to the low overall image intensity, a long photographic plate exposure may be necessary for recording purposes, and this can introduce experimental difficulties. However, if both TEM specimen drift and contamination rates are low, very high resolution micrographs may be obtained, showing narrow dislocation images with only small displacements from the real positions of the defects in the crystal.

Typical TEM diffraction conditions for weak-beam operation are illustrated by the diagram in fig 6.1, which uses the reflecting sphere construction. A systematic row of reflections is shown, and these correspond to crystal reciprocal lattice points and are labelled according to their respective reciprocal lattice vectors (g, 2g, etc). The origin of the reciprocal lattice is at 0, and from this the incident electron wave vector in the crystal $\underline{k}'$ is drawn with a magnitude equal to the reciprocal of the electron wavelength(λ'). Its end point corresponds to the centre of the reflecting sphere, which intersects the row of reflections at 0 and ng. This condition corresponds to strong excitation of the reflection ng (wave vector $\underline{k}''$), and if a micrograph is recorded using either of reflections g or -g (which are only weakly excited), a typical dark-field weak-beam image is obtained. Also illustrated is the deviation vector $\underline{s}$, corresponding to reflection -g. Its magnitude may be determined using geometric considerations, giving

$$s = \mp\lambda'(n \pm 1)/2d^2 \qquad \text{(for reflection } \mp g) \qquad (6.3)$$

where $d = |\underline{g}|^{-1}$ and is the spacing of the crystal lattice planes giving rise to reflection g.

The physical process by which weak-beam image contrast arises may be understood, for dislocations, by noting that crystal lattice planes are

only severely distorted near the dislocation cores. If the bulk crystal is set with a large deviation from the Bragg reflecting position for the appropriate planes, the first order diffracted beam is only weakly excited in the crystal matrix. However, near dislocation cores, the excitation may increase considerably when severely bent planes approach the Bragg reflecting position. The greater the matrix deviation, the more severe must be the plane bending. Therefore, reflection excitation is especially large only close to core regions, which leads to the production of very narrow images, with an intensity which is large compared to that of the background. The crystal deviation may not be increased to an arbitrary extent, since in the limit, the reflection excitation even close to a dislocation core becomes undetectable. However, it is desirable to employ as large a deviation as possible, and e.g. Ray and Cockayne (1971) have carried out much work for values of s near 2×10^{-2} $Å^{-1}$.

To illustrate the advantages of weak-beam microscopy, fig 6.2 shows a closely spaced dislocation network in deformed Si, under both strong- and weak-beam conditions. The extra detail visible under the latter conditions is evident.

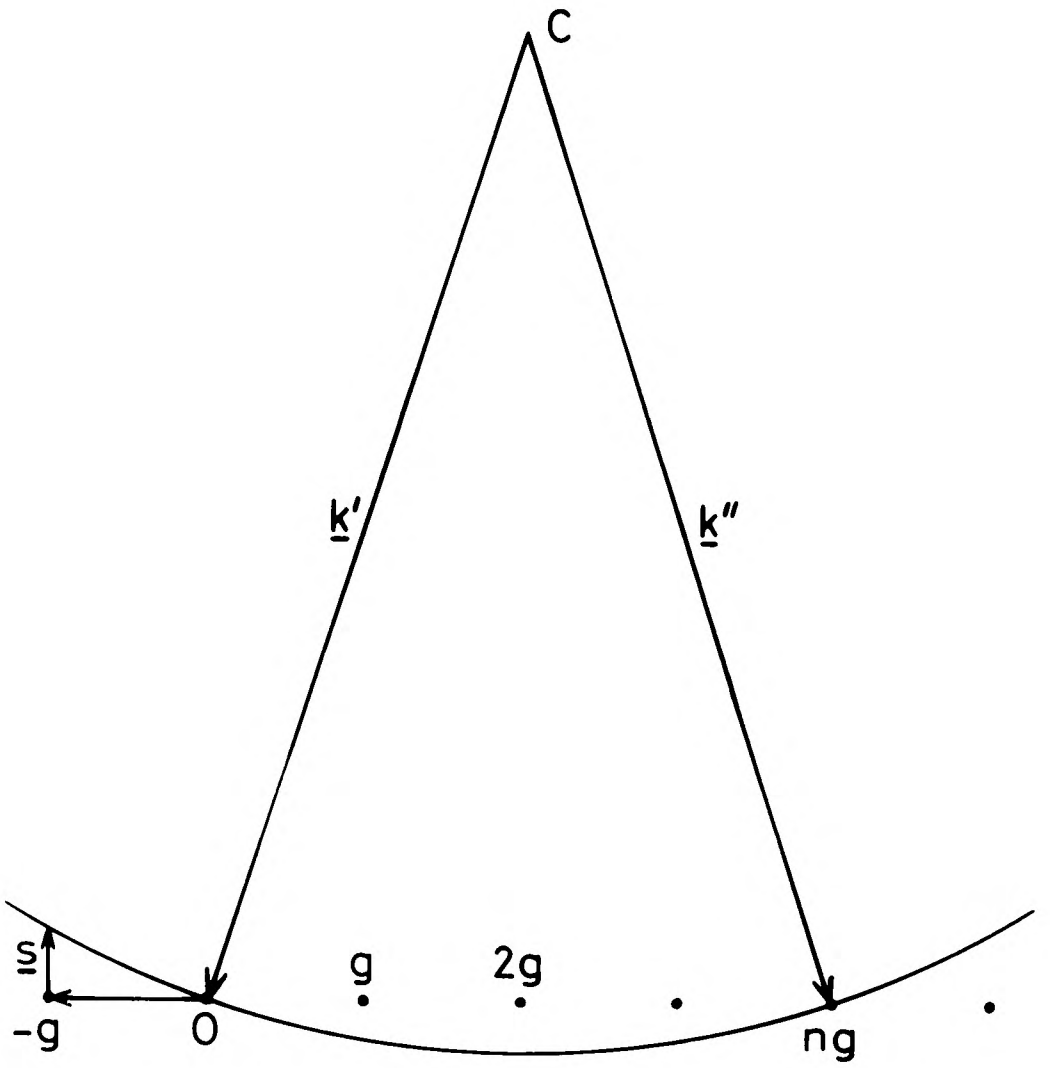
6.3) Observations of Dislocations at the Germanium/(111)Silicon Interface

6.3.1) Nature of Ideal Dislocation Networks

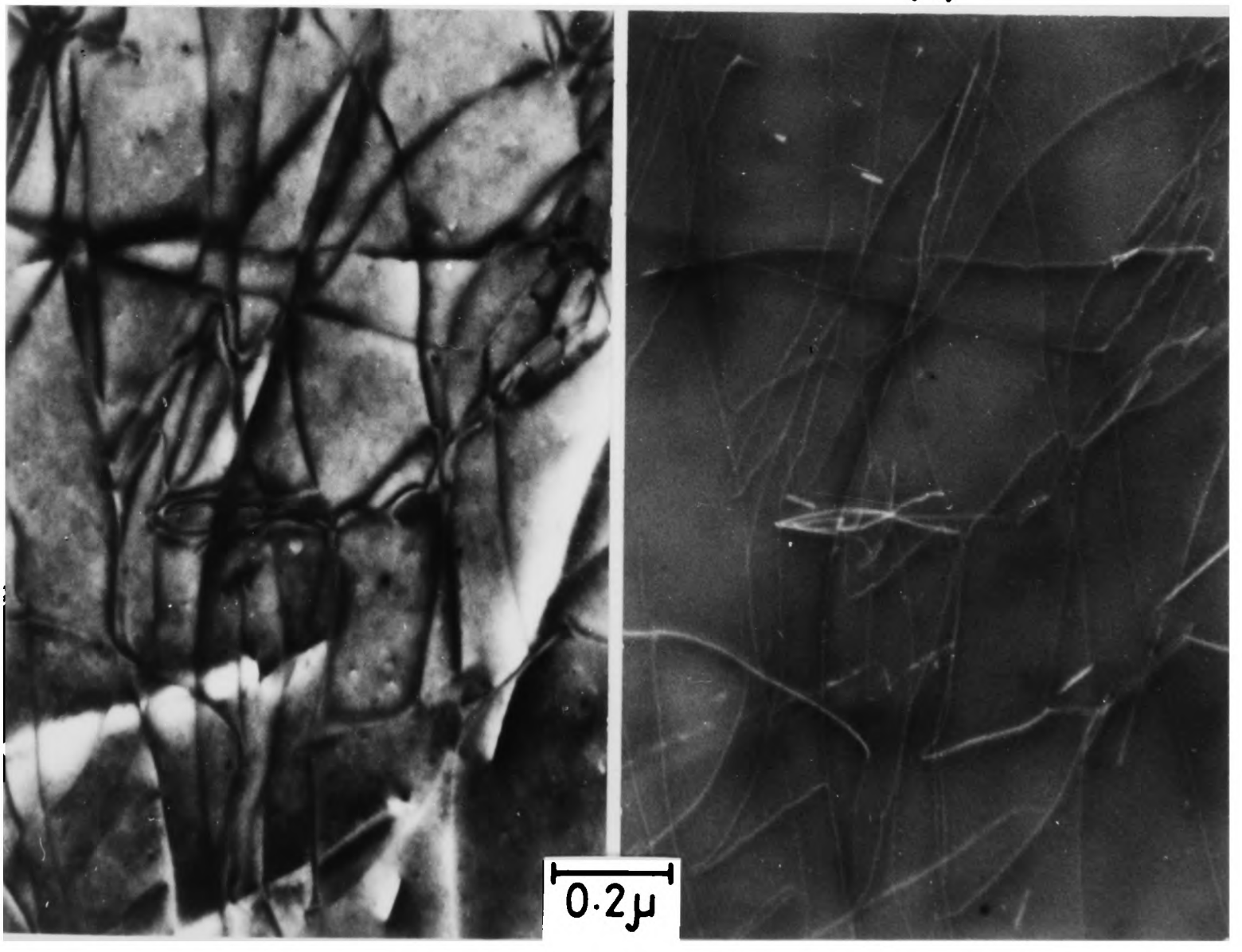
To understand the manner in which misfit dislocations are generated at the Ge/(111)Si interface, it is instructive to study the Moiré-like pattern formed by the superposition of two mismatching hexagonal arrays of dots. Fig 6.3 shows such an assembly, where one array has a spacing ~10% larger than that of the other. These arrays may be considered to represent the touching (111) interfacial atom double layers of Ge and Si respectively, if each dot takes the place of an atom pair.

Fig 6.1 Diagram illustrating typical diffraction conditions necessary for weak-beam operation - reflecting sphere construction (see text). Deviation vector $\underline{s}$ corresponding to reflection $-g$ also shown.

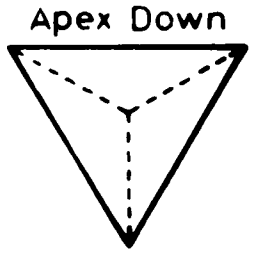
Fig 6.2 Micrographs illustrating the differences in appearance of typical strong-beam (a) and weak-beam (b) images. Note very narrow dislocation images in (b). (Transmission electron micrographs of same specimen area, dark-field, $2\bar{2}0$ type reflection strongly excited in (a) and weakly excited in (b))



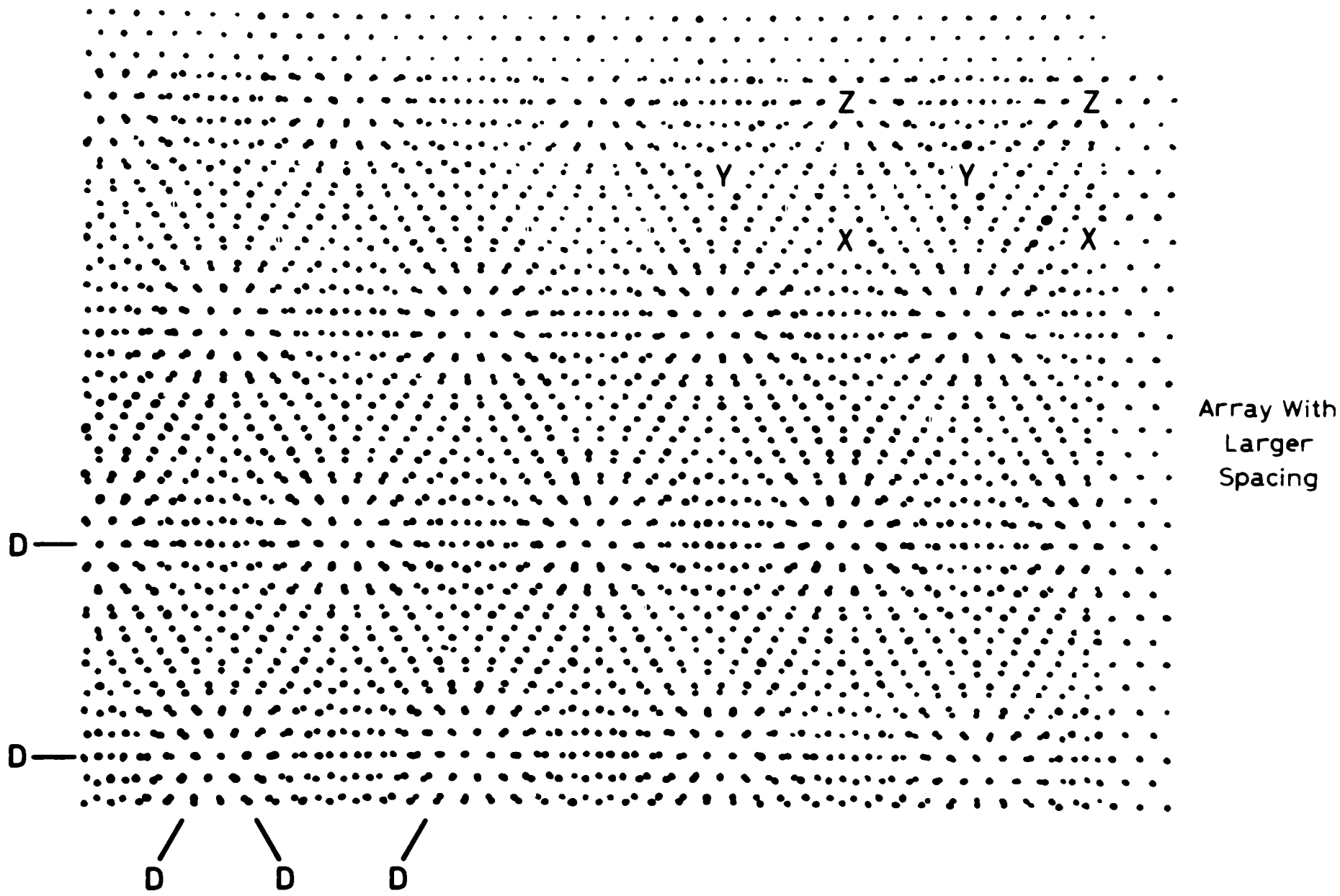
(a) (b)



Apex Down



Array With Smaller Spacing



Array With Larger Spacing

It is emphasised that the mismatch in fig 6.3 is solely due to lateral spacing differences (chosen from optimum visual effect), and there is no rotational component. First, consider the Ge layer (larger spacing dots) to be on the upper side of this interface, and next define that the [111] direction projects upwards from the page, with the Thompson tetrahedron apex down as shown. By inspection, it is then apparent that there are regions which correspond to different types of atomic stacking. Those labelled X correspond to the correct stacking sequence in the diamond lattice, ABCABCABC (A, B and C represent the atom double layers). The regions labelled Y correspond to crystal which contains a stacking fault at the interface, ABC↓ACABC, such that a complete double layer is missing. Last, regions labelled Z represent crystal containing a different higher energy stacking fault at the interface, ABCA↓ABCABC, such that an extra double layer is present. Other regions between those just described correspond to all possible intermediate cases.

Consider now that the atoms on opposite sides of the interface of this model atomic array are allowed to interact with one another, so that the interface relaxes with the introduction of misfit dislocations. This may be considered to occur in two hypothetical stages. First, the interfacial atoms reorganize to produce Shockley partial dislocations along the lines labelled D, and in accordance with this, regions with stacking of types X and Y expand up to these dislocation lines, which cross in regions of the type Z. Second, the partial dislocations move to assume equilibrium positions, such that a balance is produced between their mutual repulsions and the energy necessary to maintain faulted regions of crystal. Regions X and Z then become, respectively, the intrinsic and extrinsic nodes of an arbitrarily dissociated hexagonal dislocation network. The nodes are named after the types of stacking fault which they each contain. However, the extrinsic stacking fault does not retain its initial high energy

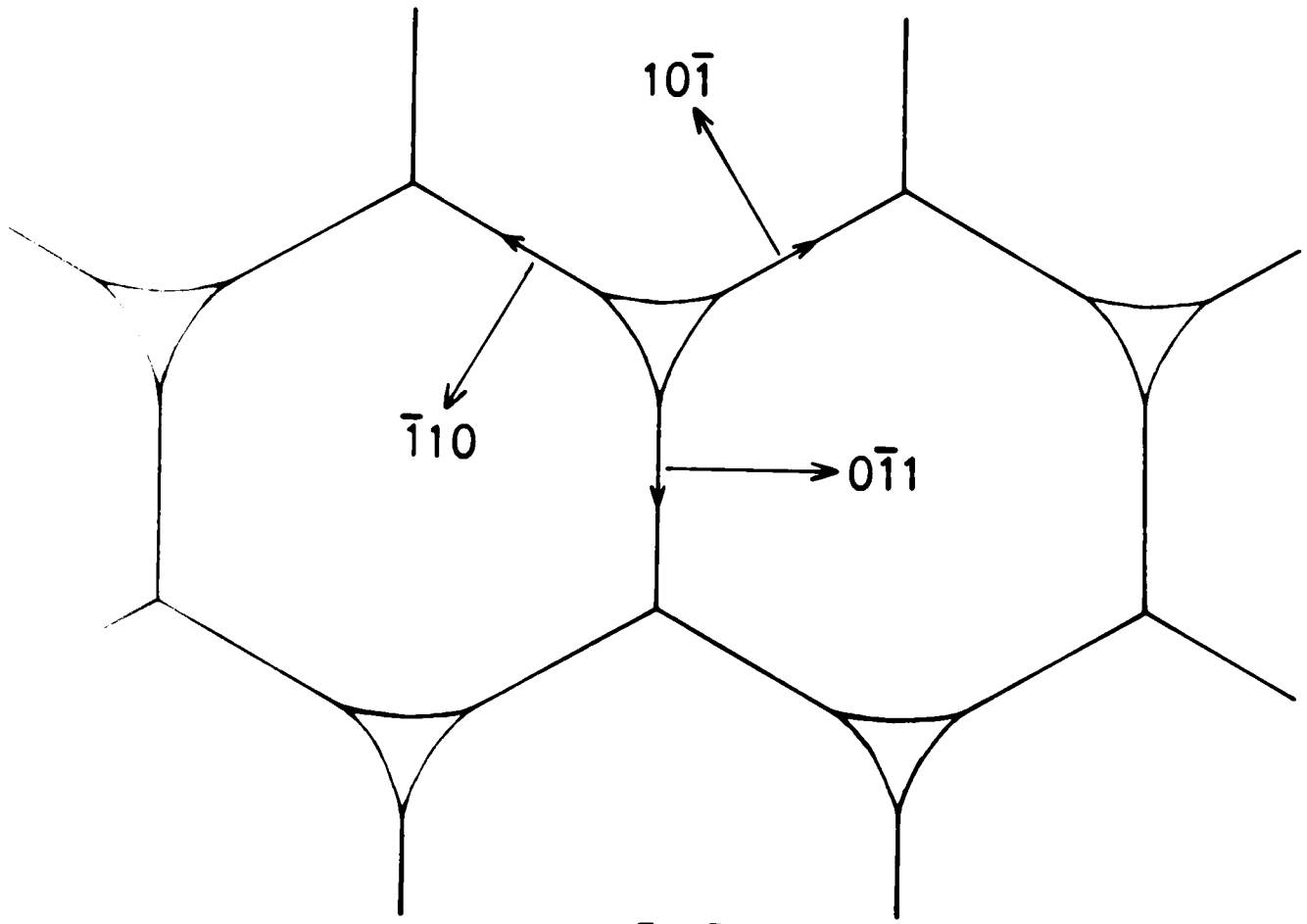
structure, but distributes itself between two levels with the formation of, effectively, two adjacent intrinsic faults. This would occur during the first stage of the hypothetical reorganisation described above, and give an extrinsic fault with stacking sequence ABCA$\overset{\downarrow\downarrow}{C}$BCABC, surrounded by pairs of Shockley partial dislocations (see e.g. Hirth and Lothe, 1968).

The intrinsic and extrinsic node regions would be extended (dissociated) to a degree determined by energy considerations. Fig 6.4a shows a diagram of such a hexagonal dislocation network, with the intrinsic nodes partially extended and the extrinsic nodes fully contracted. The segments of whole dislocation lie along $\langle 11\bar{2} \rangle$ type directions, are of edge character and have Burgers vectors of the type $\frac{a}{2}[\bar{1}10]$. The diagram requires that the extra latticeplanes associated with the dislocations should be beneath the plane of the paper (i.e. Ge on top of Si). The convention used to assign these Burgers vectors requires the application of the FSRH (Finish → Start, Right Hand) rule to a Burgers circuit around the dislocation lines (see Read, 1953), when they are viewed by looking outwards from the intrinsic nodes, in the direction of the sense vectors indicated in the diagram. This procedure emphasizes that all the whole dislocations are of completely equivalent edge character. If this network is further hypothetically dissociated so that no whole dislocations remain, the Shockley partial dislocations so formed could have the configurations shown in fig 6.4b. This diagram gives the Burgers vectors of these partials which are of the type $\frac{a}{6}[11\bar{2}]$, once again using the convention stated above. The fact that the partials invert their Burgers vectors whenever they change direction does not imply that there is any accompanying physical change. This inversion is simply due to the labelling convention, since the direction in which a partial is viewed to apply the FSRH rule continually changes along the dislocation line.

Fig 6.4a Diagram of hexagonal edge dislocation network with intrinsic nodes partially extended, showing Burgers vectors of remaining whole dislocations.

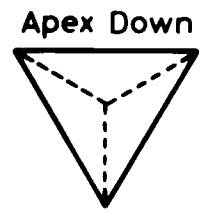
Fig 6.4b Diagram of network similar to that given in fig 6.4a, but with further dislocation dissociation to show all Shockley partial dislocations and their associated Burgers vectors.

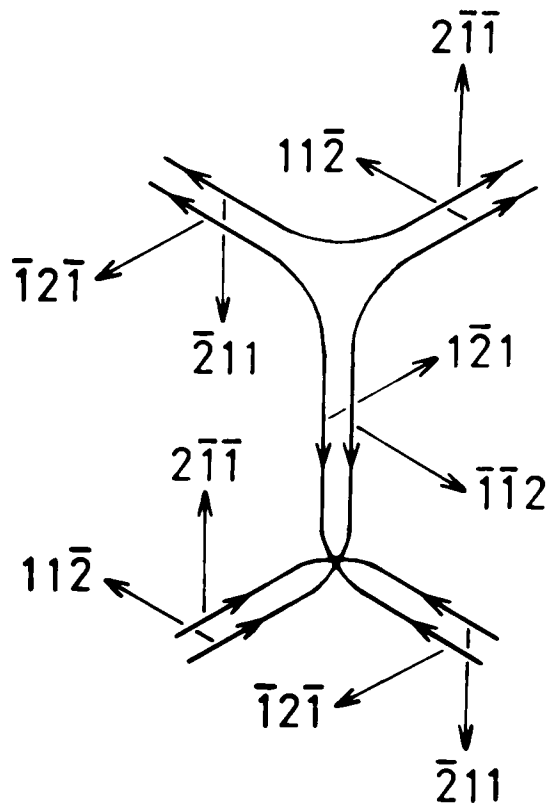
(a)



$\underline{b} = \frac{a}{2}[\quad]$

(b)





$\underline{b}_p = \frac{a}{6}[\quad]$

6.3.2) Basic TEM Contrast Behaviour

Edge dislocations have two lattice displacement components, one parallel to $\underline{b}$ (R_1) and the other normal to the slip plane i.e. the interface (R_2). The intensity of the TEM contrast due to displacements R_1 and R_2 depends upon the magnitude of $\underline{g}.\underline{b}$ and $\underline{g}.\underline{b}\wedge\underline{u}$ (Hirsch et al, 1965), respectively, under operating reflection g and where $\underline{u}$ is a unit vector along the positive direction of the dislocation line. For dislocations with $\underline{b}$ in the (111) foil plane observed under conditions such that $\underline{g}$ for the operating reflection is also in or near the foil plane, $\underline{g}.\underline{b}\wedge\underline{u}$ will be zero or small. Now, calculations indicate that if $\frac{1}{8}(\underline{g}.\underline{b}\wedge\underline{u}) \lesssim 0.08$, the R_2 displacement component will contribute only an undetectable amount of image contrast (Hirsch et al, 1965). Therefore, from table 6.1 it is clear that edge dislocations, with Burgers vectors of the type $\frac{a}{2}[\bar{1}10]$ in the interface, will exhibit no R_2 type contrast when the operating reflection is of the type $2\bar{2}0$, $11\bar{3}$, $11\bar{1}$, or $22\bar{4}$. For these reflections, the whole dislocation image contrast will depend only upon the R_1 displacement component, with an intensity dependent upon the magnitude of $\underline{g}.\underline{b}$, the dislocation being invisible if $\underline{g}.\underline{b}=0$. Table 6.2 gives relevant $\underline{g}.\underline{b}$ values for both partial and whole edge dislocations with Burgers vectors in the interface. However, caution is necessary if the sign of $\underline{g}.\underline{b}$ is important, and in each individual case due account must be taken of the convention used to define $\underline{b}$.

Table 6.1

For whole edge dislocations, $\underline{b} = \frac{a}{2}[\bar{1}10]$

$\underline{g}$	$\underline{g}.\underline{b}\wedge\underline{u}$	$\frac{1}{8}\underline{g}.\underline{b}\wedge\underline{u}$
$2\bar{2}0$	0	0
$11\bar{3}$	0.4	0.05
$11\bar{1}$	0.4	0.05
$22\bar{4}$	0	0

Table 6.2

b	g.b			
g	$2\bar{2}0$	$11\bar{3}$	$11\bar{1}$	$22\bar{4}$
a/2 [$\bar{1}$10]	-2	0	0	0
a/2 [0$\bar{1}$1]	+1	-2	-1	-3
a/2 [10$\bar{1}$]	+1	+2	+1	+3
a/6 [$\bar{2}$11]	-1	$-\frac{2}{3}$	$-\frac{1}{3}$	-1
a/6 [1$\bar{2}$1]	+1	$-\frac{2}{3}$	$-\frac{1}{3}$	-1
a/6 [11$\bar{2}$]	0	$+1\frac{1}{3}$	$+\frac{2}{3}$	+2
a/6 [2$\bar{1}\bar{1}$]	+1	$+\frac{2}{3}$	$+\frac{1}{3}$	+1
a/6 [$\bar{1}$2$\bar{1}$]	-1	$+\frac{2}{3}$	$+\frac{1}{3}$	+1
a/6 [$\bar{1}\bar{1}$2]	0	$-1\frac{1}{3}$	$-\frac{2}{3}$	-2

When a dislocation is observed with one operating reflection (two beam conditions), such that there is a deviation from the exact Bragg orientation, calculations show that its image is generally displaced to one side of the real position of the core (Hirsch et al, 1960). The manner in which this occurs is illustrated in fig 6.5, which shows a TEM electron beam incident upon an edge dislocation in a lattice with a small positive deviation from a Bragg orientation. In regions A and D of the crystal, the corresponding reflection g is only weakly excited, so that it would contribute little intensity to a dark-field image. This is also true for region C, where the crystal lattice planes are bent even further away from the Bragg orientation by the dislocation core. However, in region B the core bends the lattice planes back towards the Bragg orientation, so that much more intensity is scattered into the reflection, giving image contrast displaced to this side.

If a (111) interfacial hexagonal dislocation network, with no extended nodes, is imaged using either the $\bar{2}20$ or $2\bar{2}0$ reflection, the ideal theoretically predicted contrasts are shown in fig 6.6. It is assumed

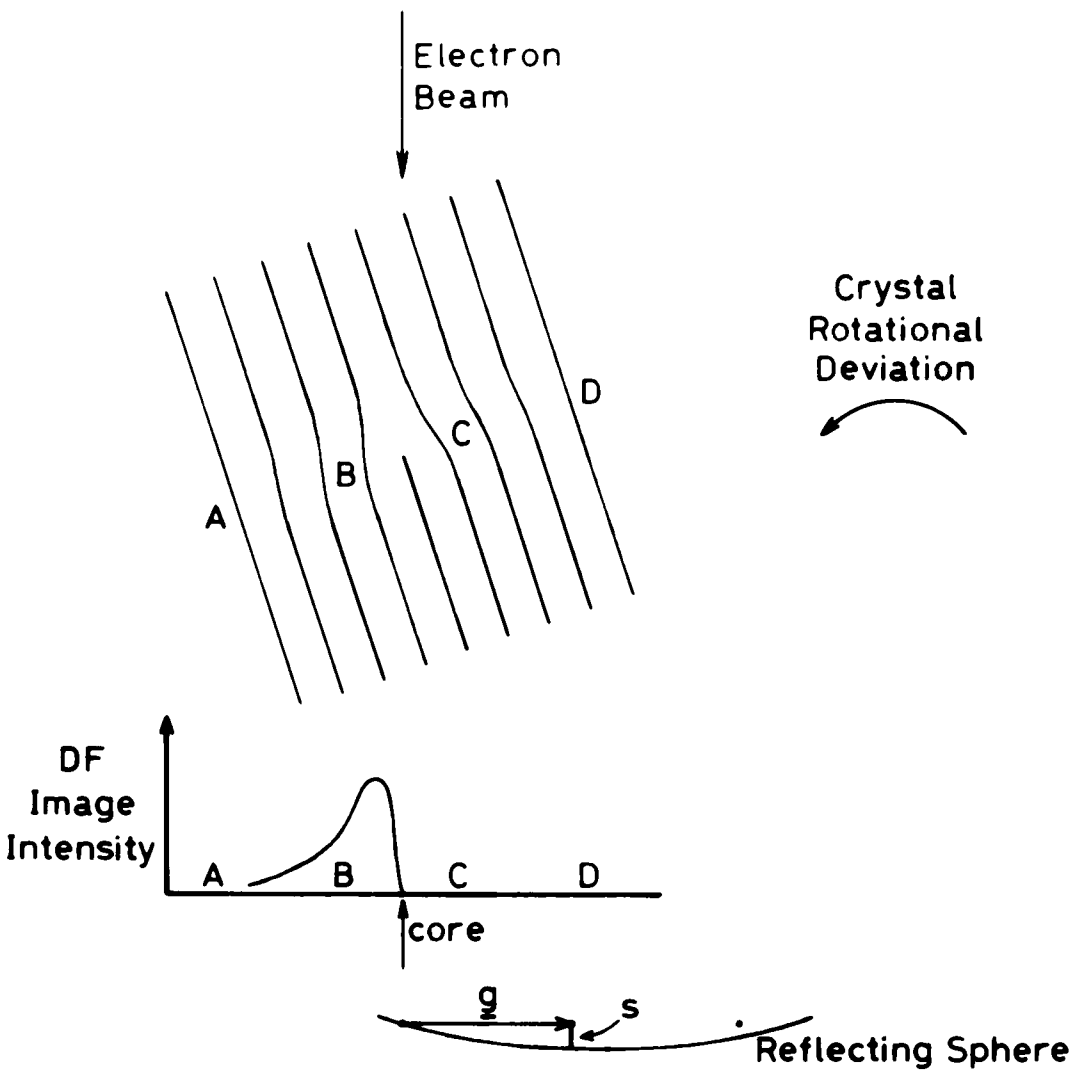
that the Ge is on the upper side of the heterojunction, with the extra atom planes of the dislocations beneath in the Si, which has the smaller lattice parameter. The contrast behaviour is analogous to that observed by Booker and Brown (1965) for screw dislocation networks in Si. Two prominent features are that (a) the contrasts are asymmetric, and (b) the nature of the asymmetry reverses when $\underline{g}$ is reversed. The dislocation segments perpendicular to $\underline{g}$ have $\underline{g}.\underline{b} = 2$, and are most intense. All other parts of the network have $\underline{g}.\underline{b} = 1$ and give weaker contrast. The network asymmetry is produced by movement of the dislocation images from the core positions, in accordance with the scheme illustrated in fig 6.5. The displaced line images are broken at points where they approach an underlying dislocation core. The nature of the contrast should change markedly when the operating reflection is changed to either $\bar{1}\bar{1}3$ or $11\bar{3}$, as also shown in fig 6.6. In either case, dislocations parallel to $\underline{g}$ have $\underline{g}.\underline{b} = 0$, and therefore, are out of contrast. All other parts of the network have $\underline{g}.\underline{b} = 2$. The image asymmetries are produced in a manner similar to those which occurred for $\bar{2}20$ type reflections.

When Ge films, which had been grown on (111) Si substrates under conditions that minimized alloy formation (section 4.6.1), were examined using $2\bar{2}0$ and $\bar{1}\bar{1}3$ type reflections with moderate positive deviations from the Bragg positions, interfacial network images of the type shown in fig 6.7 were obtained. The images changed considerably with g, and closely resembled their respective idealized theoretical contrasts, expected for hexagonal edge dislocation networks. Further, the contrast asymmetries observed for these two reflections are consistent with one another, and confirm that the extra atom planes of the dislocations were, indeed, below the plane of the networks in the Si substrates.

When Ge films were grown under conditions of enhanced Ge/Si alloy formation, the interfacial dislocation networks were less regular. Such

Fig 6.5 Diagram illustrating the manner in which a dark-field TEM image of an edge dislocation is displaced to one side of the actual dislocation core position.

Fig 6.6 Diagram illustrating the ideal theoretically predicted contrasts which should be given by a hexagonal edge dislocation network. Note contrast asymmetries and the way in which these change with $\underline{g}$ vector. ($\bar{2}20$, $2\bar{2}0$, $\bar{1}\bar{1}3$ and $11\bar{3}$ reflections, strong-beam conditions)


Electron
Beam
Crystal
Rotational
Deviation
A
B
C
D
DF
Image
Intensity
A
B
C
D
core
g
s
Reflecting Sphere

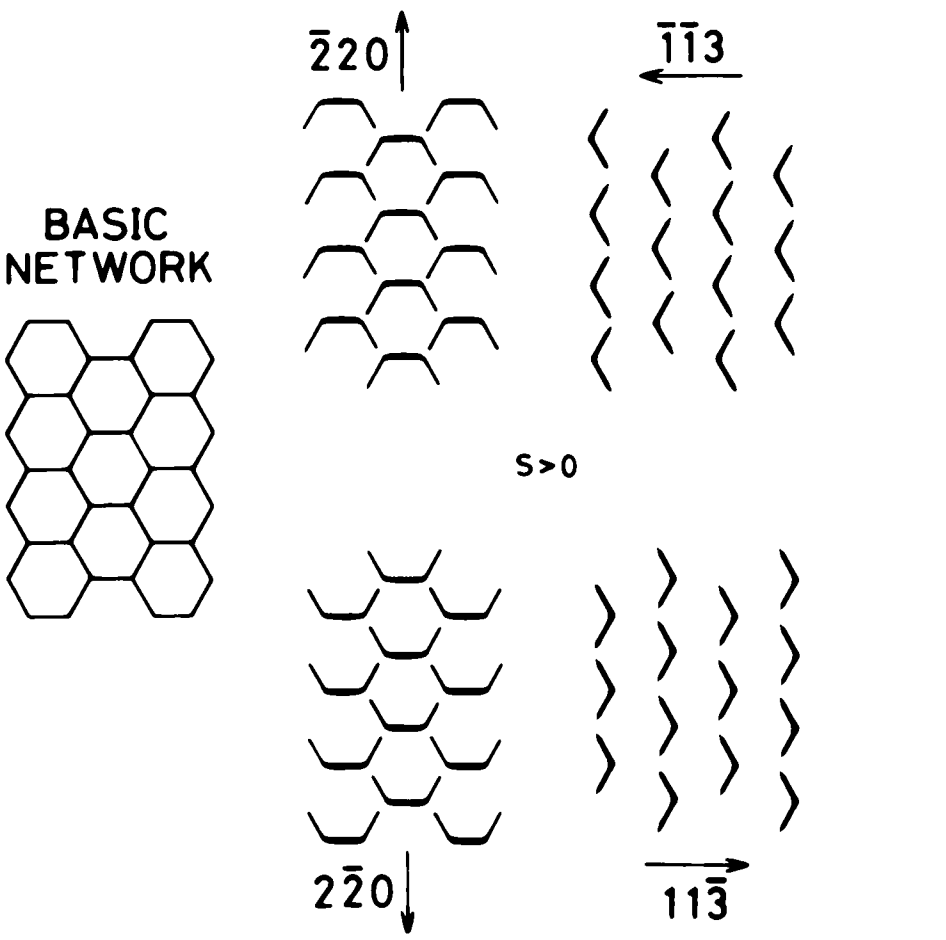
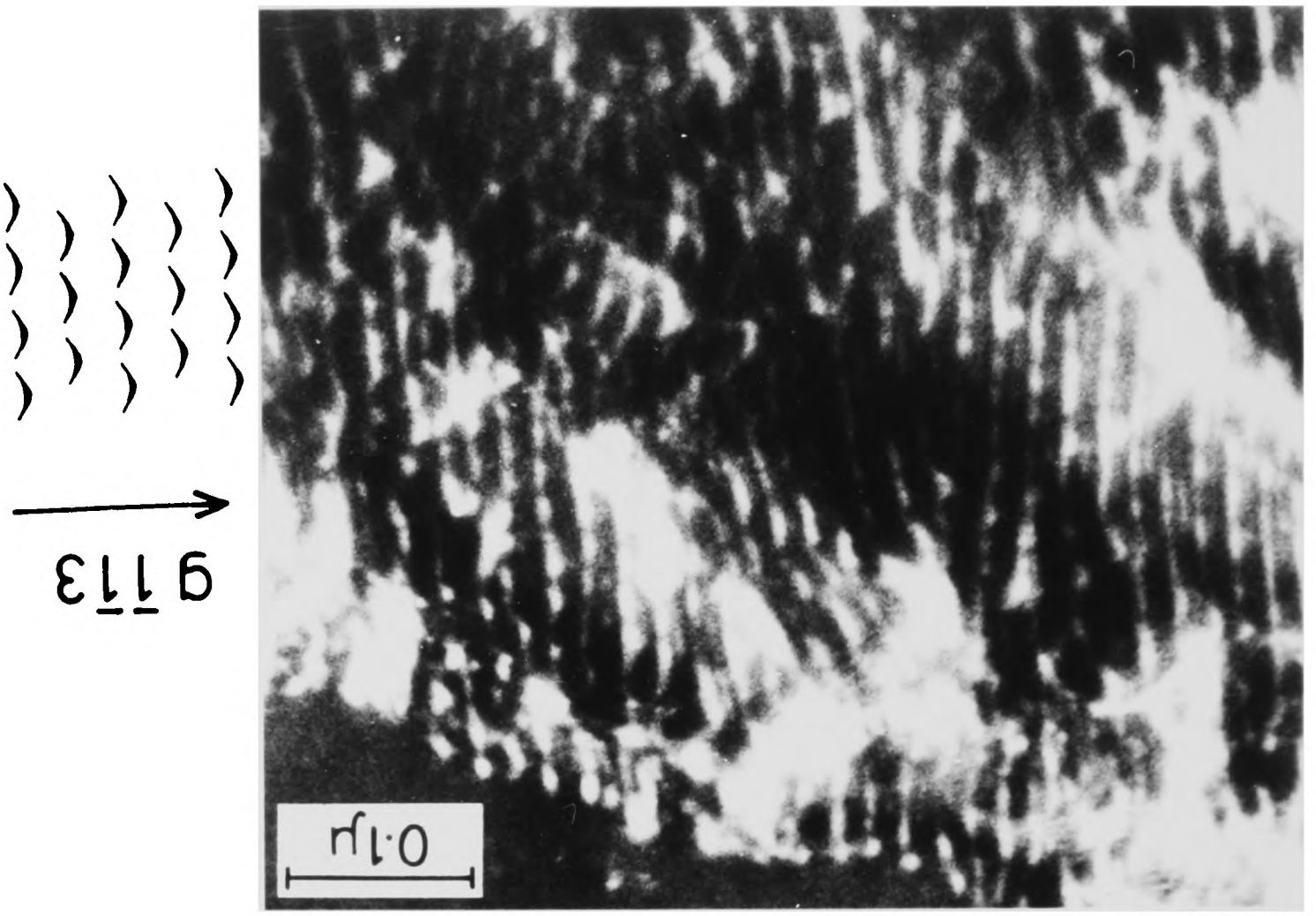

BASIC
NETWORK
$\bar{2}20$
$\bar{1}\bar{1}3$
S>0
$2\bar{2}0$
$11\bar{3}$

Fig 6.7 A hexagonal dislocation network at the Ge/(111)Si interface. Note that the contrasts correspond to those theoretically predicted (also shown). (Transmission electron micrographs of same specimen area, dark-field, $2\bar{2}0$ and $\bar{1}\bar{1}3$ type reflections)


g 11̄3
0.1μ

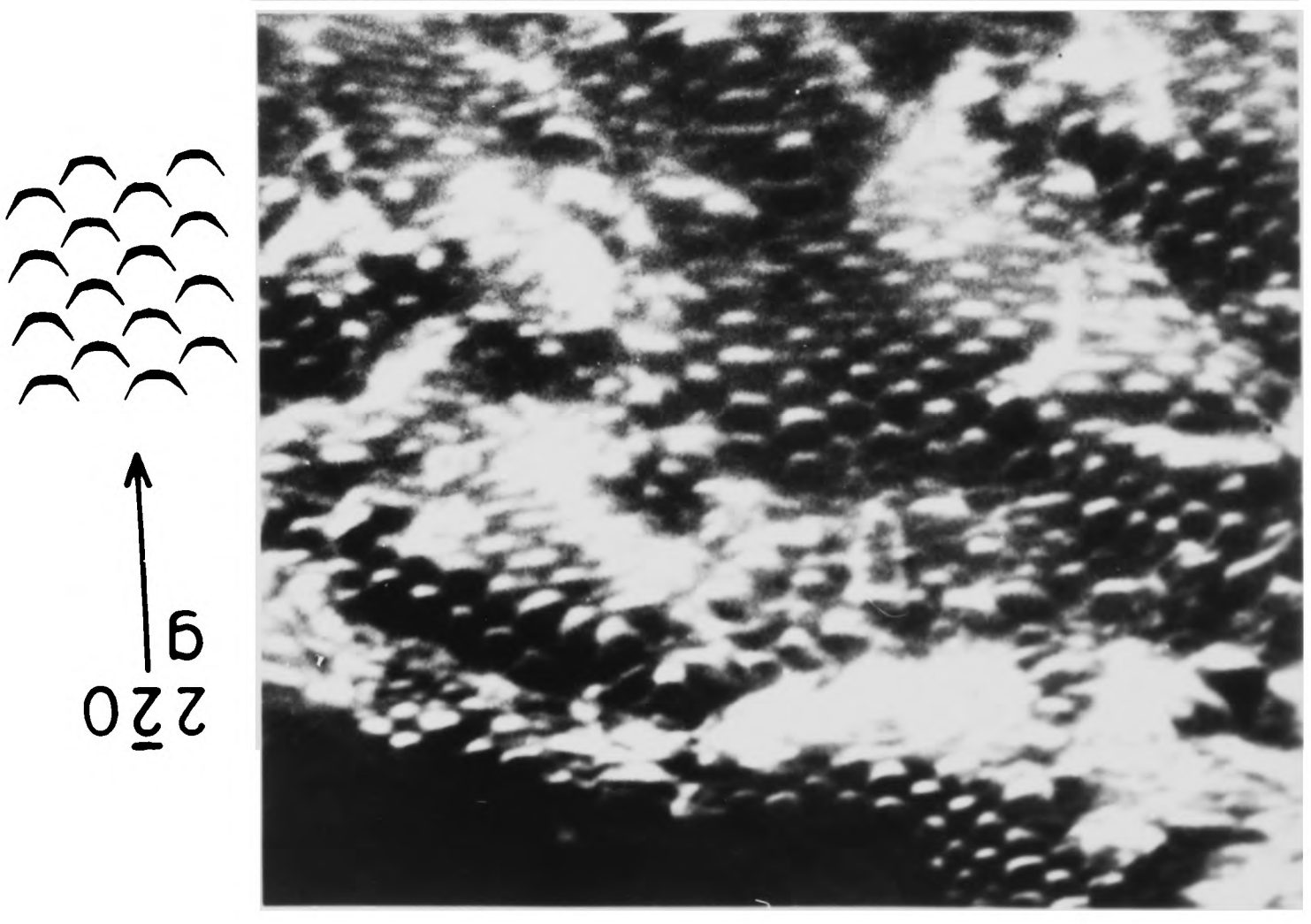
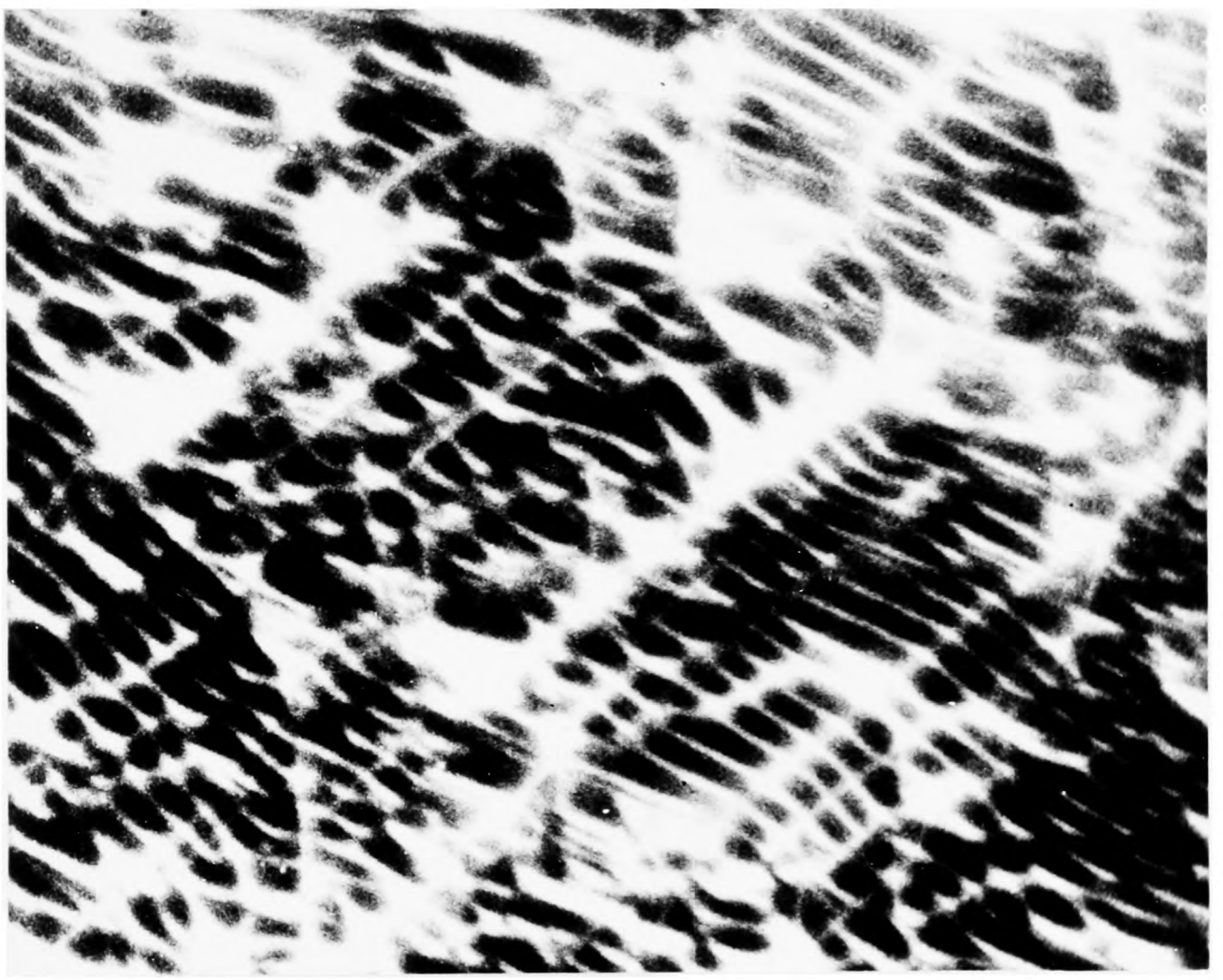
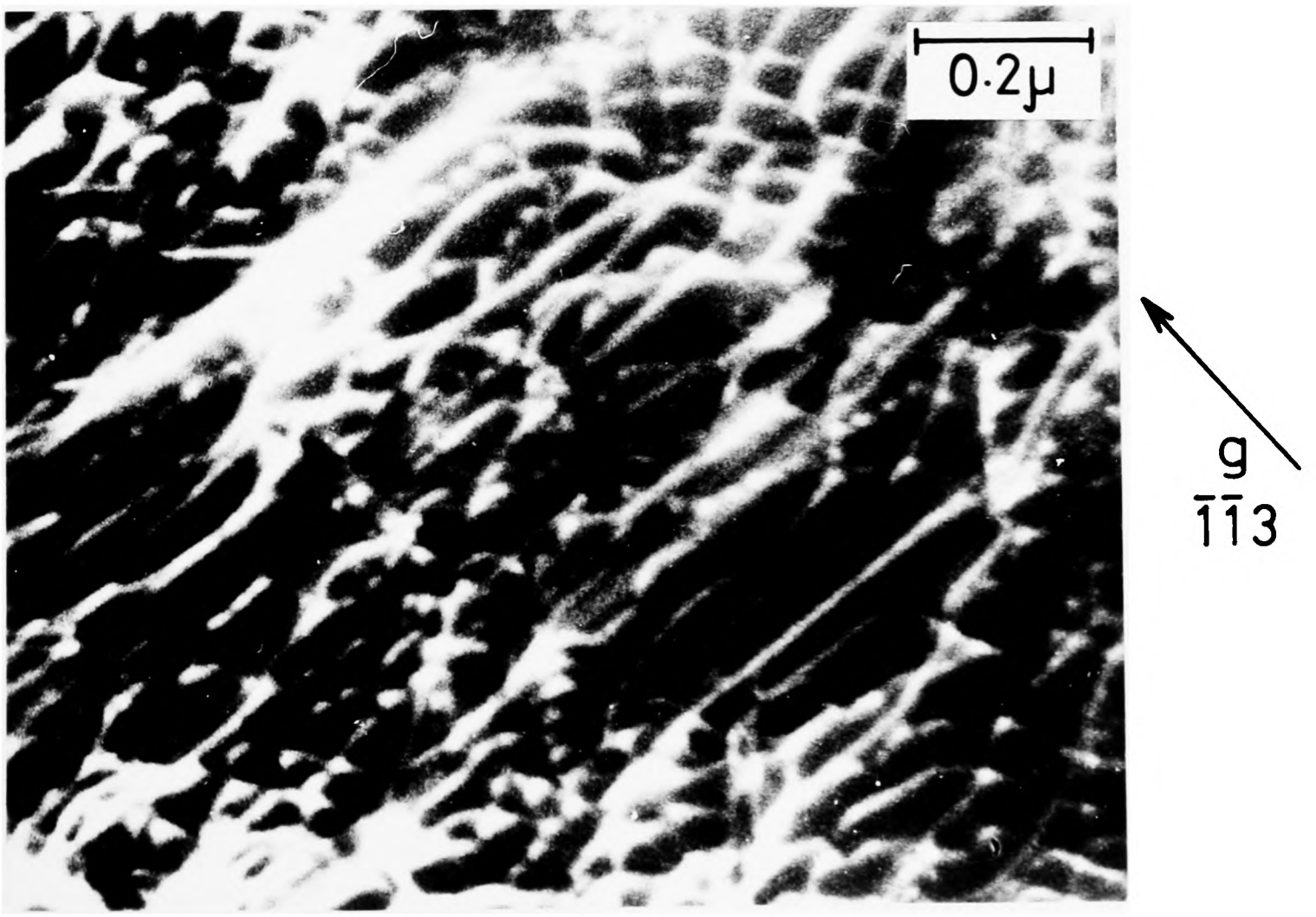

g
220

Fig 6.8 An irregular dislocation network at the Ge/(111)Si interface. Note many dislocations give change in image intensity with change in direction of $\underline{g}$ vector. (Transmission electron micrographs of same specimen area, dark-field, $3\bar{1}\bar{1}$ and $\bar{1}\bar{1}3$ reflections)


g
3$\bar{1}\bar{1}$


0·2μ
g
$\bar{1}\bar{1}$3

a network is shown in fig 6.8 separately imaged using two rotationally displaced $11\bar{3}$ type reflections. The set of parallel dislocations passing diagonally across the top micrograph are invisible in the lower micrograph, indicating that $\underline{g}.\underline{b} = 0$ when $\underline{g}$ is parallel to the dislocation lines. This implies that these dislocations are in edge orientation and that such networks had, overall, substantial edge character, as would be expected for misfit accommodation.

6.3.3) Interfacial Fringe Images

In the literature, there exists a certain confusion regarding the expected TEM image contrast from networks of closely spaced dislocations. To make clear the contrast behaviour of such a network as the deviation from an operating Bragg reflection varies, it is desirable first to discuss the contrast produced by different interfacial atomic arrangements. Fig 6.9 shows a cross-section through a mismatching (111) FCC interface, with no rotational displacement, and across which there are no atomic interactions (i.e. a section through an interface of the type given in fig 6.3). The lines represent pairs of $\{1\bar{1}0\}$ type lattice planes (spacings d_1 and d_2 respectively), and coincidence between the two sets occurs at intervals given by $d_1 d_2/(d_1 - d_2)$. In the TEM, using a $2\bar{2}0$ type reflection, such an interface would give a Moiré pattern with half this periodicity, since the reflecting planes have half the $(1\bar{1}0)$ plane spacing. In general terms, using reflection g (hkl), the Moiré spacing (D_m) produced by interference of electron waves diffracted into reciprocal lattice points $\underline{g}_1$ in the first crystal and $\underline{g}_2$ in the second crystal is given by

$$D_m = |\underline{g}_1 - \underline{g}_2|^{-1} = |\Delta \underline{g}|^{-1} \qquad (6.4)$$

Remembering that $|\underline{g}| = 1/d$, this way be re-written

$$D_m = \frac{a_1 a_2}{(a_1 - a_2)(h^2 + k^2 + l^2)^{\frac{1}{2}}} \qquad (6.5)$$

where a_1 and a_2 are the FCC lattice parameters of the mismatching crystals ($a_1 > a_2$). The form of the $2\bar{2}0$ type Moiré fringes is also shown in fig 6.9, and their intensity (I_m) is given (Hirsch et al, 1965) by an expression of the type

$$I_m = \frac{1}{w^2}\left(\sin^2\pi h_1 s + \sin^2\pi(h-h_1)s + 2\sin\pi h_1 s \sin\pi(h-h_1)s \cos(\pi sh + \alpha)\right) \tag{6.6}$$

where h is the foil thickness, h_1 is the depth of the interface and α is the wave phase factor

$$\alpha = 2\pi\Delta g.\underline{r} \tag{6.7}$$

where $\underline{r}$ is the position vector in the interface parallel to Δg. Eq 6.6 assumes the kinematical approximation, and that both ξ_g and s are the same for each of the overlapping crystals. Although more comprehensive expressions are given by e.g. Gevers (1962) and Jacobs et al (1966), eq 6.6 shows that the fringes are cosinusoidal, and that while their general spacing is fixed (eq 6.5), their phase and intensity depend upon h, h_1 and s.

If the atoms on either side of the interface are allowed to interact and attain equilibrium positions (section 6.3.1), then the lattice planes deform to produce an array of edge dislocations as illustrated in fig 6.10 (a cross-section through fig 6.4a). Since overall coincidence between the $\{1\bar{1}0\}$ planes still occurs at intervals of $d_1\, d_2/(d_1 - d_2)$, the ideal dislocation spacing (D_d) also has this magnitude, and may be written

$$D_d = \frac{a_1 a_2}{(a_1 - a_2)2^{\frac{1}{2}}} \tag{6.8}$$

Also, if $D_d \gg \xi_g$, the form of the TEM interfacial image contrast changes with the introduction of the dislocation strain fields. This change may be considered in terms of a sharpening of some of the original Moiré contrast peaks, and a broadening of others. The form of a $\underline{g}.\underline{b} = 2$ image (i.e. using a $2\bar{2}0$ type reflection) is also illustrated in fig 6.10, where the periodicity is now half that of the original Moiré fringes, and the position of contrast

peaks is fixed in relation to the film dislocations (Howie and Whelan, 1962).

While this treatment of interfacial image contrast behaviour is valid in the presence of misfit dislocations when $D_d \gg \xi_g$, if the dislocations are very closely spaced such that $D_d < \xi_g$ they interact with one another, and the image begins to resemble a Moiré pattern once again. The relationship between Moiré and dislocation images was noted by Baker (1970), but Thölén (1970) carried out the appropriate computations for a twist boundary, and then generalized his results to a treatment of any interface.

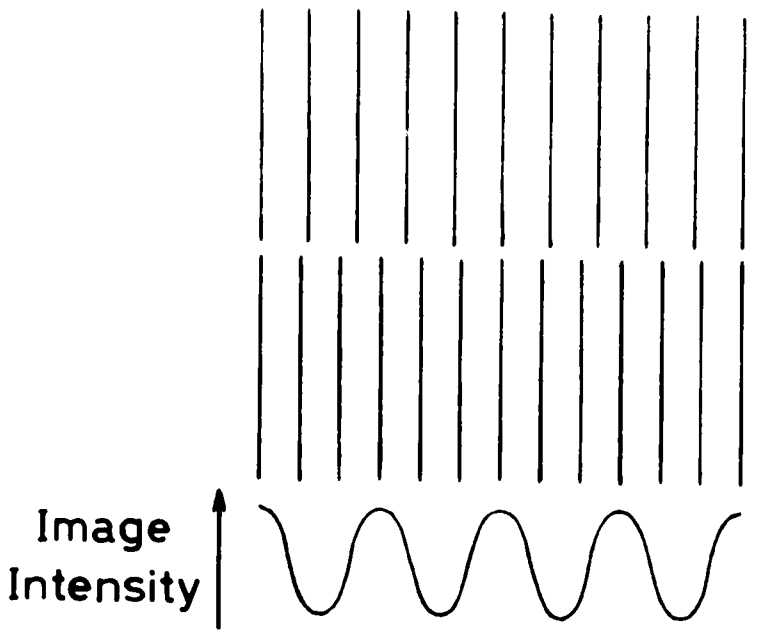
Thölén considered two different situations, which are illustrated in fig 6.11. While integrating down a column through the foil in the standard manner (Hirsch et al, 1965) to obtain the diffracted beam intensity (two-beam approximation), he considered the possibility that the interfacial phase shift $2\pi\Delta\underline{g}.\underline{R}$ could occur in two different ways, ($\underline{R}$ is the lattice displacement vector across the column). These were either (i) as a step-function at the interface, or (ii) as a linear function of distance (Δz) across the interface (these correspond approximately to the diagrams shown in figs 6.9 and 6.10 respectively). He found that under relatively strong-beam conditions, when Δz became sufficiently small compared to the extinction distance, both ways of treating the phase shift yielded the same result - a uniform fringe profile. It then became impossible to distinguish between dislocation images and Moiré fringes, because the electron waves were insensitive to the details of the actual atomic arrangement at the interface.

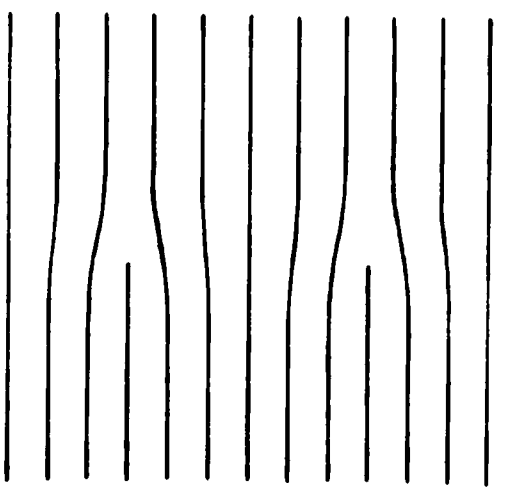
When edge dislocations of the same sign are packed closely together at an interface, their strain fields overlap and those from adjacent dislocations tend to cancel one another. In this way, the mean displacement of the crystal lattice at a substantial distance from the interface decreases

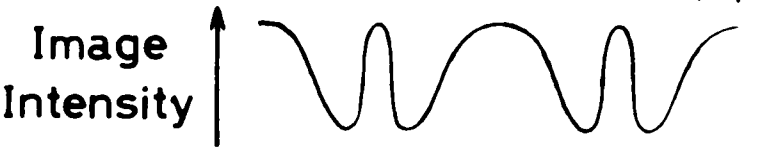
Fig 6.9 Diagram showing cross-section through mismatching (111) FCC interface, across which there are no atomic interactions. Lines represent pairs of $\{1\bar{1}0\}$ type lattice planes. Idealized TEM Moiré fringe image also shown, corresponding to $2\bar{2}0$ type reflection ($s = 0$).

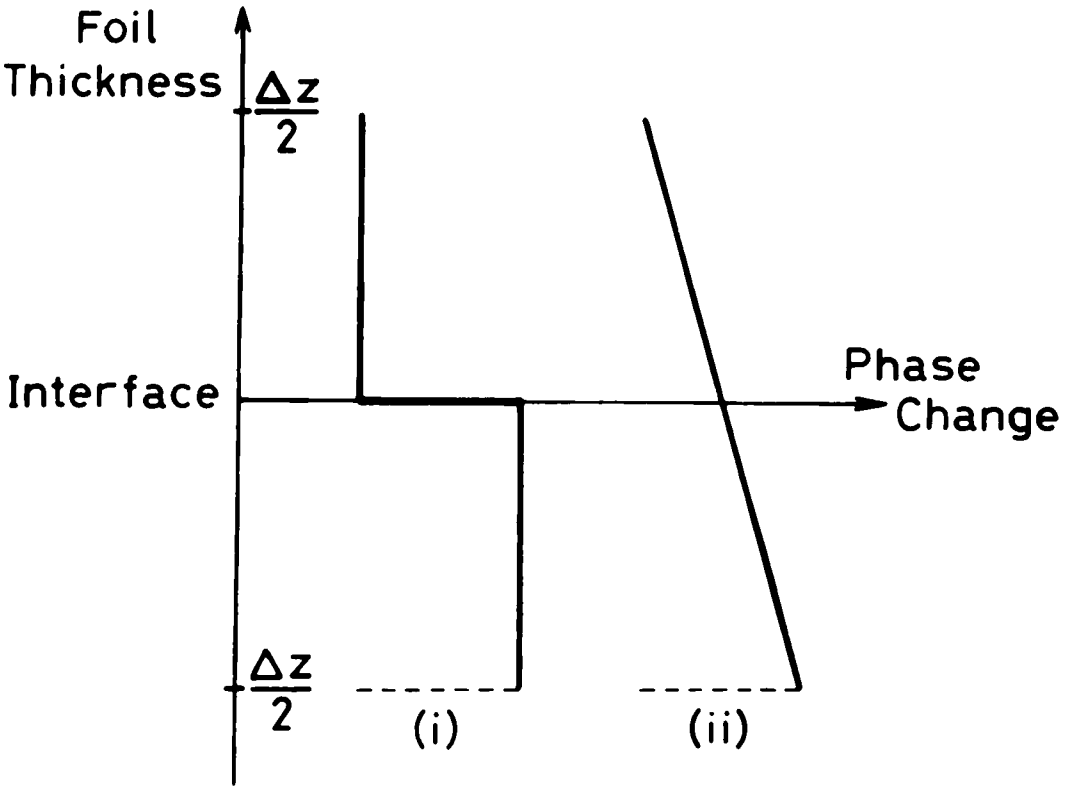
Fig 6.10 Diagram showing cross-section through mismatching (111) FCC interface, across which there has been complete relaxation to form an array of edge dislocations. Lines represent pairs of $\{1\bar{1}0\}$ type lattice planes. Idealized TEM dislocation images also shown, corresponding to $2\bar{2}0$ type reflection ($s = 0$).

Fig 6.11 Diagram illustrating two different ways in which interfacial electron wave phase change may occur: (i) as a step function at the interface, or (ii) as a linear function of distance (Δz) across the interface (after Thölén, 1970).


Image
Intensity




Image
Intensity


Foil
Thickness
Δz/2
Interface
Phase
Change
Δz/2
(i)
(ii)

as D_d decreases, and for this reason, the phase change $2\pi\Delta g.R$ across the interface occurs in an even narrower zone (Δz wide). Thölén's results indicate that when $D_d \lesssim \frac{1}{3}\xi_g$, Δz has become sufficiently small so that a strong fringe profile, corresponding to the Moiré image, should be produced.

When Ge/(111)Si interfacial dislocation networks were imaged in the TEM using strong two-beam conditions (i.e. $s \simeq 0$), it has already been stated (section 4.6.1) that, for sufficiently small values of D_d, a strong fringe image was obtained. This is the image expected, according to Thölén's calculations, for closely spaced dislocations, and an example is shown in fig 6.12. However, it is also clear from this figure that, as the foil bends away from the Bragg reflecting position, the image gradually transforms and details of the dislocation network are revealed. This transformation was noted in section 4.6.1, and was fundamental to the discussion in section 6.3.2. This may be considered to occur due to the effective decrease in ξ_g, and the necessity to replace it by ξ_g^w according to eq 6.1, as $|s|$ increases. In these circumstances, Thölén's criterion for the production of fringe image should perhaps be re-written as $D_d \lesssim \frac{1}{3}\xi_g^w$, so that as $|s|$ increases (ξ_g^w decreases), more closely spaced dislocations are progressively 'resolved'. In the limit of weak-beam conditions ($|s|$ large), all the dislocation networks examined during the present work were effectively 'resolved', and the next section gives a detailed description of the Ge/(111)Si network structure.

Although Thölén showed the relationship between Moiré fringe and dislocation images, unfortunately he did not consider the use of weak-beam conditions. Instead, he discussed images only in relation to ξ_g, and he concluded that it was impossible to distinguish a genuine Moiré image from that of closely spaced dislocations ($D_d \lesssim \frac{1}{3}\xi_g$) by any operations in a conventional TEM. Since this included specimen tilting experiments, his conclusion is clearly invalid as demonstrated by much of the present work.

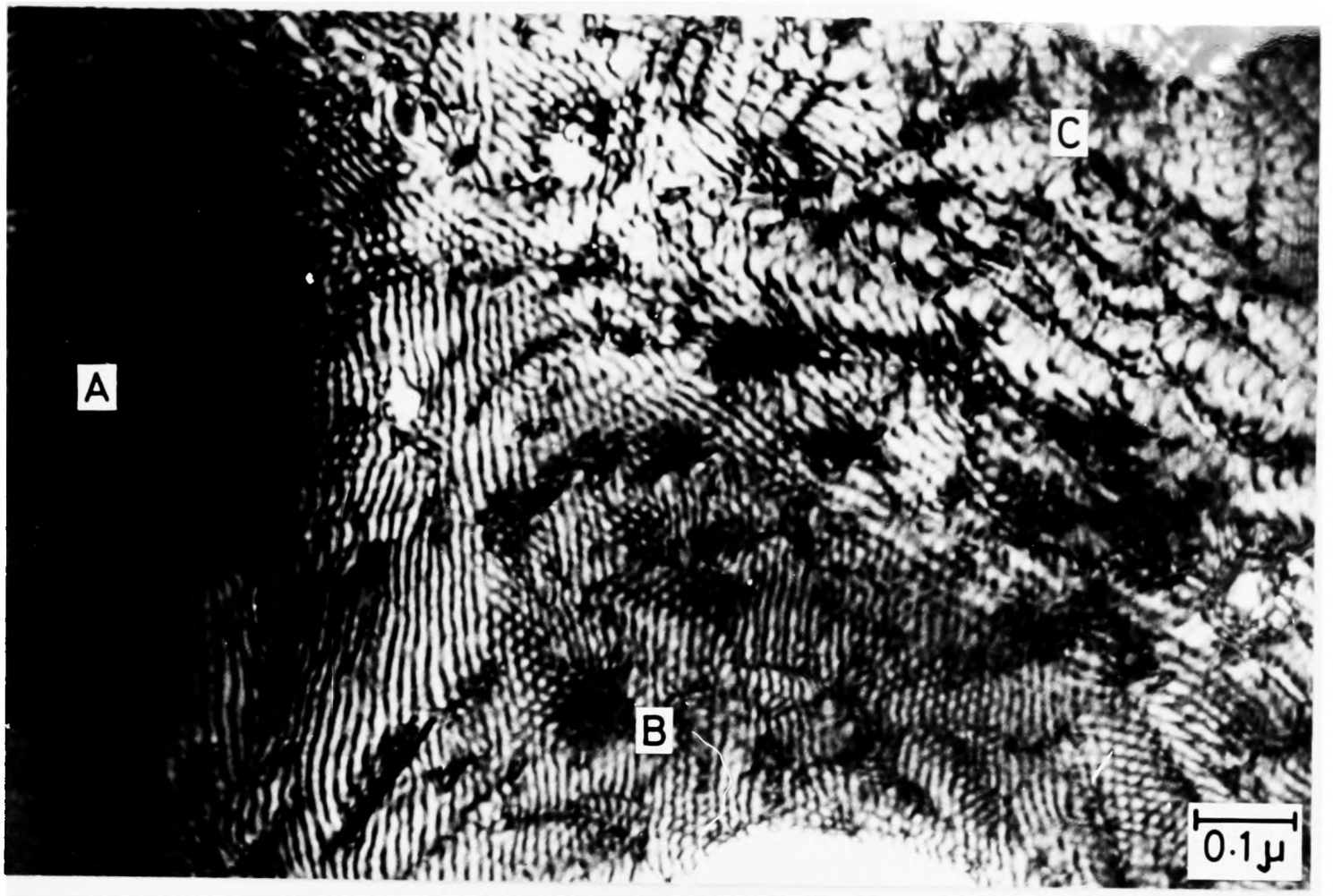
These considerations also provide an explanation for an otherwise potential anomaly. It was stated in section 4.6.1 that when the Ge/(111)Si fringe image was removed by tilting specimens from the appropriate Bragg position, underlying film defects, including inclined stacking faults, became visible. Now, using the kinemetical approximation (valid when |s| is large), stacking fault image intensity (I_f) is given by an expression analogous to eq 6.6, so that $I_f \propto \frac{I}{w^2}$ (Whelan and Hirsch, 1957). Therefore, the intensities of conventional Moiré fringes and stacking fault fringes both depend upon w, and hence s, in the same manner. However, the experimentally observed fringes violated this dependence, since they became invisible for much smaller values of |s| than stacking fault fringes. This, then, emphasizes the fact that the dislocation network fringes encountered in the present work were not produced under the same circumstances as conventional Moiré fringes, but arose by electron wave interference across a phase shift zone, the width of which could not be neglected.

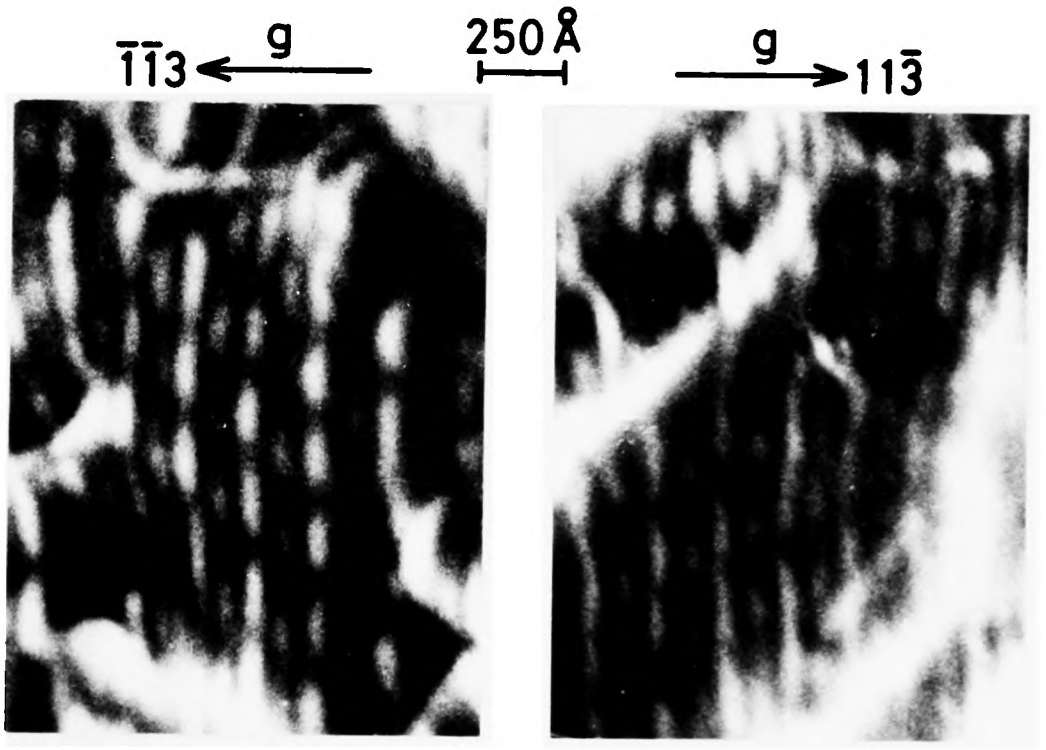
The discussion in this section raises an interesting question concerning the terminology used to describe fringe images of dislocation networks. Should they be called dislocation images or Moiré fringes? The author considers that either description is acceptable, provided that it is correctly applied. Thus, if the dislocation description is used, it is important to recognise that the overall form of the image is determined by diffraction conditions, rather than by details of network structure (presumably, e.g. contrary to the description used by Ito and Takahashi (1968): see section 4.7.2). Alternatively, if the Moiré description is used, it is important to note that the interfacial wave phase change takes place over a zone which has non-zero width in the general case. Dislocation strain fields in this zone may introduce a distortion of the fringes, and induce them to become non-cosinusoidal to an extent dependent upon experimental conditions.

Fig 6.12 [111] pole region (A) gives hexagonal fringe pattern, but as foil bends so that only one $2\bar{2}0$ type reflection is strongly excited, only one set of fringes results (B). Further bending from this Bragg orientation gives an image which shows the underlying defects (C). (Transmission electron micrograph, bright-field, $2\bar{2}0$ type reflections)

Fig 6.13 Ge/(111)Si interfacial dislocation network. Note reversal of contrast asymmetries with reversal of $\underline{g}$ vector. (Transmission electron micrographs, dark-field, $\bar{1}\bar{1}3$ and $11\bar{3}$ reflections)

Fig 6.14 Diagram illustrating idealized strong-beam TEM images which should be given by a hexagonal dislocation network with all intrinsic nodes extended; $\bar{1}\bar{1}3$ and $11\bar{3}$ reflections.





BASIC NETWORK

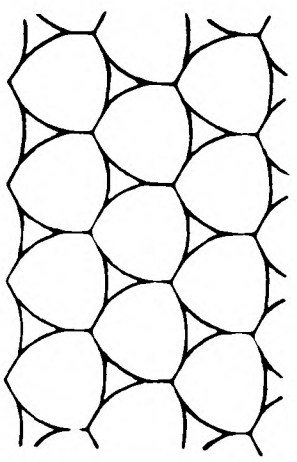
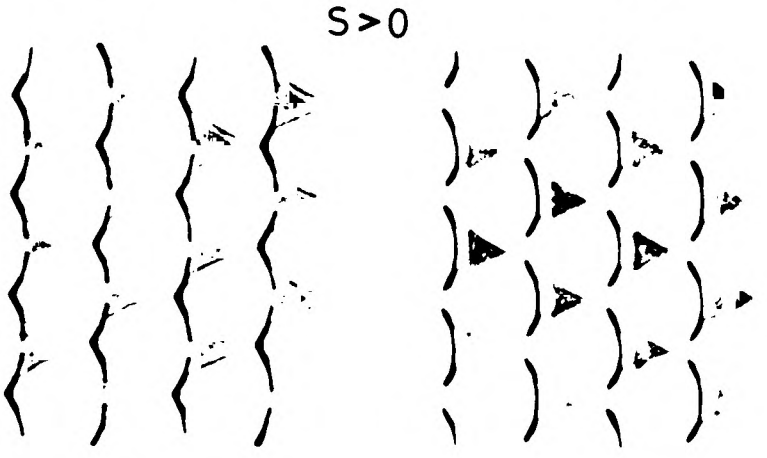


IMAGE CONTRAST (Strong Beam)

$\bar{1}\bar{1}3 \longleftarrow g \longrightarrow 11\bar{3}$



6.3.4) Observations Using Weak Beams

Careful examination of micrographs of the type shown in fig 6.7a, taken using $2\bar{2}0$ type reflections, indicated that while the interfacial contrasts were substantially as expected for edge dislocation networks, they were, nevertheless, subject to detailed distortions. This suggested that some of the dislocation nodes may have been extended to produce a region of stacking fault, possibly as in fig 6.4a, which would lead to a distortion of the basic hexagonal structure of the network. Now, for a stacking fault on a (111) plane, the image intensity depends upon the magnitude of $\underline{g}.\underline{R}$, where $\underline{R}$ is the fault lattice displacement vector, which can take values $\pm \frac{a}{3}[111]$ depending upon the intrinsic or extrinsic nature of the fault. If $\underline{g}.\underline{R}$ is an integer (or zero), then the fault is invisible. Therefore, if any of the dislocation nodes were extended, the associated stacking fault would exhibit no contrast with an operating $2\bar{2}0$ type reflection ($\underline{g}.\underline{R} = 0$). However, such a fault would exhibit contrast with operating reflections of types $\bar{1}\bar{1}3$ or $\bar{1}\bar{1}1$, since in either case $\underline{g}.\underline{R} = \pm\frac{1}{3}$. Therefore, images recorded using reflections of these types were studied in detail (Cullis and Booker, 1971b).

Micrographs were recorded using opposing $\bar{1}\bar{1}3$ and $11\bar{3}$ reflections with moderate positive deviations from the respective Bragg positions ($s \sim 4 \times 10^{-3}$ Å^{-1}). Fig 6.13 shows such a pair, where the epitaxial film was grown by Ge deposition at ~ 1 Å sec^{-1} with a substrate temperature of 840°C. The $\bar{1}\bar{1}3$ image is similar to fig 6.7b, but shows more detail. For comparison, fig 6.14 provides diagrams illustrating, in an idealized way, the images which would be given under strong-beam conditions ($s > 0$) by a network ($D_d \gtrsim \xi_{113}$) with all intrinsic nodes extended, as shown. These diagrams indicate that when the direction of $\underline{g}$ is reversed, the extended node fault contrast remains the same, while the dislocation contrast behaviour is asymmetrical. For example, the dislocation contrast

immediately to the left of a particular node (fig 6.14) is a minimum for the $\bar{1}\bar{1}3$ reflection, and a maximum for the $11\bar{3}$ reflection. The micrographs (e.g. fig 6.13) also showed this reversal effect, if it was assumed that the 'blobs' between the dashed lines of dislocation contrast were the extended node fault contrast. However, the dislocation contrast was further from the fault contrast for the $\bar{1}\bar{1}3$ reflection than expected, and also the fault contrast was not clearly triangular. These differences may be partly due to incomplete elimination of the fringe image (section 6.3.3), since in this case, on deviating from the Bragg position alternate fringes disappeared, i.e. fringes originally linked the remaining 'blobs' of contrast. This possibility was given support, since when the specimen was further tilted (towards weak-beam conditions), the resulting network images more closely resembled the diagrams. However, the contrast then became rather weak, and it was found that a significant improvement could be achieved using $\bar{1}\bar{1}1$ type reflections. This may be related to the dependence of fault contrast upon $\frac{1}{w^2}$ (section 6.3.3), which, for a given value of s, is larger for a $\bar{1}\bar{1}1$ than a $\bar{1}\bar{1}3$ type reflection.

Epitaxial films were examined using both $\bar{1}\bar{1}1$ and $11\bar{1}$ operating reflections under weak-beam conditions, and values of $|s|$ were typically $0.8 - 1.3 \times 10^{-2}$ Å^{-1}. When images were recorded using the $\bar{1}\bar{1}1$ reflection with the sign of s negative, large arrays of similarly orientated triangular contrasts (often 150 - 200 Å across) were observed. Fig 6.15a shows such an image, where the film was grown by Ge deposition at ~ 2 Å sec^{-1} with a Si substrate temperature of 920°C. The triangular contrasts were taken to be intrinsic stacking faults present in one set of extended interfacial dislocation nodes, since the image expected for such a network is somewhat similar to that shown in fig 6.14 for the $\bar{1}\bar{1}3$ reflection. However, under weak-beam conditions, the displacements of the dislocation images from the edges of the stacking faults are expected to be quite small,

as can be observed in fig 6.15a. Comparison with fig 6.4 confirms that the triangular contrasts point in the direction expected for intrinsic nodes. Also, from fig 6.4 and table 6.2 it is clear that the parallel lines of contrast are partial dislocations for which $\underline{g}.\underline{b}_p = \pm\frac{2}{3}$. The partial dislocations bounding the other two sides of the intrinsic nodes are out of contrast, and for them $\underline{g}.\underline{b}_p = \pm\frac{1}{3}$. Although the relative intensities of the partial dislocation images are in good agreement with the respective $\underline{g}.\underline{b}$ values (Hirsch et al, 1965), caution must be used in interpreting weak-beam images in this way, as will be demonstrated in section 6.5.2.

While many of the intrinsic nodes were spread over most of the distance between the dislocation rows, some were markedly truncated indicating that they may have been touching opposing extrinsic dislocation nodes. However, careful examination of micrographs such as fig 6.15a revealed that these extrinsic nodes were out of contrast. This supposition was verified when, for the operating $\bar{1}\bar{1}1$ reflection, the sign of s was inverted (i.e. s became positive). The overall appearance of the image changed strikingly, as shown in fig 6.15b, and while the relatively large intrinsic nodes became invisible, some smaller, oppositely orientated, trucated triangular contrasts were rendered visible for the first time. These were identified as extended extrinsic nodes in the interfacial dislocation network (Cullis and Booker, 1971b). However, while all the intrinsic nodes (e.g. fig 6.15a) were extended and of relatively uniform size, the extrinsic nodes were mostly much smaller, and were present in a range of sizes, sometimes being completely contracted. To illustrate the relative dimensions of the two sets of nodes, the central portions of figs 6.15a and b are shown at higher magnification in fig 6.16. An idealized model of the interfacial dislocation network is provided in fig 6.17 to demonstrate the manner in which the nodes interacted with one another (the extrinsic set are drawn of uniform size for convenience of illustration).

Fig 6.15 Weak-beam $\bar{1}\bar{1}1$ dar'-field TEM images of Ge/(111)Si interfacial dislocation network (same specimen area). Accompanying diagrams give approximate diffraction conditions:

a) s negative, note the relatively large, similarly oriented, triangular contrasts;

b) s positive, note the smaller truncated triangular contrasts.

(125 kV)

(a)

$\bar{1}\bar{1}1$

WB ⊙

• BF

500Å

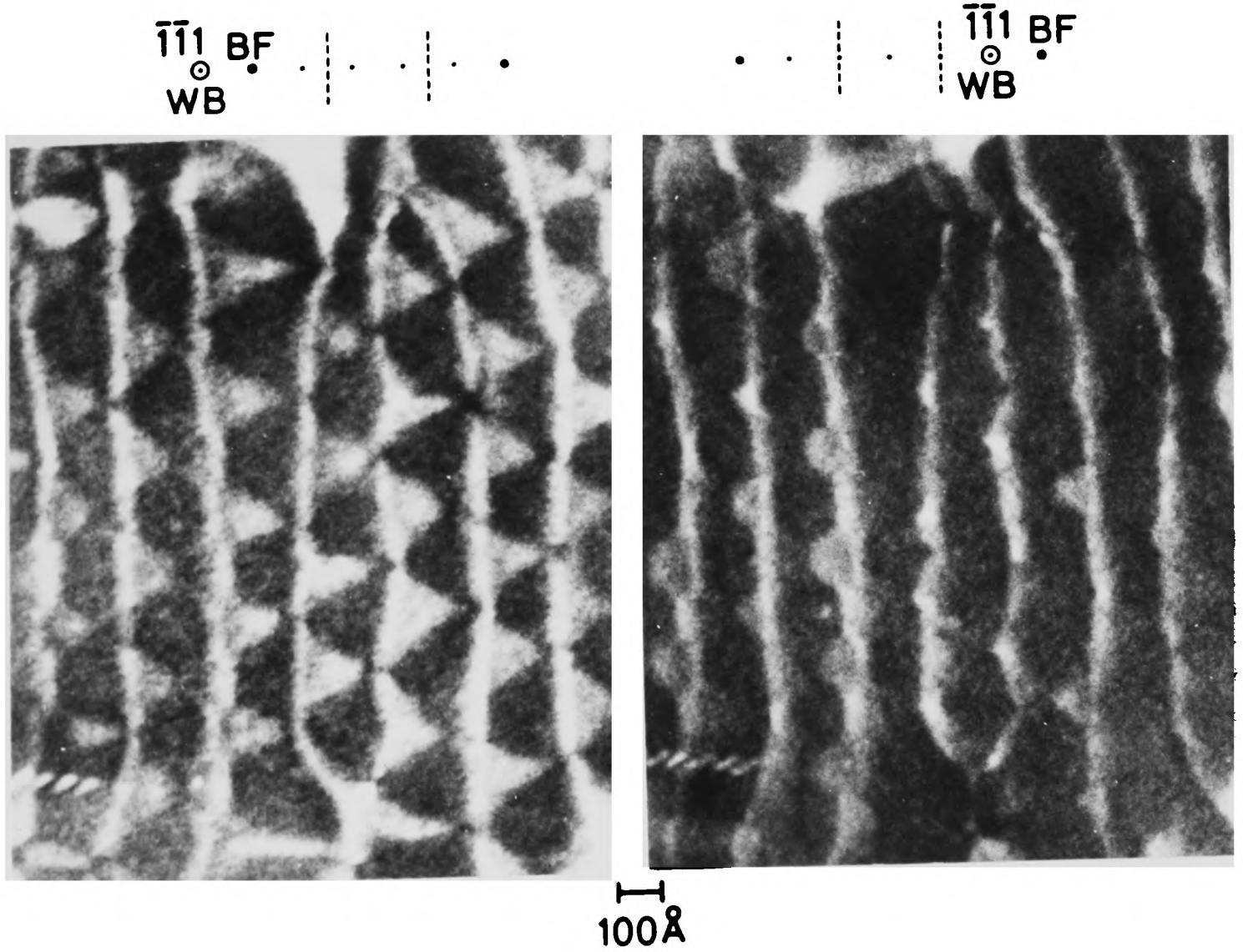
(b)

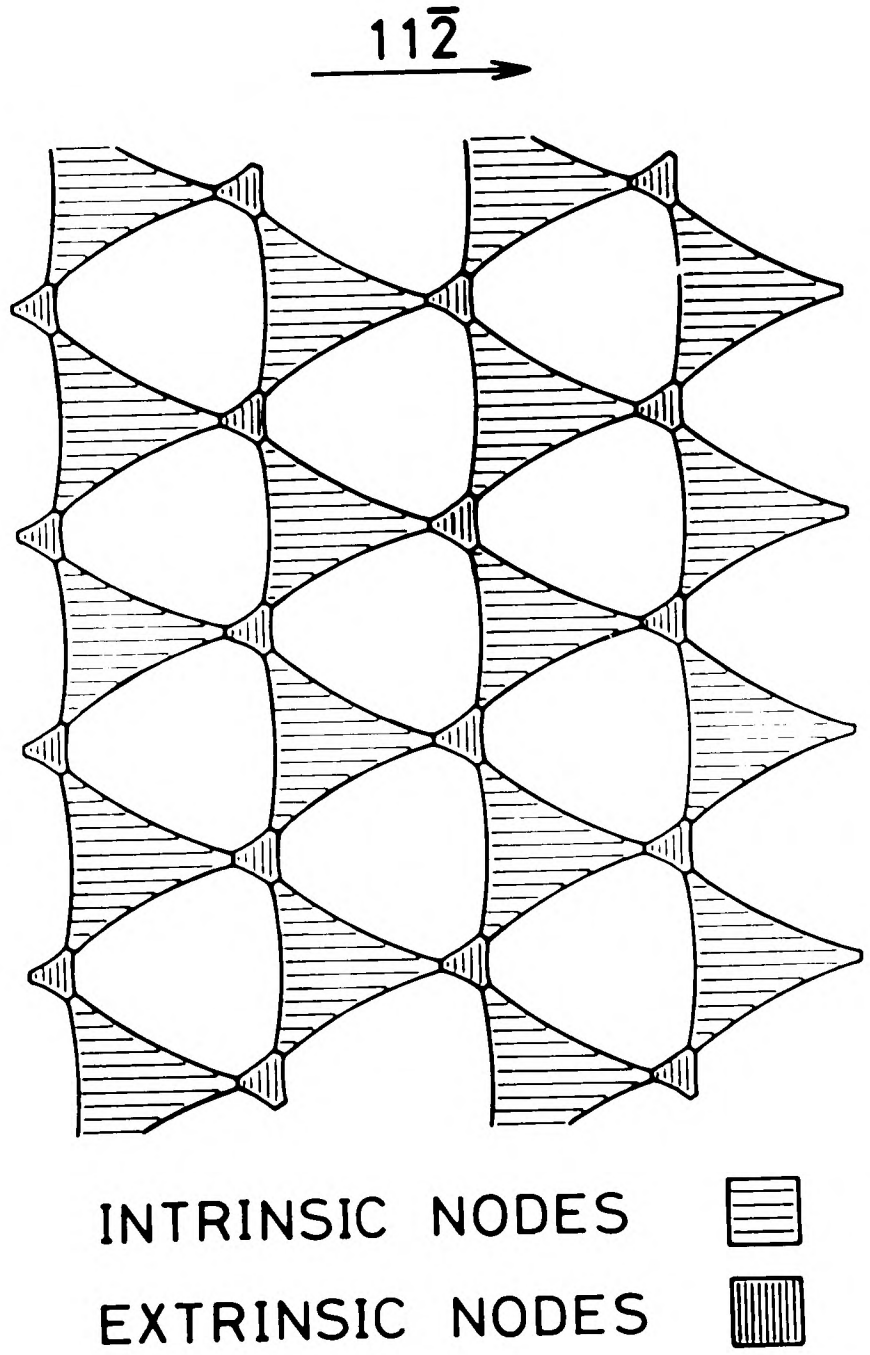
WB ⊙ $\bar{1}\bar{1}1$

• BF

Fig 6.17 Idealized model of Ge/(111)Si interfacial dislocation network. Note large intrinsic nodes and small extrinsic nodes.

Fig 6.16 Central portions of figs 6.15a and b at higher magnification, emphasizing the close relationship between the nature of the image contrast and the sense of the deviation from the Bragg position of the $\bar{1}\bar{1}1$ reflection.


$\bar{1}\bar{1}1$ BF
WB
$\bar{1}\bar{1}1$ BF
WB
100Å


$11\bar{2}$
INTRINSIC NODES
EXTRINSIC NODES

Weak-beam stereomicrographs confirmed that the dislocation networks lay in a plane in the expected region of the interface. Examination of micrographs such as those of fig 6.15 showed that the general structure of the networks sometimes changed over the areas of individual growth centres. This occurred when the epitaxial films had been grown under conditions which promoted Ge/Si alloy formation (i.e. high temperatures or low deposition rates). The uniformity of such a network was usually good at the middle of a growth centre, but became somewhat degraded towards the edges.

The inversions of stacking fault contrast at the dislocation nodes, which occurred with changes in the diffraction conditions as described above, were unexpected. To illustrate the observed behaviour, a TEM Kikuchi band diagram for a diamond lattice material is given in fig 6.18. The directions of the $\bar{1}\bar{1}1$ and $11\bar{1}$ **g** vectors are shown, and table 6.3 gives the experimentally determined visibility of the node stacking faults for each of these reflections. Fault contrast inverted for a change in either the direction of **g** or the sign of **s**, but was not critically dependent upon the magnitude of **s**. This behaviour was consistently observed with at least six different specimens produced using three different sets of film growth conditions, and will be discussed in section 6.5.2.

Table 6.3

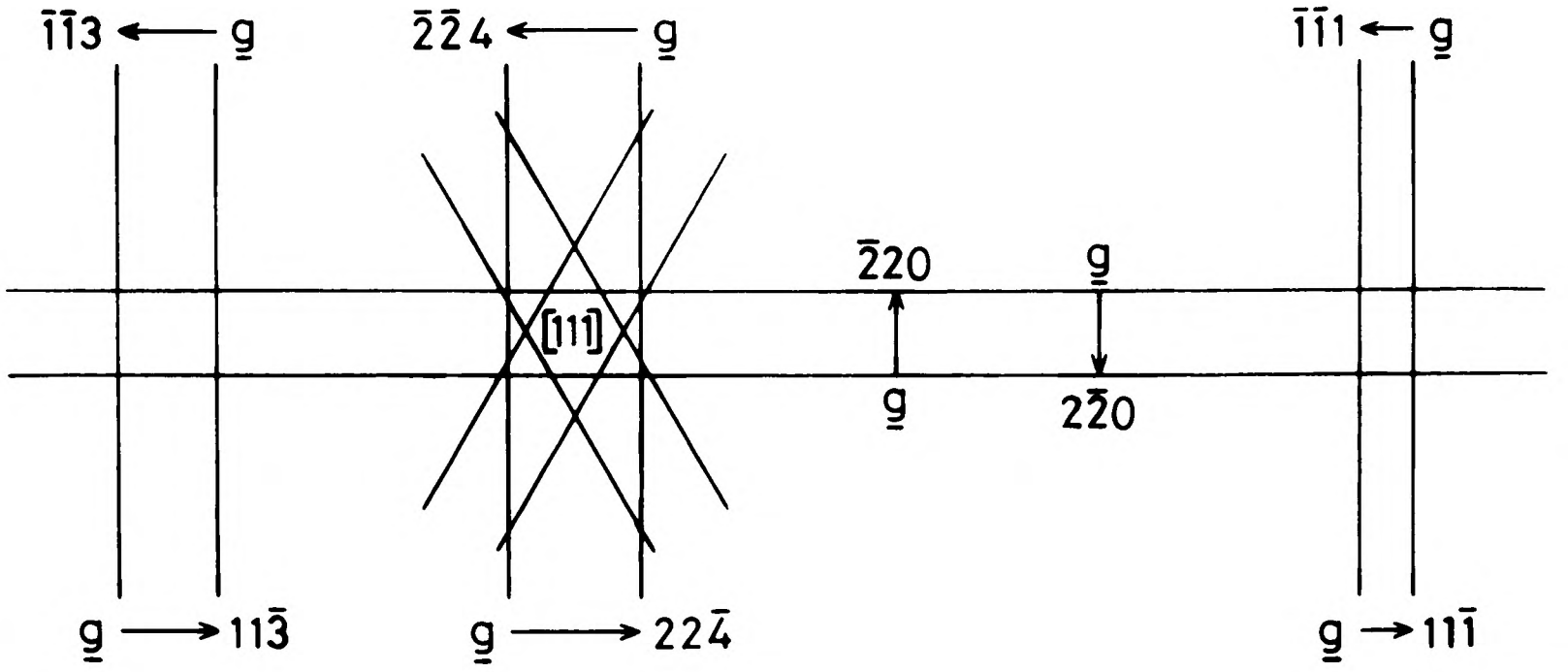
Stacking faults at dislocation nodes

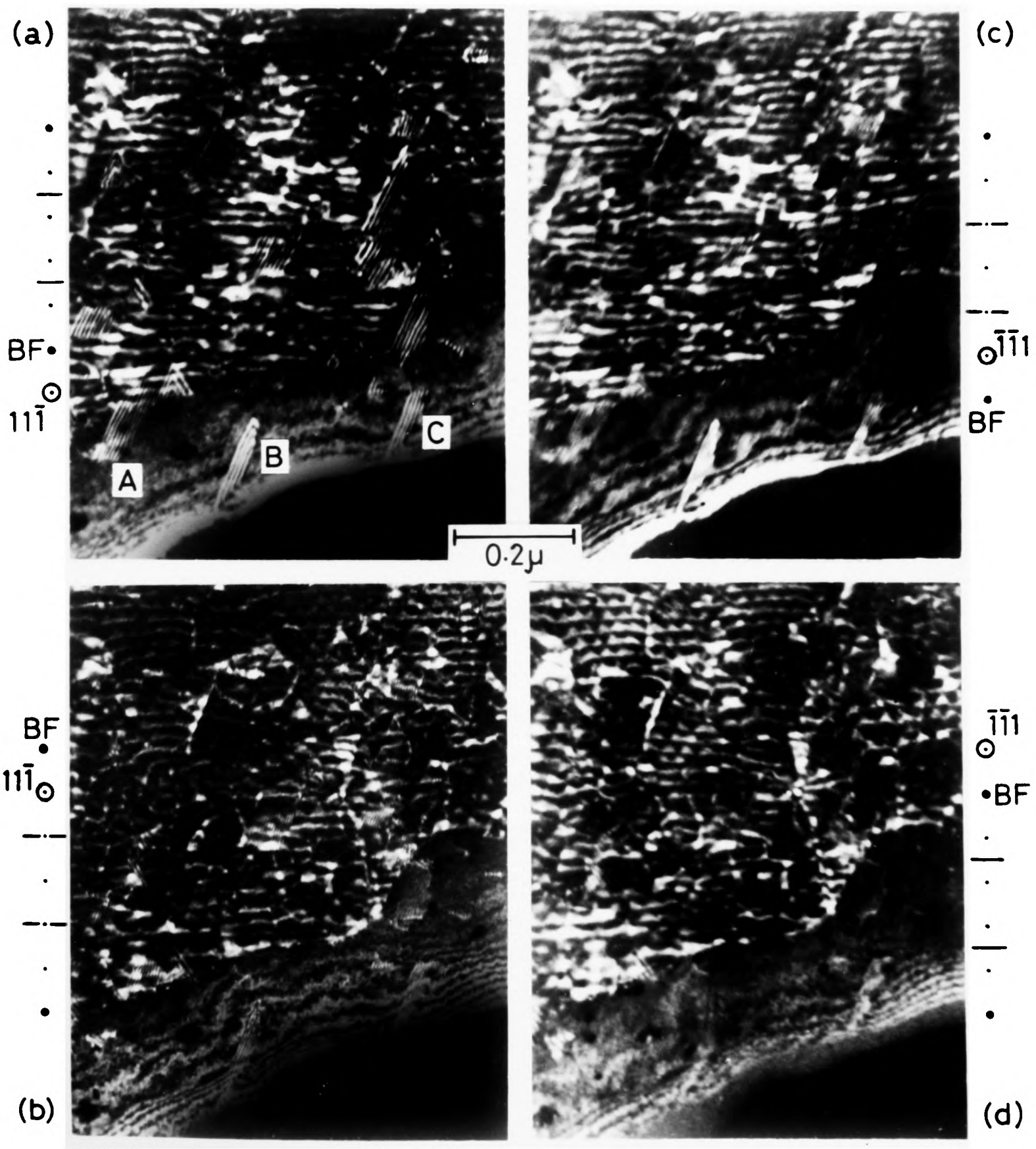
g	$\bar{1}\bar{1}1$		$11\bar{1}$	
s	+	-	+	-
Intrinsic Faults	invisible	visible	visible	invisible
Extrinsic Faults	visible	invisible	invisible	visible

Other film defects exhibited a related contrast anomaly. Stacking faults had often grown up through the films on inclined $\{1\bar{1}\bar{1}\}$ type planes (see fig 4.8). When these were imaged using either the $\bar{1}\bar{1}1$ or $11\bar{1}$

Fig 6.18 Kikuchi band diagram around a [111] pole for a diamond lattice material. (At pole, [111] direction projects upwards out of page)

Fig 6.19 Weak-beam $11\bar{1}$ and $\bar{1}\bar{1}1$ dark-field TEM images, illustrating dependence of inclined stacking fault image intensity upon diffraction conditions. (125 kV)


$\bar{1}\bar{1}3$ ← g
$\bar{2}\bar{2}4$ ← g
$\bar{1}\bar{1}1$ ← g
$\bar{2}20$
g
[11]
g
$2\bar{2}0$
g → $11\bar{3}$
g → $22\bar{4}$
g → $11\bar{1}$


(a)
BF•
⊙ $11\bar{1}$
A
B
C
0·2μ
(c)
⊙ $\bar{1}\bar{1}1$
•BF
BF
•
⊙ $11\bar{1}$
(b)
⊙ $\bar{1}\bar{1}1$
•BF
(d)

reflection under weak-beam conditions, the contrast obtained depended markedly upon the sign of s as demonstrated in figs 6.19a-d. The stacking faults labelled A, B and C exhibited strong contrast for $\underline{g}\ 11\bar{1}$ ($s<0$) and $\underline{g}\ \bar{1}\bar{1}1$ ($s>0$) but weak contrast for $\underline{g}\ 11\bar{1}$ ($s>0$) and $\underline{g}\ \bar{1}\bar{1}1$ ($s<0$). This behaviour is the same as that exhibited by extrinsic nodes in the interfacial dislocation network, and the appropriate network contrast changes can be seen in the background. However, it was not possible to determine the nature of the inclined stacking faults (using e.g. the method of Gevers et al (1963)), due partly to their small size and partly to the overlapping network fringe images obtained under strong-beam conditions.

In the work described above, information was obtained concerning dislocation network structures and their related TEM contrast effects, together with the contrast behaviour of inclined stacking faults in the Ge/(111)Si system. To permit a more complete understanding of the various results, the experiments were extended to TEM studies of both dislocation networks and relatively large inclined stacking faults in single crystals of Si. This work is described in the next section.

6.4) Observations of Defects in Single Crystal Silicon

6.4.1) Weak-Beam Observations of Dislocation Networks

Dislocation networks in single crystals of Si were examined by use of the weak-beam technique. The networks had been produced by deformation of the Si in tension up to $\sim 7\%$, at a temperature of 900°C (Howe, 1968), and the specimens were cut parallel to the (111) slip plane. TEM observations involved the use of $11\bar{1}$, $2\bar{2}0$, $11\bar{3}$ and $22\bar{4}$ type reflections, over a range of associated values of s. The results using $2\bar{2}0$ type reflections were least informative, and will not be described further.

When such networks on {111} planes were examined using the $\bar{1}\bar{1}1$

reflection under weak-beam conditions ($s < 0$), as shown in fig 6.20a, all whole dislocations were observed to have dissociated into Shockley partial dislocations separated by ribbons of stacking fault, as previously seen by Ray (1971). The intensity of the contrast exhibited by the partial dislocations (Burgers vectors ($\underline{b}_p$) of the type $\frac{a}{6}[\bar{2}11]$) depended upon $|\underline{g}.\underline{b}_p|$ which could take values $\frac{1}{3}$ or $\frac{2}{3}$ (see table 6.2). For example, the whole dislocation A (in $\sim 60^\circ$ orientation; $\underline{g}.\underline{b} = 0$) was bounded by partial dislocations for which $|\underline{g}.\underline{b}_p| = \frac{1}{3}$, and which exhibited only weak contrast. However, the ribbon of stacking fault produced by the dissociation was expected to be visible (see section 6.3.4), and this, presumably, contributed most of the image intensity. For whole dislocations B and C (in $\sim 60^\circ$ and edge orientations, respectively; $|\underline{g}.\underline{b}| = 1$) the lower partial dislocations had $|\underline{g}.\underline{b}_p| = \frac{2}{3}$ and exhibited relatively strong contrast. The other two partials had $|\underline{g}.\underline{b}_p| = \frac{1}{3}$ and mostly exhibited much weaker contrast, although they were not always invisible. This enabled separations between the partial dislocation images to be measured, and for micrographs recorded such that $|s| \gtrsim 1.2 \times 10^{-2}$, the values obtained varied between $\sim 65 - 75$ Å for dislocations between 60° and edge orientations. Indeed most dislocations were observed to have an orientation in this range, and accordingly, few were present in screw orientation.

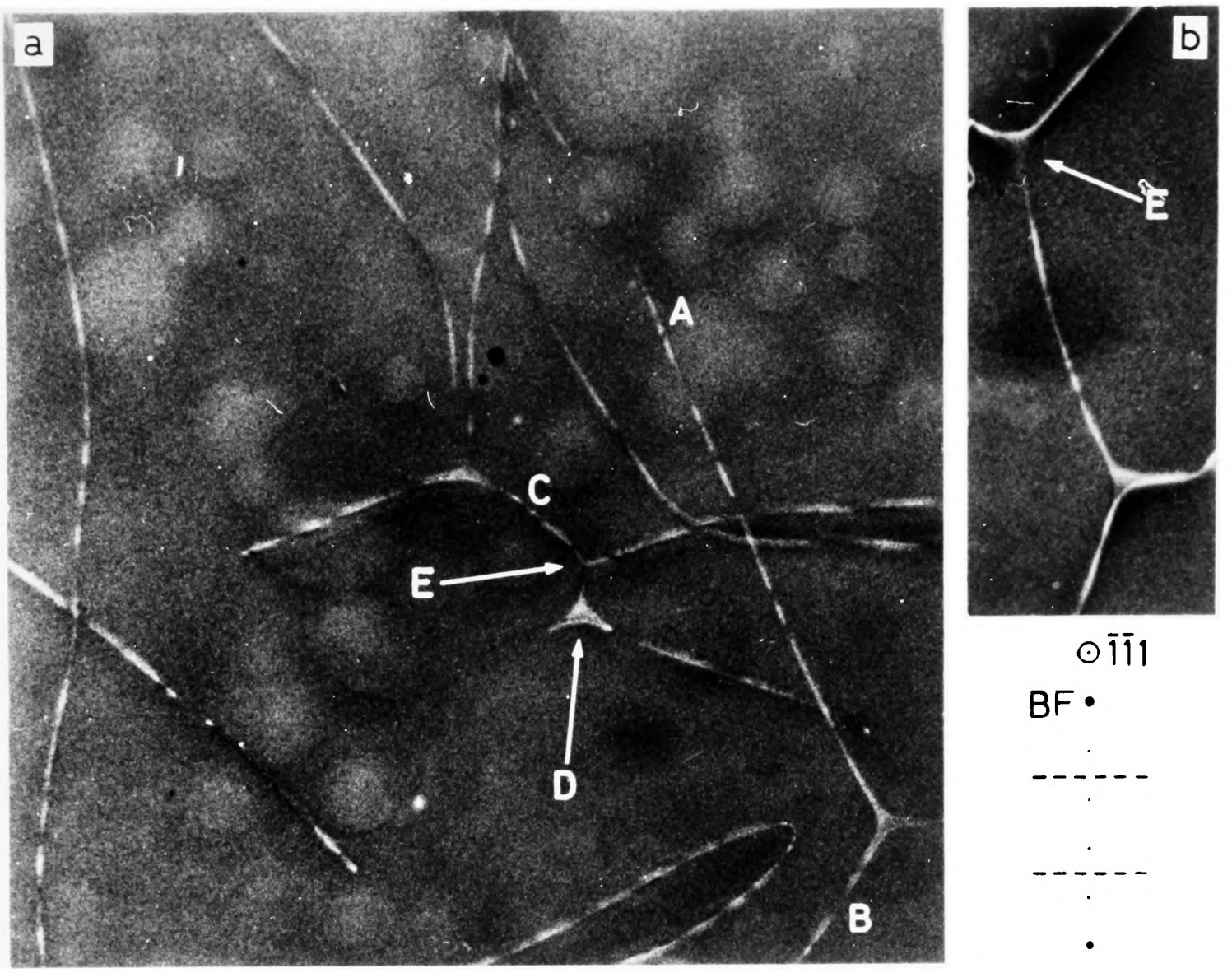
All intrinsic threefold dislocation nodes were observed to be extended. The orientation of a node is specified by either the character of the whole dislocations leading into it, or the character of the partial dislocations at their points of maximum curvature within the node; both give the same result. During the present work, most nodes were observed to lie between 60° and edge orientations. The intrinsic nodes were of uniform size, and the radius of an inscribed circle (fig 6.25) was generally 120 ± 20 Å. The minimum radii of curvature of partial dislocations bounding intrinsic nodes (fig 6.25) were difficult to measure, and were observed to

Fig 6.20 Weak-beam $\bar{1}\bar{1}1$ dark-field TEM images of a dislocation network, illustrating dependence of image contrast upon diffraction conditions, and showing extent of dislocation node dissociation:

a) and b) s negative

c) and d) s positive

(a and b same specimen areas as c and d, respectively)


a
b
A
C
E
D
B
E
⊙ 1̄1̄1
BF •
c
0·2μ
d
⊙ 1̄1̄1
BF •

vary somewhat. However, for 60° nodes measured values were usually 510 ± 60 Å, and for edge nodes the values were marginally lower. In contradistinction to this, approximately half of all extrinsic nodes were observed to be contracted (e.g. E in fig 6.20a), while the other half had a reasonably uniform extension approximately equal to that of the intrinsic nodes (e.g. E in fig 6.20b). The curvature of the partial dislocations bounding extrinsic nodes was always less than the curvature of those bounding intrinsic nodes of the same size.

The contrast exhibited by both dislocations (for which $\underline{g}.\underline{b} = 0$) and dislocation nodes depended markedly upon TEM imaging conditions. Using the $\bar{1}\bar{1}1$ reflection ($s < 0$), both the dislocations and the intrinsic nodes showed strong contrast, while extended extrinsic nodes exhibited relatively weak contrast, (figs 6.20a and b). Similar results were obtained using the $11\bar{1}$ reflection ($s > 0$). However, using either the $\bar{1}\bar{1}1$ reflection ($s > 0$) (figs 6.20c and d) or the $11\bar{1}$ reflection ($s < 0$) the intensity of the contrasts reversed. In these cases, both $\underline{g}.\underline{b} = 0$ dislocations and intrinsic nodes were only weakly visible, while extended extrinsic nodes showed stronger contrast as illustrated.

Unfortunately, weak-beam observations of dislocation networks using $11\bar{1}$ type reflections were complicated by another contrast effect. Image structures sometimes exhibited periodic contrast extinctions (fig 6.20), which were thought to be produced in a manner analogous to fringes at inclined stacking faults, as the crystallographic defects changed their depths in the specimen foils. However, the extinctions were usually closely spaced, and it was often difficult to determine e.g. whether specific nodes were out of contrast simply due to depth extinction, or alternatively, due to the nature of the imaging conditions. Nevertheless, it had been observed that depth extinctions were much less pronounced in weak-beam images recorded using $11\bar{3}$ type reflections. Therefore, examinations were continued using

such reflections, since they would also be expected to yield (111) stacking fault contrast, as previously noted in section 6.3.4.

Investigations showed that the overall form of $11\bar{3}$ type images of dislocation networks depended upon diffraction conditions in a manner analogous to the form of the corresponding $11\bar{1}$ type images, as given in table 6.4. This is illustrated in fig 6.21 which shows the reversals of the dislocation and node contrast intensities, for the operating $11\bar{3}$ reflection with values of $|s|$ of both $\sim 3 \times 10^{-3}$ and $\sim 1.1 \times 10^{-2}$ Å^{-1}. It is clear from fig 6.21 that the overall form of the image depended markedly upon the sign of s. The dislocations approximately parallel to the $11\bar{3}$ $\underline{g}$ vector were close to edge orientation so that $\underline{g}.\underline{b} = 0$, and for their bounding partial dislocations $|\underline{g}.\underline{b}_p| = \frac{2}{3}$ (table 6.2). This implies that these partial dislocations may have contributed substantial image contrast, unlike their counterparts imaged with the $11\bar{1}$ reflection for which $|\underline{g}.\underline{b}_p| = \frac{1}{3}$. Therefore, it was not immediately clear, when using $11\bar{3}$ type reflections, to what extent the node and $\underline{g}.\underline{b} = 0$ dislocation weak-beam images were produced by a combination of stacking fault and partial dislocation contrasts. Indeed, the $11\bar{3}$ type node images appeared rather more 'wing-shaped', and accordingly less uniform, than the corresponding $11\bar{1}$ type images, indicating that the bounding partial dislocations were probably visible.

Table 6.4

Dislocation network image contrast

g	$\bar{1}\bar{1}1$		$11\bar{1}$		$\bar{1}\bar{1}3$		$11\bar{3}$	
s	+	−	+	−	+	−	+	−
Intrinsic Nodes	W	S	S	W	W	S	S	W
Extrinsic Nodes	S	W	W	S	S	W	W	S
$\underline{g}.\underline{b} = 0$ Dislocations	W	S	S	W	W	S	S	W

W = weak, S = strong

To investigate this possibility, weak-beam images were recorded with operating $22\bar{4}$ type reflections, since these would be expected to show no (111) stacking fault contrast ($\underline{g}.\underline{R} = 0$, section 6.3.4). Separate micrographs were recorded using the $22\bar{4}$ reflection with $s < 0$ and then $s > 0$ (fig 6.22, which shows the same specimen area as fig 6.21). The $\underline{g}.\underline{b} = 0$ dislocations exhibited similar contrast in both $11\bar{3}$ and $22\bar{4}$ reflections, indicating that the partial dislocation images were probably more prominent than the stacking fault contrast in the $11\bar{3}$ type micrographs. Since the various node images were weaker in the $22\bar{4}$ type reflections, it is possible that fault contrast made a substantial contribution to the node images in the appropriate $11\bar{3}$ type micrographs, although, as noted earlier, contrast due to the bounding partial dislocations was also probably visible.

Examination of $22\bar{4}$ type weak-beam images of dislocation networks at higher resolution, showed the partial dislocation contrast behaviour more clearly. This is demonstrated in fig 6.23, which shows a small network of dislocations $\sim 10^{\circ}$ from edge orientation. The $\underline{g}$ vector is nearly parallel to dislocation TS for which $\underline{g}.\underline{b} = 0$, and for partial dislocations RS and TU $|\underline{g}.\underline{b}_p| = 1$, while for PQ $|\underline{g}.\underline{b}_p| = 2$ (table 6.2). For the diffraction conditions of fig 6.23a, the images of the partial dislocations RS and TU were displaced towards one another across dislocation TS, and exhibited stronger contrast in that region than when opposite partial dislocation PQ (fig 6.23b). When the sign of s was changed (figs 6.23c and d), these features changed as shown, as did the contrast given by partial dislocation PQ. Although $|s|$ is not quite the same for each micrograph (figs 623a and c), the contrast behaviour originally shown in fig 6.22 is readily explicable. The observed image dependence upon the sign of s will be discussed in section 6.5.2.

It is also clear from figs 6.22a and c that dislocations were undissociated at some points, as shown in the circled regions. This type of

Fig 6.21 Weak-beam $11\bar{3}$ dark-field TEM images of a dislocation network (same specimen area). Illustrates dependence of image contrast upon both sign and magnitude of s (approximate diffraction conditions given).

a) and b) $s \simeq 3 \times 10^{-3}$ Å^{-1}

c) and d) $s \simeq 1.1 \times 10^{-2}$ Å^{-1}

Dislocations nearly parallel to $11\bar{3}$ $\underline{g}$ vector show relatively strong contrast when s positive, but only weak contrast when s negative. Also, note strong characteristic 'kinematical' contrast given by diagonal dislocations in a) and b) (displaced image with sharp cut-off at core position (Hirsch et al. 1960)).

Fig 6.22 Weak-beam $22\bar{4}$ dark-field TEM images of a dislocation network (same specimen area as fig 6.21). Compare a) and b) with fig 6.21 c) and d), respectively.

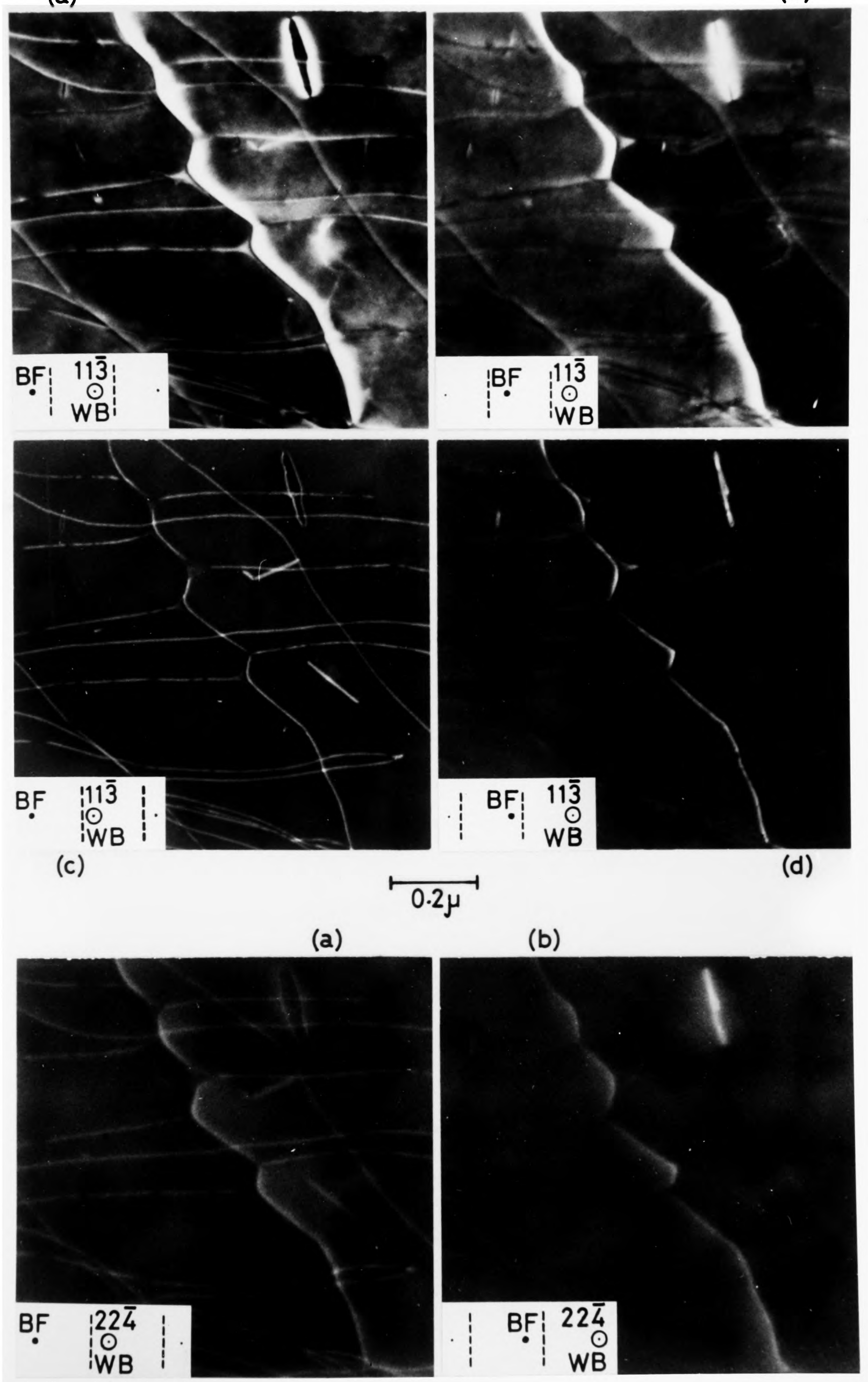

(a)
(b)
BF
$11\bar{3}$
WB
BF
$11\bar{3}$
WB
BF
$11\bar{3}$
WB
BF
$11\bar{3}$
WB
(c)
(d)
0·2μ
(a)
(b)
BF
$22\bar{4}$
WB
BF
$22\bar{4}$
WB

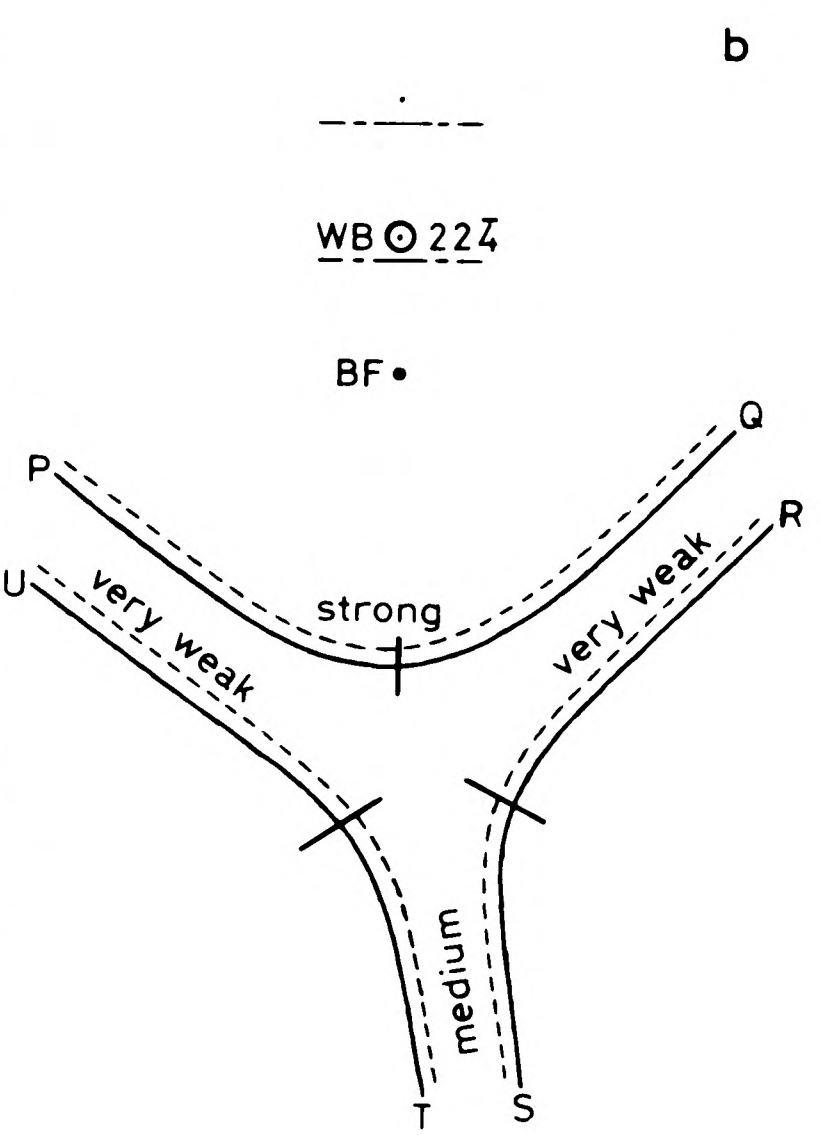
Fig 6.23 Weak-beam $22\bar{4}$ dark-field TEM images of a dislocation network (same specimen area), with illustrative diagrams of intrinsic node region showing displaced images and giving an indication of their relative intensities.

a) s positive, c) s negative

Circled regions show constrictions of partial dislocations.

(Short straight lines at node region in diagrams lie along the directions of the partial dislocation Burgers vectors.)

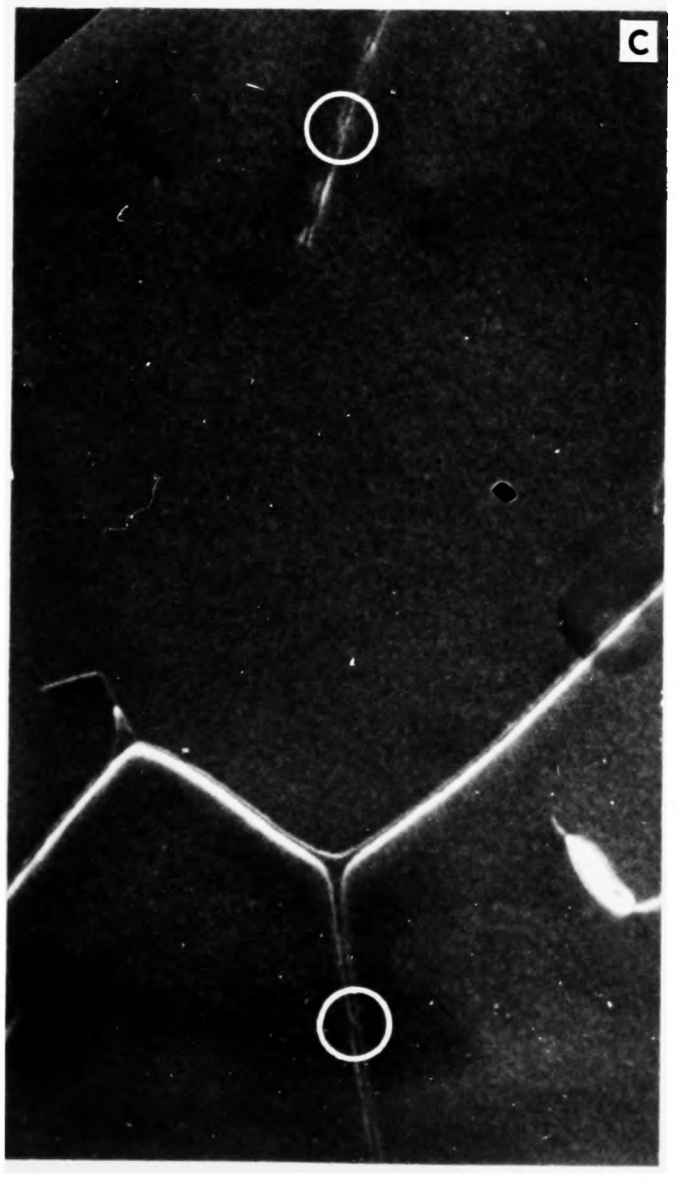


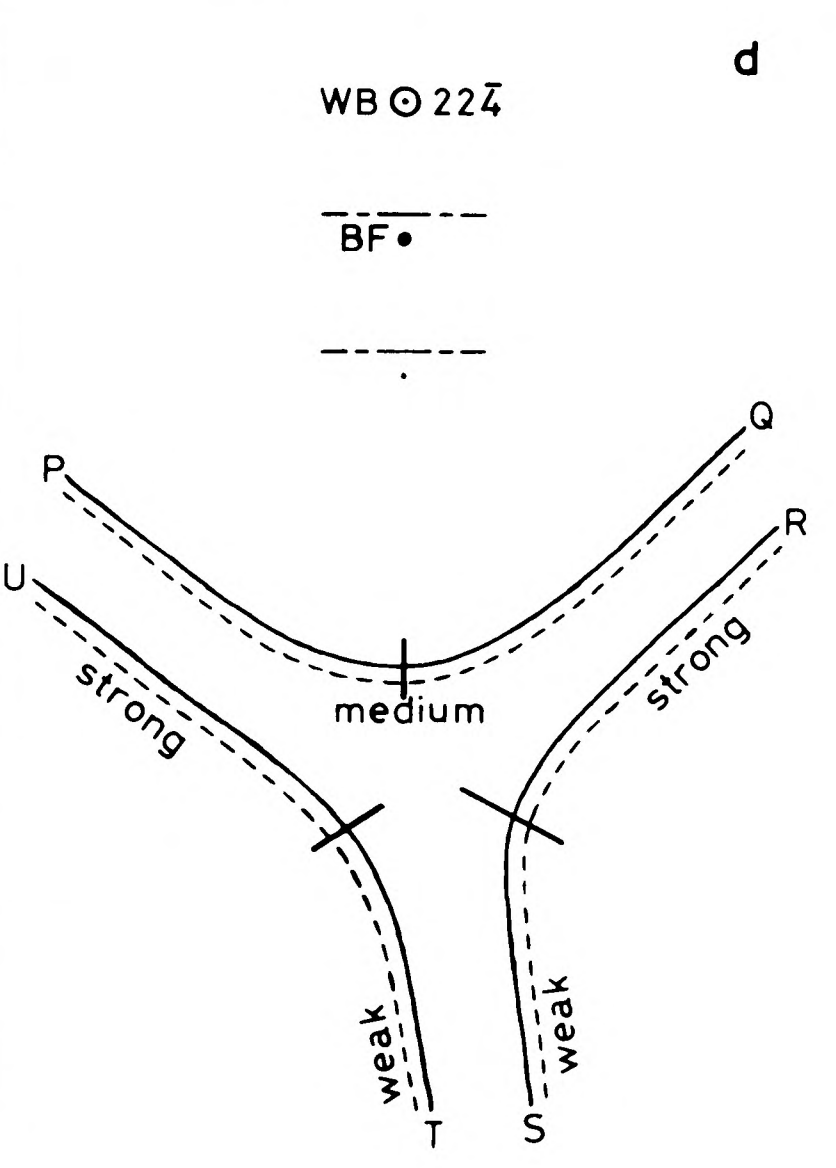


0·2μ

——— Partial Dislocations

----- Images





constriction was often seen, and may be analogous to that reported by Ray (1971).

The observations presented here have shown that both node and $\underline{g}.\underline{b} = 0$ dislocation weak-beam image contrast depended markedly upon diffraction conditions. However, it was often difficult to distinguish between stacking fault and partial dislocation contrast due to the small dissociation of the whole dislocations, which often made the images overlap one another. Therefore, the contrast behaviour of relatively large stacking faults was also investigated, to avoid these image overlap effects.

6.4.2) Weak-Beam Observations of Inclined Stacking Faults

When Si films had been grown on Si substrates in previous experiments (Unvala and Booker, 1964), initial surface contamination induced the formation of stacking fault defects. These were present on inclined $\{1\bar{1}\bar{1}\}$ type planes, and had grown larger as the film thickness increased. In the present work, such faults were examined in the TEM, and by use of the rule provided by Gevers et al (1963) it was observed that most of them were intrinsic in nature.

When these intrinsic stacking faults were examined using $\bar{1}\bar{1}1$ type reflections, the image contrast intensity depended markedly upon the absolute sense of the deviation from the Bragg reflecting positions. With the operating $11\bar{1}$ reflection, the expected bright/dark fringes were observed for $s = 0$. However for $s > 0$, the fringes became more closely spaced and rapidly decreased in intensity as s increased (fig 6.24). In thick crystals, such faults were effectively invisible before s had attained the value of 5×10^{-3} Å^{-1}, although their edges were still delineated by weak line contrast. In contradistinction to this behaviour, with the operating $\bar{1}\bar{1}1$ reflection, and again for $s > 0$, such faults remained visible even for extremely large deviations when s attained values of $> 1.6 \times 10^{-2}$ Å^{-1} (fig 6.24)

Fig 6.24 Weak-beam $\bar{1}\bar{1}1$ and $11\bar{1}$ dark-field TEM images of inclined stacking faults in Si (same specimen area). Illustrates dependence of image intensity upon diffraction conditions.

w	3.7	4.9	6.2	7.4	8.7	9.9	
s	0.57	0.76	0.95	1.14	1.33	1.52	$\times 10^{-2}$ Å^{-1}

$\bar{1}\bar{1}1$ g

$11\bar{1}$ g

0.5μ

Due to preferential chemical attack, during the thinning procedure required for TEM specimen preparation, the stacking faults were always present in Si crystals of non-uniform thickness. It was observed that the fault contrast inversions described above were most pronounced in crystals of thickness > several ξ_g (fig 6.24). However, in regions of decreasing crystal thickness, the contrast inversions became gradually less complete, first for stacking faults near the foil surfaces, and ultimately for faults at any position in the foil.

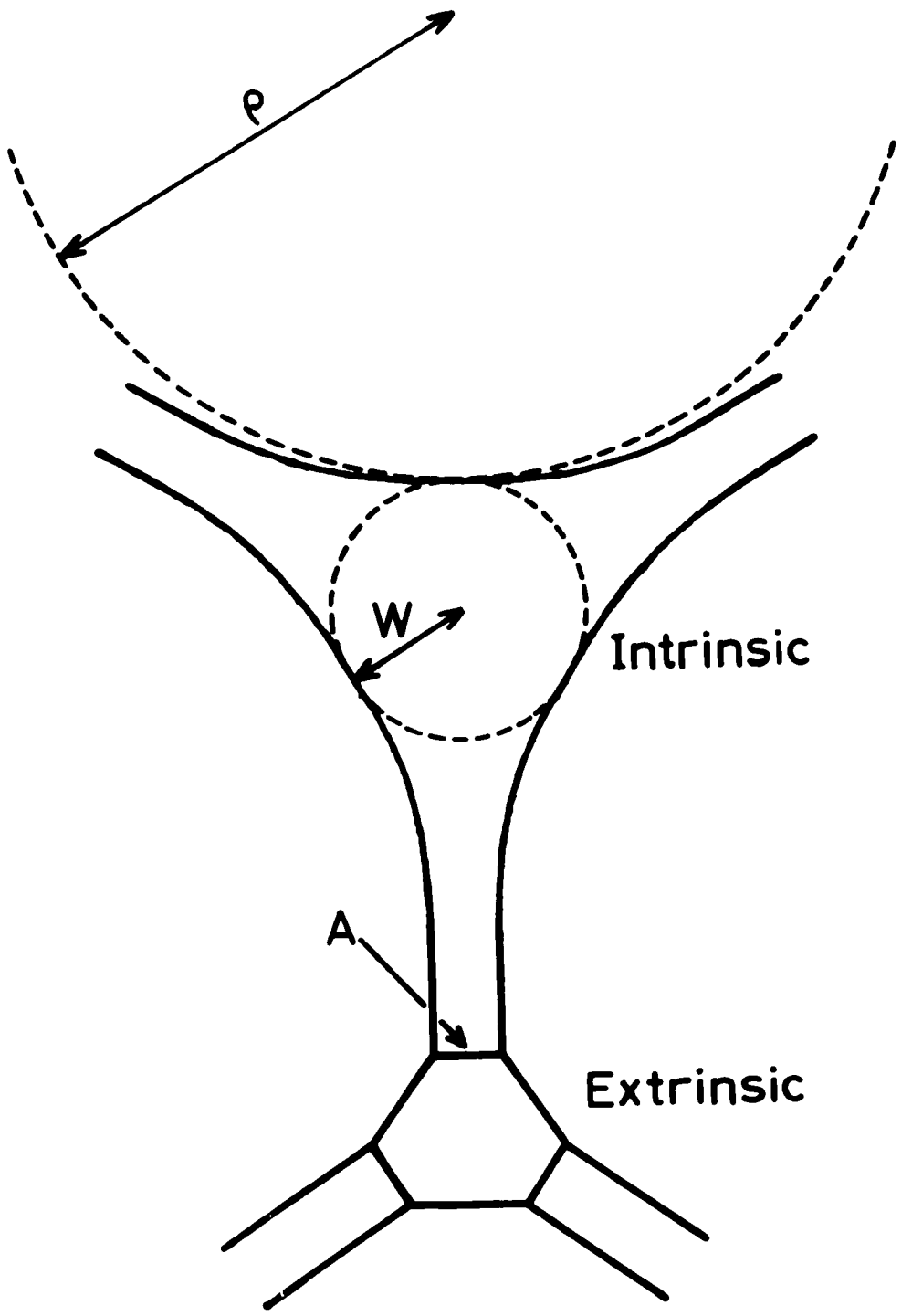
6.5) Discussion

6.5.1) Threefold Dislocation Nodes

The misfit dislocation networks produced in the Ge/(111)Si system (section 6.3) were very much more closely spaced than the networks present in the deformed single crystal Si (section 6.4.1). However, apart from these differences in scale, there were many similarities in the dislocation node behaviour. In both systems, all the intrinsic nodes and approximately half the extrinsic nodes were extended. These were quite well represented by the model originally proposed by Thompson (1953), shown in fig 6.25. The regions in which pairs of Shockley partial dislocations (section 6.3.1) cross over one another around the extrinsic nodes may be composed, as shown, of segments of the third type of partial dislocation pair. The truncated character of the extended extrinsic nodes in the Ge/(111)Si system indicates that this modification had probably occurred. However, while truncation of extended extrinsic nodes in single crystal Si was also sometimes observed, and was previously reported by Ray (1971), it was usually less pronounced.

Approximately half of the extrinsic nodes in both the Ge/(111)Si and single crystal Si systems were observed to be contracted. Possible explanations for this are in terms of either a very high extrinsic stacking

Fig 6.25 Diagram illustrating configuration of partial dislocations at intrinsic and extrinsic nodes. The regions where pairs of partial dislocations cross over one another around the extrinsic node may be composed of segments of the third type of partial dislocation pair (e.g. A).


ρ
W
Intrinsic
A
Extrinsic

fault energy (γ_E) or the presence of an energy barrier to node extension (Booker and Brown, 1965). The former possibility is unlikely, since no extrinsic nodes would then be expected to be extended, contrary to the observations. It is much more likely that there was an energy barrier to the initial extension of extrinsic nodes. Since they were surrounded by pairs of partial dislocations, it is possible that the nucleation of this double structure was kinetically unfavourable (Hirth and Lothe, 1968). Also, if e.g. unit jogs were associated with the dislocations at the extrinsic nodes, their presence might have influenced, in some way, the initial redistribution of atoms necessary for node extension. The general concept of an energy barrier is also in agreement with the observations of Ray (1971), who found that all extrinsic nodes were extended in Si deformed in torsion at 1200°C, when presumably, the proposed barrier would have been completely overcome. Whelan (1959) first showed that the equilibrium shape of extended threefold intrinsic nodes may be used to estimate the intrinsic stacking fault energy (γ_I). The important parameters are the radius of the inscribed circle (W) and the minimum radius of curvature of the bounding partial dislocations (ρ), as illustrated in fig 6.25. Brown and Thölén (1964) assumed isotropic elasticity, and gave equations derived from computed data which related W and ρ to γ_I

$$\frac{\gamma_I \rho}{Gb_p^2} = 0.27 - 0.08\left(\frac{\nu}{1-\nu}\right)\cos 2\phi + \left\{0.104\left(\frac{2-\nu}{1-\nu}\right) + 0.24\left(\frac{\nu}{1-\nu}\right)\cos 2\phi\right\}\log_{10}\frac{\rho}{\eta} \qquad (6.9)$$

$$\frac{\gamma_I W}{Gb_p^2} = 0.055\left(\frac{2-\nu}{1-\nu}\right) - 0.06\left(\frac{\nu}{(1-\nu)^2}\right)\cos 2\phi + \left\{0.018\left(\frac{2-\nu}{1-\nu}\right) + 0.036\left(\frac{\nu}{1-\nu}\right)\cos 2\phi\right\}\log_{10}\frac{\rho}{\eta} \qquad (6.10)$$

where G is the shear modulus of the material, ν is its Poisson ratio, ϕ is the angular deviation of the node from screw orientation and η is a dislocation core parameter (taken to be equal to b_p).

The application of these formulae to parameters derived from the

intrinsic nodes in the Ge/(111)Si networks is probably not useful, since the size and shape of these nodes would have been severely affected by interactions with other regions of the networks. However, the much more isolated intrinsic nodes of the networks in the deformed Si would be expected to have approached equilibrium configurations more closely. For these, as reported in section 6.4.1, when $\phi = 60^{\circ}$, $W = 120 \pm 20$ Å and $\rho = 510 \pm 60$ Å. For Si, taking $G = 7.9 \times 10^{11}$ dynes cm^{-2}, $\nu = 0.215$ (Hirth and Lothe, 1968) and $b_p = 2.22$ Å, eq 6.9 gives

$$\gamma_I = 58 \pm 13 \text{ ergs cm}^{-2}$$

and eq 6.10 gives

$$\gamma_I = 71 \pm 16 \text{ ergs cm}^{-2}$$

These values include an error of $\pm$ 10% to allow for uncertainties in the equations (Brown and Thölén, 1964).

Although the most probable values of γ_I from these individual determinations are separated by ~ 13 ergs cm^{-2}, nevertheless, they are in reasonable agreement since the error ranges are quite large. The experimental measurements of ρ and W are also reasonably consistent with one another since the ratio $\rho/W \simeq 4.2$, and this is approximately as expected for $\phi = 60^{\circ}$ (Brown, 1964).

In earlier work, Aerts et al (1962) obtained a value for γ_I of ~ 50 ergs cm^{-2} by measurements of Si intrinsic node geometry from TEM images recorded using unspecified diffraction conditions. However, from their micrographs, it is clear that there were several strongly excited operating Bragg reflections. Subsequent work by Booker and Brown (1965) and Shaw and Brown (1967) showed that, under such conditions, images of nodes with small extensions can be completely determined by contrast effects. Therefore, the results of Aerts et al may be subject to indeterminate errors.

Recently, for Si deformed in torsion at 1200°C, measurements of ρ from weak-beam images of intrinsic nodes were used by Ray (1971), in

conjunction with eq 6.9, to give $\gamma_I = 50 \pm 15$ ergs cm^{-2}. While this is a little lower than the values deduced from the present work, the possible error ranges overlap to a considerable extent. Ray also determined $\gamma_I = 51 \pm 5$ ergs cm^{-2} from measurements of partial dislocation separations along single dislocation lines. The calculations made allowances for anisotropic elasticity, and therefore, special confidence can be placed in this treatment. It is relevant that partial dislocation separations measured during the present work (section 6.4.1) are similar to those found by Ray, although only a small number of measurements were carried out. It should also be noted that for Si deformed at the highest temperatures impurity segregation may occur at the dislocations, and if this is the case it would be necessary to take it into account.

Intrinsic nodes at the Ge/(111)Si interface were usually smaller than their counterparts in the deformed single crystal Si, due to interactions in the closely spaced dislocation networks. However, in some interfacial regions with the largest dislocation spacings, the dimensions of the intrinsic nodes approached those of the nodes in single crystal Si, indicating that the values of γ_I were probably similar.

Extended extrinsic nodes exhibited somewhat different behaviour in the two systems. At the Ge/(111)Si interface, they were present over a range of sizes between that of the intrinsic nodes and the contracted form. While the reason for this is not completely clear, it may be due to general network interactions or to alloying between the Ge and the Si across the interface. In the single crystal Si specimens, the extended extrinsic nodes were of a more uniform size, approximately equal to that of the intrinsic nodes. This suggests that γ_I and γ_E were of the same order of magnitude (Ray, 1971). The edges of the extrinsic nodes had only a relatively small curvature, and this may have resulted from a minimization of the length of the bounding double partial dislocations, which probably

had a higher net core energy than the single partial dislocations around intrinsic nodes (Hirth and Lothe, 1968).

Although an accurate value for γ_E was not determined directly from experimental data, it is possible to make a reasonable estimate by the study of atomic models. In the covalently bonded Si lattice, both intrinsic and extrinsic stacking faults introduce closely similar unfavourable atomic repulsions and bond opposition strains, suggesting that $\gamma_I \simeq \gamma_E$. This conclusion is also obtained by consideration of faults in simple FCC structures (Hirth and Lothe, 1968), and experimental results for metal alloys suggest that it is correct (e.g. Loretto, 1964; Gallagher, 1966).

6.5.2) TEM Image Contrast and Crystal Defects

The nature of the TEM images expected for networks of closely spaced dislocations was described earlier in section 6.3, and will not be considered here.

One prominent feature of the observations described earlier concerns the changes in stacking fault image intensity with changes in both the direction of $\underline{g}$ and the sign of s. The most clearly defined examples of this behaviour are provided by the observations both of intrinsic and extrinsic faults within dislocation nodes in the foil planes (sections 6.3.4 and 6.4.1), and of relatively large inclined intrinsic faults (sections 6.3.4 and 6.4.2), with operating $11\bar{1}$ type Bragg reflections. This was not previously expected, and in each of the two cases the image intensity appeared to depend upon the sign of $(\underline{g}.\underline{R})\,s$. However, the behaviour of inclined intrinsic faults was analogous to that of the extrinsically faulted nodes in the foil plane, so that the angle or inclination was also apparently important. Furthermore, not all inclined faults exhibited these image intensity changes to the same extent (e.g. fig 6.19), and it is possible that the position of a stacking fault in the specimen foil may

also have been significant. Indeed, faults in thick foils exhibited the strongest contrast inversions (section 6.4.2), and therefore, anomalous absorption of electrons may have been involved. While the exact mechanism of the fault image intensity reversals is not yet clear, it may be directly associated with nature of the diamond lattice structure. It is possible that a complex interplay of selective electron Bloch wave excitation and absorption is involved.

The weak-beam image intensity changes with the direction of $\underline{g}$ and the sign of s, for both dislocation nodes and $\underline{g}.\underline{b} = 0$ dislocations, was probably dominated by partial dislocation contrast for operating $11\bar{3}$ type reflections. The manner in which this occurred is shown by micrographs recorded using $22\bar{4}$ type reflections (fig 6.23), which would be expected to show no accompanying stacking fault contrast. The various partial dislocation image displacements shown in fig 6.23 may be understood by consideration of dislocation models, in the way illustrated in fig 6.5. However, the image intensity at any position depended upon the magnitude of the component of the lattice strain in the direction of $\underline{g}$, and this varied in a complex manner due to interactions between the strain fields of adjacent partial dislocations.

In fig 6.23a, the image of partial dislocation RS ($\underline{g}.\underline{b}_p = 1$) was displaced towards both PQ and TU (fig 6.23b). The strain field of PQ strongly cancelled that of RS in the direction of $\underline{g}$, so that the image of RS was very weak when parallel to PQ. However, the strain field of TU moderately enhanced that of RS in the direction of $\underline{g}$, so that the image of RS became more intense accordingly. The image of PQ ($\underline{g}.\underline{b}_p = 2$) was displaced as shown, and was strong both due to the large value of $\underline{g}.\underline{b}_p$, and due to an enhancement of the strain field parallel to $\underline{g}$ by adjacent partial dislocations. When the sign of s was changed, the partial dislocation images moved and changed in intensity as shown (figs 6.23 c and d). The

explanations for this are analogous to those given above, and it is interesting to note that there was a region of enhanced intensity in one corner of the extrinsic node. Subsequent computations, performed for these specific micrographs (Saldin (1972), private communication), confirmed the basis for this contrast behaviour, and provided theoretical image profiles in good agreement with those obtained experimentally. However, the image contrast changes (especially for dislocation ST, $\underline{g}.\underline{b} = 0$) could be confusing if unanticipated, and illustrate that it is unwise to apply the simple $\underline{g}.\underline{b}$ method (Hirsch et al, 1965) for Burgers vector determinations using weak-beam images.

Partial dislocation constrictions of the type circled in fig 6.23 were frequently seen in the deformed Si specimens. Since these constrictions were point-like, it is possible that they were undissociated unit jogs in the dislocation lines. The line-tension of the 'stair rod' dislocations associated with such jogs could be responsible for the constriction.

In conclusion, it was reported earlier that when depth oscillations in image intensity were observed, then, for a given foil thickness and value of s, they were much more prominent with operating $11\bar{1}$ type reflections than with either $11\bar{3}$ or $22\bar{4}$ type reflections. While it is difficult to put forward a definite explanation for this behaviour, it may be explicable in terms of differences in Bloch wave scattering in the different crystal directions, although calculations would be necessary for confirmation.

6.6) Summary

The crystallographic structure of misfit dislocation networks at (111) crystal interfaces was discussed in detail. The information obtained was then related to the TEM image contrast expected under various diffraction

conditions. For strong two-beam operation, using a Bragg reflection with extinction distance ξ_g, Thölén (1970) has shown that if the dislocation spacing was $\lesssim \frac{1}{3} \xi_g$, a fringe image should be obtained, closely related to that produced by a basic Moiré effect. This general behaviour was confirmed by the present investigations, using observations of the misfit dislocation networks at the Ge/(111)Si interface. However, Thölén also claimed that it was impossible to resolve individual dislocations in such closely spacednetworks by any operations in the TEM. Nevertheless, the present work showed that this conclusion was incorrect, and important structural information was obtained concerning the nature of the interfacial networks by use of the weak-beam technique. It was observed that:

a) all intrinsic threefold dislocation nodes had a relatively large and uniform extension;

b) the extrinsic nodes had mostly a much smaller extension, but they were not of a uniform size and some appeared to be completely contracted;

and c) using $11\bar{1}$ type Bragg reflections, the intensity of the TEM contrast exhibited by the different kinds of node stacking fault were markedly dissimilar, and depended upon the sense of the deviation from the exact Bragg position.

In order to make comparisons of crystallographic structure, and to investigate the unusual node contrast behaviour, the TEM studes were extended to observations of crystallographic defects in single crystal Si.

TEM weak-beam examination of dislocation networks, present in the (111) slip plane of deformed Si specimens, showed that the extension of intrinsic threefold nodes was analogous to that observed in the Ge/(111)Si system. However, approximately half of the extrinsic nodes had a similar fairly uniform extension, while the other half were contracted. Based on these observations:

a) the dimensions of the intrinsic nodes were correlated with available theory, and this yielded values for the intrinsic stacking fault energy of 58 ± 13 or 71 ± 16 ergs cm^{-2}, depending upon the type of measurement employed;

and b) the extrinsic node behaviour was interpreted in terms of an initial energy barrier to node extension.

Using $11\bar{1}$ type reflections, both node and $\underline{g}.\underline{b} = 0$ dislocations gave weak-beam contrast which depended markedly upon the sense of deviation from the Bragg position. The behaviour was analogous to that observed for the Ge/(111)Si system. When observations were continued using $11\bar{3}$ type reflections, it was more difficult to distinguish between the stacking fault and partial dislocation contrasts. However, the manner in which partial dislocation contrast depended upon diffraction conditions was studied using $22\bar{4}$ type reflections, which rendered the (111) stacking faults invisible. The observed THI image behaviour was interpreted in terms of interactions between the partial dislocation strain fields.

The contrast behaviour of relatively large inclined $\{1\bar{1}\bar{1}\}$ type stacking faults in epitaxial Si films was also examined. These observations, together with those of (111) faults in dislocation network nodes, suggested that, 'ceteris paribus', the intensity of the weak-beam image contrast exhibited by stacking faults in thick foils may depend upon the sign of $(\underline{g}.\underline{R})$ s.

CHAPTER 7 SUGGESTIONS FOR FUTURE WORK

During epitaxial film growth by vacuum sublimation or evaporation techniques, an important factor in determining film quality is the effect of ambient residual gases. The extent of this effect will depend not only upon the nature and partial pressures of the various gases, but also upon other deposition conditions such as deposition rate and substrate temperature. In general, the use of relatively high deposition rates should favour the production of films of highest quality, since this minimizes the ratio of gas molecules to deposited atoms incident upon the substrate surface. However for a given substrate temperature the deposition rate may not be increased indefinitely, due to the nature of surface film growth processes. Concerning the properties of individual gases, those which contain carbon and are at least moderately reactive are the most undesirable (see sections 2.2 and 3.6). Fortunately, gases such as ethylene are rarely unintentionally present in conventional vacuum systems, although both CO and CO_2 are commonly found. Due to these considerations, for basic film growth studies, especially at low deposition rates, the vacuum capabilities of the film deposition apparatus could profitably be improved. It would be desirable to achieve a total ambient pressure of $< 10^{-10}$ torr during film growth, and to have the capability of maintaining this even during any substrate high temperature pretreatments. Apart from the provision of vacuum pumps with a higher pumping speed, it would be useful to employ water-cooled electrical lead-throughs for both source and substrate assemblies.

Considering specifically the Si/Si system, it was shown in chapters 2 and 3 that the form of film growth depended critically upon the state of the substrate surface prior to deposition. One method of cleaning the surface was pretreatment at a high temperature in vacuum, although this induced a certain amount of substrate surface step bunching and ultimately led to the formation of grown films with deep depressions at growth step pinning sites. The formation of these sites was caused by the presence on

the substrate surface of particles of SiC, which may have been a residue from the cleaning pretreatment. It is possible that their formation may be inhibited by modifying the temperature cycling, and it would be interesting to determine the optimum procedure. However, it would probably also be advantageous to develop other cleaning techniques.

One such technique which was investigated involved the use of gas polishing in H_2 (with a trace of H_2O vapour). Progress was made towards obtaining improved Si film uniformity, although certain limitations were placed upon the procedure since the vacuum apparatus had not been designed for use at atmospheric pressure. Accordingly, to take full advantage of the technique, it might be useful if it were carried out in a separate chamber constructed to allow the transfer of a cleaned substrate bar directly into UHV, through a 'vacuum-lock'. In this way it would be possible to test the use of more conventional polishing reagents, such as HCl and HBr. Furthermore, it would not be necessary to rebake the vacuum chamber, which would eliminate the possible recontamination of a substrate surface. A further improvement in the procedure would be produced by the use of the highest purity H_2 (e.g. from a large Pd diffuser), to avoid the presence of all possible undesirable impurity gases. Also, difficulty was experienced in achieving uniform electrical contact between the substrate bars and the W clips in which they were held, and therefore, a more convenient mounting arrangement would be desirable. There are other 'in situ' cleaning techniques, and one of the most recent is laser bombardment. This has a potential advantage over other methods, since it might be possible by careful wavelength selection to excite the desorption (but not decomposition!) of certain surface impurity species. If this could be carried out without imparting significant energy to the Si surface, it would minimize surface reactions and possibly reduce e.g. SiC formation.

Some features of Si film growth are not well understood, and in

particular, the general role of impurities in influencing film structure is unclear. Certain suggestions were put forward in chapters 2 and 3, and it would be desirable to conduct experiments to test them. Furthermore, studies of the detailed effects of contaminating gases could be extended, and related to e.g. surface adsorption and reaction kinetics. However, such an examination would probably require the use of other experimental methods of analysis such as Auger spectroscopy, and therefore would be a longer term project. Also, since it was found that under certain circumstances the presence of O_2 could be apparently beneficial to film growth, it would be interesting to determine the optimum treatment with O_2, and to decide whether this is a useful growth technique.

It is, of course, essential that carefully controlled impurities (dopants) should be present in Si films grown for electronic device applications. Therefore, it would be important to determine the effect of such dopants upon initial growth processes and upon resulting film perfection. Furthermore, it would be most interesting to investigate the uniformity of the transfer of dopants from source to grown films, and to examine the impurity concentration profiles through such films, especially in the region of p - n junctions fabricated 'in situ'.

Si film growth on unpreheated substrates led to the formation of optically observable growth centres (chapter 2). Their observed number densities were correlated with standard nucleation theory, and although consistent relationships were found to exist, uncertainties in the treatment remain to be resolved. These related to the generally lower than expected growth centre number densities, and to the range of values for energy parameters which could be derived depending upon which of the alternative theoretical treatments was employed. It is considered that more information is required concerning the nature of Si surfaces, together with the impurities present upon them, before a full understanding of initial growth processes

can be achieved.

Concerning the growth of Si on other substrate materials, experiments are at present in progress to continue the work initiated on the Si/diamond and Si/β-SiC systems. Difficulties have been encountered in the complicated TEM specimen preparation procedures required by the extremely hard substrates. However, these have now been overcome, and a full analysis of the Si film structures should soon be available. A most useful extension of this work would be to make an examination of the growth of Si on the insulator spinel. Although crystals of this material with a suitable crystalline quality have only recently become commercially available, it offers several potential advantages for film growth over the more easily available sapphire. It has a cubic lattice, giving the possibility of a unique epitaxial relationship with Si, and the crystallographic mismatch between the two is quite small. Furthermore, Si films are apparently contaminated much less by Al than corresponding films grown on sapphire.

The general study of heteroepitaxial systems using the TEM offers many advantages over other methods (e.g. optical, X-rays, etching studies, etc), due to its inherent high resolution. Also, many interesting defect structures would be expected to occur. In particular, by analogy with the Ge/Si system (chapter 4), in the absence of any special chemical interaction at the interface, a network of misfit dislocations would be expected to be present over the entire region of the heterojunction. Furthermore, general strains may induce the formation of numerous other film defects, which are conveniently analysed in the TEM.

During the high resolution TEM study of stacking faults both in Si and at the Ge/Si interface, unexpected image contrast behaviour was observed under weak-beam conditions. It is important to determine whether these observations are characteristic only of diamond lattice materials, or whether they may be reproduced using materials with other lattice structures.

Further, since the origin of this contrast behaviour remains uncertain, computer calculations to give the theoretically predicted images may be necessary for clarification.

In conclusion, the growth and investigation of thin epitaxial films has great relevance to many fields of both fundamental physics and its technological applications. It is, therefore, expected to assume increasing importance in the future.

APPENDIX A REVIEW OF HETEROGENEOUS NUCLEATION THEORY

A brief review will be given of nucleation theories relating to the initial heterogeneous growth of films produced by vapour condensation upon a solid surface. A historical sequence will generally be followed, and whilst many points of detail will be omitted to achieve a concise presentation, more extensive reviews are given by Hirth and Pound (1963), and Frankl and Venables (1970).

Nucleation theory originated in descriptions of the homogeneous nucleation of liquid droplets by vapour condensation in cloud chamber experiments. In this case, initial nuclei were relatively large (possibly greater than 100 atoms), since vapour supersaturations during the period of nucleation were relatively low. Under these conditions, it was permissible to use a Gibbs thermodynamic treatment as in the classical work of Volmer and Weber (1925), and Becker and Döring (1935). since the nuclei were large enough to be assigned bulk thermodynamic properties. When attention was transferred to heterogeneous nucleation upon a solid surface, with which we are concerned here, two dissimilar theoretical approaches were devised. The capillarity model, which evolved first, was based on the thermodynamic treatment of homogeneous nucleation, and was developed first by Volmer (1939), and later by many other workers including Pound, Simnad and Yang (1954), and Hirth (1959). This model also ascribes bulk thermodynamic properties to the initial nuclei, although vapour supersaturations for the process now considered are often so high (possibly greater than 10^{15}) that these nuclei may consist of only a few atoms. Therefore, in its basic form, this treatment is subject to serious reservations. The second model is an atomistic approach which is presented in terms of the binding energies of the nuclei, and although these must be determined experimentally, the problems of the

thermodynamic formulation are avoided. This atomistic model was developed initially by Frenkel (1924), Semenoff (1930) and Walton (1962), though recently it has been extended with more complex and varied treatments, such as those of Zinsmeister (1966), Lewis and Campbell (1967), Logan (1969), Halpern (1969), Stowell (1970), Frankl and Venables (1970) and Dettmann (1972).

A.1) The Capillarity Model

If one considers single atoms from a vapour incident at rate R upon a solid surface, for the case of incomplete condensation, where adatoms have a lifetime τ on the surface before re-evaporation, the equilibrium concentration of adatoms n_1 may be expressed

$$n_1 = \beta R \tau \qquad (A.1)$$

where β is the condensation coefficient. For thermally equilibrated adatoms, assuming β to be unity

$$n_1 = \frac{R}{\nu_o} \exp\left[\frac{\Delta G^*_{des}}{kT}\right] \qquad (A.2)$$

where ν_o is the surface vibration frequency of the adatom, ΔG^*_{des} is the Gibbs free energy of activation for desorption, T is the absolute temperature of the substrate and k is Boltzmann's constant.

The equilibrium concentration of nuclei containing i atoms is given by

$$n_i = n_1 \exp\left[\frac{-\Delta G_i}{kT}\right] \qquad (A.3)$$

which is the Van't Hoff isotherm where ΔG_i is the free energy of formation of such a nucleus. This latter parameter may be derived by thermodynamic arguments based on a physical model of the nucleus shape, which can be idealized as a spherical cap as shown by Pound et al (1954), although a disc-shaped model is sometimes a better approximation

(Hruska, 1963). In either case, ΔG_i increases with nucleus size up to a maximum of ΔG_{i*} for the so-called critical nucleus containing i* atoms. After this, ΔG_i decreases with increasing nucleus size, and yields a stable, growing cluster. For the cap-shaped model (Volmer, 1939; Pound et al, 1954),

$$i^* = - \frac{32\pi \sigma_{cv}^3 \phi(\theta)}{3\Omega' \Delta G_v^3} \qquad (A.4)$$

and $$G_{i*} = \frac{16\pi \sigma_{cv}^3 \phi(\theta)}{3\Delta G_v^2} + kT \ln\left(\frac{n_1}{N_o}\right) \qquad (A.5)$$

where σ_{cv} is the condensate-vapour specific interfacial free energy, Ω' is the condensate atomic volume, N_o is the number density of substrate surface sites for adatoms,

$$\phi(\theta) = \frac{2 - 3\cos\theta + \cos^3\theta}{4} \qquad (A.6)$$

$$\Delta G_v = - \frac{kT}{\Omega'} \ln\left(\frac{R}{R_e}\right) \qquad (A.7)$$

θ is the nucleus-substrate contact angle and R_e is the equilibrium departure rate of single atoms from bulk condensate. Hence, from eqs A.3 and A.5 the concentration of critical nuclei may be written

$$n_{i*} = N_o \exp\left[- \frac{16\pi \sigma_{cv}^3 \phi(\theta)}{3kT \Delta G_v^2}\right] = N_o \exp\left[\frac{-\Delta G_*}{kT}\right] \qquad (A.8)$$

Following from these important results, the steady-state nucleation rate I (rate of growth of nuclei through the size i*) has been derived (Frenkel, 1946; Russell et al, 1963) by treating the problem of nucleus growth in terms of nuclei diffusing through a size space, subject to a 'potential' gradient of $\partial \Delta G_i / \partial i$. In the general case, when nucleus growth by surface diffusion of adatoms dominates growth by direct addition of atoms from the vapour (Pound et al, 1954), one obtains

$$I = RZ\ 2\pi r^* a_s N_o \sin\theta\ \exp\left[\frac{\Delta G^*_{sd} - \Delta G^*_{des} - \Delta G_*}{kT}\right] \qquad (A.9)$$

where a_s is the intersite adatom jump distance, ΔG^*_{sd} is the free energy of activation of this surface diffusion process, Z is the Zeldovitch correction factor measuring the deviation of the adsorbate system from equilibrium and given by

$$Z = \left(\frac{\Delta G_{i*}}{3\pi kTi^{*2}}\right)^{\frac{1}{2}} \qquad (A.10)$$

and r* is the radius of curvature of the critical nucleus given by

$$r^* = -\frac{2\sigma_{cv}}{\Delta G_v} \qquad (A.11)$$

The factor $Z2\pi r^* a_s N_o \sin\theta$ in eq A.9 is a relatively insensitive function of R and T, and is typically near 10^{-1}. However, I is very sensitive to changes in R and T, and its dependence upon ΔG_* (and hence ΔG_v) is so decisive that we may effectively define a 'critical super-saturation', given by $(R/R_e)_{crit}$, below which I is zero and above which I is extremely large. Although in an actual experiment this transition may be judged somewhat arbitrarily, depending upon the observation technique, the onset of nucleation is predicted to be so sensitive to changes in (R/R_e) that correlations with capillarity theory may be satisfactorily examined.

General nucleation kinetics at macroscopic surface steps have been studied by Chakraverty and Pound (1964). They showed that the observed behaviour should vary markedly with changes in adsorbate contact angle and step structure. Also, the effect of an incoherent nucleus-substrate interface has been treated by Turnbull and Vonnegut (1952).

Modifications to the basic theory are necessary if ΔG^*_{des} is large enough to give initially complete adsorbate condensation, so that there is a time-dependent adatom concentration. Here, at time t we have

$$n_1 = Rt \qquad (A.12)$$

and eq A.7 is no longer valid in the form already given, since the system is not in overall equilibrium. In fact, one must write

$$\Delta G_v = - \frac{kT}{\Omega'} \ln \left(\frac{n_1}{n_{1e}} \right) \qquad (A.13)$$

where n_{1e} is the equilibrium concentration of adatoms at temperature T. The expressions for ΔG_{i*}, I, etc change accordingly.

Under circumstances where critical nuclei contain only a few atoms major theoretical changes are necessary, since macroscopic thermodynamic concepts cannot meaningfully be applied to such small nuclei. Alternative treatments are considered in the next section.

A.2) Atomistic Models

In principle, a statistical mechanical model should be valid under all circumstances. However, in practice it becomes extremely complex when applied to large nuclei, so that the methods of the last section may then be preferable. Walton (1962) developed a simplified treatment, applicable to small nuclei, and approximated the partition function Q'_i of a nucleus containing i atoms in terms of N_o ground states at energy $-E_i$, so that

$$Q'_i = N_o \exp \left[\frac{-E_i}{kT} \right] \qquad (A.14)$$

This then led to the general relation

$$\frac{n_i}{N_o} = \left(\frac{n_1}{N_o} \right)^i \exp \left[\frac{-E_i}{kT} \right] \qquad (A.15)$$

and this has been widely used by other workers. Walton used it to calculate the nucleation rate by assuming that all nuclei larger than the critical nucleus i* are effectively removed from the system. Although equilibrium does not then strictly prevail, and the decay of

supercritical nuclei is also neglected, he derived

$$I = \frac{R\sigma_{i^*}}{a_s}\left(\frac{R}{\nu_o N_o}\right)^{i^*} \exp\left[\frac{(i^*+1)E_{ad} + E_{i^*} - E^*_{sd}}{kT}\right] \qquad (A.16)$$

Where σ_{i^*} is the capture width of a critical nucleus for a single atom, E_{ad} is the binding energy of a single atom to the surface and E^*_{sd} is the activation energy for adatom surface diffusion. In this case it is not possible to obtain an analytical expression for i*, since E_i* is determined by the internal bonding which, in turn, depends upon the shape of the critical nucleus. However, a trial and error method may be used to find i* in a given situation, and Walton showed that in many common systems (e.g. condensation of a metal on an inert substrate) i* may be less than 7. This illustrates the inapplicability of the capillarity model in such a system. Also, since i* may vary with T, changes in the growth orientation of the deposit may occur as the shape of the critical nucleus changes.

This statistical mechanical approach was extended by Hirth (1963), who used a more realistic expression for Q'_i which involved excited states. However, the complexity of the resulting equations has restricted their usefulness. Also, Lewis (1967) compared this atomistic treatment with that of the capillarity model by formulating both in terms of bond energies. He then found that they shared a wide area of agreement, but this is hardly surprising since statistical mechanics forms a microscopic basis for macroscopic thermodynamics.

A major advance was made by Lewis and Campbell (1967) who based their approach on surface migration and capture considerations. They recognized that each deposited atom can be consumed by one of three competitive processes: 1) capture by a stable nucleus; 2) capture by a critical nucleus to form a stable nucleus; 3) desorption. They then developed the concept of capture areas, that is, hypothetical regions around nuclei within which deposited atoms are certain to be captured.

These ideas led to the same expression for nucleation rate I (eq A.16) as found previously by Walton, but they were further developed to show that the concentration of stable nuclei increases only up to a well defined saturation value N_s - an important finding. This occurs when the whole substrate surface is covered by the capture areas. Assuming that pairs of atoms are stable, for initially incomplete condensation (i.e. when desorption of adatoms is important)

$$N_s = N_o \exp\left[-\frac{(E_{ad} - E^*_{sd})}{kT}\right] \tag{A.17}$$

but, for initially complete condensation

$$N_s = \left(\frac{N_o}{\nu_o}\right)^{\frac{1}{2}} R^{\frac{1}{2}} \exp \frac{E^*_{sd}}{2kT} \tag{A.18}$$

Joyce et al (1967) extended these results to treat the case of a three atom smallest stable nucleus (complete condensation)

$$N_s = \left(\frac{N_o}{\nu_o^2}\right)^{\frac{1}{3}} R^{\frac{2}{3}} \exp\left[\frac{E_2 + 2E^*_{sd}}{3kT}\right] \tag{A.19}$$

and a four atom smallest stable nucleus

$$N_s = \left(\frac{N_o}{\nu_o^3}\right)^{\frac{1}{4}} R^{\frac{3}{4}} \exp\left[\frac{E_3 + 3E^*_{sd}}{4kT}\right] \tag{A.20}$$

While the arguments employed are, in fact, somewhat implausible for $i^*>1$, these equations are essentially similar to those obtained using assumptions of greater validity, as described below.

For the case of initially incomplete condensation, Halpern (1969) applied two-dimensional random walk theory to the migration of atoms over the substrate. Except when τ is very small this treatment gave results which were probably more exact than those of Lewis and Campbell, though the complexity of the formulation was so great that simplifying approximations were still required. Lewis (1970) used the random diffusion capture relation derived by Halpern and extended it beyond the

desorption controlled case, assuming a uniform depletion of the adatom population. While this is a further approximation, it was then possible to study the concentration of nuclei as a function of time.

For the case of complete condensation Stowell (1970) also solved a model diffusion problem to allow for the capture of adatoms by existing nuclei, giving a decreased nucleation probability in their vicinity. This was achieved by the provision of time-variable 'diffusion zones' around the nuclei such that the nucleation rate was zero inside the zones while being uniform outside. In the derivation of the diffusion zone radius, a curve fitting procedure was employed which relied upon experimentally observed values for certain parameters, and ultimately an analytical expression for N_s was obtained

$$\dot{N}_s = Q(i^*)\left(\frac{N_o^{\,2}}{\nu_o^{\,i^*+1}}\right)^{\frac{1}{i^*+3}} R^{\frac{i^*+1}{i^*+3}} \exp\left[\frac{E_{i^*} + (i^*+1)E^*_{sd}}{(i^*+3)kT}\right] \qquad (A.21)$$

relating to a critical nucleus of size i^*, where $Q(i^*)$ is a numerical factor of the order of unity. When $i^* = 1$, this equation is identical to that proposed by Lewis and Campbell (eq A.18) if $Q(i^*)$ is neglected. However, when $i^* = 2$ or 3, while this relation is not the same as that proposed by Joyce et al (eq A.19 or A.20), the differences are not of general form but are restricted to points of relative detail. Stowell also derived a modified version of eq A.21 in the case of nucleation at preferred sites, and further developed his theory to give an analytical expression for the time taken to reach nucleus saturation (t_s),

$$t_s = P(i^*)\left(\frac{N_o^{\,i^*+1}}{\nu_o^{\,2}}\right)^{\frac{1}{i^*+3}} R^{-\frac{i^*+1}{i^*+3}} \exp\left[\frac{E_{i^*} + 2E^*_{sd}}{(i^*+3)kT}\right] \qquad (A.22)$$

where $P(i^*)$ is a small numerical factor. More recently Routledge and Stowell (1970) extended the general approach by considering the nucleation which actually takes place within the diffusion zones, and also by allowing for the consequences of coalescence of stable nuclei. However, these

two effects change predicted N_s values by only small factors.

A final and alternative treatment of nucleation processes was based on the original work of Frenkel (1924), who considered the rates of formation and decay of atom pairs. This was extended to nuclei of arbitrarily large size by Zinsmeister (1966, 1968), who set up microscopic rate equations and solved them assuming n_1 to be constant and all nuclei to be stable. These are fairly restrictive conditions, and therefore this treatment is somewhat limited.

Important developments were made by Logan (1969), and following him we may write the generalised rate equations in the form

$$\frac{dn_1}{dt} = R - K_e n_1 + \sum_{i=3}^{\infty} K_{di} n_i + 2K_{d2} n_2 - n_1 \sum_{i=2}^{\infty} K_{f,i+1} n_i - 2K_{f2} n_1^2$$
$$\frac{dn_i}{dt} = K_{fi} n_1 n_{i-1} + K_{d,i+1} n_{i+1} - K_{f,i+1} n_1 n_i - K_{di} n_i \qquad \text{(A.23)}$$

where K_e is the rate constant for desorption of adatoms, K_{di} is the rate constant for decay of a nucleus of i atoms into an adatom plus a nucleus of i-1 atoms and $K_{f,i+1}$ is the rate constant for formation of a nucleus of i+1 atoms from collision between an adatom and a nucleus of i atoms. Certain assumptions are implicit in these equations, including the uniformity of all the various n_i over the substrate surface. While it is not, in general, possible to obtain an analytical solution from eqs A.23, Logan reduced them to a simplified dimensionless form, and by imposing two convenient and reasonable saturation criteria he derived expressions for N_s and t_s. These criteria, which had to be operative simultaneously, were first, that the depletion of adatoms due to growth of stable nuclei should be equal to the depletion of adatoms due to all other causes, and second, that dn_1/dt should be negative. Two cases were treated: (1) pairs stable (with possible desorption) and (2) triplets stable (with no desorption) assuming a quasi steady-state equilibrium

value for n_2. In each case the rate equations were constructed to depend upon single dimensionless parameters, which were respectively α (representing the rate of desorption of adatoms) and λ (representing the rate of decay of pairs). In case (1), the expressions obtained for N_s were nearly identical to those derived by Lewis and Campbell (eqs A.17, A.18). In case (2), Joyce's expression (eq A.19) and that of Stowell (eq A.21) were obtained (with small numerical differences) as alternative solutions under different conditions, though eq A.21 was produced in the more physically realistic situation. This work, which predated that of Stowell, is notable in that it unified the results of other workers who used completely different methods of analysis. In turn, this gives confidence that our present concepts of the basic nucleation processes are correct, at least in general terms.

In conclusion we may note that activity in this field of research is at present proceeding at a great rate. Stowell's approach was recently developed by Stowell and Hutchinson (1971 a, b), with the inclusion of considerable work on nucleation at preferred sites. Frankl and Venables (1970) extended Logan's treatment by numerical solution of the rate equations. However, Venables (1972) further developed this approach in a more general manner, and made an attempt to bridge the gap between the bases of the various theories. Dettman (1972) has also given a related treatment. Finally, it is interesting to note that the growth of crystals at low supersaturations has been re-investigated by Lewis (1971), who applied atomistic nucleation theory and studied the stabilities of individual nuclei. It was then claimed that the original treatment of Burton et al (1951) was not correct in its conclusion that growth can only occur in the presence of screw dislocations. However, this new result has not been generally accepted.

APPENDIX B REVIEW OF SELECTED NUCLEATION STUDIES

The various models proposed for heterogeneous nucleation phenomena are reviewed in Appendix A. The capillarity model led to an expression for the nucleation rate (I) as a function of experimental variables (eq A.9). This relation has been directly verified in certain systems, e.g. Na on CsCl (Hruska et al, 1967), but I is not an easy parameter to measure since it depends sensitively upon T. Therefore, many investigators have studied the relationship of both R and T to the 'critical supersaturation', which determines the point at which I becomes greater than zero. Cockcroft (1928), who investigated the deposition of Cd on to Cu, gave results which correlated well with capillarity theory, and the difference between the activation free energies for desorption and surface diffusion ($\Delta G^*_{des} - \Delta G^*_{sd}$) was found to be 17·2 kcal gm-atom^{-1} (Hruska, 1963).

The statistical mechanical model of Walton (1962), which may be applied when very small critical nuclei are formed, has also been tested. However, once again it was necessary to measure I (eq A.16), but this has been achieved by e.g. Walton et al (1963) who studied the deposition of Ag on to NaCl in UHV. They deduced that at 250°C there was a transition from a 1- to a 3-atom critical nucleus, and that the latter had a potential energy of formation (E_{i*}) of -2·2 eV. They also found that the energy for adsorption (E_{ad}) of Ag on NaCl was 0·4 eV, and that the activation energy for surface diffusion (E^*_{sd}) was less than 0·2 eV.

An important feature of more recent models of nucleation is that they lead to definite saturation values for the number density of stable nuclei. Lewis and Campbell (1967) investigated the deposition of Au on to NaCl cleaved in air, and found that the system did, indeed, give good N_s values. These were correlated with the theoretical treatment also devised by the authors (eqs A.17 and A.18), and the T dependence indicated a predicted transition from incomplete to complete condensation.

Joyce et al (1967, 1969a) studied the deposition of Si on to both (111) Si and (100) Si substrates, using the pyrolysis of SiH_4 as the deposition technique. Their results have already been given in section 2.2, and the work has special relevance to the experiments described in the remainder of chapter 2. It should be noted that although N_s values for the observed growth centres showed expected R and T dependences, the absolute values found were approximately seven orders of magnitude lower than predicted. This has yet to receive a completely satisfactory explanation, and was discussed in section 2.7.1.

Recently, Venables and Ball (1971) studied the growth of Xe, Kr and Ar on graphite at low temperatures, and carried out deposition during observation in a TEM specimen stage. For these adsorbate/substrate systems binding energies were already known, so that nucleation theory was subjected to a critical test. In fact, N_s values for growth centres exhibited the behaviour expected for a system under conditions of complete condensation, which is consistent with the adsorption energies known to be involved. Absolute N_s values appeared to be close to those expected using the Stowell theory (eq A.21), and also agreed well with independent solutions of rate equations related to those given in eqs A.23. However, the general interpretation was complicated since in some cases growth appeared to have taken place on top of an initial monolayer of adsorbed gas, and not directly upon the graphite.

APPENDIX C SILICON SURFACE STRUCTURE

The Si/Si crystal growth system is one in which there is strong binding of adsorbate to the substrate (Si - Si, 2·0 eV). Therefore, the initial growth of a Si film might be expected to be dependent upon the exact nature of these strong interactions, since they provide energy constraints for the growth processes. As an example of surface structures, the (111) Si surface will be discussed, since much work has been carried out using this Si orientation.

If a single crystal of Si is hypothetically sectioned to expose a (111) plane, with complete retention of atomic configurations, the so-called 'ideal' (111) Si surface is generated (top layer of atoms in fig 3.28). This exhibits a hexagonal array of unpaired Si bonds (sp^3 orbitals) projecting normal to the surface. It would be surprising if this artificially produced surface had a minimum of free energy, and in fact, it is found that all real (111) Si surfaces have undergone re-arrangement. This has also been predicted theoretically (Ducros, 1968), on the basis of Jahn-Teller splitting of otherwise degenerate electron energy levels.

Extensive LEED studies of (111) Si surfaces have shown that the diffraction patterns obtained vary with the method of surface preparation, and at present there is conflicting evidence as to which represents the clean surface. For instance, the production of the Si(111) - 7 x 7 pattern has been correlated with the presence of impurities such as Fe (see e.g. Thomas and Francombe, 1970), introduced by out-diffusion from the bulk crystal. However, this 7 x 7 structure has also been obtained from a (111) surface prepared by crystal cleavage at room temperature (Ridgway and Haneman, 1970), and in this case, impurity diffusion would be too slow to account for the result.

At least two different atomic models of (111) Si surfaces have been proposed to account for the general LEED data, and the basic structural

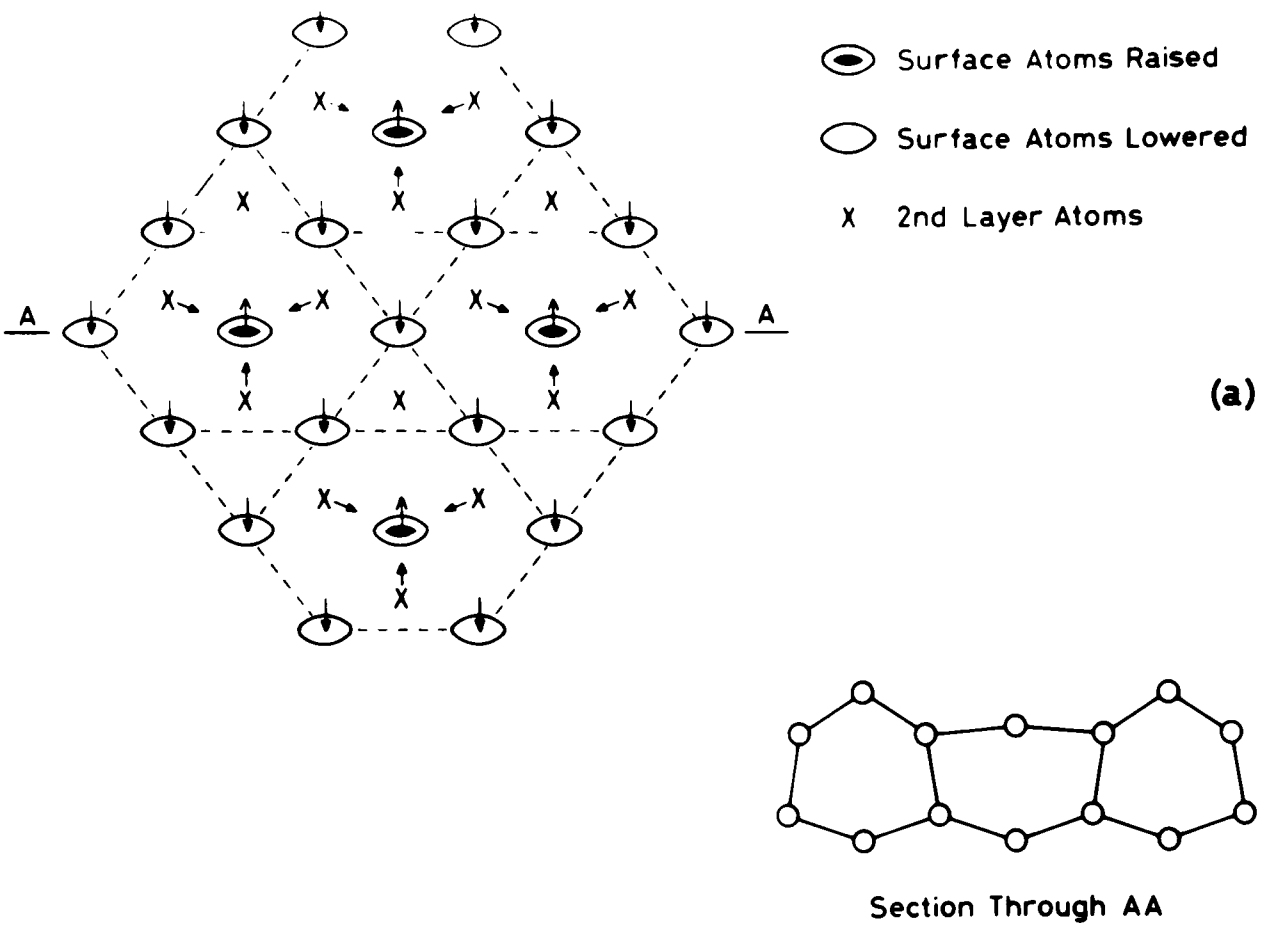
units of these are shown in fig C.1. The model originally devised by Haneman (1961) simply involved a surface rumpling, and was found to correlate well with LEED observations (Hansen and Haneman, 1964). Some atoms were raised while others were lowered, and Taloni and Haneman (1967) estimated the equilibrium atomic displacements. Atomic orbital rehybridization schemes showed that the lowered atoms would have 'dangling bonds' with enhanced p character, suggesting the possibility of electron delocalization by p - p overlap. The other model, proposed by Lander and Morrison (1963), required initial atom migration with the formation of large corrugated surface ring systems, probably involving substantial multiple bonding. However, the accompanying resonance stabilization would be unlikely to attain the magnitude of that found in benzenoid hydrocarbons. This is due partly to the Si ring non-planarity, and partly to the low tendency of Si to form multiple bonds in isolated molecules of its compounds.

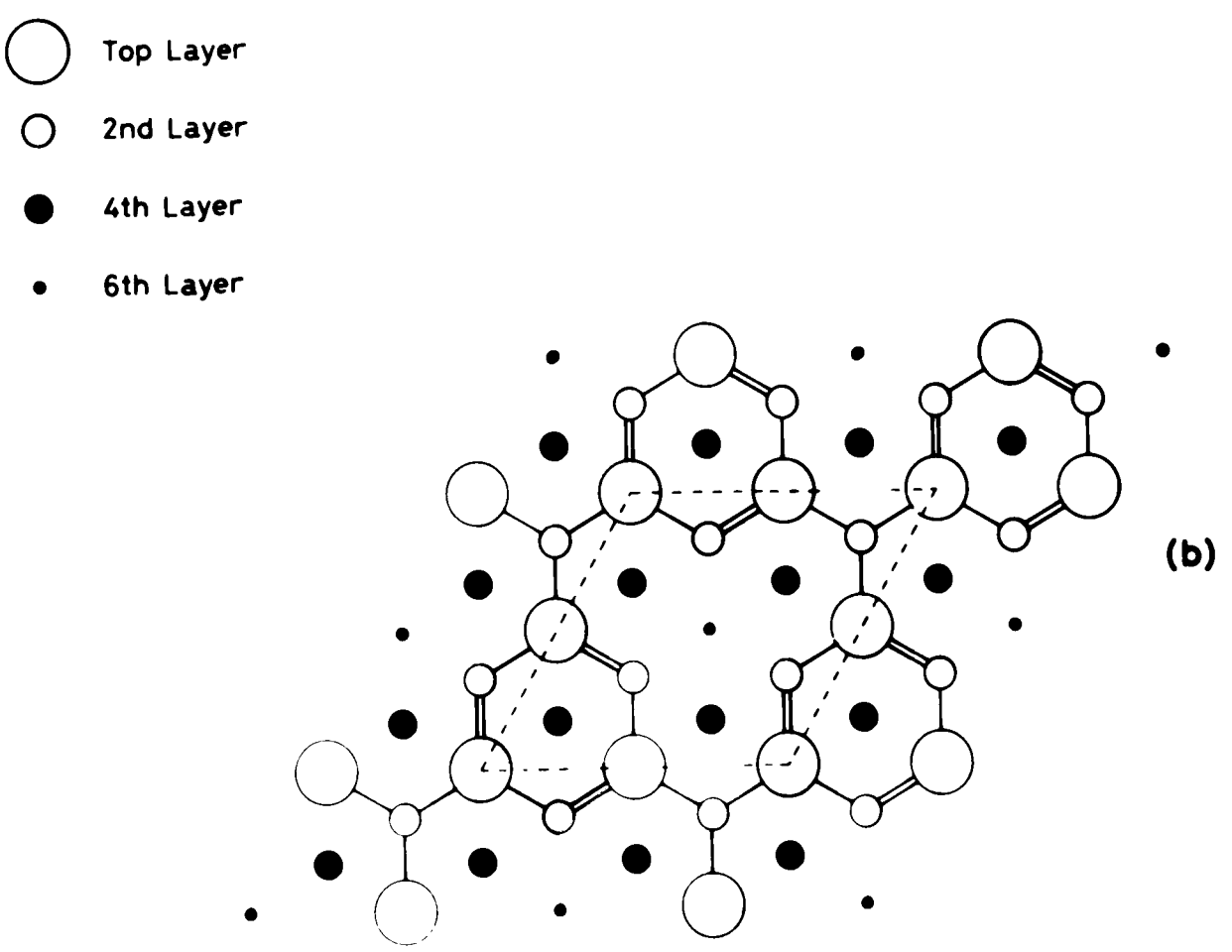
At the present time, it is not possible to give a definite structure for the (111) surface of Si. However, it may be surmised that the surface Si atoms will adopt a highly symmetrical superstructure, involving the formation of more than one type of surface adsorption site, due to atomic displacements. It is further expected that there will be a significant amount of surface electron delocalization, with the production of multicentre π - orbitals which conform to the symmetry of the surface structure. This expectation is supported by electron spin resonance (ESR) studies of cleaved (111) Si surfaces (Haneman, 1968), which indicated that the unpaired electron spin density is only approximately 8×10^{13} cm^{-2}. Since this is less than 10% of the number expected for an 'ideal' surface, substantial electron pairing must have taken place.

Fig C.1 Basic structural units of atomic models of (111) Si surface.

a) proposed by Haneman (1961)

b) proposed by Lander and Morrison (1963)


Surface Atoms Raised
Surface Atoms Lowered
X 2nd Layer Atoms
A
A
(a)
Section Through AA


Top Layer
2nd Layer
4th Layer
6th Layer
(b)

REFERENCES

Abbink H.C., Broudy R.M. and McCarthy G.P. (1968)
J. Appl. Phys. 39, 4673

Aerts E., Delavignette P., Siems R. and Amelinckx S. (1962)
J. Appl. Phys. 33, 3078

Allen F.G. (1957)
J. Appl. Phys. 20, 1510

Baker G.S. (1970)
D.Phil. Thesis, Oxford

Bassett G.A. (1960)
Proc. European Conf. Electron Microscopy, Delft, vol.1, p.270

Becker R. and Döring W. (1935)
Ann. Phys. [5] 24, 719

Bedair S.M. and Smith Jr. H.P. (1969)
J. Appl. Phys. 40, 4776

Berman R. (1965)
Physical Properties of Diamond, ed. R. Berman (Clarendon Press) p.371

Bicknell R.W., Charig J.M., Joyce B.A. and Stirland D.J. (1964)
Phil. Mag. 9, 965

Bicknell R.W., Joyce B.A., Neave J.H. and Smith G.V. (1966)
Phil. Mag. 14, 31

Billig E. (1956)
Proc. Roy. Soc. A229, 346

Biondi M.A. (1960)
Proc. Amer. Vac. Soc. Meeting, Cleveland

Booker G.R. (1970)
Modern Diffraction and Imaging Techniques in Material Science, eds. Amelinckx S., Gevers R., Remaut G. and van Landuyt J. (North-Holland), p.613

Booker G.R. and Brown L.M. (1965)
Phil. Mag. 11, 1315

Booker G.R. and Joyce B.A. (1966)
Phil. Mag. 14, 301

Booker G.R. and Stickler R. (1962a)
Brit. J. Appl. Phys. 13, 446

Booker G.R. and Stickler R. (1962b)
J. Appl. Phys. 33, 3281

Booker G.R. and Unvala B.A. (1965)
Phil. Mag. 11, 11

Brack K. (1965)
J. Appl. Phys. 36, 3560

Brown L.M. (1964)
Phil. Mag. 10, 441

Brown L.M. and Thölén A. (1964)
Discussions Faraday Soc. 38, 35

Burns J.R. and Scott J.H. (1969)
Proc. AFIPS Conf. 35, 469

Burton W.K., Cabrera N. and Frank F.C. (1951)
Phil. Trans. Roy. Soc. A243, 299

Chang C.C. (1971)
J. Vac. Sci. Technol. 8, 500

Chakraverty B.K. and Pound G.M. (1964)
Acta Met. 12, 851

Charig J.M. and Skinner D.K. (1969)
Surface Sci. 15, 277

Chu T.L., Francombe M.H., Gruber G.A., Oberly J.J. and Tallman R.L.(1965)
Westinghouse Res. Lab. Rep. No. AFCRL-65-574. AD61992

Cockayne D.J.H., Ray I.L.F. and Whelan M.J. (1969)
Phil. Mag. 20, 1265

Cockcroft D.J. (1928)

Proc. Roy. Soc. A119, 293

Craig R.D. and Harden E.H. (1966)

Vacuum 16, 67

Cullen G.W. (1971)

J. Crystal Growth 9, 107

Cullen G.W., Gottlieb G.E. and Wang C.C. (1970)

RCA Rev. 31, 355

Cullen G.W., Gottlieb G.E., Wang C.C. and Zaininger K.H. (1969)

J. Electrochem. Soc. 116, 1444

Cullis A.G. (1968)

B.A. Thesis, Oxford

Cullis A.G. and Booker G.R. (1970)

Proc. 7th Intern. Conf. Electron Microscopy, Grenoble, vol.2, p.423

Cullis A.G. and Booker G.R. (1971a)

J. Crystal Growth 9, 132

Cullis A.G. and Booker G.R. (1971b)

Proc. 25th Anniversary Meeting EMAG, Inst. Phys., Cambridge, p.320

Davidson S.M., Booker G.R. and Stickler R. (1971)

Proc. 25th Anniversary Meeting EMAG, Inst. Phys., Cambridge, p.298

Delavignette P., Tournier J. and Amelinckx S. (1961)

Phil. Mag. 6, 1419

Dettmann K. (1972)

Phil. Mag. (in press)

Dickson E.W. and Pashley D.W. (1962)

Phil. Mag. 7, 1315

Ditchburn R.W. and Custers J.F.H. (1965)

Physical Properties of Diamond, ed. R. Berman, (Clarendon Press) p.295

Ditchfield R.W. and Cullis A.G. (1970)

Proc. 7th Intern. Conf. Electron Microscopy, Grenoble, vol.2, p.125

Ducros P. (1968)

Surface Sci. 10, 295

Dumin D.J. (1970)

Solid State Electron 13, 415

Dumin D.J. and Robinson P.H. (1968)

J. Appl. Phys. 39, 2759

Dumin D.J., Robinson P.H., Cullen G.W. and Gottlieb G.E. (1970)

RCA Rev. 31, 620

Dushman S. (1962)

Scientific Foundations of Vacuum Technique, ed. J.M. Lafferty, (John Wiley)

Driver D., Wilks E.M. and Wilks J. (1971)

Proc. Intern. Conf. Synthetic Diamonds, Kiev, p.C1.

Evans T. and James P.F. (1964)

Proc. Roy. Soc. A277, 260

Faktor M.M., Fiddyment D.G. and Newns G.R. (1967)

J. Electrochem. Soc. 114, 356

Filby J.D. (1966)

J. Electrochem. Soc. 113, 1085

Filby J.D. and Neilsen S. (1967)

Brit. J. Appl. Phys. 18, 1357

Filyand M.A. and Semenova E.I. (1968)

Handbook of the Rare Elements, ed. M.E. Alferieff (MacDonald) vol. 1

Fowler H.A. and Marton L. (1965)

J. Appl. Phys. 36, 1986

Frank F.C. (1958)

Growth and Perfection of Crystals, eds. R.H. Doremus, B.W. Roberts and D. Turnbull (John Wiley) p.411

Frank F.C., Puttick K.E. and Wilks E.M. (1958)

Phil. Mag. 3, 1262

Frank F.C. and van der Merwe J.H. (1949)
Proc. Roy. Soc. A198, 216

Frankl D.R. and Venables J.A. (1970)
Advan. Phys. 19, 409

Frenkel J. (1924)
Z. Phys. 26, 117

Frenkel J. (1946)
Kinetic Theory of Liquids, (Oxford University Press)

Fujimoto T. and Yamaguchi J. (1968)
Jap. J. Appl. Phys. 7, 562

Gallagher P.C.J. (1966)
Phys. Status Solidi 16, 95

Gevers R. (1962)
Phil. Mag. 7, 1681

Gevers R., Art A. and Amelinckx S. (1963)
Phys. Status Solidi 3, 1563

Gjostein N.A. (1967)
Surfaces and Interfaces I, eds. J.J. Burke, N.L. Reed, V. Weiss (Syracuse University Press) p.271

Gottlieb G.E., Corboy J.F., Cullen G.W. and Scott J.H. (1971)
Met. Trans. 2, 653

Halpern V. (1969)
J. Appl. Phys. 40, 4627

Handelman E.T. and Povilonis E.I. (1964)
J. Electrochem. Soc. 111, 201

Haneman D. (1961)
Phys. Rev. 121, 1093

Haneman D. (1968)
Phys. Rev. 170, 705

Hansen N.R. and Haneman D. (1964)
Surface Sci. 2, 566

Hart P.B., Etter P.J., Jervis B.W. and Flanders J.N. (1967)
Brit. J. Appl. Phys. 18, 1389

Henderson R.C., Marcus R.B. and Polito W.J. (1971)
J. Appl. Phys. 42, 1208

Henderson R.C., Polito W.J. and Simpson J. (1970)
Appl. Phys. Letters 16, 15

Hirsch P.B., Howie A., Nicholson R.B., Pashley D.W. and Whelan M.J. (1965)
Electron Microscopy of Thin Crystals (Butterworths) p.371

Hirsch P.B., Howie A. and Whelan M.J. (1960)
Phil. Trans. Roy. Soc. A252, 499

Hirth J.P. (1959)
Acta Met. 7, 755

Hirth J.P. (1963)
Ann. New York Acad. Sci. 101, 805

Hirth J.P. (1965)
Energetics in Metallurgical Phenomena, ed. W.M. Mueller (Gordon and Breach) vol.2, p.1

Hirth J.P. and Lothe J. (1968)
Theory of Dislocations (McGraw-Hill)

Hirth J.P. and Pound G.M. (1957)
J. Chem. Phys. 26, 1216

Hirth J.P. and Pound G.M. (1963)
Condensation and Evaporation - Nucleation and Growth Kinetics, (Pergamon Press)

Holland L. (1965)
Thin Film Microelectronics (Chapman and Hall) p.122

Honjo G. and Yagi K. (1969)
J. Vac. Sci. Technol. 6, 576

Howe C.R. (1968)
B.A. Thesis, Oxford

Howie A. and Whelan M.J. (1962)
Proc. Roy. Soc. A267, 206

Hruska S.J. (1963)
Trans. Met. Soc. AIME, 227, 248

Hruska S.J., Hirth J.P. and Pound G.M. (1967)
Surfaces and Interfaces I, eds. J.J. Burke, N.L. Reed and V. Weiss (Syracuse University Press) p.305

Humphreys C.J., Thomas L.E., Lally J.S. and Fisher R.M. (1971)
Phil. Mag. 23, 87

Ito K. and Takahashi K. (1968)
Jap. J. Appl. Phys. 7, 821

Jacobs M.H., Pashley D.W. and Stowell M.J. (1966)
Phil. Mag. 13, 129

Jesser W.A. and Kuhlmann-Wilsdorf D. (1967)
Phys. Status Solidi 19, 95

Jesser W.A. and Matthews J.W. (1967)
Phil. Mag. 15, 1097

Jesser W.A. and Matthews J.W. (1968a)
Phil. Mag. 17, 461

Jesser W.A. and Matthews J.W. (1968b)
Phil. Mag. 17, 595

Johnson E.R. and Christian S.M. (1954)
Phys. Rev. 95, 560

Jona F. (1966)
Appl. Phys. Letters 9, 235

Joyce B.A. and Bradley R.R. (1966)
Phil. Mag. 14, 289

Joyce B.A., Bradley R.R. and Booker G.R. (1967)
Phil. Mag. 15, 1167

Joyce B.A., Bradley R.R., Watts B.E. and Booker G.R. (1969a)
Phil. Mag. 19, 403

Joyce B.A., Neave J.H. and Watts B.E. (1969b)
Surface Sci. 15, 1

Kimura T., Nunoshita M. and Yamaguchi J. (1966)
Jap. J. Appl. Phys. 5, 639

Lander J.J. and Morrison J. (1963)
J. Appl. Phys. 34, 1403

Larssen P.A. (1966)
Acta Cryst. 20, 599

Lewis B. (1967)
Thin Solid Films, 1, 85

Lewis B. (1970)
Surface Sci. 21, 273

Lewis B. (1971)
Paper presented at 2nd Intern. Conf. Crystal Growth and Epitaxy from the Vapour Phase, Marseilles

Lewis B. and Campbell D.S. (1967)
J. Vac. Sci. Technol. 4, 209

Linnington P.F. (1970)
Proc. 7th Intern. Conf. Electron Microscopy, Grenoble, vol.2, p.447

Linnington P.F. (1971)
Proc. 25th Anniversary Meeting, EMAG, Inst. Phys., Cambridge, p.182

Logan R.M. (1969)
Thin Solid Films, 3, 59

Loretto M.H. (1964)
Phil. Mag. 10, 467

Manasevit H.M. and Forbes D.H. (1965)
Proc. Amer. Phys. Soc. Meeting, New York

Manasevit H.M. and Forbes D.H. (1966)
J. Appl. Phys. 37, 734

Manasevit H.M., Forbes D.H. and Cadoff I.B. (1966)
Trans. Met. Soc. AIME 236, 275

Manasevit H.M., Miller A., Morritz F.L. and Nolder R.L. (1965)
Trans. Met. Soc. AIME 233, 540

Manasevit H.M., Nolder R.L. and Moudy L.A. (1968)
Trans. Met. Soc. AIME 242, 465

Manasevit H.M. and Simpson W.I. (1964)
J. Appl. Phys. 35, 1349

Matthews J.W. (1961)
Phil. Mag. 6, 1347

Matthews J.W. (1966)
Phil. Mag. 13, 1207

Matthews J.W. (1967)
Phys. Thin Films, vol.4, p.137

Mercier J. (1970)
Proc. Electrochem. Soc. Meeting, Los Angeles

Metherell A.J.F. (1971)
Advan. Optical and Electron Microscopy, eds. R. Barrier and V.E. Cosslett (Academic Press) vol.4, p.263

Miller A. (1967)
Electronics 40, 171

Mueller C.W. (1970)
J. Vac. Sci. Technol. 7, 147

Mullins W.W. and Hirth J.P. (1963)
J. Phys. Chem. Sol. 24, 1391

Naber C.T. and O'Neal J.E. (1968)

Trans. Met. Soc. AIME 242, 470

Nolder R.L. and Cadoff I.B. (1965)

Trans. Met. Soc. AIME 233, 549

Nolder R.L., Klein D.J. and Forbes D.H. (1965)

J. Appl. Phys. 36, 3444

Nunoshita M., Ishizu A. and Yamaguchi J. (1969)

Jap. J. Appl. Phys. 8, 1133

Pashley D.W. (1965)

Advan. Phys. 14, 327

Pashley D.W. (1970)

Recent Progr. Surface Sci., eds. J.F. Danielli, A.C.Riddiford and M.D. Rosenberg (Academic Press) vol.3, p.23

Paulus M. and Reverchon F. (1961)

Proc. Conf. 'Le Bombardment Ionique', Bellevue

Pettit H.R. and Booker G.R. (1971)

Proc. 25th Anniversary Meeting EMAG, Inst. Phys., Cambridge, p.290

Porter J.L. and Wolfson R.G. (1965)

J. Appl. Phys. 36, 2746

Pound G.M., Simnad M.T. and Yang L. (1954)

J. Chem. Phys. 22, 1215

Ray I.L.F. (1971)

D.Phil. Thesis, Oxford

Ray I.L.F. and Cockayne D.J.H. (1971)

Proc. Roy. Soc. A325, 543

Read W.T. (1953)

Dislocations in Crystals (McGraw-Hill)

Reynolds F.H. and Elliott A.B.M. (1966)

Phil. Mag. 13, 1073

Richter H. and Breitling G. (1958)
Z. Naturforschung 13a, 988

Ridgway J.W.T. and Haneman D. (1970)
Appl. Phys. Letters 17, 130

Ritchie R.H. (1957)
Phys. Rev. 106, 874

Robinson P.H. and Dumin D.J. (1968)
J. Electrochem. Soc. 115, 75

Robinson P.H. and Mueller C.W. (1966)
Trans. Met. Soc. AIME 236, 268

Routledge K.J. and Stowell M.J. (1970)
Thin Solid Films 6, 407

Russell K., Lothe J. and Pound G.M. (1963)
Condensation and Evaporation of Solids, eds. E. Rutner, P. Goldfinger and J.P. Hirth, Gordon and Breach

Scheuplein R. and Gibbs P. (1960)
J. Amer. Ceram. Soc. 43, 458

Schlötterer H. (1968)
Solid State Electron. 11, 947

Schlötterer H. and Zaminer Ch. (1966)
Phys. Status Solidi 15, 399

Schwoebel R.L. (1969)
J. Appl. Phys. 40, 614

Schwoebel R.L. and Shipsey E.J. (1966)
J. Appl. Phys. 37, 3682

Seiter H., Sirtl E. and Zaminer Ch. (1965)
Proc. 128th Electrochem. Soc. Meeting, Buffalo

Seiter H. and Zaminer Ch. (1965)
Z. Angew. Phys. 20, 158

Semenoff N. (1930)
Z. Phys. Chem. B7, 741

Shaw A.M.B. and Brown L.M. (1967)
Phil. Mag. 15, 797

Stowell M.J. (1970)
Phil. Mag. 21, 126

Stowell M.J. and Hutchinson T.E. (1971a)
Thin Solid Films 8, 41

Stowell M.J. and Hutchinson T.E. (1971b)
Thin Solid Films 8, 411

Takeishi Y., Sasaki I. and Hirabayashi K. (1967)
Appl. Phys. Letters 11, 330

Tallman R.L., Chu T.L., Gruber G.A., Oberley J.J. and Wolley E.D. (1966)
J. Appl.Phys. 37, 1588

Taloni A. and Haneman D. (1968)
Surface Sci. 10, 215

Tamura M. and Nomura M. (1967)
Appl. Phys. Letters 11, 196

Thewlis J. and Davey A.R. (1956)
Phil. Mag. 1, 409

Thölén A.R. (1970)
Phys. Status Solidi (a) 2, 537

Thomas R.N. and Francombe M.H. (1967a)
Appl. Phys. Letters 11, 108

Thomas R.N. and Francombe M.H. (1967b)
Appl. Phys. Letters 11, 134

Thomas R.N. and Francombe M.H. (1969)
Solid State Electron. 12, 799

Thomas R.N. and Francombe M.H. (1970)
Appl. Phys. Letters 17, 80

Thomas R.N. and Francombe M.H. (1971)
Surface Sci. 25, 357

Thompson N. (1953)
Proc. Phys. Soc. B66, 481

Tolansky S. (1960)
Surface Microtopography (Interscience Publishers)

Turnbull D. and Vonnegut B. (1952)
Ind. Eng. Chem. 44, 1292

Unvala, B.A. and Booker G.R. (1964)
Phil. Mag. 9, 691

van der Merwe J.H. (1963)
J. Appl. Phys. 34, 123

van der Merwe J.H. (1970)
J. Appl. Phys. 41, 4725

Venables J.A. and Ball D.J. (1971)
Proc. Roy. Soc. A322, 331

Venables J. (1972)
Phil. Mag. (in press)

Via G.G. and Thun R.E. (1961)
Proc. Amer. Vac. Soc. Meeting, New York.

Vincent R. (1969)
Phil. Mag. 19, 1127

Volmer M. (1939)
Kinetik der Phasenbildung, (Steinkopff)

Volmer M. and Weber A. (1925)
Z. Phys. Chem. 26B, 277

Walton D. (1962)
J. Chem. Phys. 37, 2182

Walton D., Rhodin T.N. and Rollins R.W. (1963)
J. Chem. Phys. 38, 2695

Watts B.E., Bradley R.R., Joyce B.A. and Booker G.R. (1968)
Phil. Mag. 17, 1163

Weisberg L. (1967)
J. Appl. Phys. 38, 4537

Weisberg L.R. and Miller E.A. (1968)
Trans. Met. Soc. AIME 242, 479

Whelan M.J. (1959)
Proc. Roy. Soc. A249, 114

Whelan M.J. and Hirsch P.B. (1957)
Phil. Mag. 2, 1121

Widmer H. and Gunther-Mohr G.R. (1961)
Helv. Phys. Acta 34, 635

Widmer H. (1964)
Appl. Phys. Letters 5, 108

Yagi K., Takayanagi K., Kobayashi K. and Honjo G. (1971)
J. Crystal Growth 9, 84

Yasuda Y. and Ohmura Y. (1969)
Jap. J. Appl. Phys. 8, 1098

Zinsmeister G. (1966)
Vacuum 16, 529

Zinsmeister G. (1968)
Thin Solid Films 2, 497